Targeting tumors and the kidney with siRNA nanoparticles and evaluation of extracellular microRNA-based methodologies to track their activity

Thesis by

Jonathan E. Zuckerman

In Partial Fulfillment of the Requirements for the

degree of

Biochemistry and Molecular Biophysics

CALIFORNIA INSTITUTE OF TECHNOLOGY

Pasadena, California

2012

(Defended May 17th 2012)

ACKNOWLEDGEMENTS

It has been a distinct pleasure working with my advisor Mark Davis. In particular, I have appreciated the level of respect he shows to his students and his commitment to them. I have also had the pleasure of working extensively with Antoni Ribas and am continually inspired by his commitment to his patients. I am also grateful for the helpful advice and critiques provided by my committee members Jim Heath and David Baltimore.

Thanks to the past and present members of the Davis lab. Thank you to Jonathan Choi and Han Han for working with me on multiple projects, to Devin Wiley for helpful discussions and technical advice, Yasho Bhawe for his out-of-field perspectives on my work, and to Leonard Medrano and Aaron Gale for their technical assistance in completing my projects. Special thanks as well to Martha Hepworth for helping me manage all the administrative intricacies of Caltech.

I would like to thank my collaborators Yun Yen, John Rossi, and Daniela Castanotto at City of Hope, and Richard Koya, Teli Hsueh, and Charles Ng in Antoni Ribas' lab at UCLA for their work and consultations. Also thanks to Gwen Williams and Jamie Rodriguez for their technical work at the Broad Animal Facility.

Thank you to my parents Jane and Jack Zuckerman for providing me with support and education to achieve my goals, and, to my grandmother Florence Adler, aunt and uncle Libby and Paul Hollombe, and sister Julia Zuckerman for their unwavering support. Thank you to my partner Jonathan Erde for putting up with my many hours in the lab and his proteomic work on the exosome project.

ABSTRACT

The goal of my thesis work is to discover new ways to enable the use of nanoparticle therapeutics to treat human disease. The work presented here touches on several areas in medicine and is united by a common theme: engineering ways to make, use, and evaluate therapeutics that maximize the benefit to the patient and minimize the harm. I have explored three interrelated strategies to achieve my objectives: (1) the use of targeted-nanoparticle-based therapeutics to deliver therapeutic entities to specific sites in the body, (2) the use of a highly specific type of therapeutic, siRNA, and (3) the evaluation of strategies for using extracellular microRNAs to non invasively monitor therapeutic activity and disease response to that activity.

In Chapter 2, I present the first evidence of targeted-nanoparticle delivery of siRNA to solid tumors following systemic administration to patients. My coworkers and I demonstrate both dose-dependent accumulation of the siRNA nanoparticles and evidence of gene knockdown via the canonical RNAi mechanism.

Chapters 3 – 5 describe the therapeutic potential of targeted nanoparticles (one version used in the clinic and described in Chapter 2) for: (i) targeting ribonucleotide reductase subunit M2 in human melanoma cell lines (Chapter 3), (ii) Herceptin-targeted nanoparticles containing siRNA against Her2 in Her2(+) breast cancer (Chapter 4), and (iii) siRNA targeting the “undruggable” protein N-Ras for N-Ras mutant melanomas (Chapter 5).

Chapters 6 – 8 focus on the interaction of nanoparticles with the kidney. Chapter 6 explores a previously unknown phenomenon of size-dependent glomerular accumulation of nanoparticles. In Chapter 7, a new mechanism of clearance for polycation-polymer-

based nucleic acid delivery systems is demonstrated, based on interactions between polymer components in the nanoparticle and the anionic surface of the renal filtration barrier, explaining the rapid clearance of these siRNA nanoparticle systems. Chapter 8 illustrates targeted-nanoparticle delivery of siRNA to the kidney.

In Chapter 9, I test the hypothesis that analysis of tumor-secreted microRNAs within patient blood samples can be used as real-time markers of drug pharmacodynamics. Specifically, I focus on efforts to characterize microRNA expression patterns following pharmacologic inhibition of the oncogene BRAF in melanoma cells and their secreted exosomes.

TABLE OF CONTENTS

LIST OF FIGURES AND TABLES

Chapter 1: Introduction and Thesis organization

1.1 Overall goal of thesis research: To develop ways to design, use, and evaluate nanoparticle-based therapeutics that seek to maximize the benefit to the patient while minimizing the harm

The results from my PhD research, prensented in this thesis, touch on many different areas of medicine including cancer treatment, evaluation of circulating microRNAs, and kidney physiology. Although diverse, each area of research presented here shares a common theme: engineering ways to design, use, and evaluate nanoparticle-based therapeutics that seek to maximize the benefit to the patient while minimizing the harm. In this work, my coworkers and I have explored three interrelated strategies: (1) the use of targeted-nanoparticle-based therapeutics to deliver therapeutic entities to specific sites in the body, (2) the use of a highly selective therapeutic, siRNA, to inhibit a single gene target with high specificity, (3) and the evaluation of strategies for using extracellular microRNAs to non-invasively monitor the activity of these types of therapeutics to aide in their clinical validation and employment.

1.2 Thesis organization

This thesis is comprised of chapters that fall into the three major research areas. The first research area focuses on evaluating siRNA nanoparticle-based therapeutics for use as anti-cancer therapies (Chapters 2-5). The second research area concentrates on understanding how nanoparticles behave at the kidney (Chapters 6-8). The final research

area (Chapter 9) focuses on evaluating the use of extracellular microRNAs as markers of drug response.

This chapter (Chapter 1) provides the background and motivation for all sections of the thesis. The advantages and behavior of nanoparticle-based therapeutics, siRNA based therapeutics, and extracellular microRNA markers are discussed.

In Chapter 2, the clinical proof-of-principle of nanoparticle delivery of siRNA to patient tumors is demonstrated. Our experiences from that study provided the motivation for the work presented in the third research area of this thesis. In Chapters 3, the therapeutic potential of the current, clinical siRNA nanoparticle formulation targeting ribonucleotide reductase subunit M2 (RRM2) via siRNA is examined in human melanoma cell lines. This example of RRM2 inhibition illustrates both the potential (activity over wide range of melanoma cell lines) of this target and its shortcomings (no induction of cell death). Chapters 4 and 5 provide examples of how siRNA based therapeutics can be used to overcome traditional barriers to cancer therapeutics. In Chapter 4 the therapeutic potential of using Herceptin targeted siRNA nanoparticles is demonstrated. siRNA inhibition of Her2 is also shown to achieve anti-tumor effects in cell lines that are resistant to Herceptin treatment. In Chapter 5 the use of siRNA targeting the “undruggable” protein N-Ras is explored as a possible therapeutic option for N-Ras mutant melanomas.

Chapters 6-8 focus on the interaction of nanoparticles with the kidney. The siRNA/CDP nanoparticle that has been used in animals and humans has been shown to have a faster than expected clearance time from circulation through a renal route. We

believe that understanding how these nanoparticles behave in the kidney will provide key insights into how to engineer a nanoparticle with a longer circulation time and thereby provide increase time to deposit in tumors. Additionally, from what we have learned in this work, we believe that siRNA nanoparticles have potential as a therapeutic modality for kidney disease.

Chapter 6 explores the general interaction of nanoparticles with the kidney and the discovery of previously unknown phenomenon of size dependent mesangial cell accumulation of nanoparticles. In Chapter 7, a new mechanism of clearance for polycation-polymer based nucleic acid delivery systems is demonstrated. This mechanism of clearance, based on interactions between polymer components in the nanoparticle and the anionic surface of the renal filtration barrier, explained the rapid clearance of the siRNA nanoparticle system and provides clues for strategies to engineer nanoparticles with longer circulation times. Chapter 8 explores the potential of targeted-siRNA nanoparticles as therapeutic modalities for kidney disease.

Chapter 9 focuses on testing the hypothesis that analysis tumor secreted microRNAs within patient blood samples can be used as real time markers of drug pharmacodynamics. Specifically, we focused on our efforts to characterize microRNA expression patterns following pharmacologic inhibition of the oncogene B-Raf in melanoma cell lines and their secreted exosomes. Chapter 9 summarizes our work to date in this area and discusses the challenges that must be overcome to translate these methodologies to the clinic.

1.3. Background:

1.3.1 Nanoparticle-based therapeutics have great potential for cancer and a multitude of other human ailments

The term nanoparticle-based therapeutics describes a varied array of therapeutic entities that are grouped together because of they are between 1 and 1000nm in size and are roughly spherical in shape. This class of therapeutic entities is usually distinguished from macromolecular-based therapeutics, such as therapeutic antibodies, that also fall into the nanoparticle size range[1]. Nanoparticle-based therapeutics are typically comprised of a therapeutic entity including small molecule drugs, nucleic acids, or proteins that are packaged together with structural components (e.g., lipids or polymers) into nanoparticle-sized objects[2]. There are also classes of nanoparticles composed of inorganic compounds such as gold, cadmium, or iron that are also being investigated as therapeutics and imaging agents[3,4].

1.3.1.1 Nanoparticle-based therapeutics can overcome two major barriers to successful drug usage and development.

The utility of traditional small molecule-based therapeutics is often limited by their side effects; sufficiently high doses for optimal therapeutic activity may not be reached before a dose limiting toxicity. Development of small molecule-based therapeutics can be stalled by the need to balance drug activity (pharmacodynamics) with the ability to be absorbed and distributed throughout the body (pharmacokinetics).

Nanoparticle formulation of drugs offers a solution to both these key problems in drug usage and development. Because of their size, nanoparticle-based therapeutics have restricted distributions throughout the body (biodistribution)[2]. Whereas small molecules

can move freely across small gaps in the cells lining blood vessel walls (endothelial cells), nanoparticles require large spaces between endothelial cells to move from blood circulation into body tissues[5]. After dosing, nanoparticle-based therapeutics are trapped in the blood stream, except when they enter tissues with fenestrated endothelium large enough to allow their passage into the tissue interstitia[6]. Endothelial barriers are compromised in many human pathologies such as cancer and inflammation. In these situations, nanoparticles can accumulate in these pathologic tissue to a high extent, while sparing the rest of the body from harmful side effects of their encapsulated drug.

Some healthy tissues possess fenestrated endothelium that allows for passive accumulation of nanoparticles and are potential sites for nanoparticle off-target toxicity. These tissues are liver, spleen and kidney. A common misconception is that nanoparticles should be readily delivered to bone marrow. Bone marrow microvasculature has an intact endothelial lining that includes diaphragmed-fenestrations[7]. Therefore, nanoparticles without surface modifications to encourage uptake by the bone marrow endothelial cells themselves[8] will not efficiently accumulate in the bone marrow.

The pharmacodynamic and pharmacokinetic properties of nanoparticle-based therapeutics can be decoupled. The structural components of nanoparticle therapeutics usually do not perform therapeutic actions; therefore, they can be modified and optimized to give the desired pharmacokinetic behavior, independent their ability to package their drug payload (or the biological activity of the drug). Because drug packaging into nanoparticles is usually mediated by hydrophobic interactions or convenient covalent linkages, drug design for a nanoparticle formulation need not be hindered by pharmacokinetic considerations. Additionally, this decoupling of pharmacodynamics and

pharmacokinetics means that the structural and therapeutic components of nanoparticles can be mixed and matched to suite the desired delivery location and therapeutic target without extensive re-design of any of the components.

1.3.1.2 Nanoparticle-based therapeutics can be tuned to enables more precise drug delivery to desired sites of action.

Besides overcoming traditional obstacles to drug usage and development nanoparticle-based therapeutic have several other desirable properties. Nanoparticles are highly tunable. Nanoparticle properties such as their size, surface composition (size and targeting-ligands), and decomposability can be tailored to specific applications. The behavior of nanoparticles in the body depends mostly on these three properties, regardless of the fundamental composition of the nanoparticle. Therefore, nanoparticles of any material and therapeutic payload can be rationally designed to behave in the desired manner in the body, provided the general characteristics (size, surface composition, decomposability) needed to behave in that desired manner are known.

1.3.1.3 Size is a major determinant of the circulation time and tissue deposition of a nanoparticle-based therapeutic.

The circulation time of a nanoparticle depends on three factors: renal excretion rate, tissue uptake rate, and nanoparticle degradation rate. The first two factors are largely dependent on size. Nanoparticles < 10nm are sufficiently small pass through the renal filtration barrier and enter the urine[1]. Nanoparticles above this size can have very long circulation times as they are not subject to first pass renal filtration, unless they degrade into components <10nm.

The circulation times of non-decomposable nanoparticle is determined by their uptake by the reticulo-endothelial system (RES)[9]. RES uptake is largely determined by size, provided surface charge is close to neutral. Nanoparticles from 10-200nm are increasingly taken up by liver Kupffer cell and splenocytes. Above 200nm (size cut off for the fenestrated endothelium of liver sinusoids) they primarily accumulate in the spleen. Examples of this phenomenon for non-targeted PEGylated gold nanoparticles are presented in Chapter 6 of this thesis.

1.3.1.4 Nanoparticle surface composition can be engineered to alter tissue uptake and intra-tissue localization.

The surfaces of nanoparticle-therapeutics are in direct contact with the plasma and tissue milieu. The nature of these interactions can influence the behavior of the nanoparticle in the body and with each other. For example, nanoparticles with high surface charges tend to be more rapidly taken up by the RES[10]. This phenomenon may be mediated by increased plasma protein binding to the surface of these particles or stronger interactions between the nanoparticles and the surface of the cells of the RES. Additionally, the surface of the nanoparticle can be engineered to encourage binding to certain plasma proteins that may facilitate their entry into non RES cell types, such as hepatocytes[11].

Using targeting ligands, the surfaces of nanoparticles can be engineered to encourage much more specific interactions between themselves and tissues within the body. Targeting ligands, including proteins, peptides, antibodies, sugars, aptamers, etc., are chemical moieties displayed on the surface of a nanoparticle that can engage one or more surface features (usually trans-membrane receptors) on a tissue of interest to

encourage nanoparticle binding. Most commonly, they are used to facilitate nanoparticle internalization by cells within target tissues. For example, the iron carrier protein transferrin is commonly used as a targeting ligand for cancer cells. When attached to the surface of a nanoparticle, transferrin can engage the transferrin receptor (often upregulated on the surface of cancer cells) and mediate receptor mediated endocytosis of the nanoparticle. Targeting ligands may also be used to bind to the surface of endothelial cells to localize nanoparticles to tissues without a fenestrated endothelium.

Targeting ligands can also be therapeutic themselves (e.g., Herceptin). Additionally, multiple targeting ligands can be incorporated onto a nanoparticles surface to enable distinct desired functions (e.g., one ligand is used for trancytosis across an endothelial layer and another is used as an internalization signal for cells beyond that endothelial layer).

1.3.1.5 Specific considerations for nanoparticle delivery to tumors.

Nanoparticle targeting to tumors is an often misunderstood process. Because anti-cancer nanoparticle-based therapeutics often employ targeting ligands, it is commonly assumed that the targeting ligand is responsible for the delivery of nanoparticles to the tumor. In fact, the major mechanism for nanoparticle accumulation within tumors is passive and ligand independent[12]. The phenomenon known as the enhanced permeability and retention (EPR) effect is responsible for nanoparticle "targeting" of tumors.

Most tumors have abnormal, dilated and tortuous vasculature, lacking in regular structure and possessing large inter-endothelial cell distances and fenestrations[13]. The spaces between endothelial cells can exceed 1μm in some tumors[13]. These vessels are therefore hyper-permeable and can allow the passage of nanoparticle sized objects from

circulation into the tumor interstitia. Tumors also have compromised lymph drainage due to compression of lymph vessels by the tumor. These two effects result in increased entry of nanoparticle sized objects into the tumor interstitia and reduced clearance and therefore a net accumulation of material. This phenomenon is known as the EPR effect. Nanoparticles and macromolecules can reach concentrations higher than plasma through this mechanism[14]. The primary consideration for increasing nanoparticle delivery to tumors is plasma circulation time.

Although nanoparticles of all sizes can accumulate in tumors due to the EPR effect, nanoparticles under 100nm are ideal for anti-tumor therapy. Once extravassated from circulation, nanoparticles must diffuse through the dense extracellular matrix that makes up the tumor interstitia to reach the tumor cells themselves. The high viscosity of the extracellular matrix inhibits the diffusion of larger nanoparticles through the tumor and they remain close to the vessels they extravesated from. Smaller nanoparticles (10-50nm) more readily diffuse through the tumor environment away from the vessels they extravessated from[15]. Because many areas of the tumor are either hypovascular or have poor perfusion, nanoparticles that can reach tumor cells great distances away from blood vessels have increased therapeutic activity[16].

Targeting ligands still play an important role in nanoparticle-based therapeutic activity in tumors. Once nanoparticles deposit in a tumor they may or may not be internalized by the tumor cells depending on their surface properties. The inclusion of a targeting ligand on the nanoparticle (e.g., transferrin) can facilitate their uptake by tumor cells, but not necessarily overall tumor accumulation[12]. Intracellular localization is

paramount for therapeutic modalities (e.g., siRNA) that can function only if delivered intracellular environment.

1.3.1.6 Nanoparticle-based therapeutics have great potential for many other diseases besides cancer.

The field of nanoparticle-based therapeutics is heavily focused on cancer. Although cancer is one of the leading causes of death in the United States, there are many other chronic diseases that impose a significant disease burden on society that could benefit from new nanoparticle-based therapeutics. Any disease that results in increased vascular permeability at the desired site of therapeutic action could potentially be targeted by a nanoparticle-based therapeutic.

Atherosclerosis and hypercholesterolemia: Nanoparticles also have great potential for both atherosclerosis and hypoercholeserolemia. A siRNA nanoparticle formulation targeting PCSK9, known as ALN-PCS, being developed by Alnylam Pharmaceuticals has been demonstrated lower plasma low density lipoprotein (LDL) levels in healthy patients with elevated LDL levels. Inhibition of liver PCSK9 results in upregulation of LDL receptors on hepatocytes and increases hepatocyte LDL uptake in a similar manner as statins but avoids common statin side effects (e.g., myopathy) and resistance. Nanoparticles have also been shown to accumulate in atherosclerotic plaques, due to increased vascular permeability in the small capillaries supplying the larger arteries and arteriols[17,18]. Direct targeting of the cells (foam cells, smooth muscles cells, etc.) could be another option for anti-plaque therapy. siRNA nanoparticles targeting monocytes have been demonstrated to reverse plaque formation (and reduce damage from myocardial infarctions)[19].

Renal disease: Chapters 6-9 of this thesis explore the interaction of nanoparticles with the kidney.

Autoimmune diseases/inflammation: A hallmark of inflammation is increased vascular permeability. Autoimmune diseases such as lupus are difficult to treat because of the low therapeutic indexes of the immunosuppressive drugs that are often used. Nanoparticle-based-therapeutics could help overcome these limitation by delivering these drugs only to sites of inflammation. Despite this potential and the unmet medical need, only a modest number of studies examining this application have appeared in the literature[20,21].

Central nervous system disorders and the blood brain barrier: Drug delivery to the CNS is often stymied by the tight junctions between the endothelial cells of the CNS microvasculature that form the blood brain barrier (BBB). Only hydrophobic compounds that can cross cell membranes can access the CNS. But even then these compounds can be pumped out. There is much interest in development of nanoparticles that can engage endothelial receptors to facilitate their trancytosis across the blood brain barrier to deliver therapeutic entities into the CNS. Nanoparticle-based therapeutics are a particularly promising strategy for this indications because they can be engineered to incorporate multiple targeting ligands to enable both trancytosis across the BBB and internalization by specific CNS cells while carrying a drug payload.

1.3.2 Small interfering RNAs (siRNAs) can be used as high potency, high specificity therapeutics

Synthetic siRNAs are 21 base pair double stranded RNA oligonucleotides than can engage the RNA interference (RNAi) machinery to induce the degradation of target

mRNAs. RNAi is an endogenous cellular mechanism for the sequence-specific regulation of mRNA transcript levels and mRNA transcript translation in eukaryotic cells[22]. The RNAi machinery is guided by double stranded RNAs including siRNAs and microRNAs. These RNAs are endogenously transcribed as long double stranded precursors that are exported from the nucleus and processed into smaller fragments of 20-30bp by the RNase-III-type enzyme Dicer. In the cytoplasm, these short double stranded RNAs are then incorporated into the RNA-induced silencing complex (RISC). RISC cleaves the sense strand of these RNAs and then uses the anti-sense strand to target itself to mRNA transcripts with complementarity to the anti-sense strand[23].

mRNA transcript silencing occurs via several mechanisms. Anti-sense strands with perfect complementarity (siRNAs) to their mRNA targets induce site specific cleavage of mRNA targets between the 10 and 11bp from the 5' end of the anti-sense sequence. Anti-sense strands with imperfect complementarity (microRNAs) to their mRNA targets, specifically, limited complementarity in their "seed region" (bp 2-8 on the antisense strand) to the 3'UTR of their mRNA targets, induce translational repression[24].

Synthetic siRNAs can be used to silence genes in cells and tissues. Exogenously applied siRNAs engage the RNAi machinery at the level of RISC and induce the cleavage of their target mRNA transcripts. Once in complex with RISC, these siRNAs are extremely stable and can induce gene knockdown lasting 3-7 days in rapidly dividing cells and over a month in non-dividing cells[25]. Dilution of the RISC/siRNA complex due to cell division is responsible for these observations. Nuclease stabilization through chemical modifications to siRNAs does not greatly alter their gene silencing kinetics *in*

vitro or *in vivo*[26], although it can improve the amount of siRNA delivered to the cytoplasm by avoiding any prior degradation in circulation or the endosome.

1.3.2.1 siRNA-based therapeutics overcome many barriers to traditional small molecule based drug development.

Historically, many therapeutically interesting proteins have been considered "undruggable" (e.g., Ras) because of the extreme difficulty in developing small molecules that can effectively inhibit these proteins' functions. Because all mRNA transcripts are susceptible to RNAi, therapeutic siRNAs can be designed to inhibit any desired gene target. Also, siRNA sequences can be designed to have extremely high selectivity and potency (IC50s in the femtomolar range).

Another major advantage of siRNA-based therapies is that they can facilitate the rapid translation of new understanding in cancer biology to new therapeutics. The timeline from concept to clinic for siRNA-based therapies can be <2 years[27]. Furthermore, it is feasible that once clinically approved delivery systems enter the market, this time can be even more rapid because only the siRNA sequence will require modification. It is possible that in the near future patients will have their whole genomes rapidly sequenced and tailor made siRNA against one or more disease targets could be ordered and delivered in a matter of weeks.

siRNAs by themselves are also fairly benign. Although siRNAs can induce immune responses in animals, these responses are often sequence and delivery system specific[28,29]. Many types of chemical modifications have been developed to circumvent these off target effects[30]. siRNAs may also induce non-immunostimulatory off target effects through several mechanisms. siRNA may inhibit expression of unintended gene

targets via microRNA like mechanisms[31]. Additionally, they may saturate the RNAi machinery and interfere with the normal function of endogenous regulatory RNAs[28]. Both these problems can be circumvented by selection of high potency siRNA sequences and through certain chemical modifications to the siRNA itself.

Because the activity of the siRNAs is only based on their sequence and not structure, siRNA delivery systems can be used to delivery several siRNAs against one or more targets. Multiple siRNA sequences in a delivery system should not significantly change the toxicity profile of the therapeutic. Additionally, different siRNAs against the same target can be used simultaneously or sequentially to avoid mutation based-resistance to therapy.

1.3.2.2 Many challenges remain in the development of successful siRNA-based therapeutics.

Cost is a significant challenge with siRNA based-therapeutics. Large scale siRNA synthesis is costly. However, the shortened time line to the clinic may help off-set this factor. Additionally, we also expect the cost of synthesis to drop as the demand increases.

Intellectual property (IP) is a short term challenge in therapeutic development. Currently, the IP for RNAi-based technology is concentrated in a few companies. This means that many gene targets and most chemical modifications to siRNAs are off limits to new companies entering the market[32]. However, these problems will ultimately resolve when the patents expire.

The biggest challenge to the development of siRNA-based therapeutics is delivery. siRNA are large, charged, and unstable. siRNAs cannot usually enter cells unaided and are rapidly degraded by nucleases in blood plasma and the extracellular milieu. Although

they are relatively large molecules, siRNAs are still rapidly cleared from circulation via first pass renal filtration following system administration, further limiting their ability to reach target tissue[33]. Therefore, siRNAs require carriers to be delivered to desired sites of action.

1.3.3 Cyclodextrin-containing polymer-based siRNA delivery system

The Davis lab has spent the past decade developing a siRNA delivery system designed to transport siRNA to tumor tissue[27]. The delivery system consists of three components (Fig. 1.1): (i) a linear, cationic cyclodextrin-based polymer (CDP), (ii) a hydrophilic polymer (polyethylene glycol (PEG) used to promote nanoparticle stability in biological fluids), and (iii) siRNA.

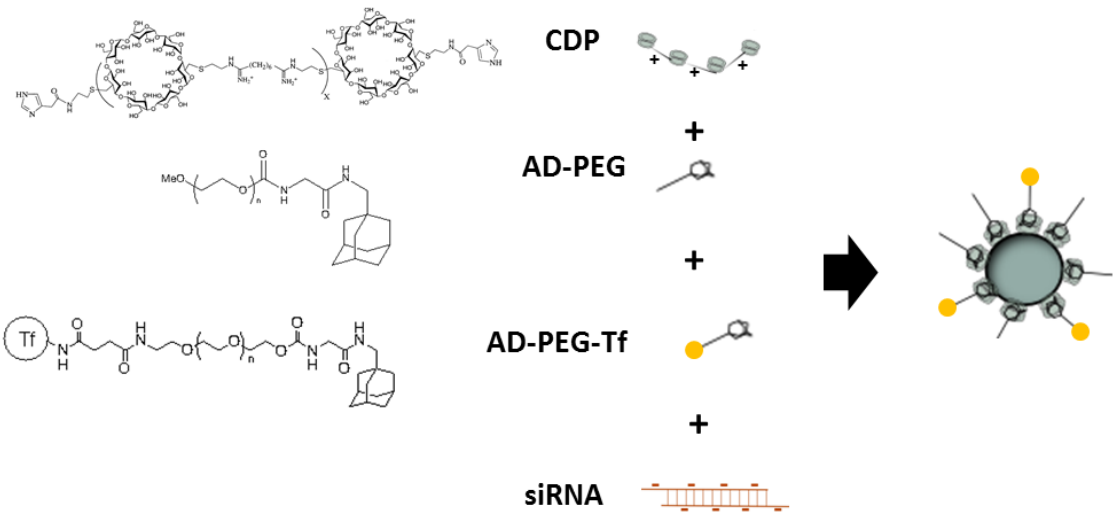

Figure1.1: Components of the siRNA/CDP nanoparticle delivery system. siRNA nanoparticles assemble due to electrostatic interactions between the cationic cyclodextrin containing polymer and the anionic siRNA. PEG provides steric stabilization and is bound to the particles via inclusion complex formation between its terminal adamantane (AD) modification and the cyclodextrin cup of the CDP. Transferrin (Tf) targeting ligand is covalently linked to AD-PEG.

The siRNA delivery system self-assembles into polyplexes through electrostatic interactions between negatively charged siRNA and the positively charged CDP. The

CDP is a linear, water soluble polymer that consists of multiple comonomers of β-cyclodextrin cups linked together with short spacer polymers containing two imine charge centers. The spacing and of these charged centers from the cyclodextrin cup and their composition has been optimized for interaction with nucleic acids[34,35]. The two terminal cyclodextrins of each polymer strand are "capped" with imidazole groups designed to buffer the endosomal pH following cellular internalization and facilitate endosomal escape[36]. A 3+/- charge ratio of CDP to siRNA was determined to be the optimal formulation for complete complexation between the two components[37].

Polyplexes of siRNA and cationic polymers are known to be unstable (will aggregate) in physiologic fluids such as blood. The CDP/siRNA nanoparticle is engineered to incorporate polyethylene glycol (PEG) steric stabilization to prevent self-aggregation or aggregation with exogenous components. For incorporation into the polyplex, 5 kDa PEG is covalently linked to a small hydrophobic molecule called adamantane (AD) that will form an inclusion complex with β-cyclodextrin cups. PEG covalently linked to AD (AD-PEG) will bind to β-cyclodextrin cups on the surface of the polyplexes and provide steric stabilization.

When the components are mixed together they self-assemble into spherical nanoparticles between 50 and 100nm in size with a slightly positive surface charge (ca.10mV). Each nanoparticle has been determined to contain ~2000 siRNA molecules, ~10,000 CDP chains, and ~4000 AD-PEG molecules[37].

The nanoparticles have been engineered to incorporate targeting ligands such transferrin (Tf)[38], sugars, or antibodies at the terminal ends of their PEGs that facilitate their uptake by target tissue. Tf targeting had been demonstrated to increase the potency

of siRNA knockdown, but not total tumor uptake, of siRNA nanoparticles following their intravenous administration to tumor bearing mice[14].

The Tf-siRNA nanoparticles delivery system was one of the first to demonstrate successfully therapeutic application of a polymer-based siRNA delivery system in an animal model. In this breakthrough study, Tf-siRNA nanoparticles containing siRNA targeting the breakpoint of the EWS-FLI1 gene product were used to inhibit the growth of disseminated Ewing's sarcoma xenografts in a mouse model[39]. To allow for broader targeting of a variety of tumor types the siRNA nanoparticles were formulated to contain siRNA against Ribonucleotide Reductase subunit M2 (RRM2)[40]. siRNA nanoparticles against RRM2 were demonstrated to inhibit tumor growth in multiple xenograft cancer models[41].

The Tf-siRNA nanoparticles have been demonstrated to have a favorable toxicity profile in mice and non-human primates. In mice, no abnormalities in interleukin-12 and IFN-A, liver and kidney function tests, complete blood counts, or pathology of major organs were observed following long term intravenous dosing[39]. In non-human primates, low (3 mg/kg) and intermediate (9 mg/kg) dosing did not results in any evidence of organ damage, changes in hematologic parameters, or immune stimulation. High dosing in primates (27mg/kg) was associated with mild kidney toxicity and slight immune stimulations evident from elevations in IL-6 and ING-γ[39]. Overall, no signs of clinical toxicity were observed at any dose.

This Tf-siRNA nanoparticle formulation targeting RRM2 was the first target, systemically applied siRNA nanoparticle to reach the clinic in 2008[39]. Chapter 2 of this thesis will discuss performance of the siRNA delivery system in this clinical trial.

1.3.3.1 Efficacy of CDP/siRNA nanoparticles is limited by poor pharmacokinetics.

Although the CDP/siRNA nanoparticle can successfully delivery siRNA to tumors from an intravenous injection, there is still much room for improvement for this system. Specifically, the CDP/siRNA nanoparticles have been demonstrated to be eliminated by first-pass renal filtration and completely cleared from circulation within 30 minutes after intravenous administration[42]. Because delivery of these nanoparticles to tumors is passive and depends on the concentration of nanoparticle in circulation, their short circulation time has likely been a major limiting factor in their efficacy.

To demonstrate that the efficacy of these nanoparticles is limited by amount of siRNA delivered rather than inherent limitations in choice of therapeutic target, the therapeutic effect of siRNA nanoparticle delivery of RRM2 siRNA was compared to endogenous expression of shRNA against RRM2 in a neuroblastoma tumor model in mice (Fig 1.2). With the siRNA nanoparticle system we observed only growth inhibition in this tumor model at high siRNA nanoparticle doses (10 mg/kg); however, induced expression of the shRNA resulted in complete cures in all mice over a similar time span of treatment. We demonstrated a similar discrepancy between CDP/siRNA nanoparticle treatment and induced shRNA expression targeting N-Ras in a melanoma tumor model described in Chapter 5. Therefore, we hypothesize that increasing the circulation time of the siRNA nanoparticles and thereby the amount delivered to tumor tissue will greatly increase the therapeutic efficacy of the CDP/siRNA nanoparticles.

The rapid clearance of these siRNA nanoparticles is puzzling because they are engineered to be above the size cutoff for single-pass clearance via renal filtration[1]. Real-time PET biodistribution data demonstrated an unexpected level of kidney

accumulation[42]. Therefore, we decided to investigate the interaction of the CDP/siRNA nanoparticles with the kidney. Chapters 6 and 7 of this thesis explore the behavior of nanoparticles in the kidney and demonstrate the mechanism of rapid renal clearance of the CDP/siRNA nanoparticles.

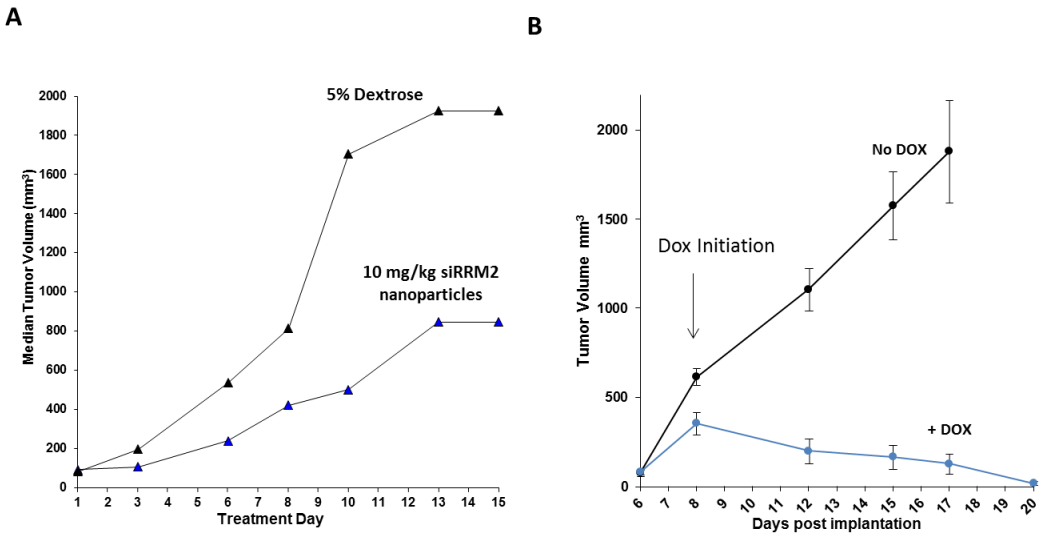

Figure 1.2: Comparison of anti-tumor effects of RRM2 knockdown via (A) siRNA nanoparticles delivery or (B) endogenous shRNA expression in Neuro2a tumors. (A) Tumor bearing A/J mice received 10 mg/kg intravenous injections of siRRM2 nanoparticles or control (dextrose) on days 1,3,8, and 10. Data are adapted with permission from Heidel et al., (2008)[41]. (B) shRRM2 was induced in Neuro2a-shRRM2 cells implanted in A/J mice on day 8 with doxycycline (DOX).

1.3.4 Need for biomarker integration into clinical studies and drug usage

In Chapter 2 of this thesis, we present work validating delivery of siRNA nanoparticle based therapeutics to human tumors. Although this study on patient materials provided us with much information, the study had many limitations. Primarily our analyses were restricted to a very limited number of biopsy samples from the patients. From these biopsies we could confirm drug mechanism of action and nanoparticle delivery; however, they provided little insight into overall patient response to treatment, kinetics of nanoparticle activity, or resistance to therapy. Our experiences in

this study taught us much about the limitations of biopsies and the challenges of validating drug response in the setting of early clinical trials. These experiences lead to our investigation of new avenues for rapid, multi-time point, non-invasive measures of drug activity and response (Chapter 9).

1.3.4.1 Circulating microRNAs are a new class of promising biomarkers

MicroRNA (miRNA) are ~22 nucleotide long, endogenous non-coding RNAs that regulate gene expression post-transcriptionally as described above. miRNAs have emerged as an extremely promising new class of biomarkers. Besides their unusually high stability in formalin fixed tissue, miRNAs have been demonstrated to be remarkably stable in human blood[43].

As blood derived biomarkers, miRNAs offer three key advantages over other types of biomarkers such as proteins and mRNA. First, because of their stability, microRNA can be quantified reproducibly from plasma samples that have been freeze thawed multiple times. mRNAs have not been demonstrated to have the same level of stability as microRNAs. Second, robust, sensitive, and accessible high throughput detection/quantification technologies exist for microRNA. These technologies include sequencing, microarrays, and PCR arrays. Finally, microRNA can be robustly and quantitatively pre-amplified to increase detection sensitivity for all these assays.

Since the stability of microRNA in plasma was demonstrated by the Tewari group in 2008[43], a large number of reports demonstrating their potential as biomarkers in many different areas of medicine have emerged. For example, circulating microRNA have been shown to be sensitive and specific markers of tissue injury in animals models[44,45]and in patients, specifically as indicators of myocardial infarction[46]. They have also been

demonstrated to be useful for in patients for detecting pregnancy and fetal complications[47,48].

Circulating microRNAs have also been shown to be useful biomarkers for cancer. Numerous literature reports have demonstrated that levels of circulating microRNA can be used to differentiate healthy from cancer patient blood samples[49–52]. One particularly promising report by Boeri et al., shown that microRNA signatures in plasma could be used to identify patients with a high risk of developing cancer[53].

Despite the abundant amount of promise for circulating microRNAs as biomarkers, many challenges still remain before their routine and successful application in the clinic. A major challenge is blood cell microRNA contamination that can confound interpretation of circulating microRNA data. Tewari and colleagues have recently demonstrated that a majority of circulating microRNA associated with many cancers originate from blood cells and their levels correlated with blood cell counts[54]. Another challenge stems from variability in sample collection and processing. The type of blood sample collected (serum or plasma) and the fractionation method applied to the sample can drastically alter the microRNA composition[55]. One method of overcoming these difficulties is isolating a subset of microRNA packaged within lipid vesicles known as exosomes.

1.3.4.1 Exosomal microRNA could be used track tumor specific microRNAs.

Some circulating miRNA are believed to be shed from tumors packaged into small membrane bound vesicles known as exosomes (c.a. 10-100nm in diameter)[56]. This packaging is thought to protect the RNA from degradation in the extra-cellular

environment. However, some evidence for the excretion of protein associated non-exosomal miRNA has been identified in human plasma[57].

Several types of cancer are associated with increases in circulating exosome population including melanoma, lung, and ovarian cancer[58–60]. In ovarian cancer the increases in circulating exosomes have been demonstrated to be proportional to increasing disease stage[58]. Exosomes can be isolated from patient blood based on their physical characteristics (size, density) and protein markers. Therefore, analysis of this population of vesicles isolated out of blood, if selected via tumor markers, may provide specific information about the tumor such drug response.

The miRNA profile of tumor derived exosomes has been reported to be representative of the intracellular miRNA profile from the cells they are derived from[61]. However, several reports have demonstrated that there may be preferential enrichment or depletion of certain miRNAs from exosomes[62]. Advanced stage melanoma patients have an increased level of exosomes in their circulation[59] and significant effort has been made to understand the miRNA expression alterations associated with progressive disease, mutational status, and survival [63,64].

Thus, the goal of the work presented in Chapter 9 was to test he hypothesis that cell-free circulating miRNAs encapsulated in tumor derived exosomes could serve as useful, time-dependent biomarkers for monitoring drug activity and disease progression in cancer patients. Specifically, we tested the hypothesis that intracellular changes to the microRNA transcriptome induced by drug treatment can be measured in tumor derived exosomes.

1.4 References:

1. Choi, H.S. et al. Renal clearance of quantum dots. Nature Biotechnology 25, 1165-70 (2007).

2. Davis, M.E., Chen, Z.G. & Shin, D.M. Nanoparticle therapeutics: an emerging treatment modality for cancer. Nature Reviews. Drug Discovery 7, 771-82 (2008).

3. Daldrup-Link, H.E. et al. MR Imaging of Tumor Associated Macrophages with Clinically-Applicable Iron Oxide Nanoparticles. Clinical Cancer Research 5695-5704 (2011).

4. Lytton-Jean, A.K.R., Langer, R. & Anderson, D.G. Five Years of siRNA Delivery: Spotlight on Gold Nanoparticles. Small 1-6 (2011).

5. Petros, R. a & DeSimone, J.M. Strategies in the design of nanoparticles for therapeutic applications. Nature reviews. Drug Discovery 9, 615-27 (2010).

6. Hashizume, H. et al. Openings between defective endothelial cells explain tumor vessel leakiness. The American Journal of Pathology 156, 1363-80 (2000).

7. Campbell, F.R. Ultrastructural studies of transmural migration of blood cells in the bone marrow of rats, mice and guinea pigs. The American Journal of Anatomy 135, 521-35 (1972).

8. Porter, C.J., Moghimi, S.M., Illum, L. & Davis, S.S. The polyoxyethylene/polyoxypropylene block co-polymer poloxamer-407 selectively redirects intravenously injected microspheres to sinusoidal endothelial cells of rabbit bone marrow. FEBS letters 305, 62-6 (1992).

9. Chrastina, A., Massey, K. a & Schnitzer, J.E. Overcoming in vivo barriers to targeted nanodelivery. Wiley Interdisciplinary Reviews. Nanomedicine and Nanobiotechnology 3, 421-37 (2011).

10. Arvizo, R.R. et al. Modulating pharmacokinetics, tumor uptake and biodistribution by engineered nanoparticles. PloS One 6, e24374 (2011).

11. Akinc, A. et al. Targeted Delivery of RNAi Therapeutics With Endogenous and Exogenous Ligand-Based Mechanisms. Molecular Therapy 1-8 (2009).

12. Choi, C.H.J., Alabi, C. a, Webster, P. & Davis, M.E. Mechanism of active targeting in solid tumors with transferrin-containing gold nanoparticles. Proceedings of the National Academy of Sciences of the United States of America 107, 1235-40 (2010).

13. Hobbs, S.K. et al. Regulation of transport pathways in tumor vessels: role of tumor type and microenvironment. Proceedings of the National Academy of Sciences of the United States of America 95, 4607-12 (1998).

14. Schluep, T. et al. Pharmacokinetics and tumor dynamics of the nanoparticle IT-101 from PET imaging and tumor histological measurements. Proceedings of the National Academy of Sciences of the United States of America 106, 11394-9 (2009).

15. Perrault, S.D., Walkey, C., Jennings, T., Fischer, H.C. & Chan, W.C.W. Mediating tumor targeting efficiency of nanoparticles through design. Nano Letters 9, 1909-15 (2009).

16. Jain, R.K. & Stylianopoulos, T. Delivering nanomedicine to solid tumors. Nature reviews. Clinical Oncology 7, 653-64 (2010).

17. Lobatto, M.E., Fuster, V., Fayad, Z. a & Mulder, W.J.M. Perspectives and opportunities for nanomedicine in the management of atherosclerosis. Nature Reviews. Drug Discovery (2011).doi:10.1038/nrd3578

18. Buono, C., Anzinger, J.J., Amar, M. & Kruth, H.S. Technical advance Fluorescent pegylated nanoparticles demonstrate fluid-phase pinocytosis by macrophages in mouse atherosclerotic lesions. Journal of Clinical Investigation 119, 1373-1381 (2009).

19. Leuschner, F. et al. Therapeutic siRNA silencing in inflammatory monocytes in mice. Nature Biotechnology 1-9 (2011).

20. Sun, D. et al. A Novel Nanoparticle Drug Delivery System: The Anti-inflammatory Activity of Curcumin Is Enhanced When Encapsulated in Exosomes. Molecular Therapy 1-9 (2010).

21. Hwang, J., Rodgers, K., Oliver, J.C. & Schluep, T. Alpha-methylprednisolone conjugated cyclodextrin polymer-based nanoparticles for rheumatoid arthritis therapy. International Journal of Nanomedicine 3, 359-71 (2008).

22. Krol, J., Loedige, I. & Filipowicz, W. The widespread regulation of microRNA biogenesis, function and decay. Nature Reviews. Genetics 11, 597-610 (2010).

23. de Fougerolles, A., Vornlocher, H.-P., Maraganore, J. & Lieberman, J. Interfering with disease: a progress report on siRNA-based therapeutics. Nature Reviews. Drug Discovery 6, 443-53 (2007).

24. Castanotto, D. & Rossi, J.J. The promises and pitfalls of RNA-interference-based therapeutics. Nature 457, 426-33 (2009).

25. Bartlett, D.W. & Davis, M.E. Insights into the kinetics of siRNA-mediated gene silencing from live-cell and live-animal bioluminescent imaging. Nucleic Acids Research 34, 322-33 (2006).

26. Bartlett, D.W. & Davis, M.E. Effect of siRNA Nuclease Stability on the In Vitro and In Vivo Kinetics of siRNA-Mediated Gene Silencing. Biotechnology 97, 909-921 (2007).

27. Davis, M.E. reviews The First Targeted Delivery of siRNA in Humans via a Nanoparticle : From Concept to Clinic. Molecular Pharmaceutics, 11-17 (2009).

28. Fedorov, Y. et al. Off-target effects by siRNA can induce toxic phenotype. RNA (New York, N.Y.) 12, 1188-96 (2006).

29. Heidel, J.D., Hu, S., Liu, X.F., Triche, T.J. & Davis, M.E. Lack of interferon response in animals to naked siRNAs. Nature Biotechnology 22, 1579-82 (2004).

30. Rettig, G.R. & Behlke, M. a Progress Toward In Vivo Use of siRNAs-II. Molecular Therapy 1-30 (2011).

31. Alemán, L.M., Doench, J. & Sharp, P. a Comparison of siRNA-induced off-target RNA and protein effects. RNA (New York, N.Y.) 13, 385-95 (2007).

32. Schmidt, C. Negotiating the RNAi patent thicket. Nature Biotechnology 25, 273-5 (2007).

33. Gao, S. et al. The effect of chemical modification and nanoparticle formulation on stability and biodistribution of siRNA in mice. Molecular Therapy 17, 1225-33 (2009).

34. Reineke, T.M. & Davis, M.E. Structural effects of carbohydrate-containing polycations on gene delivery. 1. Carbohydrate size and its distance from charge centers. Bioconjugate Chemistry 14, 247-54 (2003).

35. Reineke, T.M. & Davis, M.E. Structural effects of carbohydrate-containing polycations on gene delivery. 2. Charge center type. Bioconjugate Chemistry 14, 255-61 (2003).

36. Mishra, S., Heidel, J.D., Webster, P. & Davis, M.E. Imidazole groups on a linear, cyclodextrin-containing polycation produce enhanced gene delivery via multiple processes. Journal of Controlled Release 116, 179-91 (2006).

37. Bartlett, D.W. & Davis, M.E. Physicochemical and biological characterization of targeted, nucleic acid-containing nanoparticles. Bioconjugate Chemistry 18, 456-68 (2007).

38. Bartlett, D.W. & Davis, M.E. Physicochemical and biological characterization of targeted, nucleic acid-containing nanoparticles. Bioconjugate Chemistry 18, 456-68 (2007).

39. Hu-Lieskovan, S., Heidel, J.D., Bartlett, D.W., Davis, M.E. & Triche, T.J. Sequence-specific knockdown of EWS-FLI1 by targeted, nonviral delivery of small interfering RNA inhibits tumor growth in a murine model of metastatic Ewing's sarcoma. Cancer Research 65, 8984-92 (2005).

40. Heidel, J.D. et al. Potent siRNA inhibitors of ribonucleotide reductase subunit RRM2 reduce cell proliferation in vitro and in vivo. Clinical Cancer Research 13, 2207-15 (2007).

41. Heidel, J., Liu, J., Zeidan, R., Liang, Y., Rele, S. and Davis, M. In vivo efficacy investigation of an siRNA-containing nanoparticle formulation targeting the m2 subunit of ribonucleotide reductase (rrm2) in tumor-bearing mice. AACR Meeting Abstracts Online, Abstract No. 1382. (2008).

42. Bartlett, D.W., Su, H., Hildebrandt, I.J., Weber, W. a & Davis, M.E. Impact of tumor-specific targeting on the biodistribution and efficacy of siRNA nanoparticles measured by multimodality in vivo imaging. Proceedings of the National Academy of Sciences of the United States of America 104, 15549-54 (2007).

43. Mitchell, P.S. et al. Circulating microRNAs as stable blood-based markers for cancer detection. Proceedings of the National Academy of Sciences of the United States of America 105, 10513-8 (2008).

44. Laterza, O.F. et al. Plasma MicroRNAs as sensitive and specific biomarkers of tissue injury. Clinical Chemistry 55, 1977-83 (2009).

45. Wang, K. et al. Circulating microRNAs, potential biomarkers for drug-induced liver injury. Proceedings of the National Academy of Sciences of the United States of America 106, 4402-7 (2009).

46. Devaux, Y. et al. Use of Circulating MicroRNAs to Diagnose Acute Myocardial Infarction. Clinical Chemistry 58, 559-67 (2012).

47. Hung, E.C.W., Chiu, R.W.K. & Lo, Y.M.D. Detection of circulating fetal nucleic acids: a review of methods and applications. Journal of Clinical Pathology 62, 308-13 (2009).

48. Mouillet, J.-F. et al. The levels of hypoxia-regulated microRNAs in plasma of pregnant women with fetal growth restriction. Placenta 31, 781-4 (2010).

49. Lawrie, C.H. et al. Detection of elevated levels of tumour-associated microRNAs in serum of patients with diffuse large B-cell lymphoma. British Journal of Haematology 141, 672-5 (2008).

50. Laconti, J.J. et al. Tissue and Serum microRNAs in the Kras Transgenic Animal Model and in Patients with Pancreatic Cancer. PloS One 6, e20687 (2011).

51. Wang, Y., Zheng, D., Tan, Q., Wang, M.X. & Gu, L.-Q. Nanopore-based detection of circulating microRNAs in lung cancer patients. Nature Nanotechnology (2011).

52. Kanemaru, H. et al. The circulating microRNA-221 level in patients with malignant melanoma as a new tumor marker. Journal of Dermatological Science (2011).

53. Boeri, M. et al. MicroRNA signatures in tissues and plasma predict development and prognosis of computed tomography detected lung cancer. Proceedings of the National Academy of Sciences of the United States of America 1-6 (2011).

54. Pritchard, C.C. et al. Blood Cell Origin of Circulating MicroRNAs: A Cautionary Note for Cancer Biomarker Studies. Cancer Prevention research 5, 492-7 (2012).

55. McDonald, J.S., Milosevic, D., Reddi, H.V., Grebe, S.K. & Algeciras-Schimnich, A. Analysis of Circulating MicroRNA: Preanalytical and Analytical Challenges. Clinical Chemistry 57, 833-40 (2011).

56. Sokolova, V. et al. Characterisation of exosomes derived from human cells by nanoparticle tracking analysis and scanning electron microscopy. Colloids and Surfaces. B, Biointerfaces 13-17 (2011).

57. Arroyo, J.D. et al. Argonaute2 complexes carry a population of circulating microRNAs independent of vesicles in human plasma. Proceedings of the National Academy of Sciences of the United States of America 2-7 (2011).

58. Taylor, D.D. & Gercel-Taylor, C. MicroRNA signatures of tumor-derived exosomes as diagnostic biomarkers of ovarian cancer. Gynecologic Oncology 110, 13-21 (2008).

59. Logozzi, M. et al. High levels of exosomes expressing CD63 and caveolin-1 in plasma of melanoma patients. PloS One 4, e5219 (2009).

60. Rabinowits, G., Gerçel-Taylor, C., Day, J.M., Taylor, D.D. & Kloecker, G.H. Exosomal microRNA: a diagnostic marker for lung cancer. Clinical Lung Cancer 10, 42-6 (2009).

61. Skog, J. et al. Glioblastoma microvesicles transport RNA and proteins that promote tumour growth and provide diagnostic biomarkers. Nature Cell Biology 10, 1470-6 (2008).

62. Wang, K., Zhang, S., Weber, J., Baxter, D. & Galas, D.J. Export of microRNAs and microRNA-protective protein by mammalian cells. Nucleic Acids Research 1-12 (2010).

63. Caramuta, S. et al. MicroRNA expression profiles associated with mutational status and survival in malignant melanoma. The Journal of Investigative Dermatology 130, 2062-70 (2010).

64. Mueller, D.W., Rehli, M. & Bosserhoff, A.K. miRNA expression profiling in melanocytes and melanoma cell lines reveals miRNAs associated with formation and progression of malignant melanoma. The Journal of Investigative Dermatology 129, 1740-51 (2009).

Chapter 2: Evidence of RNAi in humans from systemically administered siRNA via targeted nanoparticles[1]

2.1 Abstract:

Therapeutics that are designed to engage RNA interference (RNAi) pathways have the potential to provide new, major ways of imparting therapy to patients.[1,2] Fire et al. first demonstrated that long, double stranded RNAs mediate RNAi in Caenorhabditis elegans,[3] and Elbashir et al. opened the pathway to the use of RNAi for human therapy by showing that small interfering RNAs (siRNAs: ca. 21 base pair double stranded RNA) can elicit RNAi in mammalian cells without producing an interferon response.[4] We are currently conducting the first-in-human Phase I clinical trial involving the systemic administration of siRNA to patients with solid cancers using a targeted, nanoparticle delivery system. Here we provide evidence of inducing an RNAi mechanism of action in a human from the delivered siRNA. Tumor biopsies from melanoma patients obtained after treatment reveal: (i) the presence of intracellularly-localized nanoparticles in amounts that correlate with dose levels of the nanoparticles administered (this is a first for systemically delivered nanoparticles of any kind), and (ii) reduction in both the specific mRNA (M2 subunit of ribonucleotide reductase (RRM2)) and the protein (RRM2) when compared to pre-dosing tissue. Most importantly, we detect the presence of an mRNA fragment that demonstrates siRNA mediated mRNA cleavage occurs specifically at the site predicted for an RNAi mechanism from a patient who received the highest dose of the nanoparticles. These data when taken in total demonstrate that siRNA administered

[1] Reproduced with permission from: Davis ME, Zuckerman JE, Choi CH, Seligson D, Tolcher A, Alabi CA, Yen Y, Heidel JD, Ribas A. "Evidence of RNAi in humans from systemically administered siRNA via targeted nanoparticles," *Nature* **464**, 1067 (2010).

systemically to a human can produce a specific gene inhibition (reduction in mRNA and protein) by an RNAi mechanism of action.

2.2 Results and Discussion:

A major challenge with the use of siRNAs in mammals is their intracellular delivery to specific tissues and organs that express the target gene. The first demonstrations of siRNA-mediated gene silencing in mammals through systemic administration were accomplished using naked siRNA and methods of administration not compatible with clinical application.[5-7] Since then, several delivery vehicles have been combined with siRNAs to improve their delivery in animal models.[1,2] Soutschek *et al.* were the first to provide direct evidence for the siRNA mechanism of action by using a modified 5'-RACE (rapid amplification of cDNA ends) PCR technique providing positive identification of the specific mRNA cleavage product.[8] Human clinical trials with synthetic siRNAs began in 2004, utilizing direct intraocular siRNA injections for patients with blinding choroidal neovascularization (CNV). Subsequently, other clinical trials have initiated[2] and early clinical data are beginning to appear.[9,10] While there are animal studies that do support the possibility of an RNAi mechanism of action from administered siRNA,[11] other animal data from siRNAs injected into the eyes of mice for the treatment of CNV suggest non-RNAi mechanisms of action for CNV suppression.[12] At this time, no direct evidence for an RNAi mechanism of action in humans from siRNA administered either locally or systemically has been reported.

We are currently conducting the first siRNA clinical trial that utilizes a targeted nanoparticle delivery system (clinical trial registration number NCT00689065).[13] Patients with solid cancers refractory to standard-of-care therapies are administered doses of

targeted, nanoparticles on days 1, 3, 8 and 10 of a 21-day cycle via a 30-minute i.v. infusion. The nanoparticles consist of a synthetic delivery system containing (Fig. 2.1a): (i) a linear, cyclodextrin-based polymer (CDP), (ii) a human transferrin protein (hTf) targeting ligand displayed on the exterior of the nanoparticle to engage Tf receptors (hTfR) on the surface of the cancer cells, (iii) a hydrophilic polymer (polyethylene glycol (PEG) used to promote nanoparticle stability in biological fluids), and (iv) siRNA designed to reduce the expression of the M2 subunit of ribonucleotide reductase (RRM2: sequence used in the clinic was previously denoted siR2B+5).[14] The TfR has long been known to be up-regulated in malignant cells,[15] and RRM2 is an established anti-cancer target.[16] These nanoparticles (clinical version denoted as CALAA-01) have been shown to be well tolerated in multi-dosing studies in non-human primates.[17] While a single patient with chronic myeloid leukemia has been administered siRNA via liposomal delivery,[18] our clinical trial is the initial human trial to systemically deliver siRNA with a targeted delivery system and to treat patients with solid cancer.[13]

In order to ascertain whether the targeted delivery system can provide effective delivery of functional siRNA to human tumors, we investigated biopsies from three patients from three different dosing cohorts; patients A, B and C, all of whom had metastatic melanoma and received doses of CALAA-01 of 18, 24 and 30 mg-siRNA/m^2, respectively. Given the highly experimental nature of this protocol, the regulatory process at both the local and federal levels explicitly precluded a provision for mandatory biopsies in all patients. Therefore, biopsies were obtained on a voluntary basis. Biopsies in these three patients were collected after the final dose of cycle 1 (denoted A_{post}, B_{post} and $C1_{post}$) and compared to archived tissue (denoted A_{pre}, B_{pre} and $C1_{pre}$). Patient C

continued on therapy beyond one cycle and provided another set of biopsy materials ($C2_{pre}$ that was obtained approximately one month after the final dose of cycle 1 and $C2_{post}$ that was collected on the day of the final dose of cycle 2). Because of limited sample amount, only immunohistochemistry (IHC) and staining for the nanoparticles could be performed on the $C1_{pre}$ and $C1_{post}$ samples, and protein (for Western blot analyses) was only available from the $C2_{pre}$ and $C2_{post}$ samples. Details of this clinical trial will be reported elsewhere when completed.

The targeted nanoparticles (ca. 70 nm diameter) were administered i.v., as they are designed to circulate and then to accumulate and permeate in solid tumors.[13] Within the tumor, the hTf targeting ligand assists in directing the nanoparticles into tumor cells overexpressing hTfR.[19] To detect the nanoparticles in tumor cells, sections of the tumor tissue were stained for the presence of the nanoparticles using a 5 nm gold particle that is capped with thiolated PEG containing adamantane (AD) at the end distal to the thiol (AD-PEG-Au) to allow for multivalent binding to the cyclodextrins (Appendix Fig. A1). The function of the stain has been previously confirmed using other cyclodextrin-containing particles,[20] and is demonstrated here for the targeted nanoparticles carrying siRNA *in vitro* (Appendix Fig. A2) and *in vivo* (Appendix Fig. A3). Transmission electron microscopy (TEM) images of the nanoparticles confirm that in mice, the nanoparticles are intracellular (Appendix Fig. A4). Samples A, B and C1, analyzed in a blinded fashion, demonstrated a heterogeneous distribution of nanoparticles only in post-dosing tumor tissue (Fig. 2.1 for post-dosing and Supplementary Fig. 4 for pre-dosing). The nanoparticles can localize intracellularly in tumor tissue and are not found in the adjacent epidermis (Fig. 2.1). In these biopsies TEM images were dominated by

melanosomes[21] inhibiting the identification of the nanoparticles (data not shown). Samples $C1_{post}$ and $C2_{post}$ reveal the highest number and intensity of stained regions, B_{post} exhibits a decreased amount of staining relative to samples $C1_{post}$ and $C2_{post}$ (Fig. 2.1b), A_{post} does not reveal the presence of the stain (Fig. 2.1b), and all the pre-dosing samples are completely negative for the stain (Supplementary Fig. 4). This is the first example of a dose-dependent accumulation of targeted nanoparticles in tumors of humans from systemic injections for nanoparticles of any type.

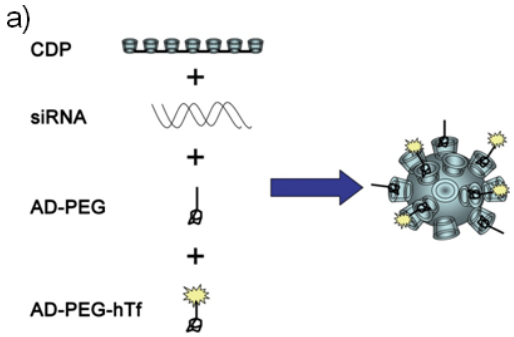

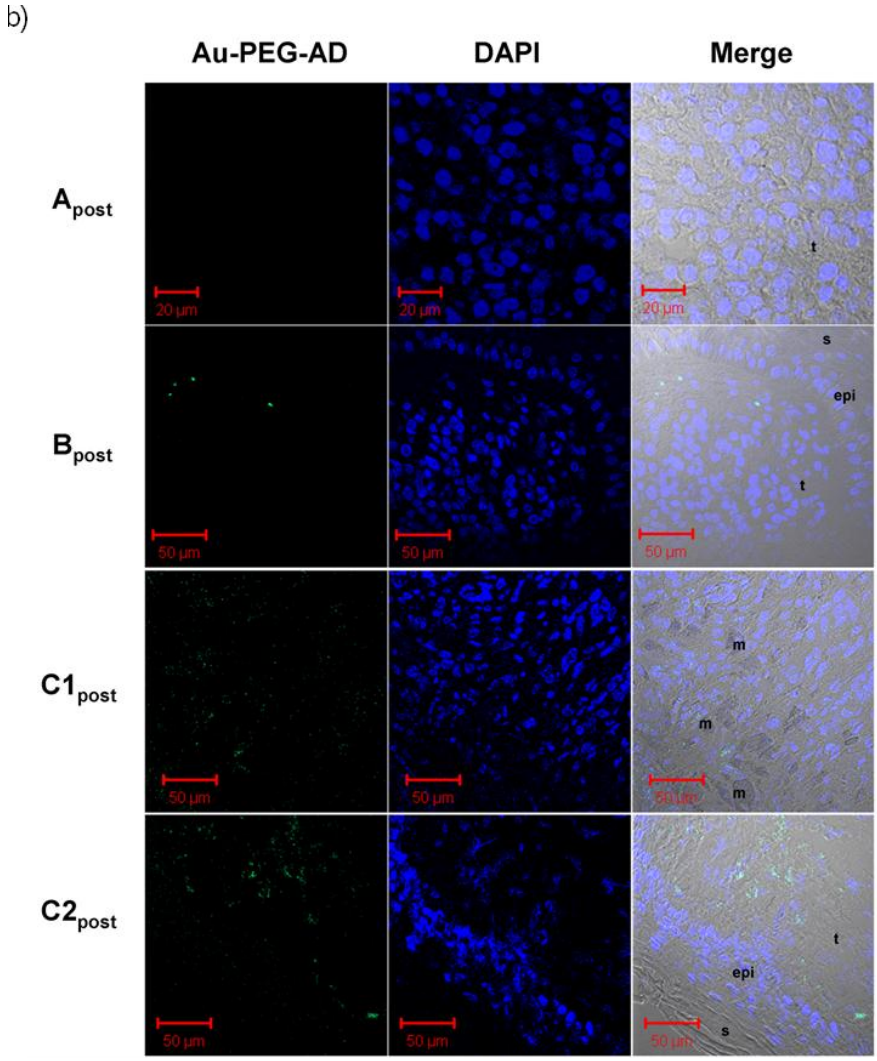

Figure 2.1. Detection of targeted nanoparticles in human tumors. (a). Schematic representation of the targeted nanoparticles. The polyethyleneglycol (PEG) molecules are terminated with adamantane (AD) that form inclusion complexes with surface cyclodextrins in order to decorate the surface of the nanoparticle with PEG for steric stabilization and PEG-hTf for targeting. (b). Confocal images of post-treatment biopsy sections from patients A, B and C: Au-PEG-AD stain (left), DAPI stain (middle), merged images of the left and right panels with the bright field (right). Image labels: epi = epidermis, t = tumor side, s = skin side, m = melanophage.

Tumor RRM2 mRNA levels were measured by quantitative real time polymerase chain reaction (qRT-PCR) and were performed in a blinded fashion.[22] Reduction in RRM2 mRNA is observed in the post-treatment samples (Fig. 2.2). Since samples A_{pre} and B_{pre} are from tissues collected many months before the initiation of siRNA treatment,

the fraction of the overall reduction in mRNA observed in A_{post} and B_{post} attributable to the nanoparticle treatment cannot be directly ascertained. Unfortunately, we were not able to perform PCR on the C1 samples. However, the PCR data from the $C2_{pre}$ vs. $C2_{post}$ samples (collected 10 days apart) provide direct evidence for RRM2 mRNA reduction via the treatment of the patient with the nanoparticles.

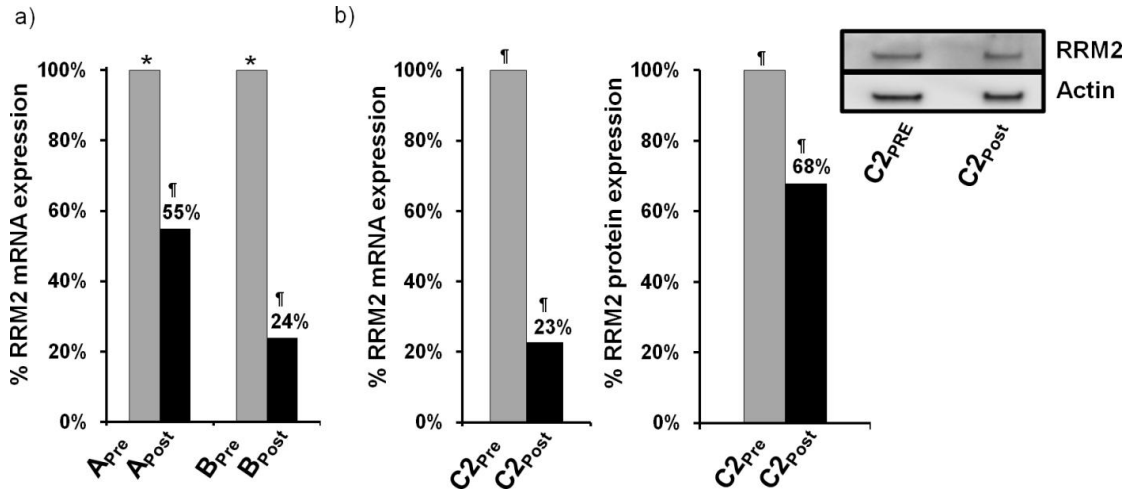

Figure 2.2. RRM2 mRNA and protein expression in tumor tissue. (a). qRT-PCR analysis of RRM2 mRNA levels in samples from patients A and B before and after dosing. RRM2 mRNA levels are normalized to TBP mRNA levels. Results are presented as percentage of the pre-dosing RRM2/TBP mRNA levels for each patient. (b). qRT-PCR and Western blot analysis of RRM2 protein expression from patient samples $C2_{pre}$ and $C2_{post}$. Bar graph is average volume of Western blot bands from two independent experiments; one representative blot is pictured. Archived samples are indicated by (*); samples obtained during the trial are indicated by (¶).

To ascertain whether the RRM2 protein level is reduced in the tumor because of the siRNA treatment, IHC and Western blotting were employed as previously described in mice.[23] Since RRM2 protein expression is largely restricted to the late G1/early S phase of cell cycle, not all of the tumor cells will be expressing RRM2. Figure 2.3 shows IHC data for RRM2 and TfR proteins in $C1_{pre}$ and $C1_{post}$ samples (IHC analyses were performed in a blinded fashion and 10 random regions of each sample were analyzed).

Significant reduction in RRM2 is observed (mean scoring of RRM2 from the 10 sections was reduced 5-fold) after treatment while TfR levels are somewhat elevated (mean scoring of TfR from the 10 sections was increased 1.2-fold) in the $C1_{pre}$ and $C1_{post}$ samples. The low level of RRM2 that is observed by IHC in the $C1_{post}$ sample is maintained in the $C2_{pre}$ and $C2_{post}$ samples (by IHC).

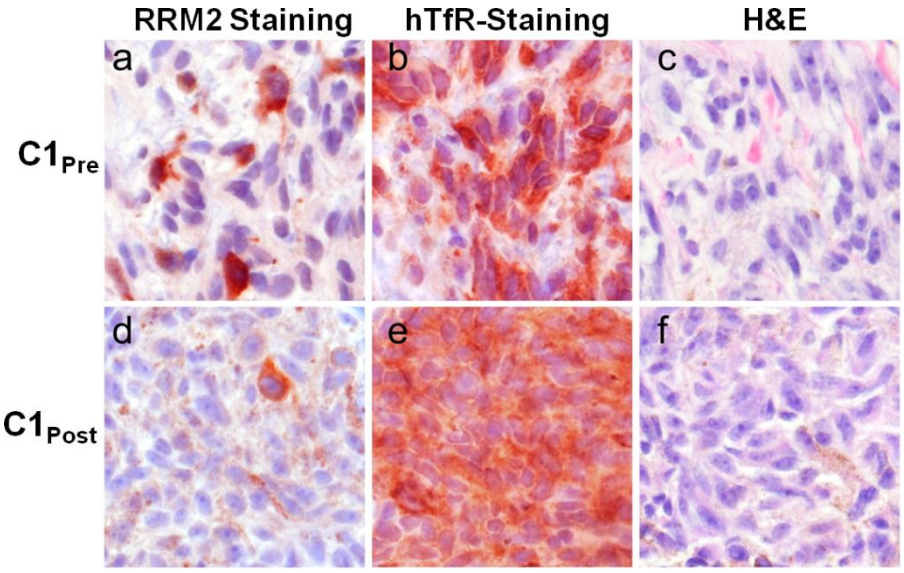

Figure 2.3. Ribonucleotide reductase (RRM2) and tranferrin receptor (TfR) protein expression in $C1_{pre}$ and $C1_{post}$ samples. Photomicrographs of malignant melanoma belonging to a, b, c, pre-treatment and d, e, f post-treatment samples. Protein expression is represented as brick-red (Nova Red) chromagen staining in immunohistochemically-treated slides (a, d: RRM2; b, e:TfR). c, f, The same tissues are stained with Hematoxylin and Eosin (H&E). d, e, f, Brown, diffuse, finely granular color seen in these images is the endogenous pigment of this lightly melanized tumor. Photomicrographs were captured using a 40X objective.

Western blot analyses of the $C2_{pre}$ and $C2_{post}$ samples reveal a reduction in the level of the RRM2 protein that is due to the siRNA treatment (RRM2 mRNA reductions exceeded the reduction levels obtained from protein but this could be due to post-transcriptional mechanisms that have been observed previously[24]). The decreases in the RRM2 mRNA and protein observed after treatment (Fig. 2.2b) suggest the siRNA

treatment remains effective after several cycles of dosing. The IHC data from patient A do not reveal changes in RRM2 expression after dosing, while results from patient B are indicative of reductions in maximal RRM2 expression (IHC scoring of the regions of maximal expression showed a 1.5-fold decrease) but the overall mean expression levels remained relatively constant (IHC scoring of the 10 sections).

To demonstrate that the siRNA delivered via the targeted nanoparticles can engage the RNAi machinery, the mRNA cleavage products were characterized using a modified 5'-RNA ligand-mediated rapid amplification of cDNA ends (5'-RLM-RACE) PCR technique (Fig. 2.4). A RRM2 mRNA fragment, whose 5' end matches the predicted cleavage site (10 base pairs from the 5' end of the antisense strand), was detected in the $C2_{pre}$ and $C2_{post}$ samples, but not from B_{post}, and A_{post} or their corresponding pre-treatment samples. RACE does not provide a quantitative measure of the amount of the fragments so the intensities of the bands cannot be correlated with amounts in the tissue samples. The presence of this RRM2 mRNA fragment from patient C indicates siRNA delivered via targeted nanoparticles can engage the RNAi machinery in a solid tumor of a human and induce the desired mRNA cleavage. Furthermore, this result suggests that at least a portion of the RRM2 mRNA and protein reductions observed from the C2 samples are due to a bona fide RNAi mechanism. The presence of the RRM2 mRNA fragment in the $C2_{pre}$ sample suggests that siRNA can provide an RNAi mechanism for several weeks (mRNA cleavage in the $C2_{pre}$ sample must originate from cycle one dosing) as the RRM2 protein levels remained relatively constant when compared to the $C1_{post}$ sample (IHC). We have shown that the length of the RNAi effects of delivered siRNA in both cells and animals (mice) is dependent on the doubling time of

the cells being analyzed (longer inhibition times with longer cell doubling times).[25] Gene silencing by siRNA can occur on the timescale observed here, ca. one month, provided the cell doubling times are long.[25] Patient C had stable disease between these biopsies, and these mostly quiescent tumors have very slow growth kinetics that would be suitable to experience lengthy RNAi effects.[25] Additionally, we do not know how long the nanoparticles reside within the cells and release siRNA. Since the nanoparticles are observed in the sample $C1_{post}$ and not the sample $C2_{pre}$, they must disassemble within one month. Thus, the pharmacodynamics of the RNAi effects could be due to the combination of the nanoparticle disassembly time and the time that the siRNA resides within the RNAi machinery.

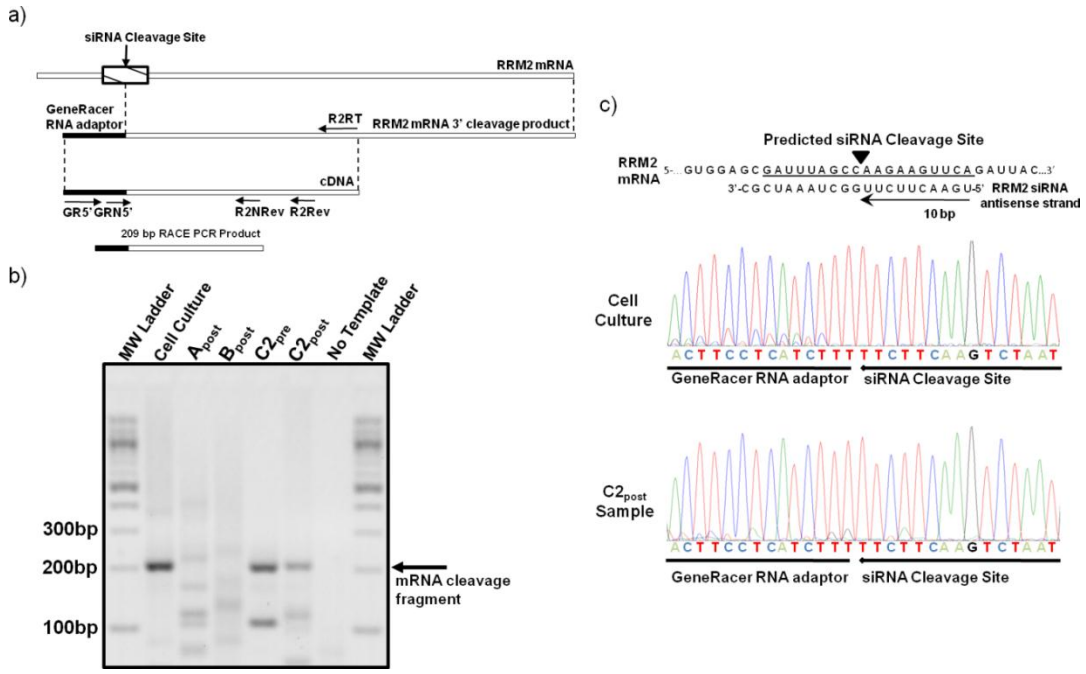

Figure 2.4. 5'-RLM-RACE detection of siRNA induced mRNA cleavage fragment. (a) Schematic depicting the location of the predicted anti-RRM2 siRNA cleavage site and the primers used for PCR amplification of the cleavage fragment. (b) Agarose gel of 5'-RLM-RACE PCR amplification products from post treatment samples (A_{post}, B_{post}, $C2_{post}$) and *in vitro* positive control (cell culture). (c) The RRM2 mRNA sequence and siRNA antisense strand are illustrated to show where the cleavage occurs with an RNAi mechanism. The sequence chromatographs

obtained from an *in vitro* cell culture experiment with HT-144 melanoma cells and the patient $C2_{post}$ sample are illustrated.

The data presented here when taken together provide the first mechanistic evidence of RNAi in a human from an administered siRNA. Moreover, these data demonstrate the first example of dose dependent accumulation of targeted nanoparticles in human tumors. The reduction of the RRM2 mRNA and protein by the RRM2-specific siRNA is observed, and the results from 5'-RLM-RACE analyses reveal that the delivered siRNA engages the RNAi machinery. These data demonstrate that RNAi can occur in a human from a systemically delivered siRNA, and that siRNA can be used as a gene-specific therapeutic.

2.3 Acknowledgements

We thank H. Sazegar, E. Seja, A. Villanueva, and the G-CRC nursing staff at UCLA, L. Kalinoski, J. Peterkin, S. Rele, Y. Liang and J.Y.C. Liu at Calando Pharmaceuticals for their assistance in conducting the clinical trial. We thank Dr. J. S. Economou at UCLA for performing the tumor biopsies, and Drs. B. Chmielowski and Z. Wainberg, also at UCLA, for patient referrals. Histotechnology support at the UCLA Biomarker Innovations Laboratory was provided by C. Savina and J. Reiss. We also thank Dr. J. Rossi at the City of Hope for discussions on RACE analyses. This work was supported in part by the National Cancer Institute Grant CA U54 119347 and the Daljit S. & Elaine Sarkaria Biomarker Laboratory Fund.

2.4 Methods

Detection of targeted nanoparticles in biopsy samples: Snap-frozen patient biopsy samples were embedded in Tissue-Tek O.C.T. compound (Sakura) to generate 6 μm-thick cryosections. Upon immersion in PBS at 37 ºC for 1 h to remove any surface O.C.T., and in acetone at −20 °C for 20

min to permeabilize the cell membrane, sections received staining of PEGylated, adamantane-modified gold nanoparticles (Au-PEG-AD; see Supplementary Information for their preparation) in the dark for 2 h. Brief rinses with PBS were used to remove any nonspecifically bound Au-PEG-AD before mounting with ProLong Gold antifade reagent and staining with DAPI (Invitrogen, Carlsbad, CA). A Zeiss LSM 510 confocal scanning microscope (with a Plan-Neofluar 40X/0.75 objective and up to 2X digital zoom) was used to collect the images (DAPI-excitation: 740 nm (two-photon laser), emission filter: 390-490 nm; Au-PEG-AD-excitation: 488 nm (argon laser), emission filter: BP 500-550 nm IR). The measured resolution at which images were acquired is 512 x 512 pixels, and the image bit-depth is 8-bit. The Zeiss LSM Image Browser Software allows the extraction of images.

RNA Extraction: Patient samples preserved in RNALater (Ambion, Austin, TX) were suspended in TRIzol reagent (Invitrogen) and homogenized in a FastPrep-24 Tissue Homogenizer (MP Biomedicals, Solon, OH). Total RNA was purified from the aqueous phase of TRIzol extract using the PureLink RNA Mini Kit (Invitrogen) following manufacturer recommendations. RNA was extracted from archived patient samples using RecoverAll total nucleic acid isolation kit (Ambion) following manufacturer instructions.

5' RNA ligand mediated-RACE: 5-RLM-RACE was performed according to the Invitrogen GeneRacer manual with modifications. 2-8 μg of total RNA was ligated directly to 250ng GeneRacer RNA adaptor (5'-CGACUGGAGCACGAGGACACUGACAUGGACUGAAGGAGUAGAAA-3') using T4 RNA ligase (5 units) for 1 h at 37°C. Following phenol extraction and ethanol precipitation the purified ligation products were reverse transcribed using SuperScriptIII (Invitrogen) and a RRM2 gene specific reverse transcription primer (5'-CTCTCTCCTCCGATGGTTTG-3') at 55°C for 45 min followed by inactivation at 70°C. 5'RLM-RACE-PCR was performed using the GeneRacer 5' primer (5'-CGACTGGAGCACGAGGACACTGA-3') and a RRM2 gene specific reverse primer

(5'-GGCCAGGCATCAGTCCTCGTTTCTTG-3'). PCR was performed using a Bio-Rad MJ Mini personal thermocycler using PCR conditions of 95°C for 3 min (1 cycle), 95°C for 30 s, 60°C for 30 s, 72°C for 1 min (40 cycles), 72°C for 10 min (1 cycle). A second round of nested PCR was then performed using the GeneRacer 5' nested primer (5-GGACACTGACATGGACTGAAGGAGTA-3') and a RRM2 gene-specific nested primer (5'-GGCCCAGTCTGCCTTCTTCTTGAC-3'). PCR products were run on a 2% agarose gel and stained with 1μg/μl ethidium bromide. PCR products were excised from gel and sequenced directly to confirm RACE band identities. For the cell culture RACE experiments, 500,000 HT-144 melanoma cells were transfected with 20 nM RRM2 siRNA using Lipofectamine RNAiMax (Invitrogen). RNA was extracted for the RLM-RACE as describe above 48 h after transfection.

qRT-PCR: Patient RNA samples were reversed transcribed using SuperScriptIII reverse transcriptase. 0.4-200ng of white blood cell (WBC) cDNA was used as PCR template for standard curves of RRM2 and Tata Binding Protein (TBP). 2 μl of prepared sample cDNA/standard cDNA was used for triplicate Taqman Real time-PCR as described elsewhere.[25] Concentrations of RRM2 and TBP in samples were calculated from the WBC cDNA standard curve, and RRM2 levels were normalized to TBP levels within the same sample.

Western blots: Total protein was recovered from the phenol/chloroform phase of TRIzol extraction (see description of the RNA extraction above). Samples were diluted to equivalent protein concentration and denatured via addition of beta-mercaptoethanol-containing Laimmli sample buffer. The primary antibodies were goat polyclonal anti-RRM2 antibody (Santa Cruz Biotechnology, Santa Cruz, CA), mouse polyclonal anti-actin antibody (BD Biosciences, San Jose, CA). The secondary antibodies were horseradish peroxidase-conjugated donkey anti-goat antibody and rabbit anti-mouse antibody (Santa Cruz Biotechnology). Development was done using SuperSignal West Dura Extended Duration Substrate (Thermo-Fisher, Waltham, MA). Blot images were captured using a Molecular Imager VersaDoc 3000 system (Bio-Rad, Hercules,

CA). Band quantification was performed using Image-Quant TL software (GE/Amersham Biosciences, Piscataway, NJ).

Tissues and immunohistochemical assay: Formalin-fixed, paraffin-embedded (FFPE) human tissue samples from patient–matched pre- and post-treatment cases were obtained under UCLA IRB approval. Immunohistochemical (IHC) assays were performed using a Dako Autostainer Plus (Dako, Carpinteria, CA) with fresh sections of pre- and post-treatment cases stained at the same time. Tissue sections 4 μm thick were deparaffinized in xylene and rehydrated in graded alcohols. The sections were then placed in a pressure cooker (17.5 PSI, 122 °C; Biocare Decloaking Chamber, Biocare Medical LLC., Concord, CA) in 0.01M sodium citrate buffer (pH 6.0) or 0.1M Tris-HCl buffer (pH 9.0) for 10 min for heat antigen retrieval of RRM2 and TfR antigens, respectively. Endogenous peroxidase was quenched with 3% hydrogen peroxide at room temperature. Primary goat anti-human R2 polyclonal antibody, (catalog # sc-10846; Santa Cruz Biotechnology, Inc., Santa Cruz, CA), was applied for 30 min at room temperature at a final concentration of 1.0 μg/ml (1:200). Mouse anti-human TfR monoclonal IgG1 antibody (clone H68.4, catalog number 13-6800; Invitrogen, Camarillo, CA) was applied for 30 min at room temperature at a final concentration of 0.5 μg/ml (1:1000). Antigen detection was accomplished using the Vectastain ABC Elite Goat HRP kit (catalog number PK-6105, Vector Labs, Burlingame, CA, USA) or the Dako Envision goat anti-mouse IgG secondary antibody with attached HRP-labeled dextran polymer (catalog number K4001; Dako, Carpinteria, CA), for RRM2 and TfR, respectively. All tissues were either amelanotic or only lightly melanized, therefore bleaching was not performed and Nova Red (catalog number SK-4800; Vector Labs, Burlingame, CA) was used as the chromagen to easily discern staining from any endogenous pigment. The sections were then counterstained with Meyer's hematoxylin, followed by dehydration in graded alcohols, xylene, and cover-slipping. Human tonsil and colon cancer served as positive assay controls. Negative controls consisted of duplicate tissue sections stained

with either non-immune pooled goat IgG (catalog number I-5000, Vector Labs, Burlingame, CA) or monoclonal mouse IgG1 (catalog number 02-6100; Invitrogen, Camarillo, CA) applied at identical final concentrations as used for RRM2 and TfR primary antibodies, respectively. For each sample, 10 random tumor regions were scored for maximal expression and mean expression.

2.5 References

1 Bumcrot, D., Manoharan, M., Koteliansky, V. & Sah, D.W.Y. RNAi therapeutics: a potential new class of pharmaceutical drugs. *Nat. Chem. Biol.* **2**, 711-719 (2006).

2. Castanotto, D. & Rossi, J.J. The promises and pitfalls of RNA-interference-based therapeutics. *Nature* **457**, 426-433 (2009).

3. Fire, A., *et al.* Potent and specific genetic interference by double-stranded RNA in *Caenorhabditis elegans*. *Nature* **391**, 806-811 (1998).

4. Elbashir, S.M., *et al.* Duplexes of 21-nucleotide RNAs mediate RNA interference in cultured mammalian cells. *Nature* **411**, 494-498 (2001).

5. McCaffrey, A.P., *et al.* RNA interference in adult mice. *Nature* **418**, 38-39 (2002).

6. Lewis, D.L., Hagstrom, J.E., Loomis, A.G., Wolff, J.A. & Herweijer, H. Efficient delivery of siRNA for inhibition of gene expression in postnatal mice. *Nat. Genet.* **32**, 107-108 (2002).

7. Song, E., *et al.* RNA interference targeting Fas protects mice from fulminant hepatitis. *Nat. Med.* **9**, 347-351 (2003).

8. Soutschek, J., *et al.* Therapeutic silencing of an endogenous gene by systemic administration of modified siRNAs. *Nature* **432**, 173-178 (2004).

9. DeVincenzo, J., *et al.* Evaluation of the safety, tolerability and pharmacokinetics of ALN-RSV01, a novel RNAi antiviral therapeutic directed against respiratory syncytial virus (RSV). *Antivir. Res.* **77**, 225-231 (2008).

10. Leachman, S.A. et al. First-in-human mutation-targeted siRNA phase Ib trial of an inherited skin disorder. *Mol. Ther.* **18**, 442-446 (2010).

11. Alvarez, R. et al. RNAi-mediated silencing of the respiratory syncytial virus nucleocapsid defines a potent anti-viral strategy. *Antimicrob. Agents Chemother.* **53**, 3952-3962 (2009).

12. Kleinman, M.E., *et al.* Sequence- and target-independent angiogenesis suppression by siRNA via TLR3. *Nature* **452**, 591-597 (2008).

13. Davis, M.E. The first targeted delivery of siRNA in humans via a self-assembling, cyclodextrin polymer-based nanoparticle: from concept to clinic. *Mol. Pharm.* **6**, 659-668 (2009).

14. Heidel, J.D., *et al.* Potent siRNA inhibitors of ribonucleotide reductase subunit RRM2 reduce cell proliferation *in vitro* and *in vivo*. *Clin. Cancer Res.* **13**, 2207-2215 (2007).

15. Gatter, K.C., Brown, G., Strowbridge, I.S., Wollston, R.E. & Mason, D.Y Transferrin receptors in human tissues: their distribution and possible clinical relevance. *J. Clin. Pathol.* **36**, 539-545 (1983).

16. Cerqueira, N.M.F.S.A., Pereira, S. Fernandes, P.A. & Ramos, M.J. Overview of ribonucleotide reductase inhibitors: an appealing target in anti-tumor therapy. *Curr. Med. Chem.* **12**, 1283-1294 (2005).

17. Heidel, J.D., *et al.* Administration in non-human primates of escalating intravenous doses of targeted nanoparticles containing ribonucleotide reductase subunit M2 siRNA. *Proc. Nat. Acad. Sci. USA* **104**, 5715-5721 (2007).

18. Koldehoff, M., Steckel, N.K., Beelen, D.W. & Elmaagacli, A.H. Therapeutic application of small interfering RNA directed against *bcr-abl* transcripts to a patient with imatinib-resistant chronic myeloid leukaemia. *Clin. Exp. Med.* **7**, 47-55 (2007).

19. Bartlett, D.W., Su, H., Hildebrandt, I.J., Weber, W.A. & Davis, M.E. Impact of tumor-specific targeting on the biodistribution and efficacy of siRNA nanoparticles measured by multimodality *in vivo* imaging. *Proc. Nat. Acad. Sci. USA* **104**, 15549-15554 (2007).

20. Schluep, T., *et al.* Pharmacokinetics and tumor dynamics of the nanoparticle IT-101 from PET imaging and tumor histological measurements. *Proc. Nat. Acad. Sci. USA* **106**, 11394-11399 (2009).

21. Rudiger, R., Schartl, M. & Kollinger, G. Comparative studies on the ultrastructure of malignant melanoma in fish and human by freeze-etching and transmission electron microscropy. *J. Cancer Res. Clin. Oncol.* **107**, 21-31 (1984).

22. Juhasz, A., Vassilakos, A., Chew, H.K., Gandara, D. & Yen,Y. Analysis of ribonucleotide reductase M2 mRNA levels in patient samples after GTI-2040 antisense drug treatment. *Oncol. Rep.* **15**, 1299-1304 (2006).

23. Bartlett, D.W. & Davis, M.E. Impact of tumor-specific targeting and dosing schedule on tumor growth inhibition after intravenous administration of siRNA-containing nanoparticles. *Biotechnol. Bioeng.* **99**, 975-985 (2008).

24. McClarty, G.A., Chan, A.K., Engstrom, Y, Wright, J.A. & Thelander, L. Elevated expression of M1 and M2 components and drug-induced posttranscriptional

modulation of ribonucleotide reductase in a hydroxyurea-resistant mouse cell line. *Biochemistry* **26**, 8004-8011 (1987),

25. Bartlett, D.W. & Davis, M.E. Insights into the kinetics of siRNA-mediated gene silencing from live-cell and live-animal bioluminescent imaging. *Nucl. Acids Res.* **34**, 322-333 (2006)

2.6 Supplementary Information for Chapter 2

Part I. Creation of stain for CALAA-01

Materials

Methoxy-PEG-thiol (MW 1000 g/mol) was purchased from Laysan Bio (Arab, AL). SPDP-dPEG$^{TM}_{12}$-NHS (MW 912.08 g/mol) ester was purchased from Quanta Biodesign (Powell, OH). 5 nm spherical gold nanoparticles were obtained from Nanopartz (Salt Lake City, UT).

Methods

Preparation of SPDP-dPEG$^{TM}_{12}$-AD (see Scheme SI 1)

To a solution of SPDP-dPEG$^{TM}_{12}$-NHS (100 mg, 0.11 mmol) in 3 mL of anhydrous dichloromethane was added adamantanemethylamine (0.11 mmol, 21 µL). The solution was stirred for 16 hours at room temperature, after which the solvent was removed and the product dried under vacuuo. (MALDI-TOF) $[M+Na]^+$ 984.08, $[M+K]^+$ 1000.16

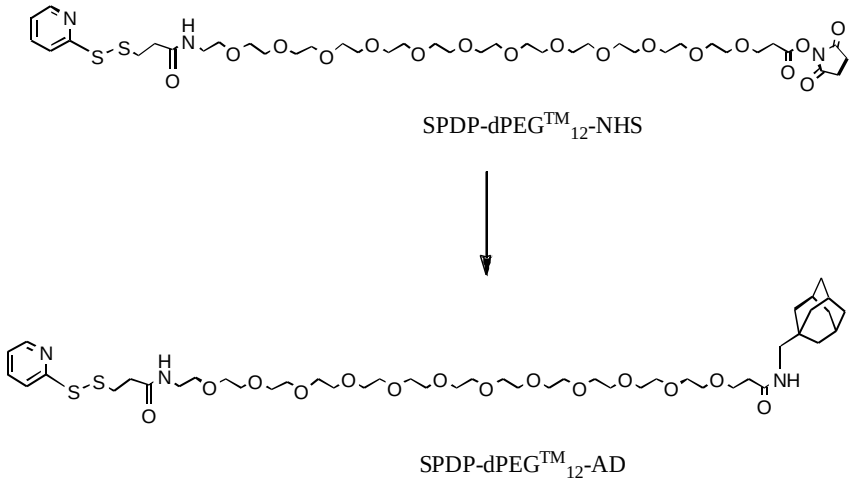

Scheme SI 1: Synthesis of SPDP-dPEG$^{TM}_{12}$-AD

PEGylation of 5 nm gold nanoparticles with SPDP-dPEG$^{TM}_{12}$-AD (Au-PEG-AD)

To a pre-sonicated 1 mL solution of 5 nm gold nanoparticles (10^{13} particles per mL) was added mPEG-thiol (14 µg, 14 nmol) and SPDP-dPEG$^{TM}_{12}$-AD (16 µg, 14 nmol). The solution was vortexed for 30 minutes and diluted to 4 mL with deionized water. The resulting 4 mL solution was diafiltered twice with a 10 kDa membrane (Millipore) and finally resuspended to 1 mL.

PEGylation of 5 nm gold nanoparticles with methoxy-PEG-thiol (Au-PEG)

To a pre-sonicated 1 mL solution of 5 nm gold nanoparticles (10^{13} particles per mL) was added methoxy-PEG-thiol (28 µg, 28 nmol). The solution was vortexed for 30 minutes and diluted to 4 mL with deionized water. The resulting 4 mL solution was diafiltered twice with a 10 kDa membrane (Millipore) and finally resuspended to 1 mL.

Part II: Principle of staining

A schematic representation of the interactions between the Au-PEG-AD particles and CALAA-01 is shown in Schematic SI 2.

Key

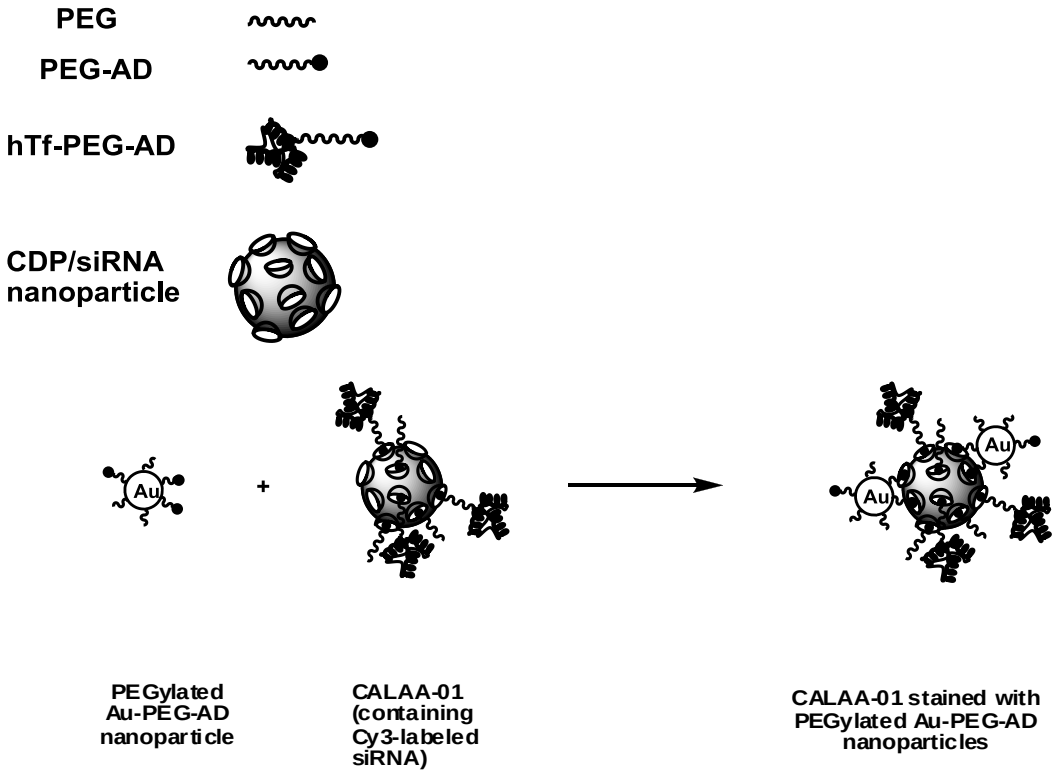

Scheme SI 2: Representation of the staining process of CALAA-01 by Au-PEG-AD particles.

Part III: In vitro validation of binding of Au-PEG-AD to the siRNA-containing nanoparticles

A sandwich ELISA assay was developed to test for the binding of the gold stain (Au-PEG-AD) onto the siRNA-containing nanoparticles.

Materials

- Coating buffer: 10 μg/mL mouse IgG against human transferrin (Bethyl Laboratories, Montgomery, TX) in 50 mM carbonate-bicarbonate buffer (pH = 9.6)
- Wash buffer: 50 mM Tris, 140 mM NaCl, 0.05 % Tween 20, pH = 8
- Blocking buffer: 50 mM Tris, 140 mM NaCl, 1 % bovine serum albumin (BSA), pH = 8
- Targeted particle solution: Transferrin-targeted particles containing siRNA (0.5 mol % AD-PEG-Tf) in 150 mM phosphate buffered saline (PBS)
- Staining solution: Au-PEG-AD or Au-PEG particles in 150 mM PBS

Method

The entire ELISA procedure was conducted at room temperature with mild shaking on a plate shaker. Into each well of a 96-well ELISA plate was coated with 0.1 mL of coating buffer that contains the primary antibody, IgG against human transferrin for 1 hour. Three rinses with 0.1 mL of wash buffer followed to remove unbound antibodies. Next, blocking with BSA by adding 0.2 mL of blocking buffer into each well took place for 1 hour, followed by three brief rinses with 0.1 mL of wash buffer. After that, each well was added with 0.1 mL of either targeted particle solution or 150 mM PBS as a negative control and incubated for 2 hours. After five rinses with 0.1 mL of wash buffer to remove unbound targeted particles, each well was loaded with 0.1 mL of staining solution containing either Au-PEG-AD or Au-PEG at different concentrations and incubated for 2 hours. Upon five rinses with 0.1 mL of wash buffer to remove unbound targeted particles, each well was loaded with 0.1 mL of 150 mM PBS for absorbance measurement at 520 nm (surface plasmonic peak for 5 nm Au-PEG particles) using a Safire^2 Microplate Reader (Tecan, Salzburg, Austria). Reported values are mean absorbance from duplicates of experiments.

Results

The binding of Au-PEG-AD to the siRNA-containing nanoparticles relies upon the interaction between ADs and the cyclodextrin (CD) in a dose dependent fashion.

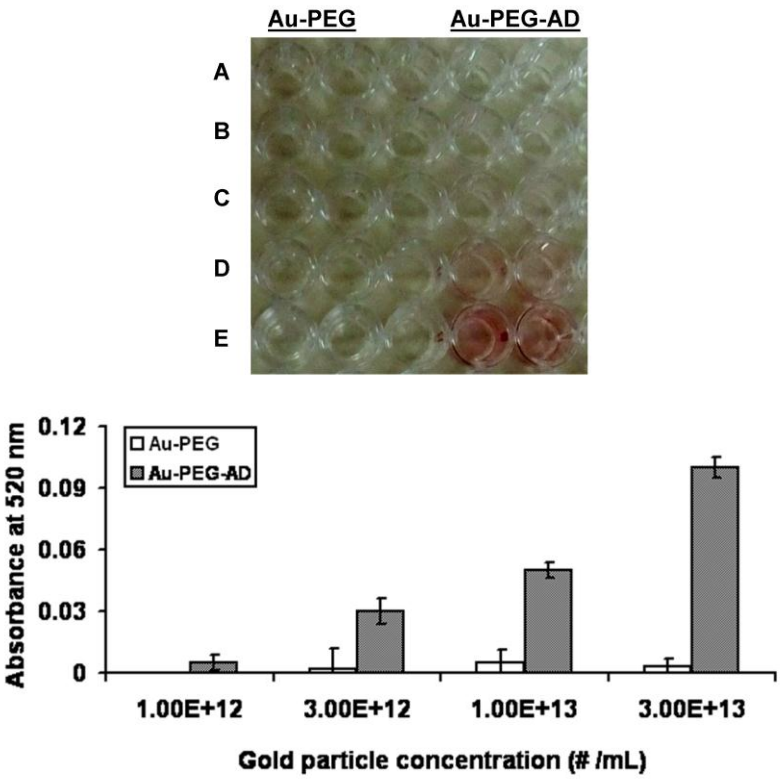

Figure S1: (A) The ELISA plate captures the red color due to binding of Au-PEG-AD onto targeted siRNA particles via specific CD-AD interactions. Legend: - A: no targeted nanoparticles + gold particles (10^{12} #/mL); B: targeted nanoparticles + gold particles (10^{12} #/mL); C: targeted nanoparticles + gold particles ($3x10^{12}$ #/mL); D: targeted nanoparticles + gold particles (10^{13} #/mL); E: targeted nanoparticles + gold particles ($3x10^{13}$ #/mL). (B) This graph demonstrates a dose-dependent binding of Au-PEG-AD onto siRNA-containing, CDP targeted nanoparticles (rows B to E in Figure S1A). As the negative control, the wells not loaded with any targeted nanoparticles do not show detectable gold absorbance (row A in Figure S1A).

Part IV: In vivo validation of binding of Au-PEG-AD to siRNA-containing nanoparticles in murine models

The use of imaging techniques serves to ascertain whether Au-PEG-AD can recognize intravenously injected targeted, siRNA-containing nanoparticles in a mouse tumor tissue.

Methods

Tumor Formation and Systemic Delivery of siRNA-containing Nanoparticles

All animal experiments were performed with sterile techniques and complied with the NIH Guidelines for Animal Care and as approved by the Caltech Institutional Animal Care and Use Committee. Neuro2A (mouse neuroblastoma) cells were cultured in complete growth medium (DMEM supplemented with 10 % fetal bovine serum (FBS),

100 units/mL penicillin, and 100 units/mL streptomycin). In the right hind flank, four immunodeficient (NOD.CB17-Prkdcscid/J) mice (The Jackson Laboratory, Bar Harbor, ME) received subcutaneous implantation of N2A cells (at 10^6 cells per mouse per 0.1 mL of DMEM). Before injection, tumors reached 100-200 mm^3 in size, as determined by caliper measurements ($0.5 \times l \times w^2$). Two mice received intravenous administration of siRNA-containing, cyclodextrin-based, targeted nanoparticles at a dose level of 10 mg siRNA/kg animal via the tail-vein. Formulated in 0.1 mL of 5 % glucose in water (D5W), the injected dose contained targeted nanoparticles carrying Cy3-labeled siRNA (20% of the total siRNA in the nanoparticles). As controls, two other mice received intravenous injections of 0.1 mL of D5W. Animal sacrifice by CO_2 overdose took place 24 hours after injection, followed by tumor extraction and immersion fixation in 4 % paraformaldehyde (PFA).

Transmission Electron Microscopy

PFA-fixed blocks (~ 1 mm^3 in volume) of mouse tumor samples received fixation with 2.5 % glutaraldehyde (in 100 mM sodium cacodylate, pH = 7.4) for 2 hours, post-stain by 1 % OsO_4 at 4 °C for 2 hours, and 0.9 % OsO_4 and 3 % $K_3Fe(CN)_6$ at 4 °C for 2 hours. Subsequent dehydration with an ethanol gradient and propylene oxide enabled the embedding tissue blocks polymerized from Epon 812 resins (EMS; Electron Microscopy Sciences, Hatfield, PA). 80 nm thick sections were deposited on carbon and formvar-coated, 200-mesh, nickel grids (EMS) and later stained with 3 % uranyl acetate (SPI Supplies, West Chester, PA) and Reynolds lead citrate for visualization under a 120 kV BioTwin CM120 TEM (Philips). All electron micrographs are from randomly chosen facets of the tissue block.

Results

Transmission electron microscopy confirms the existence of siRNA containing, targeted nanoparticles inside a mouse subcutaneous tumor.

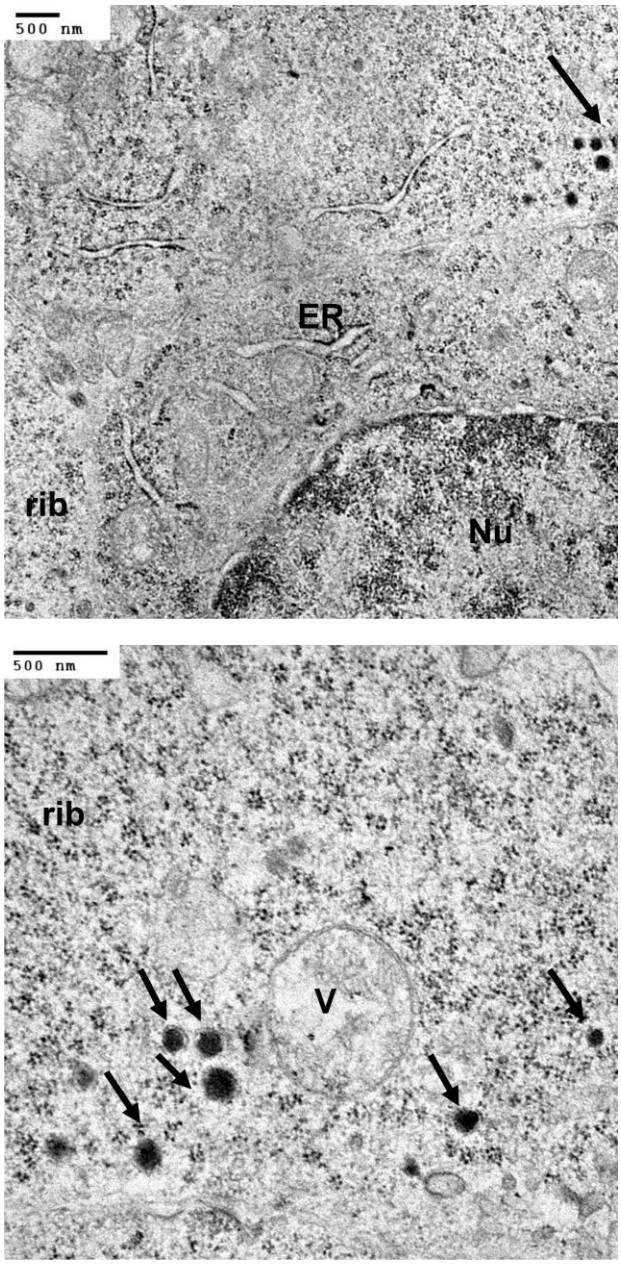

Figure S2: Transmission electron micrographs showed intracellular localization of siRNA-containing, cyclodextrin-based, targeted nanoparticles (dark round objects – the siRNA within the nanoparticle is stained by the presence of the uranyl ions that bind to the nucleic acid) inside N2A cells of the tumor subcutaneously implanted in mice (same tumor tissue used for confocal fluorescence imaging in Figure 1). (Left) The proximity of targeted nanoparticles to the nucleus shows their intracellular localization. (Right) Expanded view of nanoparticles shown in left panel (Scale bar = 500 nm). Solid arrows point to the nanoparticles. Labeling is as follows, Nu: nucleus, rib: ribosome, ER: endoplasmic reticulum, V: vesicle.

Upon the confirmation of the presence of targeted particles inside the tumor following their systemic injection, confocal microscopy can validate the utility of Au-PEG-AD as a stain for the targeted nanoparticles in the same tumor tissues extracted from the same mice.

Methods

Fluorescence Microscopy with Au-PEG-AD

After immersion fixation in 4 % PFA in PBS for 3 days, ~2 cm^3 mouse tumor tissue blocks passed through an increasing sucrose gradient up to 30 % sucrose, and were later embedded in 9 % gelatin in PBS. The gradual freezing of gelatin tissue blocks to -80 °C allowed the generation of 10 µm-thick cryosections. After brief rinsing with PBS to remove any surface gelatin as well as fixation with acetone at -20 °C to permeabilize the cell membrane, tissue sections underwent staining of PEGylated, adamantane-modified gold nanoparticles (Au-PEG-AD) in the dark for 2 hours. Rinsing with PBS removed any non-specifically bound gold particles, before the mounting of Au-PEG-AD stained tumor sections with 16.7 % (w/v) Mowiol 4-88 and 33 % (v/v) glycerol in PBS. A Zeiss LSM 510 confocal scanning microscope served to reveal the *in vivo* tumor biodistribution of the Cy3-siRNA containing targeted nanoparticles (excitation: 555 nm; emission: 570 nm), whose presence was further confirmed by its colocalization with Au-PEG-AD (excitation: 488 nm; emission: 507 nm).

Results

Cy3 Au-PEG-AD Merge

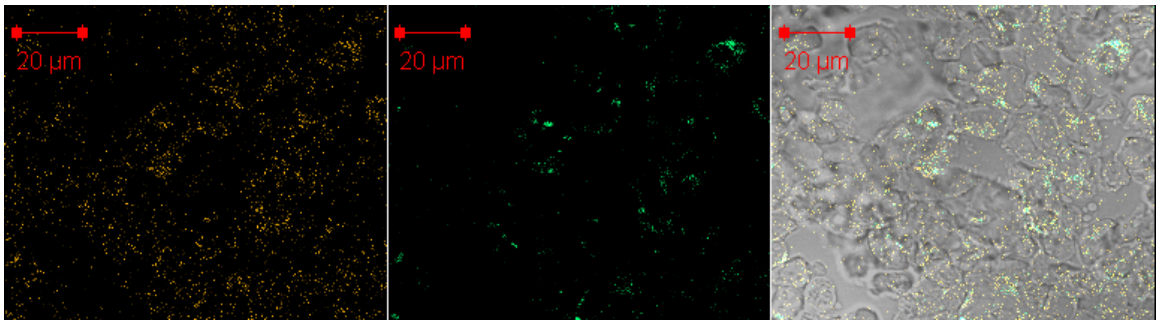

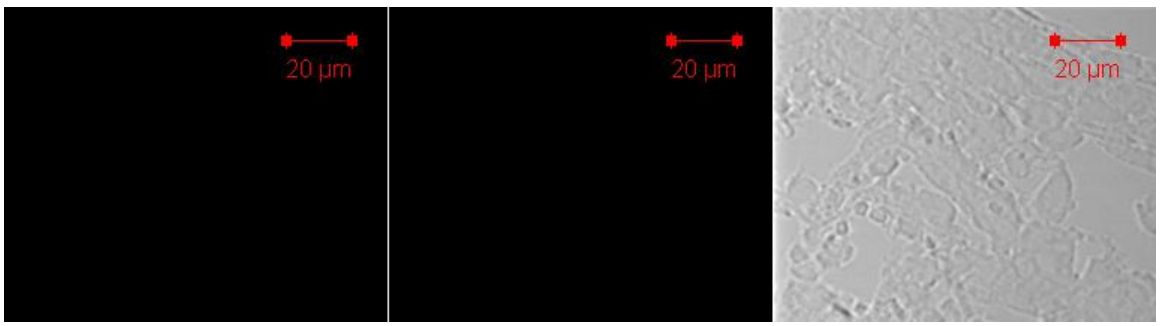

Figure S3: (Top) Tumor tissue collected from mice receiving intravenous (tail vein) injections of Cy3-siRNA containing, targeted nanoparticles. Au-PEG-AD particles (green: middle; emission: 507 nm) specifically bind to the Cy3-siRNA (orange: left; emission: 570 nm) containing, cyclodextrin-based targeted nanoparticles, whose localization was strictly intracellular, as seen from the merged bright-field image (right). (Bottom) As a negative control, tumor tissues were collected from mice that received intravenous injections of D5W. Au-PEG-AD particles failed to stain the tumor tissue in the absence of targeted nanoparticles. (Scale bar = 20 μm)

Part V: Staining of biopsy samples with Au-PEG-AD (Patient Pre-treatment samples)

Au-PEG-AD DAPI Merge

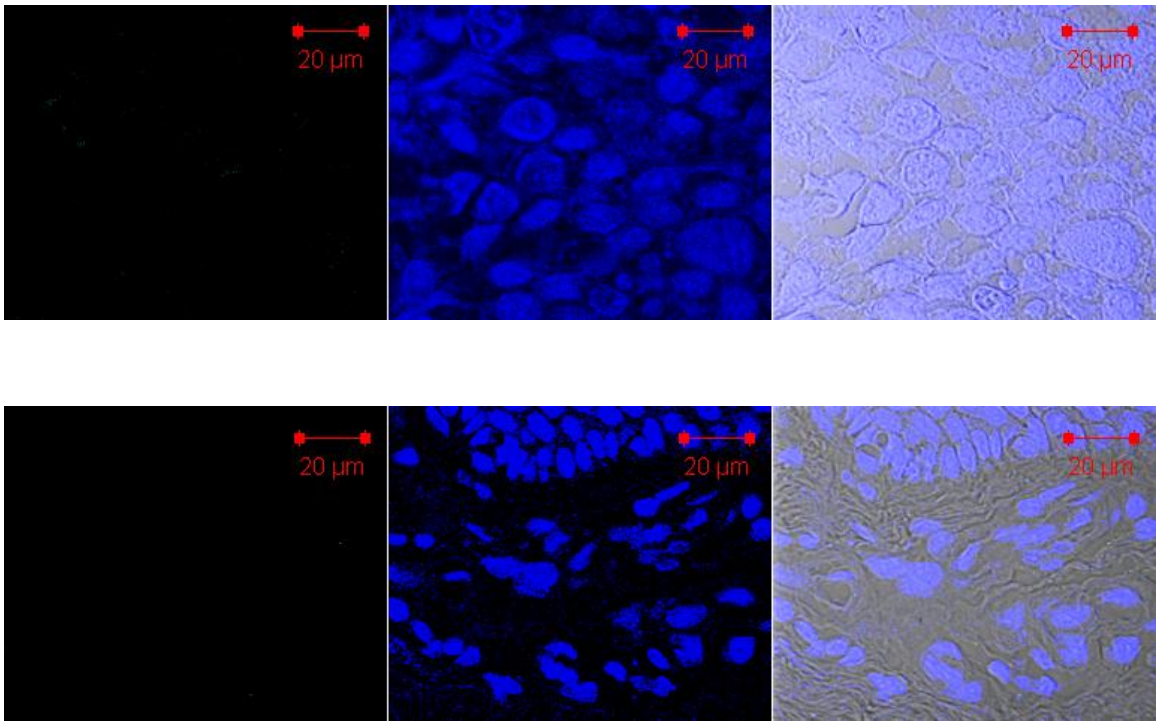

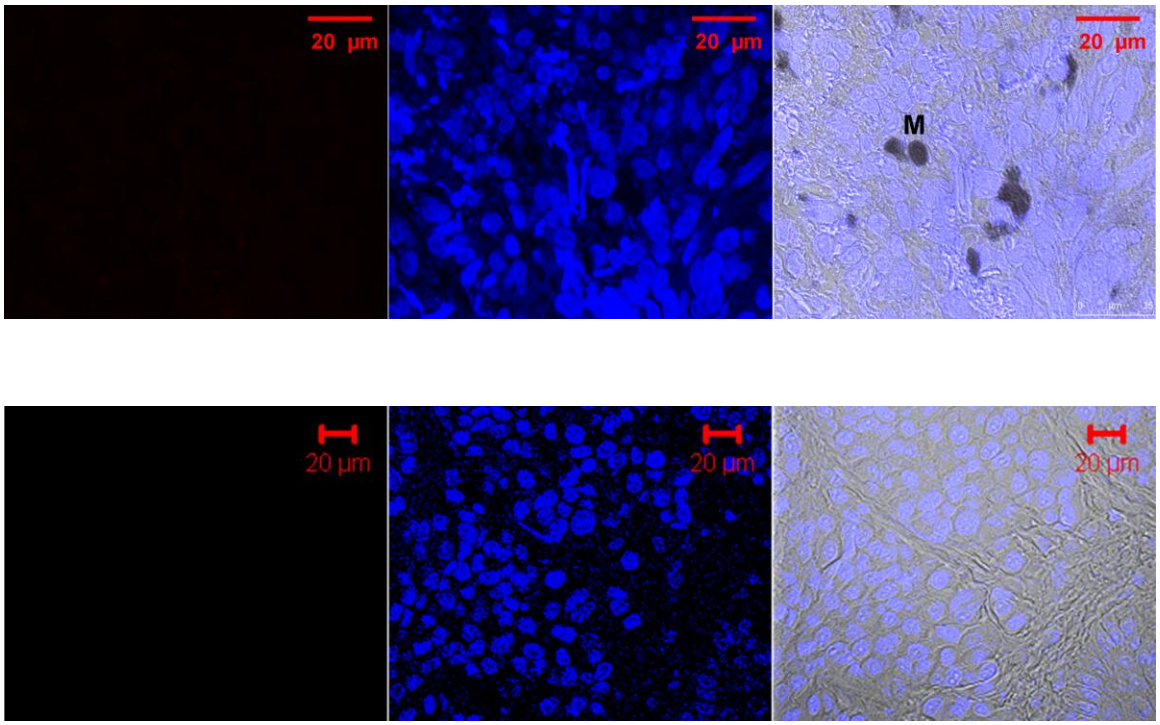

Figure S4: Au-PEG-AD staining of CALAA-01 nanoparticles in tumor biopsy samples using Au-PEG-AD and DAPI nuclear counter-stain. All pre-treatment samples, including A_{pre} (top row), B_{pre} (second row), $C1_{pre}$ (third row), and $C2_{pre}$ (bottom row), reveal undetectable gold staining. (Scale bar = 20 microns) Legend: M = melanophage (black objects inside the melanoma tissue).

.

Chapter 3: siRNA knockdown of ribonucleotide reducatase inhibits melanoma cell line proliferation alone or synergistically with temozolomide[2]

3.1 Abstract:

Systemically delivered small interfering RNA (siRNA) therapies for cancer have begun clinical development. The effects of siRNA-mediated knockdown of ribonucleotide reductase subunit 2 (RRM2), a rate limiting enzyme in cell replication, were investigated in malignant melanoma, a cancer with a paucity of effective treatment options. A panel of human melanoma cell lines was transfected with siRNA to induce the knockdown of RRM2. Sequence-specific, siRNA-mediated inhibition of RRM2 effectively blocked cell proliferation and induced G1/S phase cell cycle arrest. This effect was independent of the activating oncogenic mutations in the tested cell lines. Synergistic inhibition of melanoma cell proliferation was achieved using the combination of siRNA targeting RRM2 and temozolomide, an analogue of the current standard of care for melanoma chemotherapy. The level of transferrin on melanoma cell lines was also evaluated. In conclusion, siRNA-mediated RRM2 knockdown significantly inhibits proliferation of melanoma cell lines with different oncogenic mutations with synergistic enhancement in combination with temozolomide.

3.2 Introduction

[2] Reproduced with permission from: J. E. Zuckerman, T. Hsueh, R. C. Koya, M. E. Davis and A. Ribas, "Small interfering RNA knockdown of ribonucleotide reductase inhibits melanoma cell line proliferation alone or synergistically with temozolomide," *J. Invest. Dermatol*. **131**, 453 (2011).

The incidence of malignant melanoma is rising faster than any other cancer. The treatment outcomes of metastatic melanoma remain dismal (Miller and Mihm, 2006; Tsao *et al.*, 2004). Only 10 to 15 percent of patients with disseminated disease respond to standard of care therapy with dacarbazine (DTIC) (Augustine *et al.*, 2009). Temozolomide is a second generation alkylating agent, whose active metabolite5-(3-methyltriazen-1-yl)imidazole-4-carboximide has a mechanism of action analogous to DTIC, with the added benefit of crossing the blood-brain barrier, an important feature since metastatic melanoma frequently metastasizes to the brain (Augustine *et al.*, 2009; Tsao *et al.*, 2004).

The first experimental therapeutic to provide targeted delivery of synthetic, small interfering RNA (siRNA) in humans, CALAA-01, is currently being tested in a phase 1 clinical trial (Davis, 2009). This targeted, nanoparticle formulation of siRNA consists of a cyclodextrin-containing polymer (CDP) utilizing human transferrin as a targeting ligand for binding to transferrin receptors that are typically upregulated on cancer cells. The siRNA component of CALAA-01, called siR2B+5, was designed to target ribonucleotide reductase subunit 2 (RRM2) and had been characterized for potency, efficacy, and specificity (Davis, 2009; Heidel *et al.*, 2007a).

Ribonucleotide reductase (RR) catalyzes the rate limiting step in the production of 2'-deoxyribonucleoside 5'-triphosphates needed for DNA replication. Conversion of ribonucleoside 5'-diphosphates to 2'deoxyribonucleotides by human RR requires expression of both its subunits, RRM1 and RRM2 (Engstrom *et al.*, 1985). The subunits are differentially expressed during the cell cycle. Whereas RRM1 expression remains constant throughout the cell cycle, the RRM2 subunit is only expressed in the late

G1/early S phase of the cell cycle (Engstrom *et al.*, 1985). RRM2 is therefore an attractive therapeutic target since it is primarily expressed in proliferating cells, such as cancer cells.

RRM2 has been a validated target for cancer therapy. Several small molecule agents such as hydroxyurea, alkoxyphenols, and cytarabine inhibit RRM2 activity; however, they are also associated with dose limiting toxicities due to adverse effects on non-malignant cells, e.g., bone marrow suppression (Shao *et al.*, 2006). Antisense-RNA based therapeutics targeting RRM2 have also shown some promise in the clinic, but are also associated with severe dose limiting toxicities (hepatotoxicity) and the need to be administered via continuous infusion (Desai *et al.*, 2005). Cancer therapy using targeted nanoparticles formulated with siRNA targeting RRM2 may be able to bypass some of the undesirable non-specific effects caused by traditional small molecule-based therapeutics, since the specific targeting properties of the nanoparticle systems allows for a more selective delivery to tumor tissue (Davis, 2009). CALAA-01-like-nanoparticles have been shown to have very little non-specific toxicity. Importantly, no hematopoietic toxicity was observed following administration of high doses to cynomolgus monkeys (Heidel *et al.*, 2007b).

CALAA-01 has been administered to 15 patients with solid refractory cancers within an open-label, dose-escalation trial. Biopsies in 2 patients with metastatic melanoma demonstrated tumor targeting with the presence of particles within tumors (Davis *et al.*) . At the highest dose tested (30 mg/m^2) there was evidence of RRM2 knockdown when analyzed both at the mRNA and protein levels. Furthermore, specific confirmation of triggering the RNAi mechanism was obtained by the demonstration of

the presence of the specific cleavage sequence of siRNA targeting RRM2 in tumor samples by 5'-RNA ligand-mediated rapid amplification of cDNA ends (5'-RLM-RACE) PCR technique (Davis *et al.*).

The evidence of RRM2 silencing *in vivo* with CALAA-01 provided motivation to study the mechanism and range of effects of siR2B+5 siRNA induced RRM2 knockdown *in vitro* against a previously characterized panel of melanoma cell lines(Jonas N. Søndergaard, 2010) . Therefore, in this study we sought to elucidate the efficacy of siR2B+5 siRNA induced RRM2 knockdown to inhibit melanoma cell proliferation, to determine the mechanism of anti-proliferative effects, and to indentify the range of sensitivities of different melanoma cell lines with defined oncogenic alterations to this new therapeutic approach, which may indicate patient populations that may most benefit from this therapeutic approach. The level of transferrin receptor on melanoma cell lines was also evaluated to confirm that a Tf targeted nanoparticle approach would be reasonable. Additionally, synergy studies involving siR2B+5 siRNA and temozolomide were carried out.

3.3 Results

3.3.1 RRM2 silencing in HT-144 melanoma cells by siR2B+5 siRNA via RNAi mechanism

We first demonstrated that the siR2B+5 siRNA sequence previously characterized by Heidel *et al.* (Heidel *et al.*, 2007a) successfully knocked down RRM2 expression in melanoma cells. We transfected HT-144 cells with either 5 nmole/L siR2B+5 siRNA or a non-targeting control (siCON) siRNA and measured the RRM2 mRNA and protein expression by quantitative real time reverse transcription polymerase chain reaction

(qRT-PCR) and Western blot respectively (Figure 3.1a,b). We observed greater than 80% reduction in RRM2 mRNA and 90% RRM2 protein knockdown following siR2B+5 treatment when compared to siCON treatment (Figure 3.1a,b). We were able to obtain similar levels of RRM2 protein knockdown (60-90%) with siR2B+5 treatments in all other cell lines tested for RRM2 expression (data not shown).

In order to confirm that siR2B+5 does in fact engage the canonical RNAi machinery, RNA from HT-144 cells transfected with siR2B+5 and siCON using LipofectamineRNAiMax or targeted CPD/siRNA nanoparticles (similar to CALAA-01) were subjected to 5' RNA ligand mediated rapid amplification of cDNA ends (5'-RLM-RACE) analysis (Figure 3.1c,d). RRM2 mRNA fragments, whose 5' ends matched the predicted siRNA induced cleavage site (10 base pairs from the 5' end of the antisense strand) were detected only in those samples treated with the siR2B+5 siRNA using either LipofectamineRNAiMax or targeted CDP/siRNA nanoparticles (Figure 3.1c,d,e). LipofectamineRNAiMax was used for all subsequent transfections as it has much higher transfeciton efficiency than the targeted CDP/siRNA nanoparticles *in vitro* (data not shown). Several non-specific bands were also observed in the siCON treated samples; however, none of these bands matched the size or sequence of the correct RACE product obtained in the siR2B+5 samples.

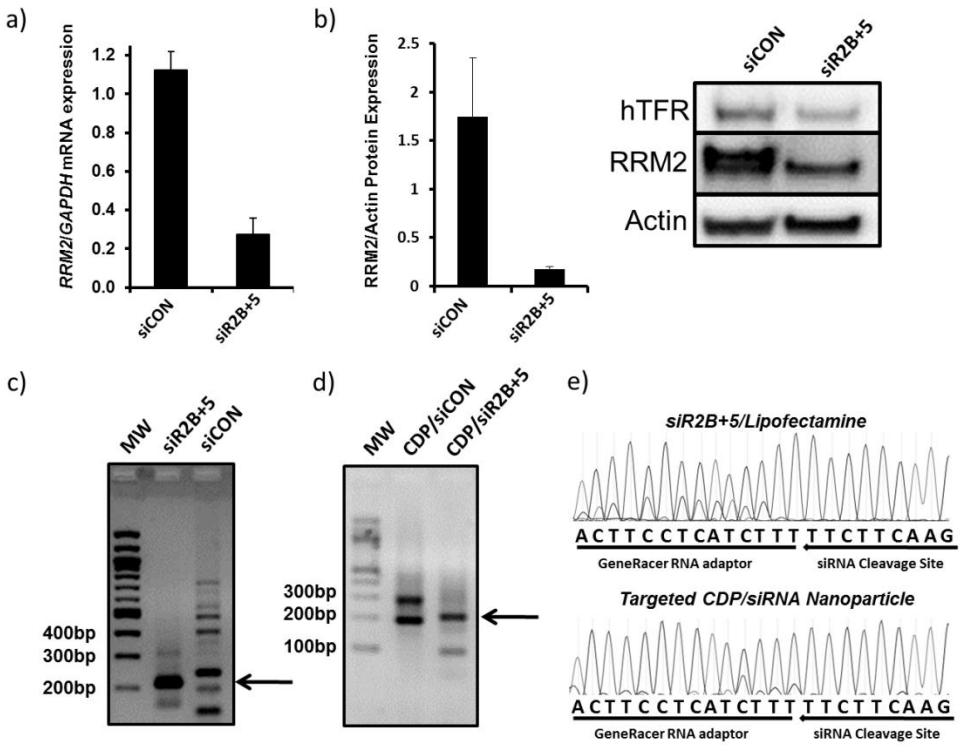

Figure 3.1: Knockdown of RRM2 mRNA and protein expression by short interfering RNA (siRNA) siR2B+5 in melanoma cells. (*a*) qRT-PCR analysis of RRM2 mRNA levels in HT-144 cells 48 hours after transfection with 5 nmol/L of RRM2 targeted siRNA (siR2B+5) or a non-targeting control (siCON) siRNA (Error bars, n=3). (*b*) Quantification of RRM2 protein expression by Western blot band densitometry analysis, average of three independent experiments; one blot is pictured (Error bars, n=3). 5'-RLM-RACE detection of siRNA induced mRNA cleavage fragment HT-144 cells transfected using either (c)

3.3.2 siR2B+5 treatment inhibits cell proliferation in a panel of melanoma cell lines in vitro

We hypothesize that RRM2 is required for melanoma cell proliferation and knockdown of its expression in melanoma cell lines would result in growth inhibition. In order to test this hypothesis, 13 human melanoma cell lines with prior detailed oncogenic characterization (Jonas N. Søndergaard, 2010) as well as 3 non-melanoma cell lines (2 breast cancer: MDA-MB-231 and MCF-7 and a normal fibroblast cell line 3T3) were treated with either 5 nmole/L siR2B+5 or siCON siRNA and their viability levels

compared to untreated control samples (Figure 3.2a). We observed up to 20% non-specific decrease in cell viability following treatment with the negative control siCON siRNA. Therefore, we considered that a cell line was sensitive to siR2B+5 siRNA treatment if cell viability was less than 80% of the untreated control following siR2B+5 siRNA treatment (dashed line). We found that 10 out of the 13 cell lines tested were sensitive to siR2B+5 siRNA treatment. Among those sensitive cell lines we observed a wide range of siR2B+5 siRNA induced proliferation inhibition, with the most sensitive cell lines (e.g., PTM, M238) demonstrating an approximate 65% decrease in viability following treatment, while the least sensitive cell lines (e.g., M207, M229) demonstrate approximately 30% decrease in viability. It is notable that 2 out of the 3 cell lines (M243, M245) which did not show anti-proliferative effects after siR2B+5 siRNA treatment at 72 hours, ultimately showed decreased proliferation at later time points (data not shown). Melanoma has frequent activating mutations in the MAPK pathway, with mutually exclusive activating mutations in NRAS and BRAF (Gray-Schopfer *et al.*, 2007). However, the differences in sensitivity appear to be independent of the activated oncogene present in each cell, as anti-proliferative effects were equivalent in cell lines that had been previously characterized as having $NRAS^{Q61L}$ or $BRAF^{V600E}$ activating mutations (Jonas N. Søndergaard, 2010). As expected siR2B+5 treatment in 3T3 cells lead to significant decrease in cell viability. Surprisingly, we observed no anti-proliferative effects of RRM2 knockdown in the two human breast cancer cell lines tested at 72 hours. The MDA-MB-231 cell line, but not MCF-7 cell line does show decreased

proliferation at later time point (data not shown).

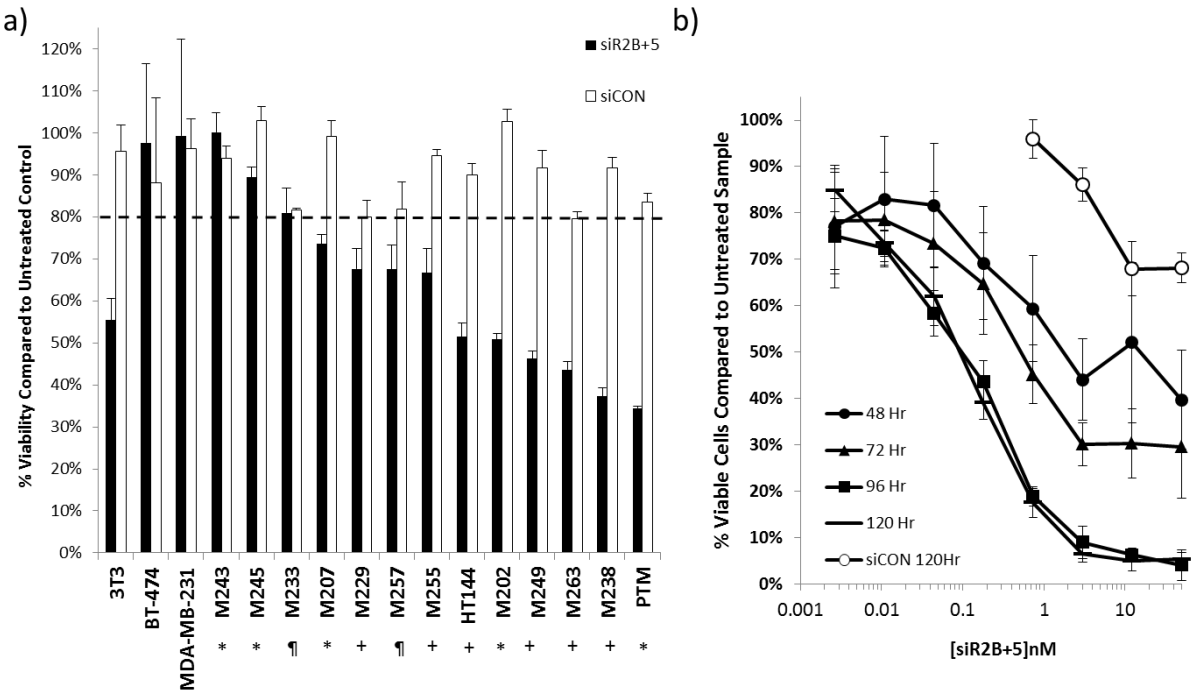

Figure 3.2: *In vitro* anti-proliferative effects of RRM2 knockdown by siR2B+5 siRNA in a panel of melanoma cell lines. (*a*) Bioluminescent-based viability assay on a panel of cell lines 72 hours after transfection with 5 nmol/L siRNAs, siR2B+5 (*black columns*) or siCON (*white columns*). Cell line oncogenic mutations are indicated by (*) NRAS codon 61 mutation, (+) BRAF V600E mutation, or (¶) NRAS/BRAF wild type. (*b*) MTS viability assay of M202 melanoma cells transfected with a range of siR2B+5 concentrations from 0.005 to 50 nmole/L (*black circles)*, or siCON 0.5-50 nmole/L (*white circles)* performed at 48, 72, 96, and 120 hours following transfection (only the 120 hour siCON time points are displayed). All cell viability data are normalized to untreated control samples (error bars, n=3).

The dose and time dependence of siR2B+5 siRNA was investigated in order to better understand the amount of siR2B+5 siRNA necessary to induce sustained anti-proliferative effects. We transfected M202 cells with a range of siR2B+5 siRNA concentrations (0.005-50 nmole/L) and measured cell viability at 48, 72, 96, and 120 hours after transfection (Figure 3.2b). We observed a clear dose and time dependent sensitivity to siR2B+5 siRNA. Anti-proliferative effects at less than 0.1 nmole/L

siR2B+5 siRNA were observed and reached a plateau at 3 nmole/L. We observed increasing anti-proliferative effects with each time point up to 120 hours where these effects stabilized. We also observed some amount of dose dependent toxicity following siCON treatment, with levels about 10 nmole/L showing significant decrease in cell viability; however, these effects were not time dependent and did not change significantly from 48 to 120 hours (only 120 hour data pictured).

3.3.3 siR2B+5 treatment induced G1/S-phase cell cycle arrest in multiple cell lines

We hypothesize that RRM2 knockdown depletes the pool of available dNTPs for DNA synthesis. Therefore, cells treated with siR2B+5 siRNA should not be able to replicate their genomes and arrest early in the cell cycle. These molecular events may lead to the observed anti-proliferative effects following RRM2 knockdown. In order to test this hypothesis, we analyzed the cell cycle distribution of HT-144 melanoma cells, a cell line sensitive to siR2B+5 siRNA treatment, using propidium iodide staining after treatment with either 5 nmole/L siR2B+5 or siCON siRNA (Figure 3.3a). Significant changes to cell cycle distribution in siR2B+5 siRNA treated cells compared to siCON siRNA treated samples were observed. Compared to siCON siRNA treated samples, siR2B+5 siRNA treated samples had a marked increase in G1 and S phase populations, and near disappearance of the G2/M phase population, consistent with G1/S phase cell cycle arrest.

We analyzed whether RRM2 knockdown following siR2B+5 treatment leads to apoptosis in addition to cell cycle arrest. In order to examine for this possibility, we stained siR2B+5 siRNA treated HT-144 cells with Annexin-V-FITC and propidium iodide to identify live, apoptotic, and dead cellular populations by flow cytometry (Figure

3.3b). Untreated samples had a baseline

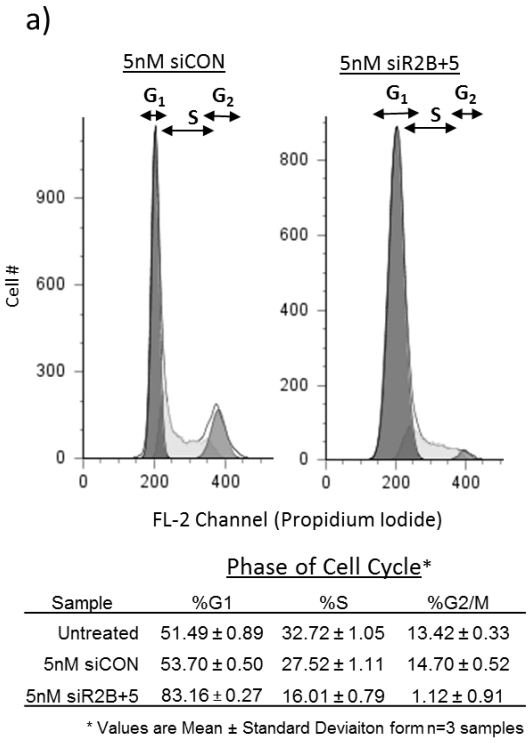

Phase of Cell Cycle*

Sample	%G1	%S	%G2/M
Untreated	51.49 ± 0.89	32.72 ± 1.05	13.42 ± 0.33
5nM siCON	53.70 ± 0.50	27.52 ± 1.11	14.70 ± 0.52
5nM siR2B+5	83.16 ± 0.27	16.01 ± 0.79	1.12 ± 0.91

* Values are Mean ± Standard Deviaiton form n=3 samples

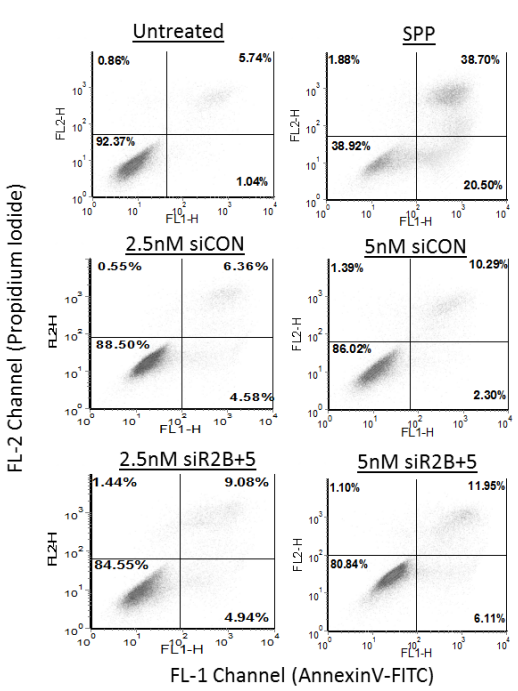

Figure 3.3: G1/S-phase cell cycle arrest, but little apoptosis is induced by siR2B+5 siRNA RRM2 knockdown. (*a*) Propidium idodide cell cycle analysis of HT-144 melanoma cells 48 hours after treatment with 5 nmol/L siR2B+5 or siCON; histograms are representative of at least 3 independent experiments. (*b*) AnnexinV-FITC/propidium iodide apoptosis analysis of HT-144 cells 72 hours after treatment with 2.5 or 5 nmol/L of siR2B+5, siCON, or staurosporin (SSP, positive control).

population made up of approximately 7% of cells with spontaneous apoptotsis detected as Annexin-V positive cells, with or without being propidium iodine positive (Figure 3.3b). Treatment with 2.5 or 5 nmole/L siCON siRNA caused an increase in this population over 10%. Samples treated with 2.5 or 5 nmole/L siR2B+5 siRNA demonstrated an additional 3-5% increase in apoptotic cell populations. There were minimal non-apoptotic dead cells in any sample. Overall, siR2B+5 siRNA treatment, compared to untreated and

siCON siRNA treated samples, resulted in marked cell cycle arrest but only a marginal increase in apoptotic cell death at the conditions and timing tested by us.

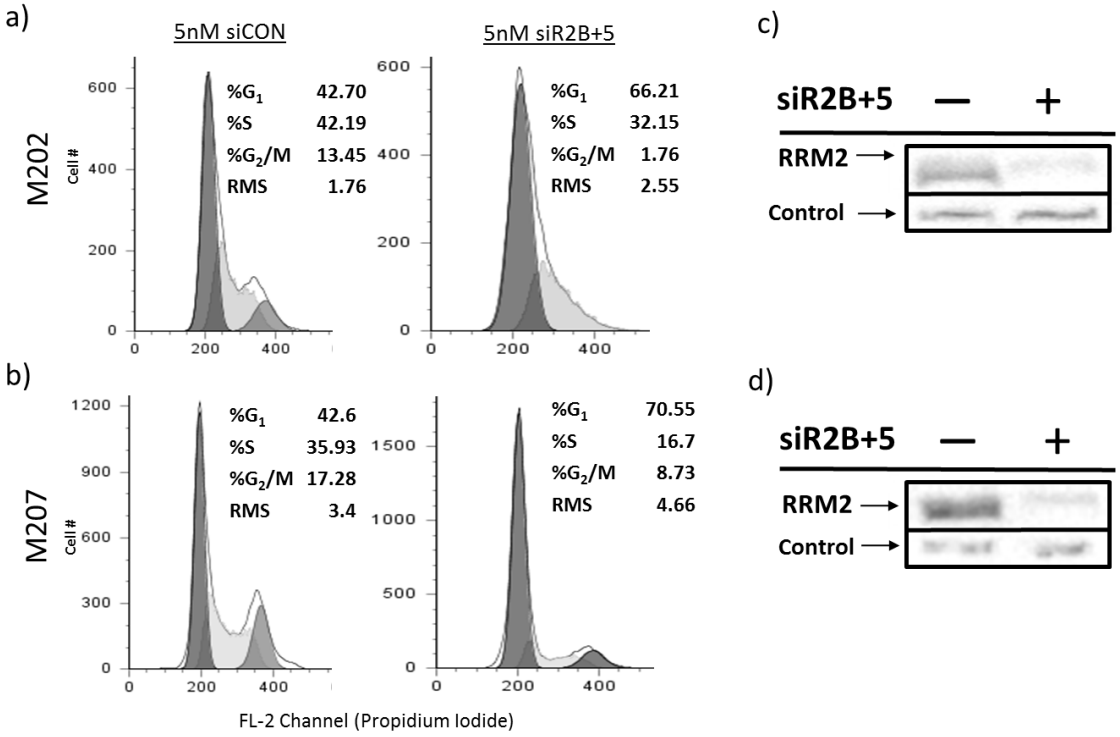

Figure 3.4: Cell cycle arrest profiles vary between different melanoma cell lines despite similar level of siR2B+5 siRNA knockdown of RRM2 expression. (*a*,*b*) Propidium iodide cell cycle analysis of (*a*) M202 or (*b*) M207 melanoma cell lines 48 hours after treatment with 5 nmole/L siR2B+5 or siCON siRNA. (*c*,*d*) Western blot analysis of (*c*) M202 or (*d*) M207 cells 48 hours after transfection with 5 nmol/L siR2B+5 siRNA in the presence of lipofectamineRNAiMax.

We further hypothesized that the differences in sensitivity among cell lines to siR2B+5 siRNA in terms of growth inhibition may be based upon the completeness of cell cycle arrest achieved following RRM2 knockdown in each cell line. We compared cell cycle analysis profiles of M202 (a good responder by cell viability assays) and M207 (a cell line with minimal response) following treatment with siR2B+5 or siCON siRNA (Figures. 3.4a,b). As shown above, M202 cell proliferation is greatly inhibited following RRM2 knockdown, whereas M207 cell proliferation is more weakly inhibited. Inspection

of the cell cycle analysis data for both cell lines after treatment with siR2B+5 siRNA demonstrate enrichment of G1 phase cell populations and diminishment of S phase populations in both cell lines; however, the G2/M phase population of M202 cells nearly disappears after RRM2 knockdown, whereas this population of M207 cells only decreases by half, suggesting that some M207 cells were still cycling, despite a similar level of RRM2 knockdown (Figures. 3.4c,d).

We also sought to rule out the possibility that a single transfection or siR2B+5 is not sufficient to induce cell death. To determine if prolonged RRM2 knockdown could result in cell death we engineered the M202 melanoma cell lines to inducibly express an shRNA version of the siR2B+5 sequence in the presence of doxycycline (Figure 3.5). Prolonged inhibition (7 days) of RRM2 expression following DOX addition caused only cell growth arrest and no apparent cell death as assessed by real time cell growth assay.

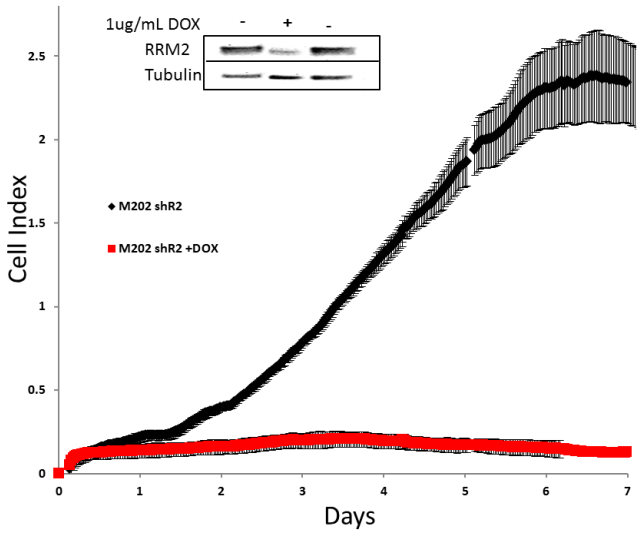

Figure 3.5: Inducible inhibition of RRM2 via shRNA resulted in cell growth arrest but not cell death. Western blot analysis revealed potent RRM2 inhibition in the presence of doxycycline. Real-time cell growth assays demonstrated that DOX addition resulted only in cell growth arrest and not cell death.

3.3.4 Combination of temozolomide and RRM2 knockdown is synergistic for inhibition of cell proliferation

We tested if RRM2 knockdown in melanoma cell lines may sensitize melanoma cells to temozolomide treatment which is an agent frequently used as standard of care in the treatment of patients with metastatic melanoma. Given the relatively high concentrations required of temozolomide (and DMSO vehicle control) for these experiments, we solubilized temozolomide using a solution of 2-hydroxypropyl-β-cyclodextrin, in order to avoid any confounding of results due to toxicities from high concentrations of DMSO. We did not observe any cytotoxic effects of 2-hydroxypropyl-β-cyclodextrin alone in our cell lines (data not shown). The initial studies focused on lower doses of temozolomide; however, no cytotoxic effects were observed for temozolomide alone at these doses. Additionally, no additional anti-proliferative activity was observed following temozolomide addition to siR2B+5 siRNA treatment at these low doses (data not shown). Therefore, we increased the dose of temozolomide to a range where a cytotoxic effect of temozolomide alone could be observed.

In these high concentration synergy studies, M202 or HT-144 melanoma cell lines were treated with increasing doses of siR2B+5 (0-20.2 nmole/L) followed by temozolomide treatment (24 hours later), with viability readings taken 48 hours after the temozolomide treatment (Figures 3.6 a,b). Samples treated with only temozolomide demonstrated minimal decrease in

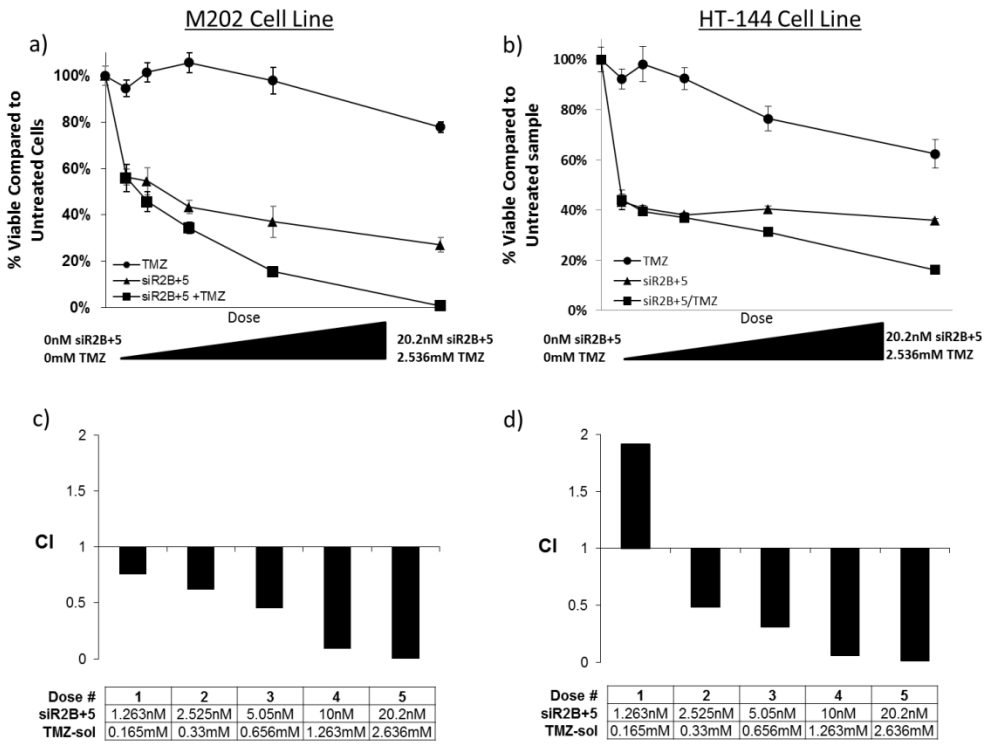

Figure 3.6: Synergy between siR2B+5 and temozolomide treatment. (*a,b*) Bioluminescence-based cell viability analysis of M202 cells (*a*) or HT-144 cells (*b*) 72 hours after treatment with increasing doses of siR2B+5 (nmole/L) (*triangular boxes)*, temozolomide-sol (mmole/L) (*circular boxes*), or co-treatment with both agents (*square boxes)*. Data are normalized to an untreated sample. (*c,d*) Synergy analysis of M202 (c*)* and HT-144 (*d*) cell viability data following co-treatment with siR2B+5 siRNA and temozolomide using the combination index (CI) method. CI values <1 indicate synergy.

viability except at the highest dose. siR2B+5 siRNA treatment produced similarly potent anti-proliferative effects as observed in previous experiments. The combination of temozolomide and siR2B+5 siRNA produced anti-proliferative effects greater than either individual agent alone. Synergy was determined by combination index (CI) methods, based on Chou-Talalay equations (Figures 3.5 c,d). We observed that all combination doses in M202 cells showed synergistic effects, with combination indexes (CI) <1, and

all but the lowest dose of the combination therapy in HT-144 cells demonstrating synergistic effects.

3.3.5 Melanoma cell lines express the Transferrin receptor (TfR) and uptake fluorescently labeled transferrin

Because the CALAA-01 delivery vehicle is transferrin targeted, we desired to confirm that melanoma cells do express the TfR and uptake transferrin like other cancer cell lines. We examined the ability of 4 melanoma cells to uptake fluorescently labeled transferrin (Alexafluor 488 labeled). All melanoma cell lines were found to readily uptake transferrin with affinities similar to two cell lines previously characterized to uptake transferrin and transferrin targeted nanoparticles (Figure 3.7a). The presence of the TfR on melanoma cell lines was also confirmed by western blotting (Figure 3.7b). HT-144 melanoma cells were found to have a similar amount of TfR as other cancer cell lines.

3.4 Discussion

In this report, we demonstrate the therapeutic potential of siRNA targeting RRM2 in melanoma cell lines. siR2B+5 siRNA efficiently knocks down RRM2 expression via the canonical RNAi mechanism in melanoma cell lines and leads to a significant decrease in proliferative capacity in the majority of melanoma cell lines tested. Moreover, we demonstrate, by 5'-RLM-RACE, that siRNA delivered via targeted CDP/siRNA nanoparticles can engage the RNAi machinery *in vitro*. Additionally, we find that the therapeutic response was durable, lasting greater than 120 hours post transfection, and potent, demonstrated by therapeutic doses less than 1 nmole/L.

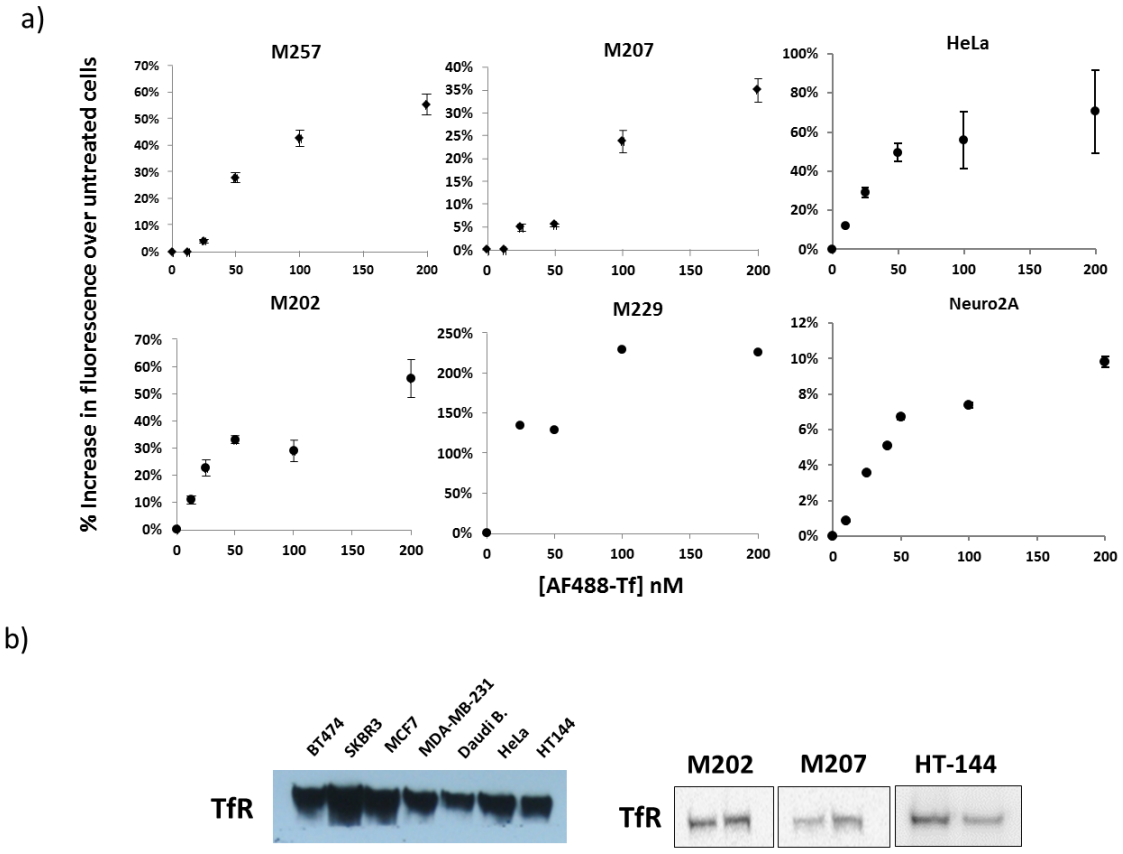

Figure 3.7: Melanoma cell lines express transferrin receptor and uptake transferrin. a) Dose dependence of AF-488 labeled transferrin in 4 human melanoma cell lines (M257, M202, M229, M207) and 2 positive control cell lines (HeLa-human cervical cancer, Neuro2A-mouse neuroblastoma). b) Western blot analysis of TfR expression in melanoma cell lines (HT-144, M202, M207) and a panel of other cancer cell lines (Breast cancer: BT-474, SKBR3, MCF7, MDA-MB-231; Lymphoma: Daudi).

These results are consistent with previous data obtained by Heidel *et al*. that demonstrated siR2B+5 siRNA induced growth inhibition of a variety of cancer cell lines *in vitro* and *in vivo* (Heidel *et al.*, 2007a). Avolio *et al*. have also reported that siRNA targeting RRM2 decreased tumor growth rates *in vivo* (Avolio *et al.*, 2007). Lee et al. demonstrated that targeting RR using antisense RNA molecules can inhibit proliferation of melanoma cell lines in *vitro* and *in vivo* (Lee *et al.*, 2003). Additionally, these authors

showed significant inhibition of lung tumor colonies following tail vein injections of A2508 melanoma cells into mice after 5-7 weeks of daily treatment with GTI-2040, a 20-nucleotide phosphorothioate oligodeoxyribunucleotide that has been reported to inhibit the production of RRM2 *in vitro* (Lee *et al.*, 2003).

Intriguingly, several reports, most notably from Doxubury *et al.*, demonstrated that RRM2 knockdown alone in certain cancer models (pancreatic adenocarcinoma cell lines) did not decrease cell viability (Duxbury *et al.*, 2004). However, Reid et al., have demonstrated that RRM2 knockdown in A549 melanoma cell lines inhibits growth *in vitro* and *in vivo* (Reid *et al.*, 2009). The variety of responses to RRM2 knockdown among melanoma cell lines used here emphasizes the importance of screening a panel of cancer cell lines when evaluating siRNA therapeutics. Additionally, the lack of any robust anti-proliferative effect in the breast cancer cell lines tested suggests that melanoma, in general, may be more sensitive to siR2B+5 therapy than other cancer types.

Our data suggest that growth inhibition following siR2B+5 siRNA treatment is due mostly to G1/S phase cell cycle arrest, with some limited contribution from apoptotic events. Cell cycle arrest following RRM2 knockdown has been observed in renal cell carcinoma cell lines; however, unlike the melanoma cell lines in this report, RRM2 knockdown caused S phase arrest with no particular enrichment of the G1 phase population of cells (Avolio *et al.*, 2007). Conversely, in colon cancer cell lines, no perturbations to the cell cycle were observed following RRM2 knockdown (Lin *et al.*, 2004).

We observed a limited amount of apoptosis in HT-144 melanoma cells following RRM2 knockdown. However, the increase in apoptotic population in siR2B+5 siRNA treated cells compared to those treated with siCON siRNA is not of sufficient magnitude to explain the large difference in growth inhibition observed between HT-144 cells treated with siR2B+5 and siCON siRNA. Therefore, it is likely that RRM2 knockdown with siR2B+5 siRNA primarily has cytostatic effects, as opposed to cytotoxic cell killing, in melanoma cell lines. It is also possible that continuous siRNA treatment for long periods of time *in vivo* through repeated dosing with targeted nanoparticles may lead to eventual melanoma cell death. However, the conditions for continued exposure to siR2B+5 siRNA are difficult to test experimentally *in vitro* due to the toxicity of repeated exposure to the transfection reagents.

We found that the magnitude of growth inhibition following siR2B+5 siRNA treatment correlated with the completeness of the observed cell cycle arrest. We found that in two similar melanoma cell lines, both with activating N-Ras^{Q61L} mutations (M202 and M207 cell lines), siR2B+5 siRNA treatment caused varying levels of cell cycle arrest despite comparable levels of RRM2 knockdown. We observed complete cell cycle arrest in the M202 cell line and partial arrest in the M207 cell line. Correspondingly, M202 cell proliferation was more strongly inhibited by RRM2 knockdown than the proliferation of M207 cells.

Temozolomide at high concentrations has been demonstrated to induce G2 cell cycle arrest, but not apoptosis, in melanoma cell lines *in vitro* (Mhaidat *et al.*, 2007). However, at more “clinically relevant” concentrations no appreciable effect on cell cycle, proliferation, or temozolomide induced DNA damage has been observed following

temozolomide treatment in human melanoma cell lines (Chen *et al.*, 2009), which may not be surprising since this agent has a low response rate in the clinic (Rietschel *et al.*, 2008). Several studies have suggested that methyl-guanine methyl transferase (MGMT) as well as RR may be involved in the temozolomide resistance mechanism in cancer (Aghi *et al.*, 2006; Augustine *et al.*, 2009). Our results suggest that RR may play a role in temozolomide resistance. We observed that co-treatment with siR2B+5 siRNA and temozolomide synergistically inhibited melanoma cell growth. Therefore, there may be an advantage to combination therapy with siR2B+5 and temozolomide and further *in vivo* studies are warranted to fully elucidate the therapeutic potential of this combination.

Our observations of TfR expression in melanoma tumors are consistent with the literature. There is a large body of self-consistent evidence demonstrating TfR expression in melanoma tissue and cells. Overall, a meta-analysis available, peer reviewed, reports of TfR expression in melanoma revealed that 65% of primary melanomas, 92% of metastatic melanomas, and 92% of the unspecified primary or metastatic melanoma samples express TfR (1017 samples in total). These data are also well confirmed at the cell lines level.

The findings in this report suggest that RRM2 knockdown via transferrin targeted siRNA nanoparticles may be an effective strategy for treatment of advanced stage melanoma. However, the lack of any robust cell death after RRM2 inhibition in melanoma suggests that this therapeutic strategy may be most advantageous in combination with other therapuerics such as TMZ.

3.5 Materials and Methods

Cell lines and culture

Melanoma cell lines M202, M207, M229, M233, M238, M245, M249, M255, M257, and M263 cell lines were established from patient's biopsies under UCLA IRB approval #02-08-067 and have been previously characterized (Jonas N. Søndergaard, 2010). PTM was provided by Bijay Mukherji (University of Connecticut, Farmington, CN). The HT-144, MDA-MB-231, MCF-7, and 3T3 cell lines were obtained from American Type Culture Collection (ATCC, Rockville, MD). All cell lines were cultured in complete serum media containing RPMI 160 with L-glutamine (Mediatech Inc., Manassas, VA) with 10% (all percentages represent v/v) fetal bovine serum (FBS, Omega Scientific, Tarzana, CA), 1% penicillin, streptomycin, and amphotericin (Omega Scientific) at 37°C with 5% CO_2 in filter-top flasks.

siRNAs duplexes

Both unmodified RNA duplexes were gifts from Calando Pharmaceuticals (Pasadena, CA). siCON was bioinformatically designed to minimize potential for targeting any human gene (Dharmacon, Lafayette,CO).

siR2B+5: 5'-GAUUUAGCCAAGAAGUUCAGA-3'

siCON: 5'-UAGCGACUAAACACAUCAAUU-3'

In vitro transfection

A reverse transfection protocol was followed for siRNA delivery. siRNA was complexed with LipofectamineRNAiMax (Invitrogen, Carlsbad, CA) according to manufacturer's instructions. 0.030 -300 nmole/L siRNA with 0.2%

LipofectamineRNAiMax was applied to each well in a total volume of 20 µl (96 well plate) or 500 µl (6 well plate) of Opti-MEM (Invitrogen). 5 x $10^{\wedge 3}$ cells/well (96 well plates) or 2.4 x $10^{\wedge 5}$ (6 well plates) were plated into wells containing the siRNA formulations, for a final siRNA concentration of 0.005-50 nmole/L. Targeted CDP/siRNA nanoparticle delivery of siR2B+5 was performed as described elsewhere (Bartlett and Davis, 2007) at a final concentration of 300 nmole/L siRNA.

Temozolomide preparation

Temozolomide (10 mg/ml) was prepared by dissolving 0.5 g of temozolomide (LKT laboratories, St. Paul, MN) into 30% (w/v) of 2-hydroxypropyl-beta-cyclodextrin (2-HP-beta-CD, Sigma-Aldrich, St. Louis, MO), at 37° C in a water-bath by stirring at 800 rpm for 60 minutes.

Cell viability assays

Cells were transfected as described above and cell viability was determined using the CellTiterGlo Assay (Promega, Madison, WI) by following the manufacturer's instructions. Luminescence was measured on a DTX 880 multimode detector (Beckman Coulter, Fullerton, CA).

qRT-PCR:

Total RNA from HT-144 cells was extracted using the RNeasy kit (Qiagen). Total RNA samples were reversed transcribed using SuperScriptIII reverse transcriptase. 2 µl of prepared sample cDNA was used for triplicate Real time-PCR as described elsewhere

(Juhasz *et al.*, 2006). RRM2 levels were normalized to GAPDH levels within the same sample.

Detection of hRRM2 protein levels by western blot

48 hours after transfection, cells were lysed in RIPA Buffer (Thermo Fisher Scientific Inc., Waltham, MA). Lysates were diluted to equivalent protein concentration in beta-mercaptoethanol-containing Laimmli sample buffer (Thermo-Fisher) and incubated at 95^{o}C for 5 minutes. Antibodies: goat polyclonal anti-R2 antibody, horseradish peroxidase-conjugated donkey anti-goat immunoglobulin G (sc-10846; Santa Cruz Biotechnology, Santa Cruz, CA). Development was done using SuperSignal West Dura Extended Duration Substrate (Thermo-Fisher). Band quantification was done using Image-Quant TL software (GE/Amersham Biosciences, Piscataway, NJ). hRRM2 expression was normalized to either Actin (BD Biosciences, San Jose, CA) or SID1B, a high molecular weight putative RNA transport protein, using a SID1B antibody (GeneScript, Piscataway, NJ).

5' RNA ligand mediated-RACE:

5'-RLM-RACE was performed as described previously (Davis *et al.*). Briefly, 3 μg or total RNA was ligated directly to 250ng GeneRacer RNA adapotor (Invitrogen) using T4 RNA ligase. Ligation products were reverse transcribed using SuperScriptIII (Invitrogen) and a RRM2 gene specific reverse transcription primer. Two rounds of PCR were performed using a Bio-Rad MJ Mini personal thermocycler and PCR conditions described previously (Davis *et al.*). PCR products were run on a 2% agarose gel and

stained with 1μg/μl ethidium bromide. PCR products were excised from gel and sequenced directly to confirm RACE band identities.

Cell Cycle analysis

Cells were trypsinized and washed twice with PBS. Ice cold 70% ethanol was added drop wise while vortexing and allowed to incubate at 4^{o}C for 30 minutes. Samples were then centrifuged at 1,300 rpm for 10 minutes and the ethanol decanted. The samples were then stained with 5 μg/ml propidium iodide at room temperature for 30 min. Cells were then analyzed by flow cytometery on a FACScan (BD Biosciences) flow cytometer and data analyzed using FlowJo version 8.7 (Tree Star, Inc., Ashland, OR).

Apoptosis analysis

Individual cell culture supernatants were collected. The remaining adherent cells were trypsinized and combined with the previously collected supernatant. The samples were then washed with PBS and re-suspended in 50 μl binding buffer (BD Biosciences). Samples were treated with 20 μl of annexinV-FITC at 4^{o}C for 30 minutes. 400 μl of additional binding buffer was then added. 5 μl of propidium iodide was added 2 minutes before cells were analyzed by flow cytometery on a FACSCalibur (BD Biosciences). Data analysis was performed using FACS Express (De Novo Software, Los Angeles, CA).

Combination studies and synergy data analysis

HT-144 cells were transfected with a range of siR2B+5 siRNA concentrations and incubated for 24 hours. Samples were then treated with a dose range (0-2.636 mmole/L)

of temozolomide solution (cyclodextrin concentration was held constant over all samples) in fresh culture media and were incubated for 72 hours and cell viability assays performed. Analysis of combined agent effects were determined by combination index (CI) methods, based on Chou-Talalay equations (Chou, 2006) using Calcusyn dose effect analyzer software (Biosoft, Cambridge, UK). This software analysis takes into account the potency of each individual agent and the combination thereof, as well as the shape of the each dose response curve to determine how much the observed response of the combination treatment differs from the predicted additive response of the each individual agent. CI values can then be generated for each dose level which indicate additive effects (CI=1), antagonistic effects (CI>1), or synergistic effects (CI<1).

Alexafluor488-Transferrin uptake studies

Human transferrin (Sigma) was labeled with AF488 using the X kit. Cells were grown in 24 well plates and washed twice with PBS. Opti-MEM (Invitrogen) containing the indicated concentration of labeled transferrin was added to the cells and incubated for 60 minutes at 37°C. The Opti-MEM was then removed and the cells washed twice with PBS. Fluorescence measurements of the cells were performed using a plate reader (Tecan).

3.6 Acknowledgements

We would like to thank Calando Pharmaceuticals for the gift of the siR2B+5 and siCON siRNAs and for help with the synergy data analysis (performed by Thomas Schluep). Jonathan Zuckerman is supported by the NIH UCLA MSTP Grant T32 GM008042. This work was also funded by the National Cancer Institute Grant U54

CA119347, The Fred L. Hartley Family Foundation and the Caltech-UCLA Joint Center for Translational Medicine. Flow cytometry was performed at the UCLA Jonsson Comprehensive Cancer Center supported by the National Institutes of Health Awards CA-16042 and AI-28697.

3.7 Citations

Aghi M, Rabkin S, Martuza RL (2006) Effect of chemotherapy-induced DNA repair on oncolytic herpes simplex viral replication. *Journal of the National Cancer Institute* 98:38-50.

Augustine CK, Yoo JS, Potti A, Yoshimoto Y, Zipfel PA, Friedman HS, *et al.* (2009) Genomic and molecular profiling predicts response to temozolomide in melanoma. *Clin Cancer Res* 15:502-10.

Avolio TM, Lee Y, Feng N, Xiong K, Jin H, Wang M, *et al.* (2007) RNA interference targeting the R2 subunit of ribonucleotide reductase inhibits growth of tumor cells in vitro and in vivo. *Anti-cancer drugs* 18:377-88.

Bartlett DW, Davis ME (2007) Physicochemical and biological characterization of targeted, nucleic acid-containing nanoparticles. *Bioconjugate chemistry* 18:456-68.

Chen M, Osman I, Orlow SJ (2009) Antifolate activity of pyrimethamine enhances temozolomide-induced cytotoxicity in melanoma cells. *Mol Cancer Res* 7:703-12.

Chou TC (2006) Theoretical basis, experimental design, and computerized simulation of synergism and antagonism in drug combination studies. *Pharmacological reviews* 58:621-81.

Davis ME (2009) The First Targeted Delivery of siRNA in Humans via a Self-Assembling, Cyclodextrin Polymer-Based Nanoparticle: From Concept to Clinic. *Molecular pharmaceutics*.

Davis ME, Zuckerman JE, Choi CH, Seligson D, Tolcher A, Alabi CA, *et al.* Evidence of RNAi in humans from systemically administered siRNA via targeted nanoparticles. *Nature*.

Desai AA, Schilsky RL, Young A, Janisch L, Stadler WM, Vogelzang NJ, *et al.* (2005) A phase I study of antisense oligonucleotide GTI-2040 given by continuous intravenous infusion in patients with advanced solid tumors. *Ann Oncol* 16:958-65.

Duxbury MS, Ito H, Zinner MJ, Ashley SW, Whang EE (2004) RNA interference targeting the M2 subunit of ribonucleotide reductase enhances pancreatic adenocarcinoma chemosensitivity to gemcitabine. *Oncogene* 23:1539-48.

Engstrom Y, Eriksson S, Jildevik I, Skog S, Thelander L, Tribukait B (1985) Cell cycle-dependent expression of mammalian ribonucleotide reductase. Differential regulation of the two subunits. *The Journal of biological chemistry* 260:9114-6.

Gray-Schopfer V, Wellbrock C, Marais R (2007) Melanoma biology and new targeted therapy. *Nature* 445:851-7.

Heidel JD, Liu JY, Yen Y, Zhou B, Heale BS, Rossi JJ, *et al.* (2007a) Potent siRNA inhibitors of ribonucleotide reductase subunit RRM2 reduce cell proliferation in vitro and in vivo. *Clin Cancer Res* 13:2207-15.

Heidel JD, Yu Z, Liu JY, Rele SM, Liang Y, Zeidan RK, *et al.* (2007b) Administration in non-human primates of escalating intravenous doses of targeted nanoparticles containing ribonucleotide reductase subunit M2 siRNA. *Proceedings of the National Academy of Sciences of the United States of America* 104:5715-21.

Jonas N. Søndergaard RN, Qi Wang, Deliang Guo, Teli Hsueh, Stephen Mok, Hooman Sazegar, Laura E. MacConaill, Jordi G. Barretina, Sarah Kehoe, Narsis Attar, Jonathan Zuckerman, Bartosz Chmielowski, Begoña Comin-Anduix, Richard C. Koya, Paul Mischel, Roger Lo, Antoni Ribas. (2010) Differential Sensitivity of Melanoma Cell Lines with BRAF V600E Mutation to the Specific BRAF Inhibitor PLX4032/RG7204. *Journal of Translational Medicine 2010* (in press).

Juhasz A, Vassilakos A, Chew HK, Gandara D, Yen Y (2006) Analysis of ribonucleotide reductase M2 mRNA levels in patient samples after GTI-2040 antisense drug treatment. *Oncol Rep* 15:1299-304.

Lee Y, Vassilakos A, Feng N, Lam V, Xie H, Wang M, *et al.* (2003) GTI-2040, an antisense agent targeting the small subunit component (R2) of human ribonucleotide reductase, shows potent antitumor activity against a variety of tumors. *Cancer research* 63:2802-11.

Lin ZP, Belcourt MF, Cory JG, Sartorelli AC (2004) Stable suppression of the R2 subunit of ribonucleotide reductase by R2-targeted short interference RNA sensitizes p53(-/-) HCT-116 colon cancer cells to DNA-damaging agents and ribonucleotide reductase inhibitors. *The Journal of biological chemistry* 279:27030-8.

Mhaidat NM, Zhang XD, Allen J, Avery-Kiejda KA, Scott RJ, Hersey P (2007) Temozolomide induces senescence but not apoptosis in human melanoma cells. *British journal of cancer* 97:1225-33.

Miller AJ, Mihm MC, Jr. (2006) Melanoma. *The New England journal of medicine* 355:51-65.

Reid G, Wallant NC, Patel R, Antonic A, Saxon-Aliifaalogo F, Cao H, *et al.* (2009) Potent subunit-specific effects on cell growth and drug sensitivity from optimised siRNA-mediated silencing of ribonucleotide reductase. *J RNAi Gene Silencing* 5:321-30.

Rietschel P, Wolchok JD, Krown S, Gerst S, Jungbluth AA, Busam K, *et al.* (2008) Phase II study of extended-dose temozolomide in patients with melanoma. *J Clin Oncol* 26:2299-304.

Shao J, Zhou B, Chu B, Yen Y (2006) Ribonucleotide reductase inhibitors and future drug design. *Current cancer drug targets* 6:409-31.

Tsao H, Atkins MB, Sober AJ (2004) Management of cutaneous melanoma. *The New England journal of medicine* 351:998-1012.

Chapter 4: Herceptin-targeted siRNA nanoparticles containing siRNA against Her2 inhibit growth of Her2 (+) tumors *in vitro* and *in vivo*.

4.1 Abstract:

We have recently demonstrated the feasibility of using targeted, polymer-based siRNA nanoparticles in the clinic. This delivery system involved the use of the human protein transferrin (Tf) that is displayed on the surface of the nanoparticles to engage cancer cell surface, transferrin receptors (TfR). Here, we demonstrate the modular nature of this siRNA delivery system by tailoring both the targeting agent and siRNA component of the nanoparticle to Her2 positive breast cancers. Specifically, we show that the siRNA nanoparticle delivery system can be modified to include an antibody targeting agent (Herceptin) without any significant alteration to size, charge, or stability. We also show that in vivo treatment of Her2 positive breast cancer tumor xenografts with Herceptin-targeted nanoparticles containing siRNA against Her2 results in a more robust anti-tumor response than either Herceptin alone or Herceptin-targeted nanoparticles containing control siRNA. These data demonstrate how nanoparticles containing the combination of antibodies and siRNA can be used to achieve enhanced therapeutic treatment against clinically validated cancer targets.

4.2 Introduction

The anti-Her2/neu humanized monoclonal antibody Herceptin (trastuzumab) is used alone or in combination as a first line therapeutic in the treatment of HER2 positive (HER2(+)) breast cancers[1]. Despite its success in the clinic, Herceptin can also cause adverse effects in non-tumor tissue and acquired resistance is common[2]. Additionally, not all Her2 positive patients respond to Herceptin[3]. Therefore, new therapeutic

modalities that can limit off-target effects of Herceptin, overcome resistance and still take advantage of Her2 positive status are needed.

Nanoparticle-based therapeutics have restricted distribution profiles in the body owing to their relatively large size compared to traditional small molecule drugs and therapeutic antibodies[4]. Adverse effects of therapeutic antibodies result from the binding of antibodies to their targets within normal tissue. Attachment of antibodies (such as Herceptin) to nanoparticles can help overcome these off-target effects because antibodies will only be able to access the restricted profile of tissues where the nanoparticles accumulate.

In many instances, Herceptin resistant tumors remain dependent on Her2[3]. We hypothesize that resistance to anti-Her2 therapy can be overcome by RNAi induced silencing of Her2. Furthermore, because Her2 is still present on the surface Herceptin of resistant cells, we hypothesize the Herceptin would be a useful targeting ligand to direct siRNA nanoparticles into Herceptin resistant tumor cells *in vivo*.

We hypothesized that RNAi induced silencing of Her2 would also recapitulate the synergistic activities of Herceptin/ lapatanib and Herceptin/pertuzumab drug combinations. One mechanism of Herceptin function is dissociation of ligand independent Her2/Her3 dimerization and subsequent phosphatidylinositol 3-kinase (PI3K) pathway down regulation[5]. Combination therapy with another Her2 binding antibody (pertuzumab) that prevents ligand dependent Her2/Her3 dimerization has been demonstrated to be more effective than either antibody alone suggesting that Herceptin mono-therapy is inadequate to down regulate Her2/3 induced PI3K pathway completely[3]. Additionally, Herceptin treatment does not efficiently block Her2 activation of the

MAPK pathway[6]. The kinase inhibitor lapatanib in combination with Herceptin has been shown to be more effective than either agent administered alone[6]. The synergy stems from enhanced inhibition of PI3K pathway and additional inhibition of the MAPK pathway. We hypothesized that effective removal of Her2 from the cell (via RNAi knockdown) would recapitulate the activity of both these combination therapies simultaneously.

Small interfering RNAs (siRNAs) are particular promising forms of RNAi based therapeutics because they engage the RNAi pathway at the level of the RNA induced silencing complex (RISC). This means that only cytosolic delivery is required for siRNA function[7]. Because of their high charge and instability, siRNAs require carriers, such as nanoparticles, to facilitate their transport through circulation and uptake at desired sites of actions. Many such siRNA/carrier systems have entered clinical trials. We have developed a polymer-based targeted-nanoparticle formulation of siRNA (clinical version denoted CALAA-01) that was shown to accumulate in human tumors and deliver functional siRNA from a systemic, intravenous (i.v.) infusion [8]. This first-in-human study demonstrated the clinical potential for cationic polymer-based siRNA delivery systems.

The siRNA nanoparticles consist of a synthetic delivery system containing: (i) a linear, cyclodextrin-based polymer (CDP), (ii) a hydrophilic polymer (polyethylene glycol (PEG) used to promote nanoparticle stability in biological fluids), and (iii) siRNA[9]. The nanoparticles have been engineered to incorporate targeting ligands such transferrin (Tf)[10], sugars, or antibodies at the terminal ends of their PEGs that facilitate their uptake by target tissue.

Here, we demonstrated that siRNA silencing is an effective therapeutic option for Her2(+) breast cancers, both sensitive and resistance to Herceptin therapy. We showed that Herceptin could be incorporated into our siRNA nanoparticle delivery system to facilitate delivery to and uptake by tumor cells *in vivo*. Furthermore, we demonstrated that Herceptin-targeted siHer2 nanoparticle resulted in a more durable response *in vivo* than Herceptin administration alone.

4.3 Results:

4.3.1 siRNA knockdown of Her2 causes cell death only in Her2(+) cell lines.

We examined the effects of siRNA induced Her2 knockdown in two breast cancer cell lines BT-474 (Her2 positive) and MCF7 (Her2 negative). siHer2 was found to facilitate Her2 knockdown at pico-molar levels (Fig. 4.1A). Treatment of BT-474 cells with siHer2 resulted in potent anti-proliferative effects and resulted in complete cell death by 12 days post treatment (Fig. 4.1B). Treatment of MCF7 cells with siHER2 did not inhibit cell growth (Fig. 4.1C). After Her2 inhibition, some change in the interaction between the MCF7 cells and its growth media surface was observed, indicated by the increased cell index; however, no indication of toxicity was noted on visual inspection of the cells. Overall, these data suggested that the anti-proliferative effects observed following siHer2 treatment in the BT-474 cell line were a result of Her2 knockdown and not off-target effects of the siRNA sequence itself.

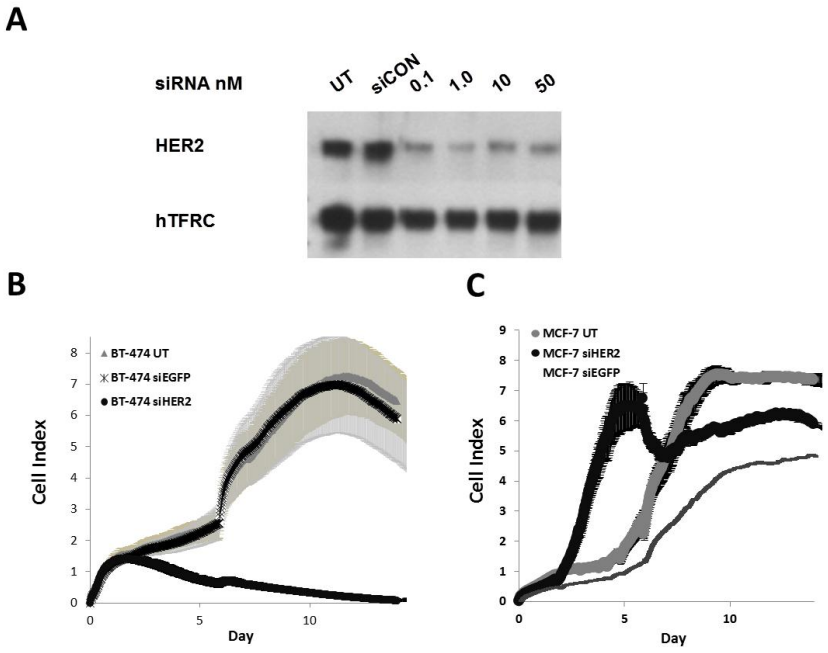

Figure 4.1: siHer2 knockdown inhibits cell growth of Her2 (+) cell line only *in vitro*. (A) Western blot analysis demonstrated potent Her2 inhibition following treatment with as little as 0.1nM siHer2 in BT-474 cells. (B,C) Real-time cell growth analysis of cells in the presence of 5nM siHer2 or siEGFP (BT-474 Her2(+); MCF-7 Her2(-)). Cell index is proportional to cell number.

4.3.2 siRNA knockdown of Her2 induces apoptosis of BT-474 cells, whereas Herceptin treatment does not.

We hypothesized that knockdown of Her2 would result in different down-stream effects than Her2 inhibition via Herceptin. To test this hypothesis we examined for apoptosis (indicated by presence of PARP cleavage fragments) and levels of phosphorylated-AKT (Fig. 4.2). We found that even at low doses cleaved PARP was clearly detectable in the siHER2 treated BT-474 cells. Herceptin treatment resulted in the appearance of very faint bands corresponding to cleaved PARP. siHER2 treatment also resulted in a robust decrease is P-AKT levels. Herceptin treatment also reduced P-AKT levels, but to a lesser extent.

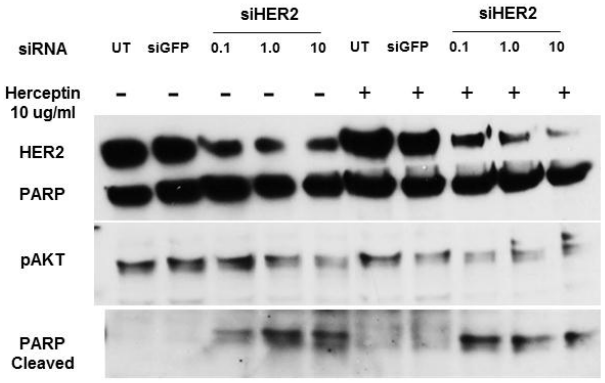

Figure 4.2: Her2 knockdown via siHER2 but not Herceptin treatment resulted in apoptosis induction, indicated by presence of cleaved PARP. Western blot analysis of HER2, PARP, cleaved PARP, and phosphorylated AKT (P-AKT), on protein extracted form BT-474 cells that received no treatment (UT), 10nM control siRNA (siEGP), or the indicated concentration (nM) of siHER2 in the presence (+) or absence (-) of Herceptin.

Combined treatment with both siHER2 and Herceptin resulted in at least additive if not synergistic effects. Herceptin treatment combined with low dose (0.1nM) siHER2 resulted in a clear increase in cleaved PARP compared to low dose siHER2 alone. P-AKT levels were also noticeably decreased at low dose siHER2 using this combination. The benefit of combination treatment at higher doses of siHER2 was unclear due to the already high amount of cleaved PARP and low levels of P-AKT induced by higher doses of siHER2.

4.3.3 Covalent attachment of PEG to Herceptin does not significantly alter Herceptin efficacy.

We covalently linked Herceptin to AD-PEG to enable its association with the siRNA nanoparticles. Covalent conjugation of Herceptin to a large PEG molecule could have interfered with its anti-tumor activity. To rule out this possibility we compared the anti-proliferative effects of Herceptin and AD-PEG conjugated Herceptin in BT-474 and MCF7 cells. As expected, Herceptin treatment resulted in potent anti-proliferative effects

only in the Her2(+) BT-474 cell line. AD-PEG-Herceptin treatment also resulted in potent anti-proliferative effects on only BT-474 cells; however, the IC50 of the drug was shifted to above 1ug/mL and its maximal potency appeared marginally reduced (Fig. 4.3). Overall, these data indicated that covalent attachment of AD-PEG to Herceptin had only a mild antagonistic effect on the therapeutic activity of Herceptin.

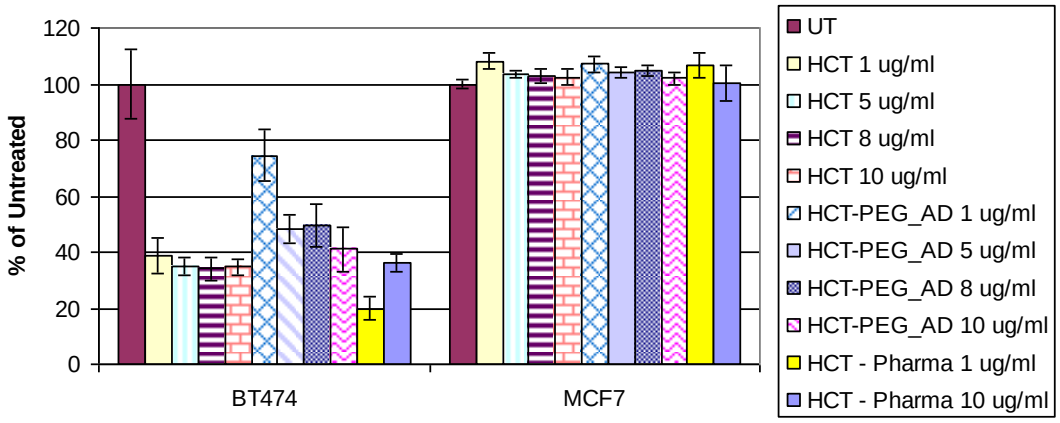

Figure 4.3: Covalent linkage to PEG results in slight decrease in therapeutic efficacy of Herceptin. Data are from MTS cell viability assays 48 hours after treatment initiation.

4.3.4 Incorporation of AD-PEG-Herceptin into siRNA nanoparticle formulation did not alter nanoparticle size, charge, or stability.

We examined the physical properties of siRNA nanoparticle formulated with 0.25 mol% AD-PEG-Herceptin. Based on previous work with the transferrin targeted nanoparticles[10] we estimated that this formulation would result in ~20 antibodies per particle. Cryo-TEM and dynamic light scattering measurements revealed that the siRNA nanoparticles with Herceptin were similar in size and charge to their untargeted counterparts (Fig. 4.4A, B). The Herceptin nanoparticles were also stable in physiologic salt conditions, as they did not aggregate in the presence of 1xPBS (Fig. 4.4C). These data suggest that AD-PEG-

Herceptin containing nanoparticles would behave in a similar fashion as transferrin or untargeted siRNA nanoparticles in the body.

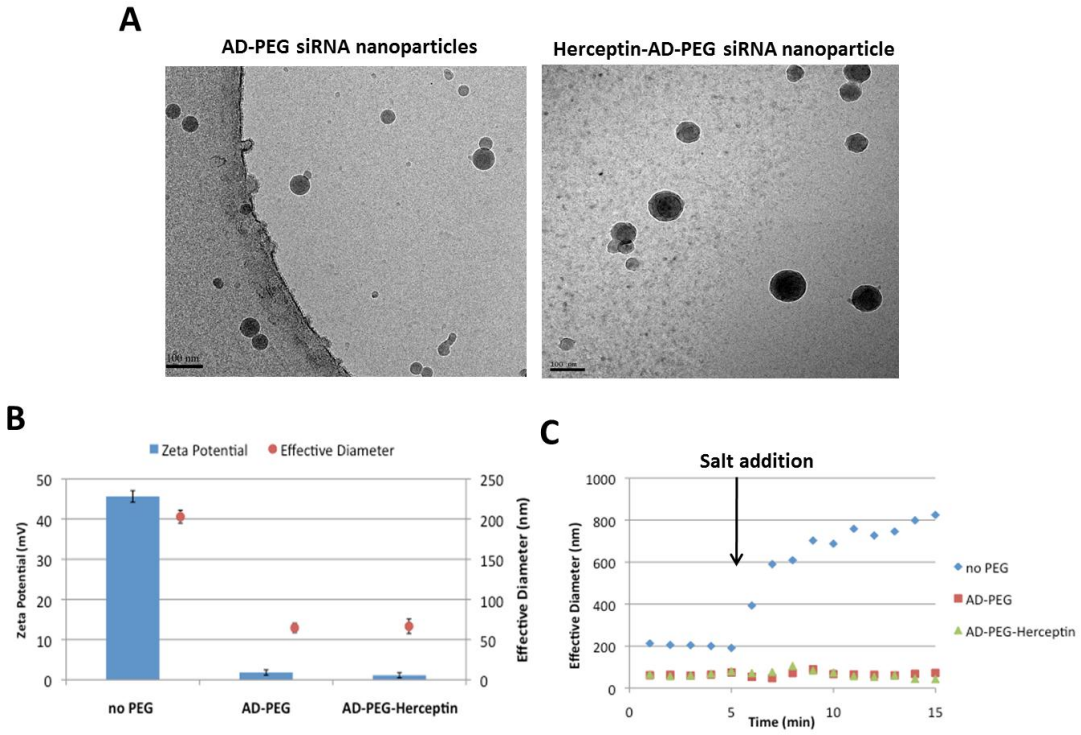

Figure 4.4: Characterization of siRNA nanoparticles formulated with 0.25 mole% AD-PEG-Herceptin. (A) Cyro-TEM images of siRNA nanoparticles formulated with and without AD-PEG-Herceptin. (B) Dynamic light scattering (DLS) measurements of size and charge of siRNA nanoparticles formulated with or without AD-PEG or AD-PEG-Herceptin. (C) DLS based salt stability analysis. Sample is brought to 1XPBS at 5 minutes and monitored for aggregation, indicated by increases to nanoparticle size.

4.3.5 Herceptin-siRNA nanoparticles accumulated to a greater extend in tumors than transferrin-siRNA nanoparticles.

We examined the tumor accumulation of siRNA nanoparticles using laser-scanning confocal microscopy (Fig. 4.5). We injected BT-474 tumor bearing mice with siRNA nanoparticles containing siRNA and polymer components labeled with Cy3 and Alexafluor350 fluorophores respectively. We also probed tumor sections from these mice with a fluorescently labeled anti-human secondary antibody to localize Herceptin.

Detection of siRNA nanoparticle components was weak. Fluorescent signal of the non-targeted siRNA nanoparticle components (siRNA and CDP) in tumor sections was nearly indistinguishable from background. Fluorescence signal of nanoparticles components in tumor sections from mice dosed with Herceptin-targeted siRNA nanoparticles was distinguishable from background; however, the signal was still weak.

Herceptin was only detected in tumor sections from mice receiving either Herceptin-targeted nanoparticles or Herceptin alone. In tumor sections from mice receiving only Herceptin, we observed Herceptin signal throughout the tumor, localizing in circular patterns around cells, suggesting plasma membrane localization. A similar pattern of fluorescence signal was observed in tumor sections from mice receiving the Herceptin-targeted nanoparticles. The overall intensity of the signal in the tumor was less than the Herceptin only case and the strongest areas of fluorescence were distributed in a punctate fashion throughout the tumor section rather than encircling cells. These punctate Herceptin fluorescence signals co-localized with the nanoparticles components. These data suggested that these punctate structures are intact nanoparticles deposited within the tumor.

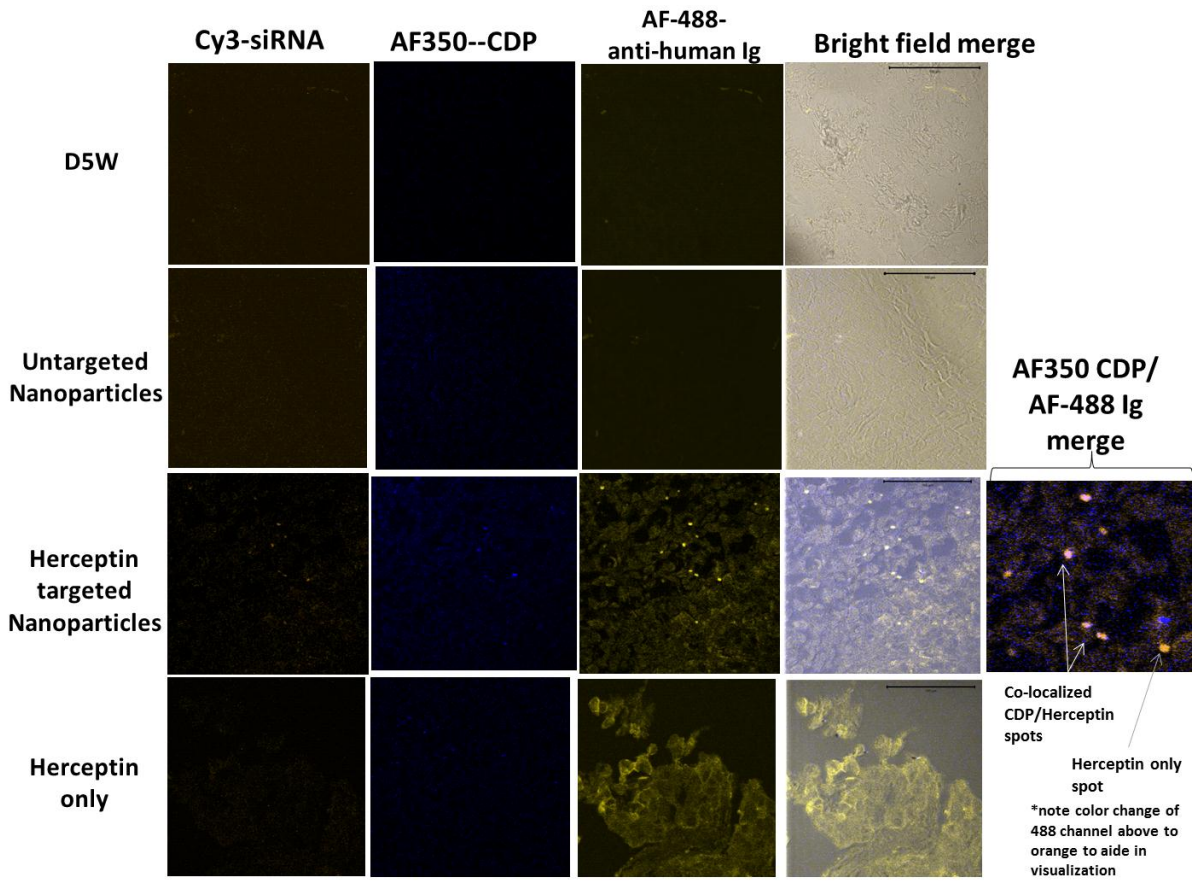

Figure 5: Herceptin targeted nanoparticles accumulate in BT-474 tumor xenografts in mice following intravenous administration. Laser scanning confocal microscopy images of tumor sections from mice receiving the indicated treatment. Scale bars are 50μm.

4.3.6 Herceptin targeted siRNA nanoparticles with siRNA against Her2 resulted in a more robust anti-tumor response than either Herceptin alone or Herceptin-targeted nanoparticles containing control siRNA.

We examined the ability of Herceptin-targeted siRNA nanoparticles to inhibit tumor growth of BT-474 xenograft tumors in mice (Fig. 4.6). For this experiment, the mice were divided into 6 treatment groups: i) 5% dextrose (D5W) ii) non-targeted siRNA nanoparticles with siHER2 iii) Transferrin-targeted siRNA nanoparticles with siHER2 iv) Herceptin-targeted nanoparticles with siEGFP (control siRNA) v) Herceptin only vi) Herceptin-targeted nanoparticles with siHER2 siRNA. The mice received 3 weeks of

treatments (twice per week) and tumor growth was followed for several weeks after this cycle of therapy.

Tumors in mice receiving non-targeted siHER2 containing nanoparticles or Tf-siHER2 containing nanoparticles had similar growth kinetics as mice receiving D5W. Some growth delay, compared to the D5W treated group, was observed in tumors from mice receiving Herceptin-targeted siEGFP nanoparticles, although this was not statistically significant. Significant growth inhibition was observed in both the Herceptin only and Herceptin siHER2 nanoparticles treatment groups compared to D5W. The Herceptin-siHER2 nanoparticles, but not Herceptin alone showed significant growth inhibition compared to the Herceptin-siEGFP nanoparticles.

After cessation of treatment, the tumors from the Herceptin only treated animals began to regrow. The tumors from the Herceptin-siHER2 nanoparticle treated mice remained stable after treatment cessation and only showed increases in size at day 62 of the experiment. The tumors from the Herceptin-siHER2 nanoparticle treated mice did not achieve statistically significant size differences from the tumors of the Herceptin only treated mice. Survival benefit of Herceptin only versus Herceptin-siHER2 nanoparticle treatment could not be assessed because several animals in both groups were euthanized due to side effects of prolonged estrogen exposure rather than tumor size, leading to termination of the experiment.

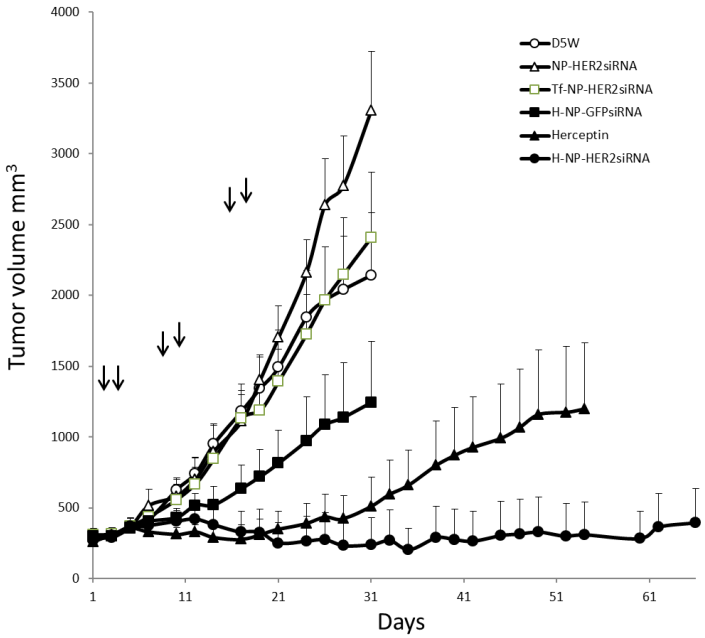

Figure 4.6. Herceptin targeted nanoparticle delivery of siHer2 resulted in more persistent anti-tumor response compared to Herceptin alone and Herceptin targeted siEGFP nanoparticles. BT-474 tumor bearing mice received either 5% dextrose (D5W), 5mg/kg Untargeted-siRNA nanoparticles with siHER2 (NP-HER2-siRNA), 5mg/kg 0.25 mole% Transferrin targeted siRNA nanoparticles with siHER2 (TF-NP-Her2siRNA), 5mg/kg 0.25 mole% Herceptin targeted nanoparticles with siEGFP (H-NP-GFPsiRNA), 8.8 mg/kg Herceptin, or 5mg/kg 0.25 mole% Herceptin targeted nanoparticles with siHER2 (H-NP-HER2siRNA). Doses were bi-weekly for three weeks (arrows). Error bars are S.E.M, n=6.

4.3.7 siRNA knockdown of Her2 causes cell death only in Her2(+) cell lines with acquired resistance to Herceptin.

Her2(+) breast tumors often become resistant to Herceptin; however, they are often still dependent on Her2. Therefore, we hypothesized that Herceptin resistant breast cancer cells would be sensitive to siHER2 treatment. We tested this hypothesis by treating a cell line with acquired resistance to Herceptin (BT474 HR6) with siHER2. siHER2 knockdown expression of Her2 in this cell line and resulted in potent growth inhibition(Fig. 4.7A, B). The growth inhibition following siHER2 treatment was similar to the level of growth inhibition observed in the parental BT-474 Herceptin-sensitive cell

line. Herceptin treatment facilitated rather than hindered growth of this cell lines (Fig. 4.7C).

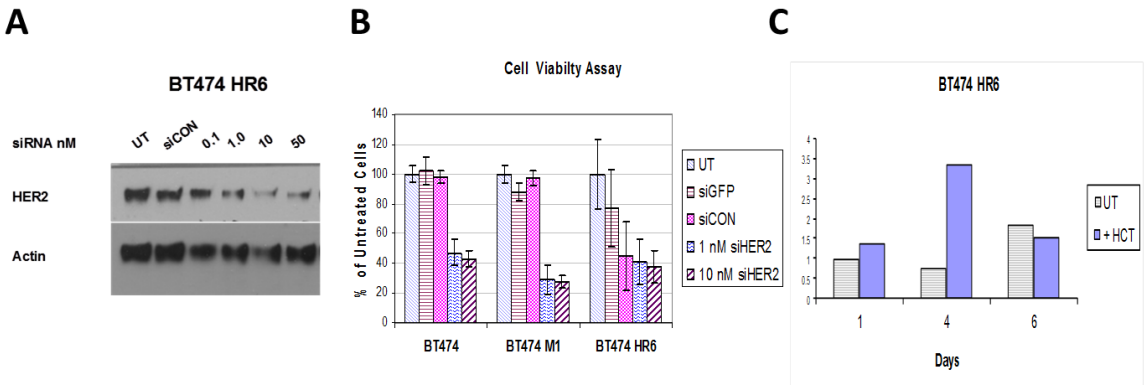

Figure 4.7. siHer2 but not Herceptin can inhibit the growth of Herceptin resistant cell line BT-474 HR6. (A) Western blot of Her2 expression following siHER2 treatment. (B) MTS cell viability assay of Herceptin sensitive (BT-474, BT-474 M1) and Herceptin resistant cell line (BT-474 HR6). (C) MTS cell viability assay of BT-474 HR6 in the presence or absence of 10ug/mL Herceptin.

We also examined the ability of siHER2 to induce apoptosis in this cell line. siHER2 treatment resulted in the appearance of cleaved PARP in this cell lines, suggesting induction of apoptosis (Fig 4.8). Surprisingly, we also observed a potentiation of apoptosis induction of low dose siHER2 in the presence of Herceptin. We were unable to perform *in vivo* studies with these cell lines as they lost their Herceptin resistance when implanted into mice.

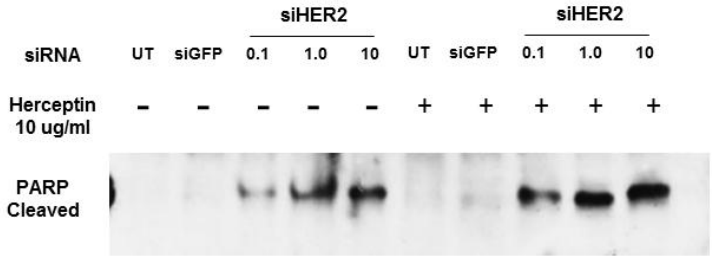

Figure 4.8: Her2 knockdown results in apoptosis induction in BT-474 HR6 cells. Western blot analysis of PARP cleavage following treatment with either 10nM siEGFP or the indicated concentration (nM) of siHER2 in the presence(+) or absence(-) of Herceptin.

4.4 Discussion

In this study, we have developed a Herceptin-targeted siRNA nanoparticle that delivery siRNA against Her2 to Her2(+) breast cancer tumors and inhibits their growth.

We first demonstrated the therapeutic efficacy of siRNA induced Her2 knockdown *in vitro*. The Her2 siRNA sequence (siHER2) was found to silence Her2 at pico-molar concentrations, sufficient for use in *in vivo* studies. Treatment of the Her2(+) cell line BT-474 with siHER2 resulted in cell death. Additionally, we demonstrated that siHER2 treatment in a Her2(-) cell line (MCF-7) did not result in anti-proliferative effects. These data suggested that the therapeutic effects observed in the BT-474 cell line resulted from RNAi induced Her2 silencing and not off-target effects of the siRNA sequence itself.

We had hypothesized that siHER2 would result in a more robust therapeutic activity than Herceptin alone. We examined downstream indicators of PIK3 pathway activation and apoptosis and found that siHER2 induced a marked increase in cleaved PARP (an apoptotic indicator) and decreased phosphor-AKT levels compared to Herceptin. These data suggest that RNAi induced Her2 knockdown resulted in a more

robust inhibition of Her2 signaling than Herceptin. We speculated that this increased efficacy resulted from the simultaneous inhibition of multiple Her2 signaling mechanisms by effectively removing Her2 from the cell. This increased therapeutic efficacy likely recapitulated the dual targeting of Her2 with Herceptin and other agents such as the kinase inhibitor lapatanib or the antibody pertuzumab that have been demonstrated to be superior to any of these agents individually[3].

Therapeutic siRNA nanoparticles containing siRNA against the receptors facilitating nanoparticle uptake may have an additional benefit. We speculate the in a multi-dose treatment regimen, siRNA nanoparticles in the later doses will be biased towards tumor cells that did not internalize nanoparticles in early doses. Tumor cells that internalized the siRNA nanoparticles during early doses will have fewer receptors on their surface than cells that did not internalize nanoparticle, due to the effect of the siRNA payload itself. The cells that did not internalize siRNA nanoparticle following earlier doses would have the highest surface receptor density and therefore would preferentially uptake the siRNA nanoparticles during later doses. Ultimately, this phenomenon would lead to a larger number of cells internalizing nanoparticles throughout the treatment regimen. Furthermore, each dose of nanoparticles will be targeted to the cells we would most desire to receive the nanoparticles.

Acquired and *de novo* resistance to Herceptin is common[11]. Many times these resistant tumors are still dependent on Her2 signaling, despite the lack of response to Herceptin. We demonstrated here that siRNA inhibition of Her2 resulted in cell death in a cell lines with acquired Herceptin resistance. These observations demonstrated the

feasibility of using siRNA inhibition of Her2 as a therapeutic in cases of acquired Herceptin resistance.

There are currently no FDA approved siRNA-based drugs for cancer. Developing new siRNA-based therapeutics against well validated oncogenes may help facilitate approval and further development of these types of therapeutics. There are many challenges to the development of siRNA-based therapeutics. Currently, siRNA therapeutics in clinical trials explore both new delivery systems for siRNA and new gene targets. Simultaneous exploration of two new concepts in the clinic is difficult and failure may results from many variables relating both to the delivery system and choice of gene target. We speculate that validating siRNA-based therapeutic against well validated clinical targets will reduce variables related to poor choices of therapeutic targets and focus clinical trials on making safe and effective siRNA-based delivery systems that, once approved, can be modified for therapeutic targets only druggable via RNAi.

4.5 Materials and Methods

Cell lines and culture: BT-474 and MCF-7cell lines were obtained from American Type Culture Collection (ATCC, Rockville, MD). BT-474 HR6 cells were a gift from Carlos Arteaga. All cell lines were cultured in complete serum media containing RPMI 160 with L-glutamine (Mediatech Inc., Manassas, VA) with 10% (all percentages represent v/v) fetal bovine serum (FBS, Omega Scientific, Tarzana, CA), 1% penicillin, streptomycin, and amphotericin (Omega Scientific) at 37°C with 5% CO_2 in filter-top flasks.

Synthesis of AD-PEG-Herceptin: Herceptin (Genentech) was reacted with a 10 molar excess of SATP and followed by addition of 50mM Hydroxylamine after a buffer

exchange to form thiols at sites of primary amines. Following purification of the Herceptin fraction of the reaction mixture a 50 molar excess of AD-PEG-malamide was added and after 1 hr the reaction was brought to 10mM of Iodoacetamide to cap any remaining free thiols. The mono-PEGylated fraction of Herceptin was purified via HPLC.

Nanoparticle formulation and siRNA duplexes: siRNA nanoparticles were formed by using cyclodextrin-containing polycations (CDP) and AD-PEG as described previously described[10] (pre-complexation). Nanoparticles were formed in 5 % glucose in deionized water (D5W) at a charge ratio of 3 +/- and a siRNA concentration of 2 mg/ml unless otherwise indicated. 21 base pair unmodified and Cy3 labeled siRNA was purchased from Qiagen.

siHER2: 5'- GGUGCUUCAUCUGGCGCUUU -3'

siEGFP[12]: 5'-GGCUACGUCCAGGAGCGCACC-3'

In vitro transfection: A reverse transfection protocol was followed for siRNA delivery. siRNA was complexed with LipofectamineRNAiMax (Invitrogen, Carlsbad, CA) according to manufacturer's instructions. Cells were transfected as described above and cell viability was determined using the Aqueous MTS Assay (Promega, Madison, WI) by following the manufacturer's instructions.

Western blots: 48 hours after transfection, cells were lysed in RIPA Buffer (Thermo Fisher Scientific Inc., Waltham, MA). Lysates were diluted to equivalent protein concentration in beta-mercaptoethanol-containing Laimmli sample buffer (Thermo-Fisher) and incubated at 95^{o}C for 5 minutes. Antibodies: PARP/cleaved PARP antibody, Her2 antibody, Actin, and Phopho-AKT, horseradish peroxidase-conjugated secondary

antibodies were purchased from Santa Cruz Biotechnology. Development was done using SuperSignal West Dura Extended Duration Substrate (Thermo-Fisher).

Animal Studies: All animals were treated according to the NIH Guidelines for Animal Care and Use as approved by the Caltech Institutional Animal Care and Use Committee. 6 to 9-week old, female nude mice (Charles River). For anti-tumor experiments, 5 million BT-474 cells were implanted into the front flanks of nude mice bearing esterdiol pellets implanted one day prior tumor inoculation. Treatments were initiated when tumors reached ~250mm^3.

Confocal microscopy: Formalin-fixed organs were dehydrated and embedded in molten paraffin to generate sections of 4-μm in thickness. Sections were deparrafinized with xylene, rehydrated, and mounted with ProLong Gold antifade reagent (Invitrogen) for viewing under a Zeiss LSM 510 inverted confocal scanning microscope (with a Plan Neofluar ×40/0.75 objective). The excitation wavelengths of Cy3-siRNAs was 543 nm (HeNe laser) and the corresponding emission filter was 560-610 nm. The measured resolution at which images were acquired is 512×512 pixels, and the image bit-depth is 8-bit. 10 sections from each organ were inspected. Typically, 5 glomeruli from each tissue section were inspected. The Zeiss LSM Image Browser Software allows the extraction of images.

Cryo-electron microscopy*:* Samples were vitrified using an automated climate-controlled plunge-freezer (Vitrobot, FEI). Briefly, glow discharged Quantifoil holey carbon grids (SPI Supplies) were loaded into the chamber of the Vitrobot and 5ul of samples were applied. Grids were blotted for 1s and drained for 1s before being plunged into the center of a Vitrobot cup filled with liquid ethane, they were then quickly

transferred into the outer ring of the cup containing liquid nitrogen. The grids were stored under liquid nitrogen for later analysis. Samples were visualized in Techni T12 Cryo-electron microscope (FEI) equipped with a cryo-specimen holder. Acceleration voltage was set at 120kV.

4.6 Acknowledgements:

We thank Carlos L. Arteaga for the BT-474 HR6 cell line. This work was funded by the Prospect Creek Foundation.

4.7 References:

1. Baselga, J. Targeting tyrosine kinases in cancer: the second wave. Science (New York, N.Y.) 312, 1175-8 (2006).

2. Stern, H.M. Improving Treatment of HER2-Positive Cancers: Opportunities and Challenges. Science Translational Medicine 4, 127rv2-127rv2 (2012).

3. Abramson, V. & Arteaga, C.L. New strategies in HER2-overexpressing breast cancer: many combinations of targeted drugs available. Clinical Cancer Research 17, 952-8 (2011).

4. Davis, M.E., Chen, Z.G. & Shin, D.M. Nanoparticle therapeutics: an emerging treatment modality for cancer. Nature Reviews. Drug Discovery 7, 771-82 (2008).

5. Junttila, T.T. et al. Ligand-independent HER2/HER3/PI3K complex is disrupted by trastuzumab and is effectively inhibited by the PI3K inhibitor GDC-0941. Cancer Cell 15, 429-40 (2009).

6. Dave, B. et al. Loss of phosphatase and tensin homolog or phosphoinositol-3 kinase activation and response to trastuzumab or lapatinib in human epidermal growth factor receptor 2-overexpressing locally advanced breast cancers. Journal of Clinical Oncology 29, 166-73 (2011).

7. Castanotto, D. & Rossi, J.J. The promises and pitfalls of RNA-interference-based therapeutics. Nature 457, 426-33 (2009).

8. Davis, M.E. et al. Evidence of RNAi in humans from systemically administered siRNA via targeted nanoparticles. Nature 464, 1067-70 (2010).

9. Bartlett, D.W. & Davis, M.E. Physicochemical and biological characterization of targeted, nucleic acid-containing nanoparticles. Bioconjugate Chemistry 18, 456-68 (2007).

10. Bartlett, D.W. & Davis, M.E. Physicochemical and biological characterization of targeted, nucleic acid-containing nanoparticles. Bioconjugate Chemistry 18, 456-68 (2007).

11. Zhang, S. et al. Combating trastuzumab resistance by targeting SRC, a common node downstream of multiple resistance pathways. Nature Medicine 17, 461-9 (2011).

12. Novina, C.D. et al. siRNA-directed inhibition of HIV-1 infection. Nature Medicine 8, 681-6 (2002).

Chapter 5: RNAi induced knockdown of N-Ras inhibits the growth of N-Ras mutant melanoma cell lines *in vitro* and *in vivo*

5.1 Abstract:

Pharmacologic inhibition of mutant B-Raf in melanoma with B-Raf mutations has had a profound impact on the treatment of this deadly disease. There is now hope for the 60% of melanoma patients possessing this mutation. However, no new treatment options have emerged for the 15% of melanoma patients with activating N-Ras mutations. Ras proteins have historically been considered undruggable. Here, we demonstrate that RNAi inhibition of N-Ras results in anti-proliferative effects in N-Ras mutant melanomas *in vitro* and *in vivo*. Despite these promising results, N-Ras inhibition did not induce significant tumor regressions in mice models, and therefore may have limited clinical utility as a monotherapy.

5.2 Introduction:

Melanomas have three mutually-exclusive driver oncogenic events, c-kit, B-Raf, and N-Ras[1]. c-kit is mutated in 3% of melanomas, B-Raf in 60%, and N-Ras in 15%[2]. Emerging clinical experiences provide clear evidence that inhibitors to c-kit or B-Raf induce objective responses in patients with metastatic melanoma[3,4]. The c-kit inhibitor imatinib can induce objective responses in metastatic melanomas with c-kit mutations[4]. Several agents in clinical development directly inhibit B-Raf or the downstream kinase Mek, and these agents selectively kill B-Raf V600E-mutated cancers but not N-Ras mutated cancers[3]. Specifically, the small molecule inhibitor specific for B-Raf, vemurafenib, has demonstrated objective tumor responses and prolonged survival in the great majority of patients with B-RAF V600E mutated melanoma[3], thereby providing a

compelling proof-of-concept that targeting oncogenic mutations in the MAPK pathway is a valid therapeutic strategy for metastatic melanoma.

N-Ras cannot be targeted with any drug in clinical development, and generally is considered undruggable. However, oncogenic mutations in Ras were the first driver oncogenes characterized by Barbacid and collaborators back in 1982[5], and are prevalent mutations in many cancers.

Melanomas with N-Ras mutations do not harbor either a c-kit mutation or a B-Raf mutation, suggesting that a mutation in one of these three contiguous signaling molecules is a dominant oncogenic event in this cancer. Based on these observations, we hypothesized that inhibition of N-Ras might have similar therapeutic potency to inhibition of B-Raf or c-Kit.

Here we demonstrated the validation of a potent siRNA sequence targeting N-Ras that specifically inhibits the growth of melanoma cells lines with activating N-Ras mutations *in vitro* and *in vivo*. However, we also demonstrate that targeting of N-Ras does not have the same therapeutic potency as analogous B-Raf inhibition in B-Raf mutant melanoma cell lines. Additionally, we found that although shRNA induced N-Ras inhibition delays tumor growth *in vivo,* siRNA delivery of N-Ras targeting siRNA did not.

5.3 Results:

5.3.1 siRNA induced N-Ras silencing in melanoma cell lines via RNAi mechanism.

We first demonstrated that a siRNA targeting N-Ras (siNRAS) induced silencing of N-Ras in multiple melanoma cell lines. The siNRAS sequence induced potent N-Ras

knockdown in all cell lines at doses as low as 0.5nM (Fig. 5.1). These data indicated that this siRNA sequence had sufficient potency for future *in vivo* studies.

We next confirmed that the siNRAS sequence inhibited N-Ras expression via the canonical RNAi mechanism. We used a 5' RNA ligand mediated rapid amplification of cDNA ends (5'-RLM-RACE) analysis for this purpose. N-Ras mRNA cleavage fragments that corresponded to the 10bp position of the 5' anti-sense strand of siNRAS were detected in RNA extracts from siNRAS treated cells but not from cells treated with control siRNA (siCON). These data confirmed that siRNAS can silence N-Ras via the canonical siRNA silencing mechanism.

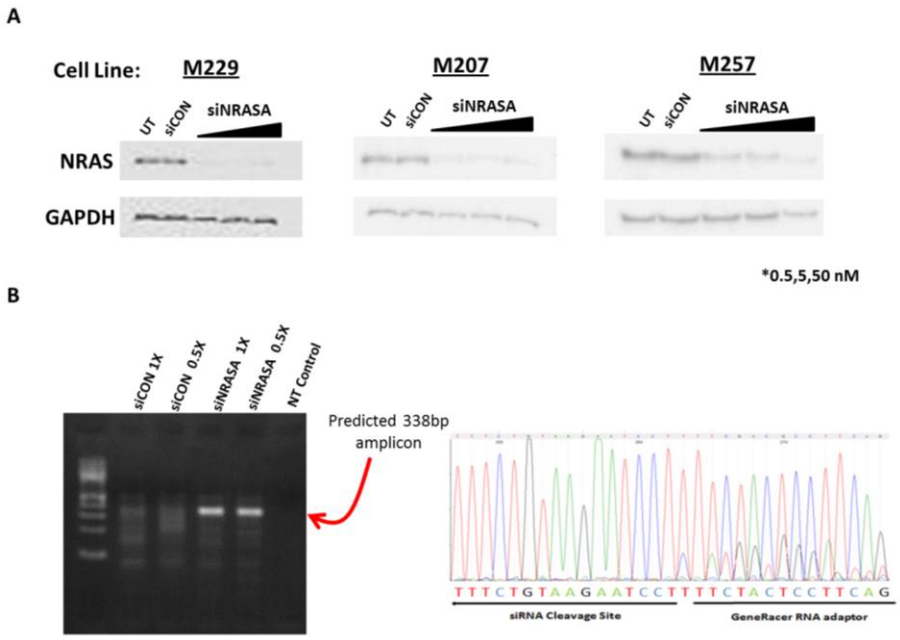

Figure 5.2: siRNA induced silencing of N-Ras in melanoma cell lines. (A) Western blot analysis of N-Ras expression following siNRAS treatment in melanoma cell lines. UT=no treatment, siCON=control siRNA, siNRASA=siRNA against N-Ras. (B) 5'-RLM-RACE analysis following siNRAS treatment of M202 melanoma cells. Gel analysis demonstrated predicted amplicons only in siNRAS treated samples and sequencing confirmed correct band identification.

5.3.2 siRNA silencing of N-Ras inhibited the growth of N-Ras mutant melanoma cell lines, but not N-Ras wild type cell lines *in vitro*.

We hypothesized that N-Ras mutant melanoma cell lines require active N-Ras signaling for growth and survival and that silencing of N-Ras would result in growth inhibition and cell death. We tested this hypothesis by treating a panel of melanoma cell lines with siNRAS (Fig. 5.2). We observed that siNRAS treatment resulted in decreased cell viability in all N-Ras mutant cell lines, but not in N-Ras wild type cell lines.

There was a high variability in the level of response to N-Ras knockdown. siNRAS treatment of M202, PTM, and M243 cell lines resulted in strong growth inhibition, whereas siNRAS treatment of M207, M244, and M245 resulted in less pronounced growth inhibition.

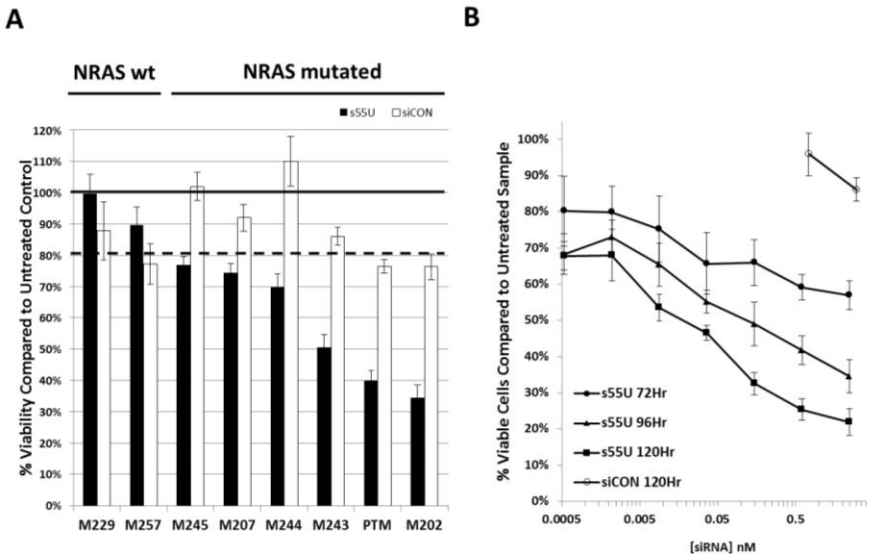

Figure 5.3: siNRAS inhibits the growth of a panel of N-Ras mutant melanoma cell lines. (A) MTS cell viability assays 96 hours after treatment with 5nM siNRAS (s55U=siNRASA) or siCON. (B) MTS cell viability assay dose titration of siNRAS (s55U) in M202 melanoma cells at varying time points post transfection. Non-specific toxicity of siCON was variable depending on time point and over different experiments in the same cell line. siNRAS effects on viability were consistent over different experiments in the same cell line.

We also examined the dose dependence of siNRAS treatment in M202 cells. We observed significant growth suppression even at pico-molar doses, although doses >5nM where required for maximal response (Fig. 5.2B).

N-Ras mutant melanoma cell lines treated with siNRAS did not appear to reduce in cell number, suggesting that N-Ras knockdown resulted in cell cycle arrest but not cell death. We confirmed that N-Ras knockdown resulted in strong G1/S cell cycle arrest (Fig. 3A). Using an electronic cell sensing assay we observed that once cell growth was arrested the total number of cells did not decrease (Fig. 5.3B). These data confirmed our observations that siNRAS treatment did not induce cell death.

5.3.3 Downstream pathway analysis suggested possible explanations for variability in response to siNRAS treatment.

We examined the phosphorylation levels of two downstream targets of N-Ras, ERK1/2 and AKT in two N-Ras mutant melanoma cell lines M202 (good responder) and M207 (poor responder). siNRAS treatment resulted in decreased levels of phospho-ERK only in the M202 cell line (Fig. 5.4). siNRAS treatment did results in decreased phospho-AKT levels in M207 cells; however, phospho-AKT levels in M202 cells were constitutively low. These data suggested that N-Ras knockdown may not inhibition ERK signaling in some N-Ras mutant melanoma cell lines, possibly due to constitutive increased AKT activity.

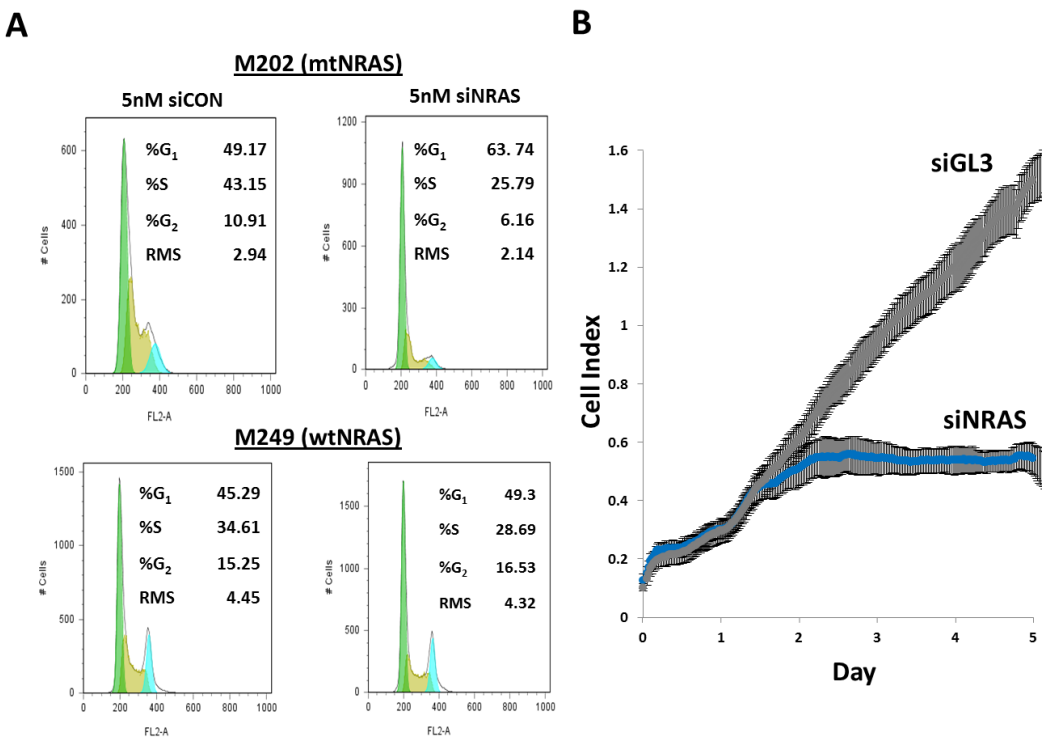

Figure 5.4: N-Ras knockdown induces potent cell cycle arrest but does not result in cell death. (A) Flow cytometry based cell cycle analysis following treatment with siCON or siNRAS in an N-Ras mutant and wild type melanoma cell line. (B) Real-time cell sensing assays of M202 melanoma cells treated with control siRNA (siGL3) or siNRAS. Cell index is proportional to cell number.

5.3.4 Inducible shRNA construct suppressed growth of an N-Ras mutant melanoma cell line in vivo.

Because the siNRAS treatment resulted in only modest growth inhibition in our *in vitro* study, we wanted to confirm that RNAi inhibition of N-Ras would result in measurable growth inhibition *in vivo*, prior to performing any studies the siRNA nanoparticle system. Therefore, we engineered N-Ras mutant melanoma cell lines that would inducibly express shRNA against N-Ras (shNRAS). As a comparison we also engineered B-RAF mutant melanoma cell lines that would inducibly express shRNA against B-RAF.

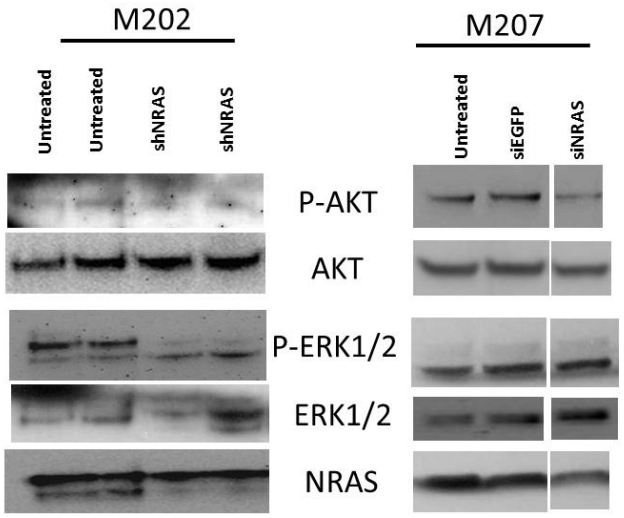

Figure 5.5: Western blot analyses of downstream targets of N-Ras signaling.

shRNA against N-Ras was found to induce a similar anti-proliferative effect as siRNAS treatment in M202 melanoma cells *in vitro* (Fig. 5.5A). No apparent decrease in cell number was observed, even after prolonged (weeks) of shRNA induction. shRNA against B-RAF, alternatively, strongly suppressed growth of a B-Raf mutant melanoma cell lines M249 to a similar extend to that of pharmacologic inhibition of B-Raf with PLX4720 (PLX) (Fig. 5.5B).

We then examined how shRNA inductions would affect the growth of M202 shNRAS and M249 shBRAF tumor xenografts in mice (Fig. 5.6A) Induction of shNRAS in the M202 cells results in ~50% reduction in tumor size within a week of induction. This growth reduction was followed by 3 weeks of stasis. The tumors began increasing in size about 4 weeks after shNRAS induction. Induction of shBRAF in M249 melanoma cells resulted in rapid reduction in tumor size over 2 weeks until tumors were no longer visible. When shBRAF induction was stopped several tumors grew back; however,

several did not. Overall, these data clearly demonstrated that B-Raf inhibition resulted in much more potent anti-tumor effects than N-Ras inhibition.

We investigated the nature of the apparent resistance to shNRAS treatment in M202 tumors. Tumors were extracted from the mice and N-Ras expression was examined by western blot (Fig 5.6B). shNRAS tumors were found to have higher levels of N-Ras expression to control tumors. Cell lines were established from these tumors and continually grown in the presence of the shRNA induction reagent doxycycline (DOX) and selection reagent (puromycin) for the shRNA cassette. The tumors grew despite the presence of DOX and puromycin, suggesting resistance to shNRAS expression (Fig. 5.6C).

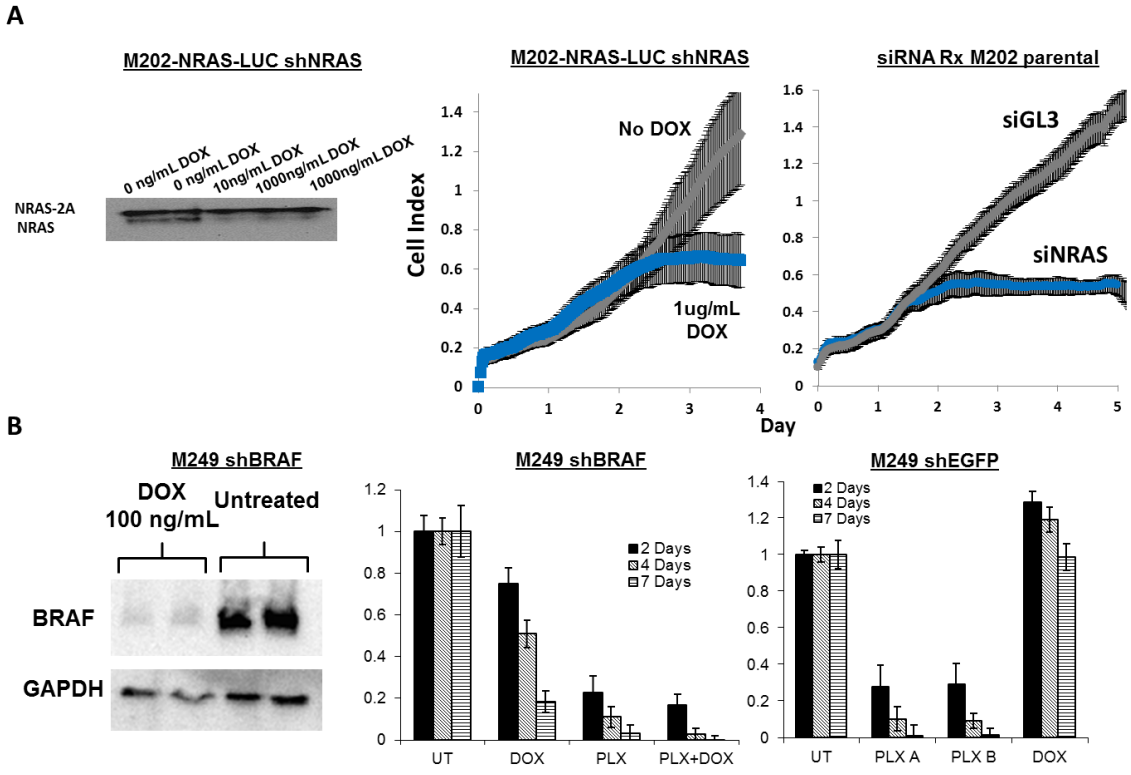

Figure 5.6: *In vitro* characterization of inducible shRNA systems targeting N-Ras and B-Raf. (A) Western blot and real time cell sensing analyses of M202 shNRAS in the presence or absence of shRNA inducing reagent doxycycline (DOX). M202-NRAS-LUC cells have been engineered to express an extra copy of wild type N-Ras with a 2A sequence on it that appears as a

slightly higher molecular weight band than the endogenous mutant N-Ras. (B) Western blot and MTS assays on M249 shBRAF cells. PLX=PLX4720.

We hypothesized that these cells were resistant to N-Ras knockdown. However, siNRAS treatment resulted in growth inhibition for these cells (data not shown). These data demonstrated that N-Ras was still sensitive to RNAi knockdown and the cells were still dependent on N-Ras signaling for growth. Therefore, we concluded that the continued growth of the tumors in the presence of DOX was due to partial loss of shNRAS expression cassettes and upregulation of N-Ras expression.

5.3.5 siRNA nanoparticles targeting N-Ras did not inhibit tumor growth in vivo.

Inhibition of M202 tumor growth via inducible shRNA knockdown of N-Ras indicated that RNAi inhibition of N-Ras is a viable strategy for treatment of these tumors. Additionally, no true resistance to N-Ras knockdown emerged. We therefore examined the ability of siRNA nanoparticles carrying siNRAS to inhibit the growth of M202 xenograft tumors.

First, we confirmed that transferrin could facilitate nanoparticle uptake by these cells. siRNA nanoparticles containing no targeting ligand or 0.25 mole% AD-PEG-Tf were incubated with M202 cells for 1 hour. Compared to the non-targeted nanoparticles, the Tf targeted nanoparticles were more readily internalized by the M202 cells (Fig. 5.7).

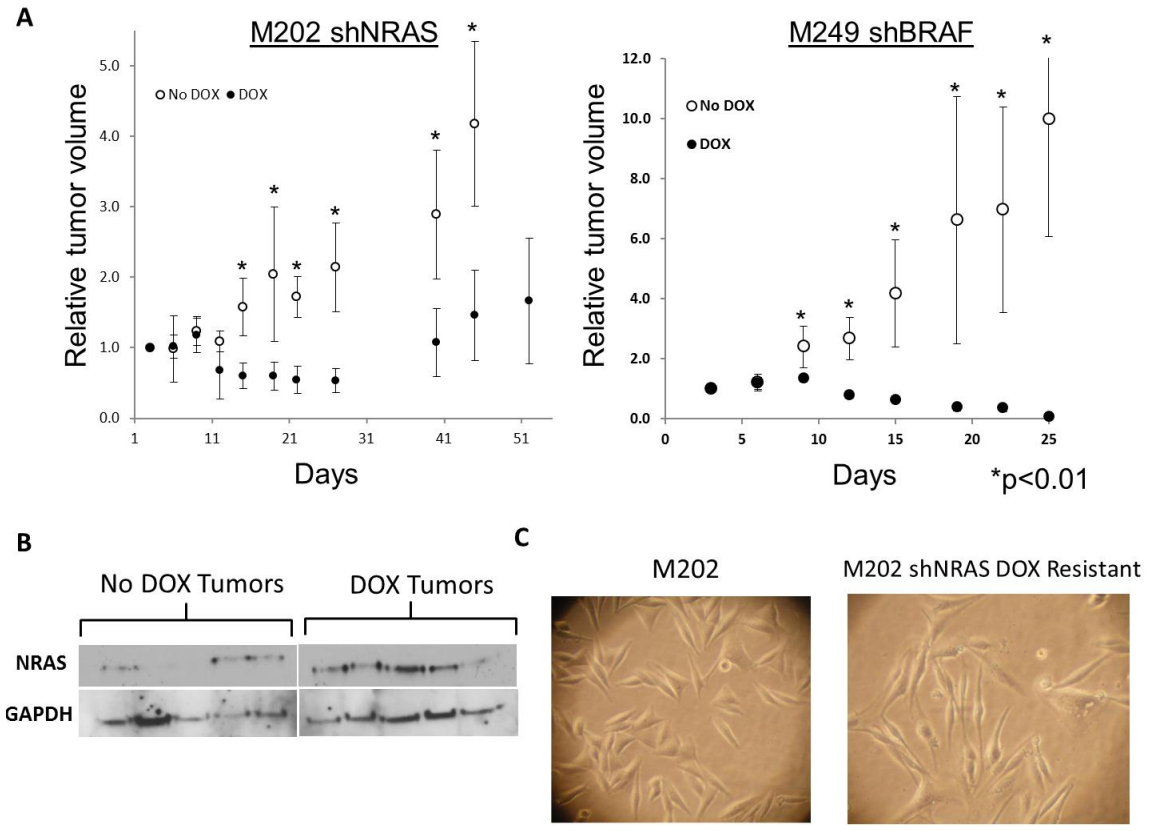

Figure 5.7: *In vivo* characterization of inducible shRNA against N-Ras and B-Raf. (A) Tumor growth experiments for M202 shNRAS and M249 shBRAF tumors in the presence of absence of shRNA inducing reagent doxycycline (DOX). Error bars=S.D., n=6, p-values are from two-tailed t-tests. (B) Western blot analysis of N-Ras levels in protein extracts from M202 shNRAS tumors collected at the end of the growth experiment. (C) Images of an M202 shRNAS cell line isolated from the DOX tumors and their parental M202 cell line.

We next examined the growth M202 xenografts in groups of mice that received one of three different treatment strategies: (i) 5% dextrose, (ii) 5mg/kg Tf-siEGFP nanoparticles, or (iii) 5mg/kg Tf-siNRAS-nanoparticles. The mice were treated twice a week for 3 weeks. No differences between the three treatment groups were observed (Fig. 8).

5.4 Discussion

Here we have demonstrated that RNAi mediated silencing of N-Ras holds some promise as a therapeutic option for melanoma patients with activating N-Ras mutations. *In vitro*, N-Ras knockdown resulted in variable anti-proliferative effects over a panel of mutant N-Ras melanoma cell lines, but not in N-Ras wild type cell lines. N-Ras knockdown was found to induce cell cycle arrest; however, no evidence for cell death even after prolonged N-Ras knockdown was observed. We confirmed that N-Ras knockdown via inducible shRNA could result in some tumor regression; however, this effect was short lived.

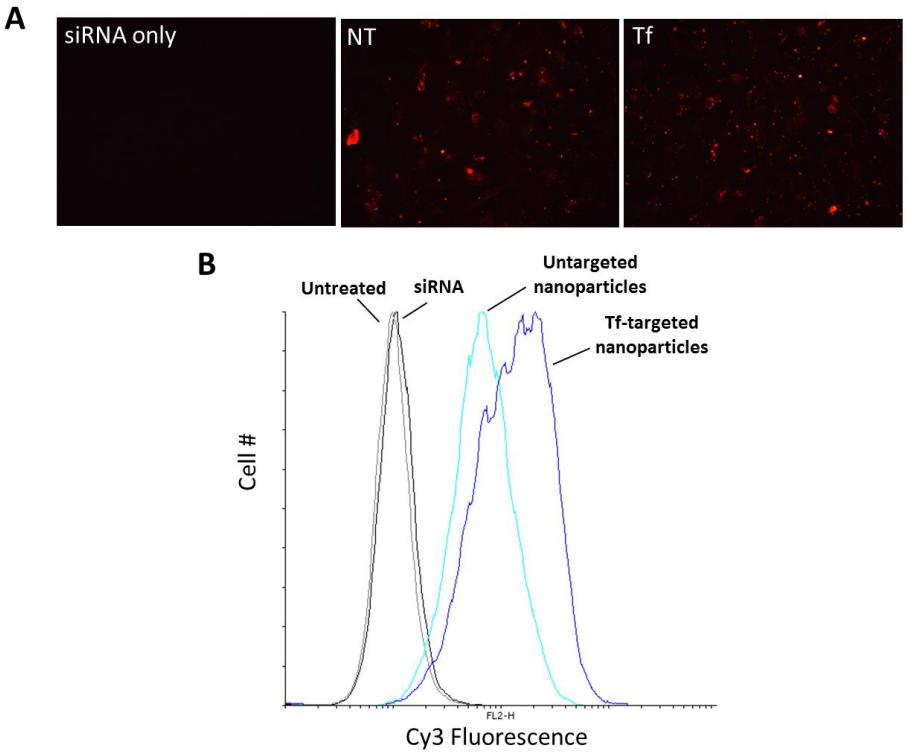

Figure 5.8: M202 melanoma cells internalized Transferrin (Tf) targeted siRNA nanoparticles more readily than untargeted siRNA nanoparticles *in vitro*. (A) Florescence micrographs of M202 cells following incubation with the indicated Cy3-labeled siRNA nanoparticle formulation. (B) Flow cytometry quantification of Cy3-siRNA uptake in M202 cells. Samples were incubated with 200nM siRNA nanoparticle formulations with 20% Cy3-labeled siRNA. 0.25 mole% Tf was used for targeted nanoparticles.

We found that RNAi silencing of B-Raf *in vitro* induced far more potent anti-proliferative effects that N-Ras silencing. Silencing of B-Raf via RNAi had effects similar in magnitude to pharmacologic B-Raf inhibition with PLX4720. Silencing of B-Raf *in vivo* resulted in rapid tumor regression and some complete cures.

RNAi silencing of N-Ras has been demonstrated by others to inhibit melanoma cell growth and in one case induce some cell death *in vitro*[6–8]. However, *in vivo,* more modest results than we observed (with no evidence of any tumor regression) have been reported following induction of anti-N-Ras shRNA in xenograft tumors[6].

Taken together with our results, these data suggest that inhibition of N-Ras as a monotherapy will have limited clinical utility. We speculate that N-Ras knockdown may result in compensatory upregulation of other cellular pathways (e.g., EGFR). This phenomenon is observed for many other targeted therapeutics including Herceptin[9], vemurafenib[10], Erlotinib[11], etc.. Silencing of K-Ras in lung cancer cell lines has been demonstrated to have a similar modest therapeutic effects *in vitro* and *in vivo*[12]. In that report, compensatory increases in phosphorylated STAT3 and EGFR were demonstrated to mediate the partial resistance to anti-k-Ras therapy. Surprisingly, this phopho-EGFR upregulation sensitized these cells to EGFR inhibition. A similar phenomenon of P-AKT upregulation following loss of feedback inhibition following shRNA silencing of k-Ras has been observed in k-Ras mutated colorectal cancer cell lines[13]. Combinatorial strategy should be further explored to improve the therapeutic efficacy of RNAi-based N-Ras targeting.

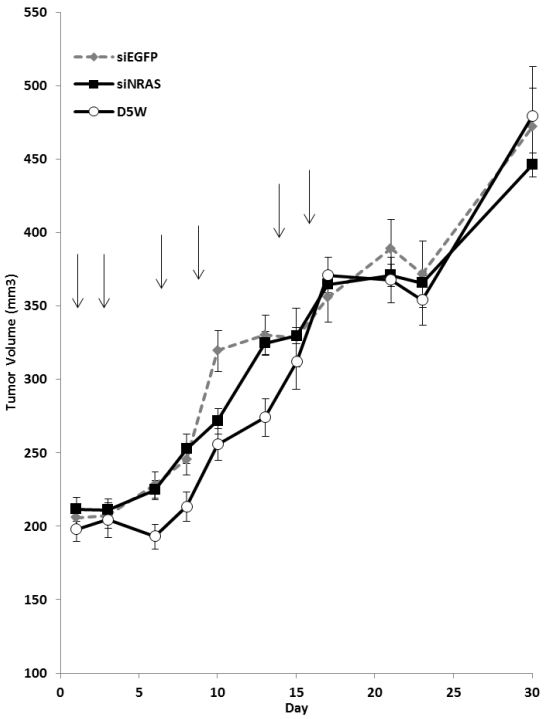

Figure 5.9: siRNA nanoparticles targeting N-Ras do not inhibit tumor growth. NOD-SCID gamma mice bearing subcutaneous M202 xenograft tumors received intravenous doses of 5mg/kg siRNA nanoparticles with controls siEGFP or siNRAS or 5% dextrose (D5W) control twice weekly (arrows) for three weeks. Error bars are S.E.M, n=7.

Although we observed tumor growth inhibition in our inducible shRNA tumor model, siRNA nanoparticles targeting N-Ras did not have therapeutic effects *in vivo*. Together, these data suggest that an insufficient amount of siRNA was delivered to the tumors to result in growth inhibition. We believe that the only way to overcome this limitation is to improve the pharmacokinetics and thereby tumor delivery of the siRNA nanoparticles delivery system.

5.5 Materials and Methods:

Cell lines and culture: Melanoma cell lines M202, M207, M229, M244, M245, M249, M255, and M257 cell lines were established from patient's biopsies under UCLA IRB approval #02-08-067 and have been previously characterized[14]. PTM was provided by

Bijay Mukherji (University of Connecticut, Farmington, CN). All cell lines were cultured in complete serum media containing RPMI 160 with L-glutamine (Mediatech Inc., Manassas, VA) with 10% (all percentages represent v/v) fetal bovine serum (FBS, Omega Scientific, Tarzana, CA), 1% penicillin, streptomycin, and amphotericin (Omega Scientific) at 37°C with 5% CO_2 in filter-top flasks.

Nanoparticle formulation and siRNA duplexes: siRNA nanoparticles were formed by using cyclodextrin-containing polycations (CDP) and AD-PEG as described previously described[15] (pre-complexation). Nanoparticles were formed in 5 % glucose in deionized water (D5W) at a charge ratio of 3 +/- and a siRNA concentration of 2 mg/ml unless otherwise indicated. 21 base pair unmodified and Cy3 labeled siRNA was purchased from Qiagen.

siNRASA: 5'-CCACCAUAGAGGAUUCUUACA -3'

siCON: 5'-UAGCGACUAAACACAUCAAUU-3'

siEGFP: 5'-GGCUACGUCCAGGAGCGCACC-3'

In vitro transfection: A reverse transfection protocol was followed for siRNA delivery. siRNA was complexed with LipofectamineRNAiMax (Invitrogen, Carlsbad, CA) according to manufacturer's instructions. Cell viability was determined using the Aqueous MTS Assay (Promega, Madison, WI) by following the manufacturer's instructions.

Western blots: 48 hours after transfection, cells were lysed in RIPA Buffer (Thermo Fisher Scientific Inc., Waltham, MA). Lysates were diluted to equivalent protein concentration in beta-mercaptoethanol-containing Laimmli sample buffer (Thermo-Fisher) and incubated at 95^{o}C for 5 minutes. Antibodies: N-Ras, GAPDH, horseradish

peroxidase-conjugated secondary antibodies were purchased from Santa Cruz Biotechnology, (P)-ERK1/2, (P)-AKT, and B-Raf antibodies were purchased from Cell Signaling Technologies . Development was done using SuperSignal West Dura Extended Duration Substrate (Thermo-Fisher).

5' RNA ligand mediated-RACE: was performed as described previously[16]. Briefly, 3 μg or total RNA was ligated directly to 250ng GeneRacer RNA adapotor (Invitrogen) using T4 RNA ligase. Ligation products were reverse transcribed using SuperScriptIII (Invitrogen) and an N-Ras gene specific reverse transcription primer. Two rounds of PCR were performed using a Bio-Rad MJ Mini personal thermocycler and PCR conditions described previously[16]. PCR products were run on a 2% agarose gel and stained with 1μg/μl ethidium bromide. PCR products were excised from gel and sequenced directly to confirm RACE band identities.

Flow cytometery: *Cell Cycle analysis:* Cells were trypsinized and washed twice with PBS. Ice cold 70% ethanol was added drop wise while vortexing and allowed to incubate at 4^{o}C for 30 minutes. Samples were then centrifuged at 1,300 rpm for 10 minutes and the ethanol decanted. The samples were then stained with 5 μg/ml propidium iodide at room temperature for 30 min. *Cy3 uptake studies:* Cells were incubated with 200nM Cy3-siRNA nanoparticles for 60 minutes. Cells were washed with detergent buffer to remove unbound complexes and scrapped into tubes for analysis. For both experiments cells were analyzed by flow cytometery on a FACScan (BD Biosciences) flow cytometer and data analyzed using FlowJo version 8.7 (Tree Star, Inc., Ashland, OR).

Animal Studies: All animals were treated according to the NIH Guidelines for Animal Care and Use as approved by the Caltech Institutional Animal Care and Use Committee.

*A*nti-tumor experiments, 5 million melanoma cells (M202 or M249) were implanted into the front flanks of 4 week old NOD/SCID gamma mice (Jackson Laboratory). Treatments were initiated when tumors reached ~200mm^3.

5.6 Acknowledgements:

This work was funded by the National Cancer Institute Grant CA119347.

5.7 References:

1. Curtin, J. a et al. Distinct sets of genetic alterations in melanoma. The New England Journal of Medicine 353, 2135-47 (2005).

2. Curtin, J. a, Busam, K., Pinkel, D. & Bastian, B.C. Somatic activation of KIT in distinct subtypes of melanoma. Journal of clinical oncology : official journal of the American Society of Clinical Oncology 24, 4340-6 (2006).

3. Chapman, P.B. et al. Improved survival with vemurafenib in melanoma with BRAF V600E mutation. The New England Journal of Medicine 364, 2507-16 (2011).

4. Hodi, F.S. et al. Major Response to Imatinib Mesylate in KIT-Mutated Melanoma . Journal of Clinical Oncology 26 , 2046-2051

5. McBride, O.W. et al. Localization of the normal allele of T24 human bladder carcinoma oncogene to chromosome 11. Nature 23-30 (1982).

6. Jaiswal, B.S. et al. Combined targeting of BRAF and CRAF or BRAF and PI3K effector pathways is required for efficacy in NRAS mutant tumors. PloS one 4, e5717 (2009).

7. Eskandarpour, M., Huang, F., Reeves, K. a, Clark, E. & Hansson, J. Oncogenic NRAS has multiple effects on the malignant phenotype of human melanoma cells cultured in vitro. International Journal of Cancer. 124, 16-26 (2009).

8. Eskandarpour, M. et al. Suppression of oncogenic NRAS by RNA interference induces apoptosis of human melanoma cells. International Journal of Cancer. 115, 65-73 (2005).

9. Narayan, M. et al. Trastuzumab-induced HER reprogramming in “resistant” breast carcinoma cells. Cancer Research 69, 2191-4 (2009).

10. Nazarian, R. et al. Melanomas acquire resistance to B-RAF(V600E) inhibition by RTK or N-RAS upregulation. Nature 1-32 (2010)

11. Jimeno, A. et al. Epidermal growth factor receptor dynamics influences response to epidermal growth factor receptor targeted agents. Cancer Research 65, 3003-10 (2005).

12. Sunaga, N. et al. Knockdown of oncogenic KRAS in non-small cell lung cancers suppresses tumor growth and sensitizes tumor cells to targeted therapy. Molecular Cancer Therapeutics 10, 336-46 (2011).

13. Ebi, H. et al. Receptor tyrosine kinases exert dominant control over PI3K signaling in human KRAS mutant colorectal cancers. Journal of Clinical Investigation 121, (2011).

14. Søndergaard, J.N. et al. Differential sensitivity of melanoma cell lines with BRAFV600E mutation to the specific Raf inhibitor PLX4032. Journal of Translational Medicine 8, 39 (2010).

15. Bartlett, D.W. & Davis, M.E. Physicochemical and biological characterization of targeted, nucleic acid-containing nanoparticles. Bioconjugate Chemistry 18, 456-68 (2007).

16. Davis, M.E. et al. Evidence of RNAi in humans from systemically administered siRNA via targeted nanoparticles. Nature 464, 1067-70 (2010).

Chapter 6: Targeting kidney mesangium by nanoparticles of defined size[†]

6.1 Abstract

Nanoparticles are being investigated for numerous medical applications, and are showing potential as an emerging class of carriers for drug delivery[1, 2]. Investigations on how the physicochemical properties (e.g., size, surface charge, shape, and density of targeting ligands) of nanoparticles enable their ability to overcome biological barriers and reach designated cellular destinations in sufficient amounts to elicit biological efficacy are of interest. Despite proven success in nanoparticle accumulation at cellular locations and occurrence of downstream therapeutic effects (e.g., target gene inhibition) in a selected few organs such as tumor[3] and liver[4], reports on effective delivery of engineered nanoparticles to other organs still remain scarce. Here, we show that nanoparticles of ca. 75 +/- 25 nm diameters target the mesangium of the kidney. These data are the first to show the effects of particle diameter on targeting the mesangium of the kidney. Since many diseases originate from this area of the kidney, our findings establish design criteria for constructing nanoparticle-based therapeutics for targeting diseases that involve the mesangium of the kidney.

6.2 Introduction

Constructing nanoparticles for drug delivery requires knowledge in colloidal science and biology, where biological constraints generally dictate the design of nanoparticle therapeutics and imaging agents. A celebrated design criterion is the notion of "renal clearance"[5, 6]. That is, nanoparticles will experience rapid clearance by the kidney if they

[†] Reproduced with permission from: C. H. J. Choi, J. E. Zuckerman, P. Webster and M. E. Davis, "Targeting kidney mesangium by nanoparticles of defined size," *Proc. Nat. Acad. Sci. USA* **108**, 6656 (2011).

are smaller than ca. 10 nm in diameter. Such clearance originates from the innate function of the kidney as a blood filter.

The structural and functional unit of the kidney, the nephron, consists of the renal corpuscle and tubule system. The renal corpuscle contains a tuft of blood capillaries and support tissue (the mesangium – Fig. S1) called the glomerulus. A fraction of blood plasma entering the glomerulus will pass through the "glomerular filtration apparatus" to produce an ultrafiltrate, which will be collected by the tubule system and ultimately be processed into urine. The first component is the glomerular endothelium with pores that have been reported to be in the range of 80 – 100 nm in diameter[7]. Next, the glomerular basement membrane (GBM), a 300 – 350 nm thick basal lamina rich in heparan sulfate[8] and charged proteoglycans with an average pore size of 3 nm[9], filters small molecules by size and charge. Behind the GBM lies podocytes, cells with interdigitating foot processes that form "filtration slits" of 32 nm width[10]. The glomerular filtration apparatus, taken in its entirety, possesses an effective size cutoff of 10 nm, and is responsible for the rapid "renal clearance" of small nanoparticles. Many nanoparticle-based contrasting agents for *in vivo* imaging were designed to be smaller than this size cutoff[11, 12]. Prolonged residency of nanoparticles in the kidney has been shown to induce toxicity in the form of cell shrinkage, due to excessive nanoparticle uptake by renal cells [13, 14]. Closer examination of the renal corpuscle reveals the existence of another intriguing size cutoff that would affect the distribution pattern. Within the renal corpuscle, in the absence of GBM and podocytes, the sole dividing barrier between the mesangium (mesangial cells and extracellular matrix) and the glomerulus is the fenestrated endothelium. Sub-micron sized nanoparticles may feasibly diffuse and accumulate indefinitely in the mesangium

once they depart from the glomerulus through these pores. Here, we illustrate the size-dependent delivery of PEGylated gold nanoparticles to the kidney mesangium.

6.3 Results and Discussion

6.3.1 Assembly of Au_x-PEG_y NPs

Gold-based nanoparticles (AuNPs) were used here for the following reasons. They are compatible with multiple imaging methods. As rigid and non-decomposable objects, submicron-sized AuNPs larger than ca. 10 nm cannot escape the kidney by renal clearance. Unmodified gold nanoparticles of different sizes have zeta potentials (ζ) ranging from -19 mV to -28 mV. The measured ζ values are consistent with predictions due to classical electrokinetic theory (Fig. S2), and suggest that unmodified AuNPs of all sizes share the same surface charge density (σ). Next, to create particles of the same surface charge, we exploit the charge screening effect of poly (ethylene glycol) (PEG).

NP	Core (x)	PEG(y)	HD-water	HD-1xPBS	ZP	$t_{1/2}$	Ω	GTE	SI
	nm	Da	nm	nm	mV	h	%ID	%	
Au_5-PEG_{5000}	5.3 ± 0.5	5000	26.2 ± 0.3	24.8 ± 0.5	-8.44 ± 0.85	48.9	0.2± 0.1	0	0
Au_{20}-PEG_{5000}	21.6 ± 0.2	5000	43.1 ± 0.2	41.4 ± 0.2	-9.62 ± 0.62	31.8	1.2± 0.5	50	+
Au_{40}-PEG_{4000}	41.2 ± 0.2	4130	59.1 ± 0.3	58.6 ± 0.5	-12.34 ± 1.21	13.8	3.0 ± 0.6	80	++
Au_{50}-PEG_{5000}	51.4 ± 0.2	5000	78.8 ± 0.2	76.5 ± 0.4	-10.91 ± 1.33	13.7	4.6 ± 0.9	100	+++
Au_{60}-PEG_{7000}	58.1 ± 0.5	7359	94.6 ± 0.5	96.2 ± 0.2	-12.51 ± 1.24	11.4	1.9 ± 0.4	90	+++
Au_{80}-PEG_{10000}	76.5 ± 0.3	10000	127.6 ± 2.1	128.9 ± 0.9	-8.93 ± 0.67	8.7	0.7 ± 0.4	70	++
Au_{100}-PEG_{20000}	98.3 ± 0.3	20000	167.4 ± 9.6	164.3 ± 8.6	-9.76 ± 0.31	6.8	0.5 ± 0.3	60	+

Table 6.1: Physicochemical properties and *in vivo* characteristics of Au_x-PEG_y NPs. x = core diameter of AuNP; y = chain length of grafted PEG; HD = hydrodynamic diameter; ZP = ζ-potential in 1 mM KCl; $t_{1/2}$ = blood half-life; Ω = kidney bulk particle content; GTE = glomerular targeting efficiency; SI = staining index (an arbitrary score that ranks both the intensity and spread of the silver stain, whereby +++ and 0 are the maximum and minimum values, respectively). The table presents *in vitro* data as average ± s.d. from triplicates of experiments as well as *in vivo* data as average ± s.d. from three animals per particle type.

The larger the gold particles, the more negative the surface charge. Thus, to create as set of nanoparticles with variable size and relatively constant surface charge would require the engraftment of longer PEG chains onto the larger nanoparticles. This concept prompted us to use an assortment of PEGylated gold nanoparticles (Au_x-PEG_y NPs) possessing gold particles of different core diameters (x) and PEGs of different chain lengths (y) (Table 6.1). The engraftment procedure entailed the use of methoxy-PEG-thiol (mPEG-SH) molecules whose terminal thiol groups can react with the gold surface via the formation of gold-thiol covalent bonds. Careful choice of x and y gave rise to a near-constant ζ (roughly -10 mV) for Au_x-PEG_y NPs of various final hydrodynamic sizes (Table 6.1). In general, the engraftment of each additional 2000 molecular weight of PEG onto the gold surface translates to an increase in 5 nm of the hydrodynamic diameter of Au_x-PEG_y NPs. This approximate linearity between the PEG corona thickness and chain length is consistent with previous predictions for tethered polymer brushes on spherical interfaces without pronounced curvature[15] (Tables S1 and S2). All Au_x-PEG_y NPs showed stability in salt solution after 24 h, with hydrodynamic sizes in phosphate-buffered saline (PBS) roughly equal to those in water (Table 6.1).

6.3.2 Blood pharmacokinetics

Balb/c mice (N = 3) received single i.v. injections of each type of Au_x-PEG_y NPs at the same particle concentration. From each mouse, blood was withdrawn via the saphenous vein at various time points to evaluate for gold content using inductively coupled plasma mass spectrometry (ICP-MS). With extensive surface engraftment of PEG ($y \geq 4000$), all particles manifested extended blood circulation with a half-life ($t_{1/2}$)

that spans from 7 h to 38 h. Particle size and $t_{1/2}$ were inversely correlated (Fig. 6.1A; Table S3). The simultaneous increase in x and y led to reduction in $t_{1/2}$, indicating that size-dependent internal clearance, not colloidal stability conferred by PEGylation, played a dominant role in determining particle blood circulation.

6.3.3 Organ level distribution

Mice were then euthanized 24 h after injection to extract organs for detection of bulk gold content using ICP-MS. For all particle sizes, gold content of the six organs plus the blood samples collected at three time points summed up to ≥ 70 %ID, thus constituting a mass balance that accounts for the destinations of most injected Au_x-PEG_y NPs. Overall, the liver, spleen, and kidney were the main sites of particle accumulation, whereas the lung, pancreas, and heart showed negligible (< 0.5 %ID) particle retention (Fig. 6.1B; Table S4).

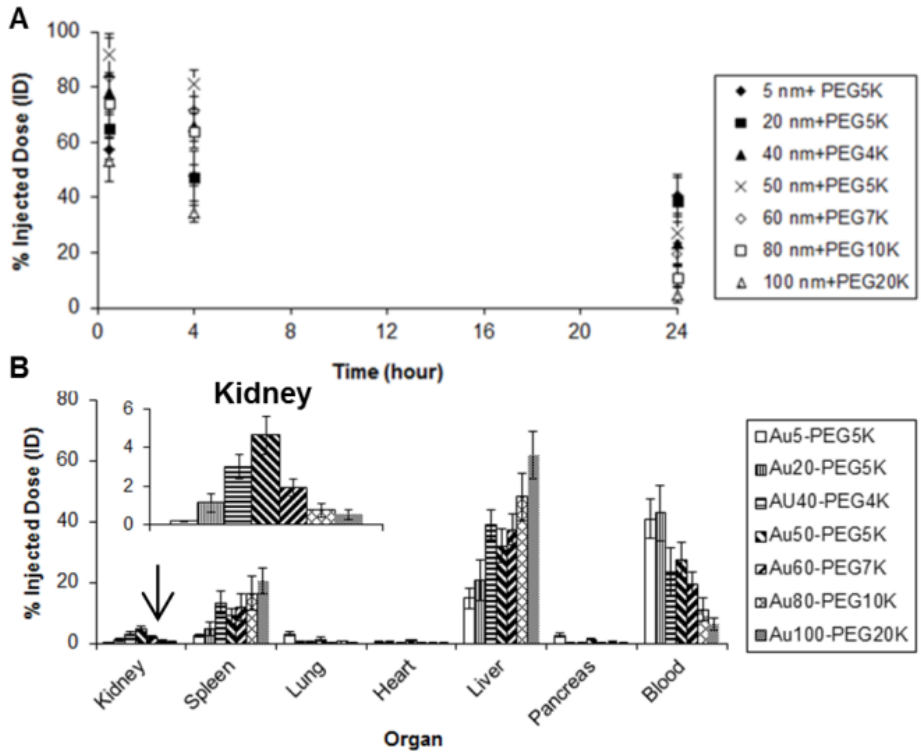

Figure 6.1: (A) Blood pharmacokinetics. All Au_x-PEG_y NPs demonstrated revealed extended circulation times in blood. (B) Organ level biodistribution. Bulk particle localization in the liver, spleen, and kidney was size dependent. Gold contents are normalized to % injected dose (% ID). For all particle sizes, the five named organs plus the blood compartment accounted for at least 70 %ID of the injected dose. Error bars indicate one s.d. from each Au_x-PEG_y NP class (N = 3).

At 24 h after dosing, the liver and spleen both showed a positive correlation between particle size and degree of particle uptake, in agreement with previous reports that the degree of particle phagocytosis by Kupffer cells and spleen macrophages is largely size-dependent (the larger the nanoparticles the greater the uptake in the reticuloendothelial system (RES))[16]. From Fig. 1, the blood nanoparticle content at 24 h appears to correlate with uptake by the RES (increased uptake by the RES is accompanied by lower content in the blood (leading to shorter circulation half-life)). Lastly and most importantly, the kidney revealed an unexpected size-dependent

nanoparticle retention pattern; there exists a particle size (Au_{50}-PEG_{5000}) at which renal accumulation was maximal.

6.3.4 Tissue level renal distribution

To understand the size-dependent accumulation in the kidney, we prepared "silver enhanced" kidney sections to reveal the distribution of Au_x-PEG_y NPs at the tissue level. Gold selectively catalyzes the reduction of silver ions and deposition of metallic silver, making nanosized objects embedded in kidney sections visible under light microscopy. Within the cortex, most particles resided either near resident phagocytes within peritubular capillaries, which intertwine the cortical tubules (proximal convoluted tubules and distal convoluted tubules), or inside renal corpuscles.

Particle accumulation at peritubular capillaries did not show clear correlation with size (Fig. S3). However, particle accumulation inside renal corpuscles reveals a strong function of size (Fig. 6.2). The smallest particles (Au_5-PEG_{5000}) were virtually undetectable in the renal corpuscles, but were found in peritubular capillaries (Fig. S4A). Au_{20}-PEG_{5000} nanoparticles merely accumulated in the renal corpuscles and rarely in the peritubular capillaries. Only ~50 % of the renal corpuscles contained Au_{20}-PEG_{5000} NPs, and the staining scattered all over the extracellular space (mesangium) outside the mesangial cells. The staining intensity appeared mild (Fig. 6.2A). For Au_{40}-PEG_{4000} NPs, particle staining within the renal corpuscles became more intense. ~80 % of the renal corpuscles were stained positive for particles and staining localized closer to mesangial cells (Fig. S4B).

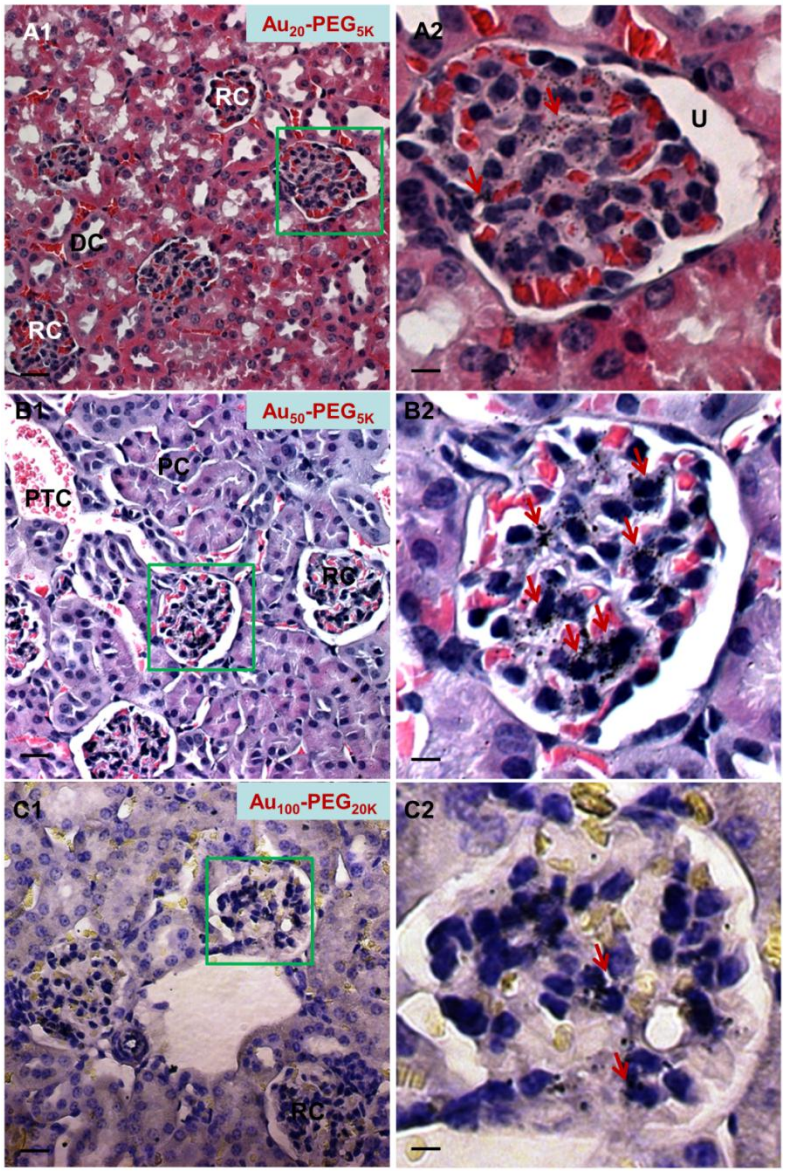

Figure 6.2: Tissue level distribution in renal corpuscles within the cortex. Representative light micrographs of "silver-enhanced" kidney sections demonstrate the extent of glomerular targeting by particles. Au_x-PEG_y NPs accumulated in a size-dependent manner. (A) Au_{20}-PEG_{5000} NPs were detectable in small quantities within renal corpuscles. (B) Au_{50}-PEG_{5000} NPs displayed most intense staining in the largest area of renal corpuscles among all particle sizes. Silver staining (dark specks indicated by red arrows) was present in every single renal corpuscle observed under the light microscope, resulting in complete glomerular targeting efficiency (GTE). (C) Au_{100}-PEG_{20000} NPs only accumulated in the renal corpuscles in minute amounts, presumably due to their inability to penetrate through the fenestrated glomerular endothelium. The right column (scale bar = 3 μm) illustrates the magnified renal corpuscle (green box) shown in the left column (scale bar = 10 μm). Legend: PTC = peritubular capillaries; RC = renal corpuscle; PC = proximal convoluted tubule; DC = distal convoluted tubule; U = urinary space.

Similar accumulation patterns were apparent for Au_{50}-PEG_{5000} NPs, except that 100 % of the renal corpuscles examined under the light microscope were stained positive for particles. Closer inspection of each renal corpuscle reveals the most intense silver adjacent to mesangial cells throughout the largest area fraction of the renal corpuscles among all particle sizes (Fig. 6.2B). Incidentally, this complete glomerular targeting efficiency (GTE) matches strongly with the maximal bulk particle content in the kidney observed for Au_{50}-PEG_{5000} NPs. The GTE for Au_{60}-PEG_{7000} NPs were also close to complete (~90 %), and such particles also elicited very intense silver staining near the mesangial cells (Fig. S4C).

Finally, Au_{80}-PEG_{10000} and Au_{100}-PEG_{20000} NPs gave a GTE of 60-70 %. Due to the catalytic nature of staining, larger Au_x-PEG_y NPs are expected to produce more silver deposition on their periphery. While silver staining can confirm the presence of Au_x-PEG_y NPs, the intensity alone does not provide the quantitation of actual particle content. Thus, besides the absolute magnitude of intensity, the spread of staining (areal fraction covered by silver) within renal corpuscles is also an important measure. We report in Table 1 what we denote as the "staining index (SI)", an arbitrary measure that accounts for both intensity and spread of staining. For the highest score (i.e., +++), particles (like Au_{50}-PEG_{5000} NPs) accumulated in the highest areal fraction of the renal corpuscles, and also at the highest intensity. Typically, the same particles can achieve a high GTE, meaning that they can be found frequently in different renal corpuscles throughout the cortex. For the lowest score (i.e., 0), particles (like Au_5-PEG_{5000} NPs) resided in limited areas of the renal corpuscles, and usually at undetectable densities. Typically, the same

particles can achieve a low GTE, implying their low occurrence in different renal corpuscles throughout the cortex.

For Au_{80}-PEG_{10000} NPs, silver staining was found in limited regions of renal corpuscles, despite their intense staining, yielding an SI score of ++. The largest particles, Au_{100}-PEG_{20000} NPs, barely occupied a sizeable areal fraction of the renal corpuscles, and showed very modest staining, leading to their score of + for the SI. Overall, the staining index of the largest nanoparticles (Au_{80}-PEG_{10000} and Au_{100}-PEG_{20000} NPs) was lower than that of Au_{50}-PEG_{5000} NPs. Taken together, Au_{80}-PEG_{10000} and Au_{100}-PEG_{20000} NPs target 60 -70% of the renal corpuscles, and within each corpuscle, a very limited area fraction and moderately intense staining.

The histological data collectively suggest a size-dependent localization of Au_x-PEG_y NPs within renal corpuscles in the kidney cortex. Because such particles do not have a constant PEG chain length, one may question whether the distribution of nanoparticles in renal corpuscles is PEG-dependent. To address this point, we investigated the tissue level in vivo distribution of Au_{80}-PEG_{5000} NPs (hydrodynamic size: 97.1 ± 1.9 nm; zeta potential: -16.77 ± 1.14 mV) in renal corpuscles, noting that such particles possess a very similar hydrodynamic size and zeta potential of Au_{60}-PEG_{7000} NPs. Histological analysis reveals accumulation of Au_{80}-PEG_{5000} NPs in the renal corpuscles in similar intensity and area as that of Au_{60}-PEG_{7000} NPs but not Au_{80}-PEG_{10000} NPs, supporting that the distribution of nanoparticles in renal corpuscles is size-dependent.

6.3.5 Cellular level renal distribution

Transmission electron microscopy (TEM) was used to determine the intracellular localization patterns of the nanoparticles residing in the renal cortex. In agreement with the histological data, particles of all sizes were either engulfed by resident phagocytes or remained as isolated entities in circulation inside pertitubular blood capillaries. Particle accumulation in peritubular blood capillaries was not size-dependent (Fig. S5). Retention of particles in renal corpuscles, however, is a strong function of size (Fig. 6.3). Smaller particles (Au_{20}-PEG_{5000} NPs) entered the mesangium within renal corpuscles in minute quantities (Fig. 6.3A). As size increases, Au_x-PEG_y NPs showed more association with mesangial cells. Au_{50}-PEG_{5000} NPs accumulated in multiple clusters either within mesangial cells or in the extracellular matrix outside mesangial cells. The clustering density was the most pronounced among all particle sizes, consistent with the histological data (Fig. 6.3B). Particles of similar sizes (Au_{40}-PEG_{4000} and Au_{60}-PEG_{7000} NPs) also demonstrated appreciable particle accumulation in the mesangium (Fig. S6). Larger particles (Au_{80}-PEG_{10000} NPs) only resided at the extracellular space in isolated amounts (Fig. 6.3C). The TEM data reveal a size at which particle association with mesangial cells was maximal (Au_{50}-PEG_{5000} NPs). This particular size maximized bulk kidney particle content and glomerular targeting. Thus, Au_{50}-PEG_{5000} represents the particle size that maximizes kidney targeting at the organ, tissue, and cellular (mesangium) levels.

The average pore diameter of the fenestrated glomerular endothelia is reported to be 80 – 100 nm, roughly the hydrodynamic size of Au_{50}-PEG_{5000} and Au_{60}-PEG_{7000} NPs. Particles larger than this size cutoff (Au_{80}-PEG_{10000} and Au_{100}-PEG_{20000} NPs) may experience steric hindrance when permeating through the pores to enter the mesangium

and access the mesangial cells. On the contrary, smaller particles (Au_{20}-PEG_{5000} and Au_{40}-PEG_{4000} NPs) are freely accessible to the mesangium. Thus, the "size exclusion" effect may account for the lower kidney particle content and weaker glomerular targeting of the largest particles. From TEM data, size-dependent uptake occurs solely at mesangial cells, which come in two types. The first type is contractile mesangial cells, which resemble vascular smooth muscle cells and fibroblasts that regulate surface area for glomerular filtration of fluids and mesangial volume.

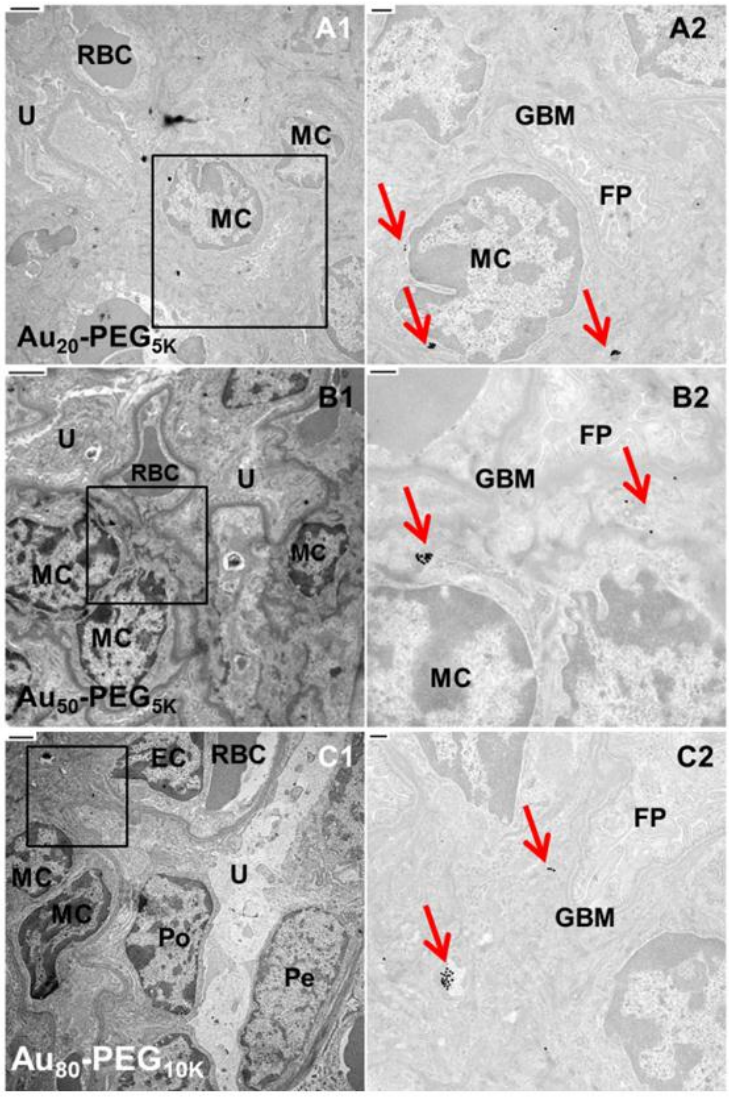

Figure 6.3: Cellular level distribution in renal corpuscles within the cortex. Representative transmission electron micrographs demonstrate particle accumulation in the mesangium (mesangial cells and extracellular matrix). The right column (scale bar = 500 nm) illustrates the magnified portion (black box) shown in the left column (scale bar = 2 μm). Red arrows in the right column indicate clusters of Au_x-PEG_y NPs. (A) A small portion of Au_{20}-PEG_{5000} NPs localized in mesangial cells within the renal corpuscles. (B) Au_{50}-PEG_{5000} NPs experienced the most prominent uptake by mesangial cells among all particle sizes. (C) Au_{80}-PEG_{10000} NPs deposited in the mesangium in drastically reduced amounts. Legend: RBC = red blood cell; Po = podocyte; FP = foot processes of podocytes; GBM = glomerular basement membrane; PC = proximal convoluted tubule; U = urinary space; EC = endothelial cell; MC = mesangial cell; Pe = parietal layer of Bowman's capsule.

The second type involves mononuclear resident phagocytes derived from the bone marrow[17]. From the ICP-MS data, particle uptake by spleen macrophages and hepatic Kupffer cells (both of bone marrow origin) increase with increasing particle size. Below the size cutoff in kidney, larger particles (Au_{50}-PEG_{5000} NPs) can penetrate through the endothelial pores, enter the mesangium, and accumulate inside mesangial cells (likely the phagocytic type mesangial cells). Smallest particles (Au_5-PEG_{5000} NPs) may transiently enter the mesangium, but may not favor prolonged retention due to lack of phagocytosis by mesangial cells. The absence of a cellular sink may lead to their low bulk particle content.

This work is the first study to systematically examine in the distribution of 10-150 nm nanoparticles in the kidney from a systemic injection. From measuring blood pharmacokinetics as well as distribution patterns at the organ, tissue, and cellular levels, the results suggest that there is an optimal size range (e.g., Au_{50}-PEG_{5000} NPs) that maximizes bulk particle uptake in the kidney, deposition of particles in renal corpuscles within the cortex, and uptake of particles by mesangial cells within renal corpuscles. When using nanoparticles as cancer therapeutics, accumulations in single digit %ID amounts in the tumor can lead to gene inhibition and tumor reduction[18]. Thus, the

accumulation of Au_x-PEG_y NPs (1 – 5 %ID) in the kidney at these amounts may be able to impart efficacy with kidney diseases. Moreover, the lack of significant localization (0.7 %ID) of larger particles (Au_{80}-PEG_{10000} NPs; ~ 130 nm in diameter) provides an *in vivo* calibration to the size of the glomerular endothelial pores. Most reported values for this pore size are derived from direct measurements of TEM and SEM images. Sample processing for microscopy involves repeated dehydration, and may lead to shrinkage of fine cellular features. The pore size reported here (130 nm) depicts the glomerular endothelial morphology at physiologically relevant conditions.

6.4 Materials and Methods

General Unless otherwise mentioned, all poly (ethylene glycol) (PEG) raw materials were purchased from Laysan Bio. All organic solvents were purchased from Sigma. Phosphate-buffered saline (PBS) comprises 150 mM NaCl and 50 mM sodium phosphate (pH = 7.4).

Synthesis of $mPEG_{4000}$-SH and $mPEG_{7000}$-SH 50 mg of amine-PEG_{3400}-thiol (14.7 μmol) was reacted with 40.4 mg of methoxy-PEG_{550}-(succinimidyl propionate) (73.5 μmol) in 50 μL of triethylamine (TEA) and 1.2 mL of anhydrous dichloromethane (DCM). The reaction proceeded at RT with stirring for 7 h. The crude mixture was dried under vacuuo, and dialyzed against deionized water using a 3 kDa Amicon MWCO membrane (Millipore). 15 mg of amine-PEG_{5000}-thiol (3.0 μmol) was reacted with 60 mg of methoxy-PEG_{2000}-(succinimidyl valerate) (30.0 μmol) in 50 μL of TEA and 1.2 mL of anhydrous DCM. The reaction proceeded at RT with stirring for 16 h. The crude mixture was dried under vacuuo, and dialyzed against deionized water using a 30 kDa Amicon MWCO membrane (Millipore). The correct fraction (7000 Da) was separated using

HPLC using a TSKgel G3000SW column (Tosoh Bioscience). Final molecular weights were confirmed by MALDI-TOF.

Assembly of PEGylated gold nanoparticles (Au_x-PEG_y NPs) Methoxy-PEG-thiol (purchased or synthesized above) of a certain molecular weight (y = 4000, 5000, 7000, 10000, and 20000), dissolved in deionized water was added to 3 mL of aqueous suspension of unconjugated gold colloids (Ted Pella) of a designated core size (x = 5 nm, 20 nm, 40 nm, 50 nm, 60 nm, 80 nm, and 100 nm) at an excess concentration of ~ 9 PEG strands per nm^2 of gold surface. e.g. To ensure complete coverage, PEGylation of 50 nm AuNPs required the addition of 10 μL of 1 mM $mPEG_{5000}$-thiol (in deionized water) to 0.5 mL of aqueous suspension of 2.25×10^{10} particles. All PEGylation reactions proceeded at room temperature for 2 h with constant stirring. To remove any unbound methoxy-PEG-thiol, the reaction mixture was dialyzed against deionized water using a 30 kDa or 100 kDa Amicon MWCO membrane (Millipore) for three times.

Physicochemical characterization of Au_x-PEG_y NPs Hydrodynamic diameter (HD) and ζ-potential (ZP) of Au_x-PEG_y NPs were measured using ZetaPals (Brookhaven). For HD measurements, the particle pellet was re-suspended in 1.2 mL of deionized water or PBS. Reported HDs are average values from 3 runs of 3 minutes each. For ZP analysis, the pellet was re-suspended in 1.4 mL of 1 mM KCl. Reported ZPs are average values from 10 runs each with a target residual of 0.012 measured at a conductance of 320 ± 32 μS.

Animal experiments For each type of Au_x-PEG_y NPs, three 9-week, female Balb/c mice (Jackson Laboratory) received i.v. injections of particles via the tail vein at a concentration of 4.5×10^{11} particles per mL, formulated in 120 μL of filtered 5 % glucose

in deionized water (D5W). At three consecutive time points after injection (30 min, 4 h, and 24 h), 30 μL of mouse blood was drawn from each mouse via its saphenous vein using Microvette CB 300 Capillary Blood Collection Tube with EDTA (Sarstedt). Blood samples were stored at 4 ºC for future use. After 24 h, mice were euthanized by CO_2 overdose for the collection of the liver, kidney, lung, heart, spleen, and pancreas. All organs were fixed in 4 % paraformaldehyde (PFA) in PBS for 3 days.

ICP-MS Homogenized organs were oxidized in 0.5 mL of acid mixture (70 % HNO_3 and 35 % HCl at a 3:1 volume ratio) in a microwave until they fully dissolved. After adding 20.5 mL of deionized water, the sample was centrifuged at 3200 x g for 15 min to remove cell debris, leaving the supernatant for gold content analysis using HP 4500 ICP-MS (Agilent). Nebulization occurred with a flow of 1.3 L/min of argon using a Babbington type nebulizer in a pyrex Scott-type spray chamber. The argon plasma power was 1200 W with a flow of 15 L/min and an auxiliary flow of 1.1 L/min. A calibration curve against known concentrations of Au_x-PEG_y NPs of all sizes was used to measure the gold content, using 2.5 % HNO_3 and 0.42 % HCl as the blank solvent and tissues from uninjected Balb/c mice to account for background organ gold content. Reported values are expressed as % of injected dose (%ID). Error bars indicate one s.d. in each mouse group (N=3). Each mouse weighed ~ 20 g at the time of experiment, and had a total blood volume of 1.6 mL (average mouse volume is 77-80 μL/g).

Histology with silver enhancement PFA-fixed organs were dehydrated and embedded in molten paraffin to generate sections of 4 μm thick. Sections were deparrafinized with xylene and rehydrated with a reducing ethanol gradient and rinsed with deionized water extensively, dried, and stained for Au_x-PEG_y NPs using the Silver Enhancement Kit for

Light and Electron Microscopy (Ted Pella) in the dark for 20 min at RT. After rinsing with running tap water for 2 min to remove excess silver, sections were counter-stained with Gill's 3 hematoxylin and 1 % eosin (in 95 % ethanol) for 40 s each, and then mounted with Permount for viewing under an Axioplan 2 light microscope (Zeiss) with a 40x objective. To estimate the glomerular targeting efficiency (GTE) of particles to renal corpuscles from light micrographs, 300 renal corpuscles, selected at random positions from 10-15 kidney sections per injected mouse, were inspected visually for the presence of silver stains. For the staining index (SI), both the staining intensity and spread of these 300 renal corpuscles were scored.

TEM Tissue blocks (~1 mm^3) were fixed in 2.5 % glutaraldehyde (in 0.1 M sodium cacodylate, pH = 7.4) for 2 h, stained by 1 % OsO_4 at 4 °C for 2 h, and 0.9 % OsO_4 and 0.3 % $K_3Fe(CN)_6$ at 4 °C for 2 h. Gradual dehydration with ethanol and propylene oxide enabled tissue embedding in Epon 812 resins (Electron Microscopy Sciences). 80 nm thick sections were deposited on carbon and formvar-coated, 200-mesh, nickel grids (EMS) and stained with 3 % uranyl acetate and Reynolds lead citrate for visualization under a 120 kV BioTwin CM120 TEM (Philips).

6.5 Acknowledgments

We thank Debbie Guerrero and Siva Wu from the House Ear Institute for advice in histology. This work was supported by the National Cancer Institute Grant CA 119347 and the NIH Grant R01 EB004657.

6.6 References:

1. Davis, M.E., Chen, Z. and Shin, D.M. Nanoparticle therapeutics: An emerging treatment modality for cancer. *Nat. Rev. Drug Discov.* **7**, 771-782 (2008).

2. Peer, D. et al. Nanocarriers as an emerging platform for cancer therapy. *Nat. Nanotechnol.* **2**, 751-760 (2007).

3. Davis, M.E. The first targeted delivery of siRNA in humans via a self-assembling, cyclodextrin polymer-based nanoparticle: From concept to clinic. *Mol. Pharm.* **6**, 659-668 (2009).

4. Zimmerman, T.S. et al. RNAi-mediated gene silencing in non-human primates. *Nature* **441**, 111-114 (2006).

5. Choi, H.S. et al. Renal clearance of quantum dots. *Nat. Biotechnol.* **25**, 1165-1170 (2007).

6. Choi, H.S. et al. Tissue- and organ-selective biodistribution of NIR fluorescent quantum dots. *Nano Lett.* **9**, 2354–2359 (2009).

7. Luft, F.C. et al. Effects of moxalactam and cefotaxime on rabbit renal tissue. *Antimicrob. Agents Chemother.* **21**, 830-835 (1982).

8. Kanwar, Y.S., and Farquhar, M.G. Presence of heparan sulfate in the glomerular basement membrane. *Proc. Natl. Acad. Sci. USA.* **76**, 1303-1307 (1979).

9. Ogawa, S. et al. High-resolution ultrastructural comparison of renal glomerular and tubular basement membranes. *Am. J. Nephrol.* **19**, 686-693 (1999).

10. Lahdenkari, A.-T. et al. Podocytes are firmly attached to glomerular basement membrane in kidneys with heavy proteinuria. *J. Am. Soc. Nephrol.* **15**, 2611-2618 (2004).

11. Tan, M. et al. An effective targeted nanoglobular manganese(II) chelate conjugate for magnetic resonance molecular imaging of tumor extracellular matrix. *Mol. Pharm.* **7**, 936-943 (2010).

12. Schipper, M.L. et al. Particle size, surface coating, and PEGylation influence the biodistribution of quantum dots in living mice. *Small.* **5**, 126-134 (2009).

13. L'Azou, B. et al. In vitro effects of nanoparticles on renal cells. *Part. Fibre. Toxicol.* **5**, 1-14 (2008).

14. Chen, Z. et al. Acute toxicological effects of copper nanoparticles in vivo *Toxicol. Lett.* **163**, 109-120 (2006).

15. Dan, N. and Tirrell, M. Polymers tethered to curved interfaces. A self-consistent-field analysis. *Macromolecules* **25**, 2890-2895 (1992).

16. Sadauskas, E. et al. Kupffer cells are central in the removal of nanoparticles from the organism. *Part. Fibre. Toxicol.* **4**, 1-7 (2007).

17. Schreiner, G.F. The mesangial phagocyte and its regulation of contractile cell biology. *J. Am. Soc. Nephrol.* **2**, S74-S82 (1992).

18. Bartlett, D.W, et al. Impact of tumor-specific targeting on the biodistribution and efficacy of siRNA nanoparticles measured by multimodality in vivo imaging *Proc. Natl. Acad. Sci. USA.* **104**, 15549-15554 (2007).

6.7 Supplemental information for Chapter 6

Appendix I: Structure of the renal corpuscle and mesangium

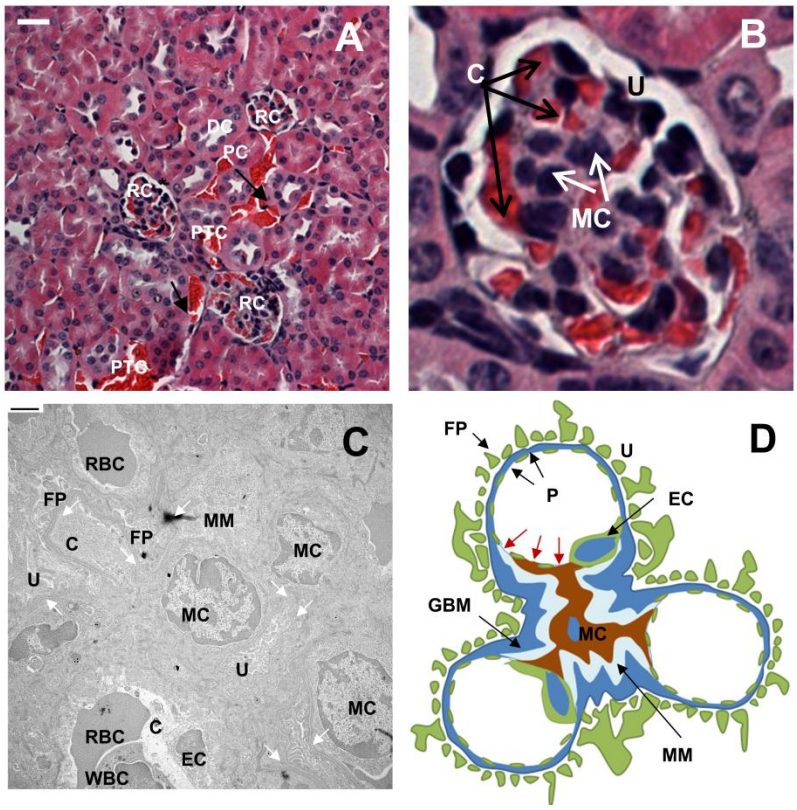

Figure S1: Illustrations of the renal corpuscle and the mesangium. (A) This light micrograph reveals the typical morphology of the renal cortex. Scale bar = 10 µm. (B) This close-up reveals the inner structure of a renal corpuscle. (C) This transmission electron micrograph shows the internal structures of the renal corpuscles. Scale bar = 10 µm. (D) This schematic diagram shows the relationship between mesangial cells and glomerular capillaries (modified from Sakai and Kriz). Legend: renal corpuscles (RC), distal convoluted tubules (DC), proximal convoluted tubules (PC), peritubular capillaries (PTC), red blood cells (RBC), leukocytes (WBC), mesangial matrix (MM), mesangial cells (MC), foot processes of podocytes (FP), urinary space (U), glomerular capillary space (C), glomerular basement membrane (GBM), and pores (P) of the fenestrated endothelium of glomerular capillaries. In panel C, white arrows trace the glomerular

basement membrane. In panel D, red arrows indicate the pores between the glomerular capillaries and mesangium. If smaller than the pore width, particles can enter the mesangium from the glomerular capillaries in the absence of GBM and podocytes as structural barriers.

Reference:

Sakai, T. and Kriz, W. The structural relationship between mesangial cells and basement membrane of the renal glomerulus. *Anat. Embryol.* **176**, 373-386 (1987).

Appendix II: Surface charge of unmodified gold nanoparticles

For any charged sphere of radius R in an electrolyte, its zeta potential (ζ) is given as follows: -

$$\zeta = \frac{\sigma}{\varepsilon}\frac{R}{1+\kappa R}$$

Above σ, ε, and κ^{-1} are the surface charge density, permittivity constant, and Debye length.

From this equation, ζ of charged gold spheres becomes more negative as R increases, consistent with data shown in Table I. For typical ζ measurements in 1 mM KCl at room temperature, κ^{-1} is roughly 9.8 nm, a constant independent of R. By curve fitting of the measured ζ as a function of R, the dimensionless charge density (σ/ε) is approximately 3. This means that unmodified gold surface of all sizes have a constant surface charge density.

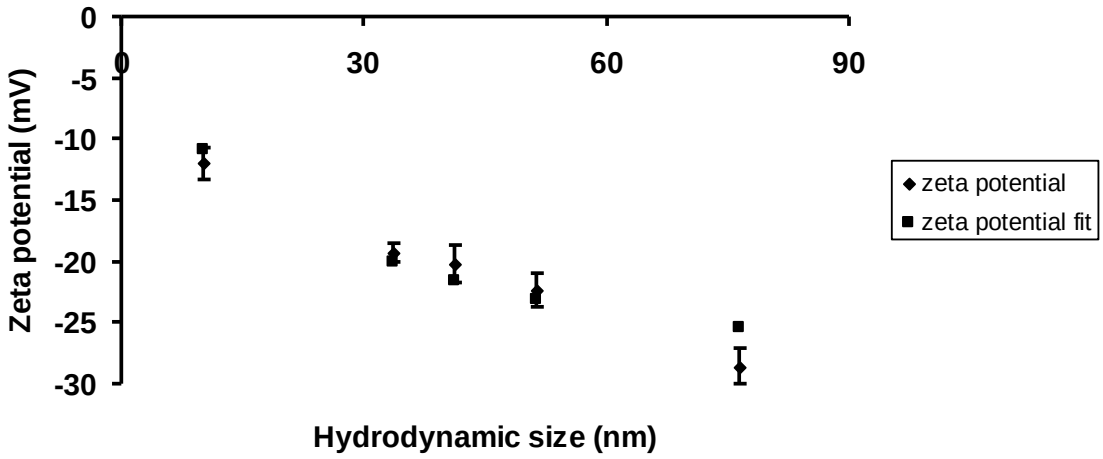

Figure S2: DLS measurements of ζ of unmodified gold nanoparticle matches reasonably with estimates based on Debye-Huckel electrokinetic theory.

Appendix III: PEG corona thickness of PEGylated gold nanoparticles

Based on a previous work by Takae et al, each 20 nm AuNP can anchor 520 PEG chains of 6000 Da each. This translates to a PEG grafting density (Σ) of 0.4 PEG/nm^2.

The Kuhn length (b) of PEG is 0.7 nm. Thus the dimensionless PEG grafting density (σ*) is: -

$$\sigma^* = b^2\Sigma = (0.7 \text{ nm})^2 \ (0.4 \text{ PEG/nm}^2) = 0.196$$

Hill et al evaluated the grafting density of oligonucleotides on submicron sized AuNPs (10-100 nm). If the oligonucleotide density data due to size curvature is applicable to the study of PEG grafting, then a rough estimate of PEG grafting density of Au_x-PEG_y NPs is provided below: -

Core size (x) (nm)	Hil et al oligo (#oligo/nm^2)	PEG (#PEG/nm^2)	PEG - σ*	
20	1.40E+13	4.00E-01	0.196	Takae et al
40	8.50E+12	2.43E-01	0.119	
50	8.10E+12	2.31E-01	0.1134	
60	7.80E+12	2.23E-01	0.1092	
80	7.10E+12	2.03E-01	0.0994	

Table S1: Rough estimates of PEG grafting density on AuNPs of different sizes.

σ* takes on the value of 0.1-0.2 (for AuNPs above the size of 20 nm), which represents a very high grafting density according to Wijman et al. Physically, how high is this density?

According to scaling analysis by deGennes on grafted polymers, the brush conformation appears if $\sigma^* > N^{-6/5}$, where N is the number of Kuhn polymer segments. How can we estimate N?

Take Au_{50}-PEG_{5000} as an example. The MW of each PEG unit is 44 g/mol. The two C-O bonds (each 0.145 nm) and C-C bond (0.15 nm) add up to 0.44 nm. The contour length (R_{max} = Nb) of a fully stretched PEG_{5000} coil is 5000/44*0.44 nm = 50 nm. If b = 0.7 nm, then N = 71.4. Clearly, σ* is greater than $N^{-6/5}$. Hence, PEG polymer chains fill are

overlapping with each other, with their blobs acting as hard spheres and cover the gold surface densely. The $\sigma^* > N^{-6/5}$ result is also apparent for all other Au_x-PEG_y NPs.

Alternatively, one can calculate the footprint (D) of each PEG chains (separation distance between each adjacent PEG chain) on the gold surface, knowing that $4\pi D^2 = \Sigma$. For Au_{50}-PEG_{5000}, D = 2.29 nm, which is shorter than the Flory radius of PEG_{5000} in a good solvent ($R_F = bN^{3/5}$ = 9.07 nm). Because $R_F > D$ result is also apparent for all other Au_x-PEG_y NPs, the grafted PEG chains all take the "brush conformation" on the gold surface for all particle sizes.

MW (g/mol)	4000	5000	7000	10000
R_max (nm)	40	50	70	100
N	57.14286	71.42857	100	142.8571
N^(-6/5)	0.007792	0.005961	0.003981	0.002595
R_F (nm)	7.930037	9.066115	11.09425	13.74166
D (nm)	2.289032	2.347735	2.389476	2.504419
x (nm)	40	50	60	80
x/2b	28.57143	35.71429	42.85714	57.14286

Table S2: Polymer parameters of grafted PEG on AuNPs. MW: molecular weight; $R_{max} = bN$: contour length; N: degree of polymerization (no. of Kuhn segments); $R_F = bN^{3/5}$: Flory radius in a good solvent; D: separation distance between PEG monomers; x = core size of AuNP.

On a planar surface, the brush height of tethered PEG corona (H) should scale linearly with N (Alexander, de Gennes). Yet on a spherical interface, $H \sim N^{3/5}$ because the chains extended away from the surface should be more diffuse compared to those densely packed chains near the surface, thus shortening H. Yet, DLS measurements revealed H ~ N, not $N^{3/5}$, suggesting that the curvature effect on H is not eminent.

For $\sigma^* \sim 0.1$ and using self-consistence-field simulations, Dan et al showed that the curvature effect becomes less important, and that H will approach the planar limit of (H ~ N) when x/2b >100. For Au_x-PEG_y NPs at hand, their values of x/2b mainly lie in the range of 28-57, so $H \sim N^{0.9}$ according to simulation results by Dan et al. This explains the observed "linearity" between H and N even on spherical particles.

Appendix IV: Tissue level accumulation of PEG-AuNPs in peritubular capillaries

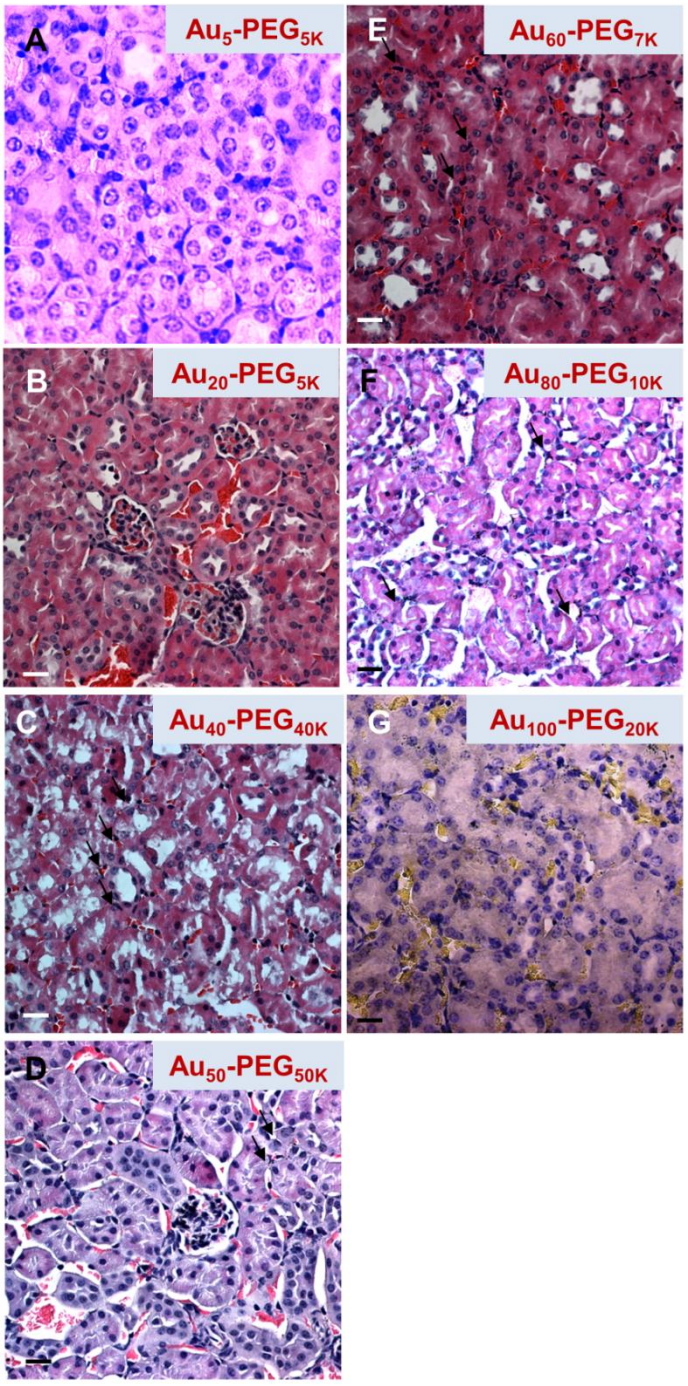

Figure S3: The deposition of PEGylated gold nanoparticles in the renal cortex excluding renal corpuscles is not a function of particle size. Typically, particles are located adjacent to peritubular capillaries or in the connective tissue space between adjacent convoluted tubule cells.

Appendix V: Tissue level accumulation of PEG-AuNPs in renal corpuscles

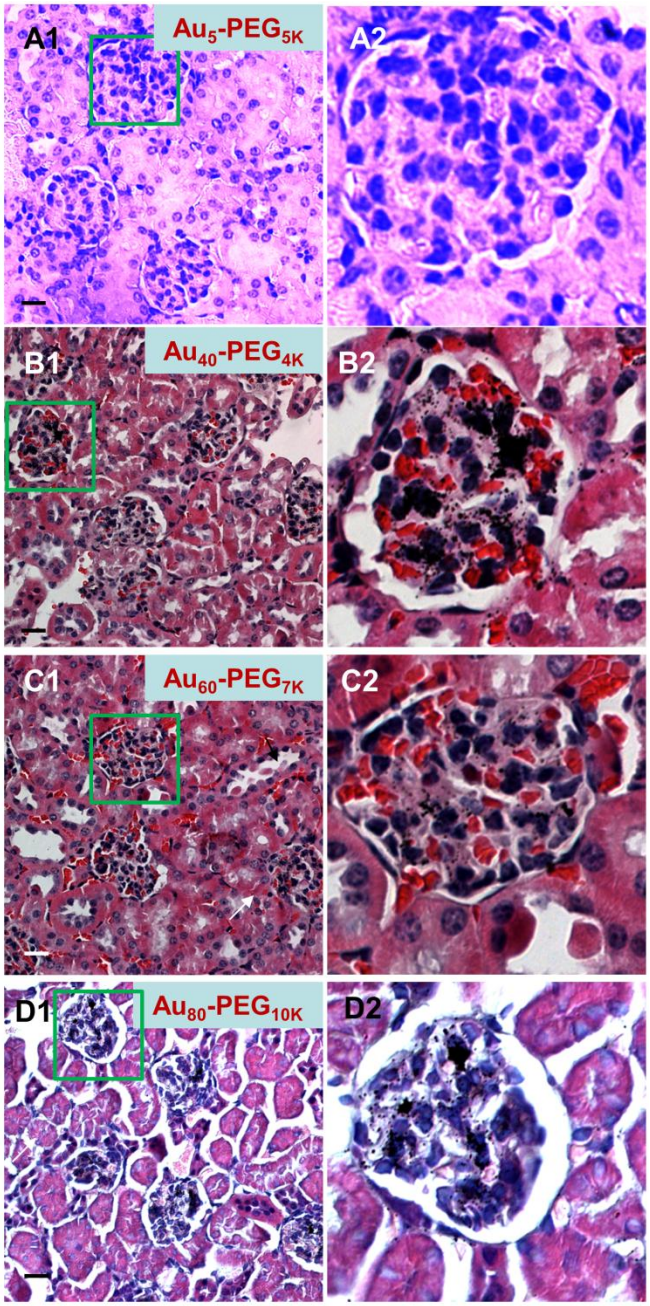

Figure S4: The deposition of PEGylated gold nanoparticles in renal corpuscles is a strong function of particle size. The right column illustrates the magnified portion (green box) of the left column. (A) Smallest particles (Au_5-PEG_{5K}) showed undetectable staining. (B, C) Middle-sized particles (Au_{40}-PEG_{4K} and Au_{60}-PEG_{7K}) showed most intense silver staining near the mesangial cells throughout the entire renal corpuscle. (D) Larger particles (Au_{80}-PEG_{10K}) showed intense staining, but at a reduced areal fraction of the renal corpuscles. Scale bar = 10 µm.

Appendix VI: Cellular level accumulation of PEG-AuNPs in peritubular capillaries

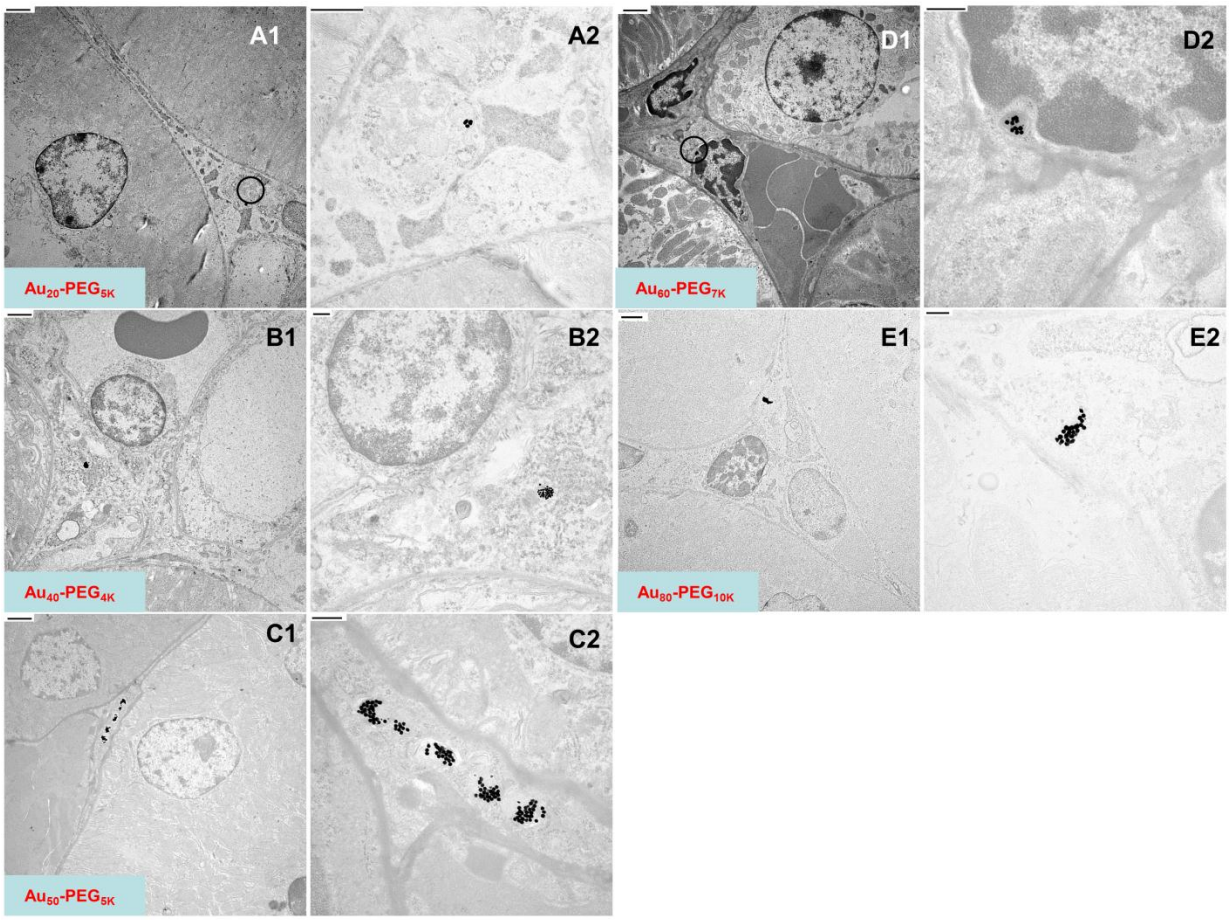

Figure S5: The deposition of Au_x-PEG_y NPs in the renal cortex excluding renal corpuscles is not a function of particle size. Particles are located adjacent to peritubular capillaries or in the connective tissue space between convoluted tubule cells. Images shown in the 2nd column (scale bar = 500 nm) are magnified versions of those shown in the 1st column (scale bar = 2 μm).

Appendix VII: Cellular level accumulation of PEG-AuNPs in renal corpuscles

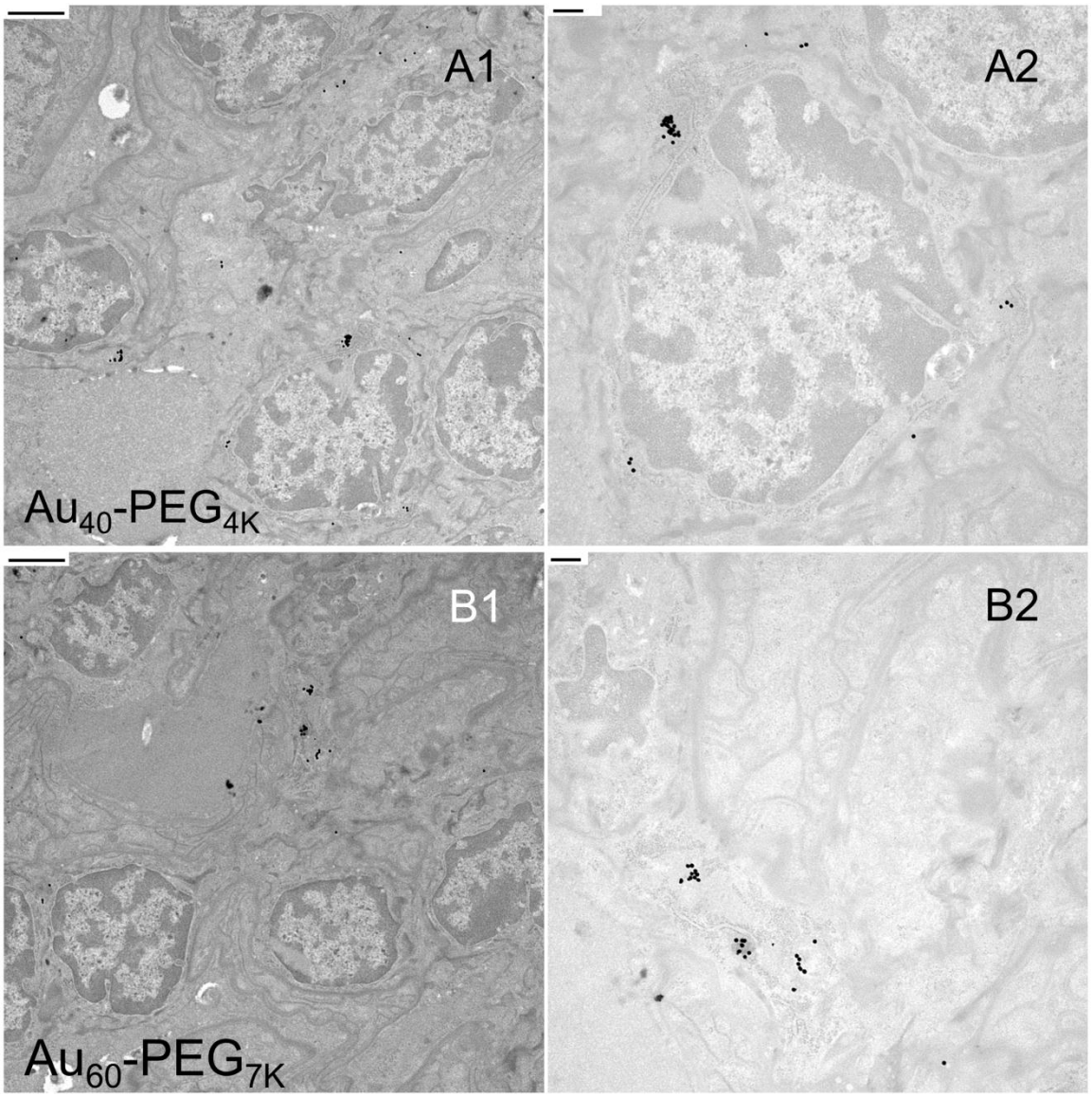

Figure S6: The deposition of Au_x-PEG_y NPs in the renal corpuscles is size-dependent. Middle-sized particles (Au_{40}-PEG_{4K} and Au_{60}-PEG_{7K}) accumulated within mesangial cells or in the mesangium as individual entities at the maximal amount. Images shown in the 2nd column (scale bar = 500 nm) are magnified versions of those shown in the 1st column (scale bar = 2 μm).

Chapter 7: Polycation-siRNA nanoparticles can disassemble at the kidney glomerular basement membrane[3]

7.1 Abstract:

Despite being engineered to avoid renal clearance, many cationic polymer (polycation)-based siRNA nanoparticles that are used for systemic delivery are rapidly eliminated from the circulation. Here, we show that a component of the renal filtration barrier – the glomerular basement membrane (GBM) – can disassemble cationic cyclodextrin-containing polymer (CDP)-based siRNA nanoparticles and thereby facilitate their rapid elimination from circulation. Using confocal and electron microscopies, positron emission tomography (PET) and compartment modeling, we demonstrate that siRNA nanoparticles, but not free siRNA, accumulate and disassemble in the GBM. We also confirm that the siRNA nanoparticles do not disassemble in blood plasma *in vitro* and *in vivo*. This hitherto unrealized clearance mechanism may affect any nanoparticles that assemble primarily by electrostatic interactions between cationic delivery components and anionic nucleic acids (or other therapeutic entities).

7.2 Introduction:

A major challenge with the use of small interfering RNA (siRNA) in mammals is their delivery to intracellular locations in specific tissues(1). The two most investigated approaches to siRNA delivery involve the combination of siRNA with cationic lipids (lipoplexes, liposomes, micelles) or cationic polymers (polyplexes)(2). Polymer-based siRNA delivery vehicles can be tuned to be non-immunogenic, non-oncogenic, non-toxic and targeted(3). A targeted nanoparticle formulation of siRNA (not chemically modified)

[3] Reproduced with permission from: Jonathan E. Zuckerman, Chung Hang J. Choi, Han Han, Mark E. Davis, "Polycation-siRNA nanoparticles can disassemble at the kidney glomerular basement membrane" *Proc. Nat. Acad. Sci. USA* **109**, 3137 (2012).

with a cationic, cyclodextrin-containing polymer (CDP)-based delivery vehicle (clinical version denoted CALAA-01) was shown to accumulate in human tumors and deliver functional siRNA from a systemic, intravenous (i.v.) infusion (4). This first-in-human study demonstrated the clinical potential for cationic polymer-based siRNA delivery systems.

Like most cationic polymer based siRNA delivery systems (5-9), the siRNA/CDP nanoparticle is rapidly eliminated from circulation (shown in mice, monkeys and humans) (10-12). In fact, polymer complexation often does not extend the circulation time of siRNA. The rapid clearance of these siRNA nanoparticles is puzzling because they are engineered to be above the size cutoff for single-pass clearance via renal filtration (13). In understanding the mechanism behind the rapid clearance of this type of cancer therapeutic, we can efficiently seek ways to increase their circulation time and thus enhance their anticancer efficacy (3).

We hypothesize that the paradoxical renal clearance of polycation-nucleic acid nanoparticles results from their binding and disassembly by components of the renal filtration barrier. Three key properties of such nanoparticles (diameters between10 and 100nm, positive zeta potentials, and electrostatically driven self-assembly) make them susceptible to this mechanism of clearance.

The renal filtration barrier, located within the glomerulus of the nephron consists of three layers that must be traversed to enter the urinary space. These three layers are the glomerular endothelial fenestrations (ca.100 nm)(14), the glomerular basement membrane (GBM), a 300 nm thick connective tissue membrane rich in heparan sulfate(15) (pore size of 3 nm)(16) and the podocyte filtration slits (ca. 32 nm)(17). The

renal filtration barrier, in its entirety, possesses an effective size cutoff of ca. 10 nm, and is known to facilitate the rapid renal clearance of small molecules drugs and free siRNA.

Gold nanoparticles of up to 130 nm in size can cross the fenestrated glomerular endothelium but not the GBM(14). Therefore, we believe that siRNA nanoparticles of diameters of ca. 100 nm in circulation can access the GBM and preferentially deposit there due to their positive surface charge. Once in the GBM, they are disassembled by the abundant negatively charged proteoglycans (e.g., heparan sulfate) present that structurally mimic the polyanionic charge of nucleic acids. After disassembly, their components are small enough to cross into the urinary space.

To test this hypothesis, we first demonstrate that siRNA nanoparticles do not disassemble in circulation. We then examine the distribution of siRNA nanoparticles in the kidney via microscopy methods and confirm that siRNA nanoparticle deposit and disassemble in the GBM. Finally, we analyze the kinetics of kidney transit by positron emission tomography (PET) studies and model the dynamic PET data using insights derived from our kidney imaging experiments. The combination of these studies provides conclusive evidence to support our hypothesis.

7.3 Results:

7.3.1 Nanoparticle components remain assembled *in vivo* and will assemble when administered separately *in vivo*.

The siRNA and polymer components of the nanoparticle (CDP/AD-PEG) assemble via electrostatic interactions into spherical 60-100 nm nanoparticles (Figs. 7.1a-c) with an average zeta potential of 10.6 ± 1.5 mV.

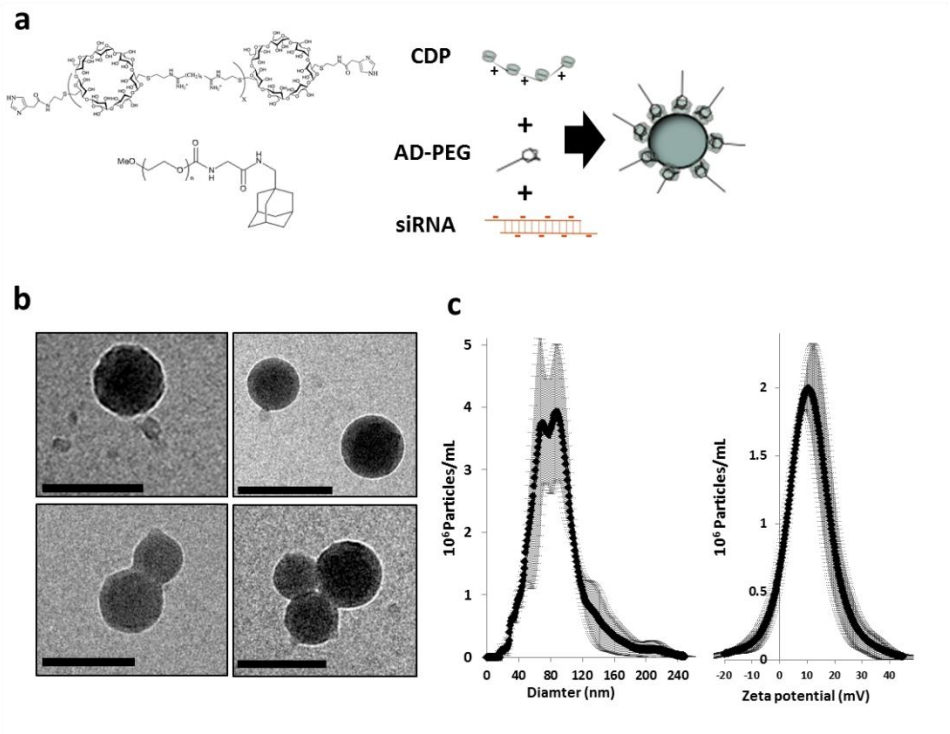

Figure 7.1: Characterization of siRNA nanoparticles. (a) siRNA nanoparticles assemble due to electrostatic interactions between the cationic cyclodextrin containing polymer and the anionic siRNA. PEG provides steric stabilization and is bound to the particles via inclusion complex formation between its terminal adamantane (AD) modification and the cyclodextrin cup of the CDP. (b) Cryo-TEM images of siRNA nanoparticles revealed sub-100 nm spherical objects, scale bars = 100nm. (c) Nanoparticle tracking analysis of siRNA nanoparticle sizes and zeta potentials (Error bars represent standard deviation of 3 measurements, n=3)

Gel mobility shift assays were used to determine siRNA/CDP association in plasma (Fig. 7.2a). In these assays the siRNA component of the nanoparticle is detected via ethidium bromide staining. Free siRNA present in a sample will migrate down the gel towards the anode. siRNA assembled within nanoparticles remains in the well or moves up towards the cathode. When incubated with 95% mouse plasma the free siRNA band is broadened and migrates slower compared to siRNA in water, likely due to general electrostatic interaction with positive plasma components. siRNA has been shown to have a half-life of 1.2 hours in 90% mouse plasma(18); therefore, all analysis

from animal plasma were performed within 1 hour of plasma collection to ensure that free siRNA present in the plasma sample could be visualized.

We first determined if siRNA is released from the nanoparticles in circulation. Gel mobility shift assays on plasma from mice receiving injections of siRNA nanoparticles demonstrate that all of the siRNA in the samples was present in the well or migrated up towards the cathode with no evidence of free siRNA traveling towards the anode. These data suggest that the siRNA component of the nanoparticles is not displaced from the polymeric delivery components *in vivo*.

Furthermore, we determined if the individual components of the nanoparticles, siRNA and polymers, could assemble *in vivo*. In these experiments, free siRNA was administered then one minute later CDP/AD-PEG polymers were added. Plasma was collected one minute later. Plasma from mice receiving these sequential injections of individual nanoparticle components was analyzed. All of the siRNA in these samples remained in the well or traveled up towards the cathode, indicating its association with polymers. These results demonstrate that not only is the siRNA component of the nanoparticle not displaced from the polymer components, but that siRNA and polymer components will self-assemble in circulation.

Next, we confirmed that injection of free siRNA or polymer components alone could not result in nanoparticle like bands on the gel. Analysis of plasma from animals receiving only siRNA demonstrated siRNA migrating down the gel towards the anode, confirming that free siRNA can be detected by the assay. Polymer components injected alone yielded no bands on the gel (except the non-specific background band always present in plasma samples). These data confirm that the gel bands present in nanoparticle

samples do not result from the association of siRNA or polymers with plasma components.

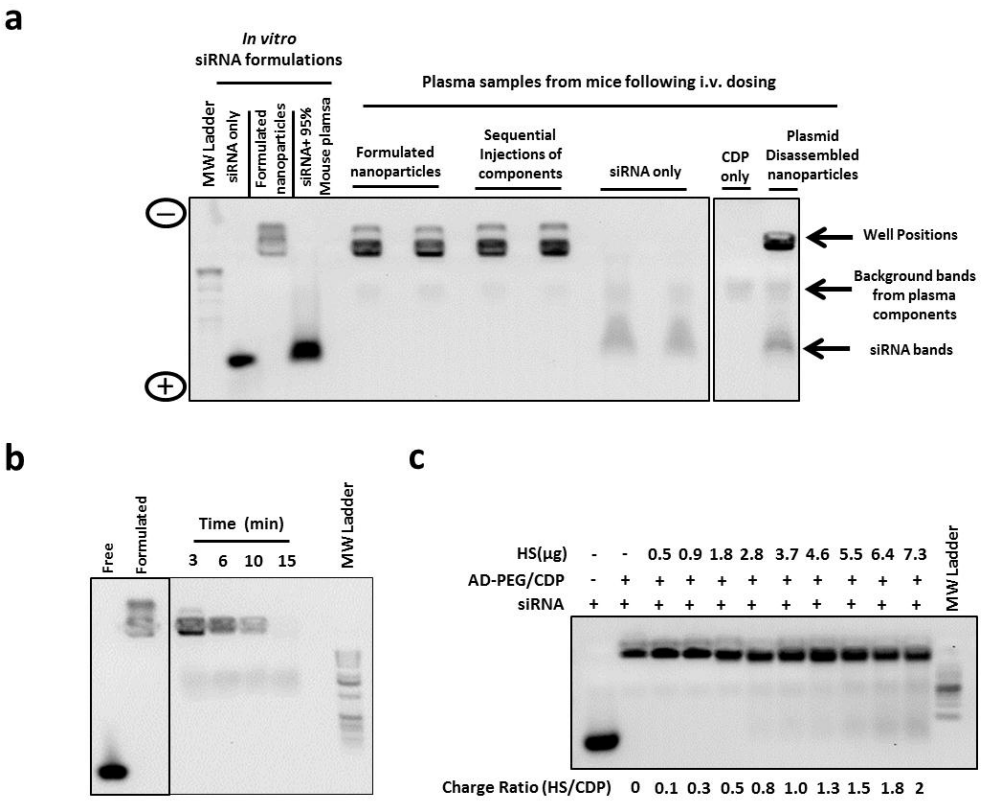

Figure 7.2: Nanoparticle components remained associated and assembled *in vivo* but were disassembled by heparan sulfate. (a-c) Gel mobility shift assays demonstrated siRNA/CDP association. Free siRNA will migrate down the gel towards the anode, whereas siRNA/CDP nanoparticles remain in the wells or migrated towards the cathode. (a) *In vitro* siRNA formulations were formulated as indicated (formulated nanoparticles = siRNA+AD-PEG/CDP in H_2O) and incubated at 37°C for 15 min. Plasma samples: Formulated nanoparticles = plasma from animals 3 min after injection of formulated siRNA+AD-PEG/CDP nanoparticles. Sequential injection of components = plasma from animals where free siRNA was injected and then 1 minute later CDP/AD-PEG were injected, plasma collected at 3 min after the first injection. siRNA or CDP only = plasma collected from animals 3 min after receiving injection of only siRNA or AD-PEG/CDP. Disassembled nanoparticles = plasma from animals where formulated siRNA nanoparticles were injected and then 1 min later an excess of ~6kb plasmid DNA was injected, plasma was collected at 3 min after the first injection. All duplicate lanes are from independent animals. (b) Plasma samples from animals receiving formulated siRNA nanoparticles taken at the indicated time point after injection. (c) Gel mobility shift assays of siRNA nanoparticles in increasing amounts of heparan sulfate in 50% mouse plasma. All plasma containing samples have a band of background staining that migrates at ~5kb as indicated in the figure.

Finally, we induced nanoparticle disassembly *in vivo* to demonstrate that disassembled nanoparticles can be visualized via gel mobility shift assay. *In vitro,* we demonstrated that plasmid DNA could rapidly displaced siRNA from the nanoparticles by competitively binding to the positively charged polymer nanoparticle components (Supplementary Fig. S1). We hypothesized that injection of plasmid DNA one minute after siRNA nanoparticle administration would induce nanoparticle disassembly *in vivo* and that free siRNA could be detected in these samples. Analysis of plasma from mice receiving sequential injections of siRNA nanoparticles and plasmid DNA confirmed our hypothesis. In these samples, the siRNA component of the nanoparticle was found to migrate down the gel towards the anode. These data demonstrate that disassembled nanoparticles can be detected via the gel mobility shift assays. Furthermore, they support our previous conclusion that siRNA is not displaced from the polymer *in vivo* by plasma components. Additionally, these data suggest that CDP can also self-assemble with plasmid DNA *in vivo*.

Gel mobility shift analysis on plasma samples taken at multiple time points after dosing of siRNA nanoparticles revealed siRNA remaining in the well for all time points (Fig. 2b). These data indicate that siRNA nanoparticles remain assembled over the entire circulation time of the particle.

Additionally, Oney et al. have demonstrated that upon injection, the CDP can bind and completely neutralize the anticoagulant activity of i.v. doses of RNA aptamers targeting the coagulation factors IXa and Xa, suggesting that CDPs are capable of scavenging all free circulating RNA from plasma(19). Taken together, these data strongly

suggest that rapid clearance of these siRNA nanoparticles is not from the result of disassembly in plasma.

7.3.2 Heparan sulfate (HS) disassembled siRNA nanoparticle *in vitro*.

HS is a major constituent of the GBM and is responsible for its negative charge (15). HS is known to disassemble nucleic acid-containing, cationic polymer polyplexes(20). We confirmed that HS (extracted from bovine kidney) did release siRNA from the nanoparticle at charge ratios (HS/CDP) above 0.8 -/+ in 50% mouse plasma, whereas plasma alone could not (Fig. 7.2c). The amount of HS per mouse glomerulus is ca. 2.5ug (estimated from(21, 22)) and 2500ug per kidney (c.a. 10,000 glomeruli(23)), a feasibly sufficient amount of HS to disassemble a single 10 mg/kg injection of siRNA nanoparticles (250ug for a 25g mouse).

7.3.3 Dynamic PET data revealed differences in kidney transit for siRNA nanoparticles and free siRNA.

We employed PET to track the dynamic, whole-body distribution of Cu^{64}-DOTA labeled siRNA in mice, and showed that siRNA in both free and nanoparticle forms demonstrated identical plasma half-lives as well as rapid clearance to the bladder*(10)*. The only significant difference was in kidney transit: Compared to free siRNA, siRNA nanoparticles revealed delayed peak and increase in bulk kidney signal, as well as delayed transit from the kidney to the bladder for the siRNA nanoparticles (Fig. 7.3 a,b). The results from the dynamic PET data lead us to hypothesize that siRNA nanoparticles, but not free siRNA, transiently accumulate in the kidney before passing to the bladder.

7.3.4 siRNA nanoparticles but not-free siRNA transiently accumulated in mouse glomeruli following i.v. administration.

We hypothesized that the transient accumulation of the siRNA nanoparticles in the kidney suggested by our PET studies occurs in the glomerulus. We tested this hypothesis using confocal microscopy to examine the distribution of free siRNA and siRNA nanoparticles in kidney during clearance. Greater than 90% of the administered nanoparticles have been shown to clear from circulation within 10 minutes and nearly completely by 30 minutes (10). Therefore, we examined the distribution of siRNA nanoparticles in the kidney at time points between 3 and 30 minutes following i.v. injection. siRNA nanoparticles were formulated with 80% fluorescently labeled siRNA (Cy3). Formulation of nanoparticles with 80% Cy3-siRNA did not alter the size, charge or stability of the nanoparticles.

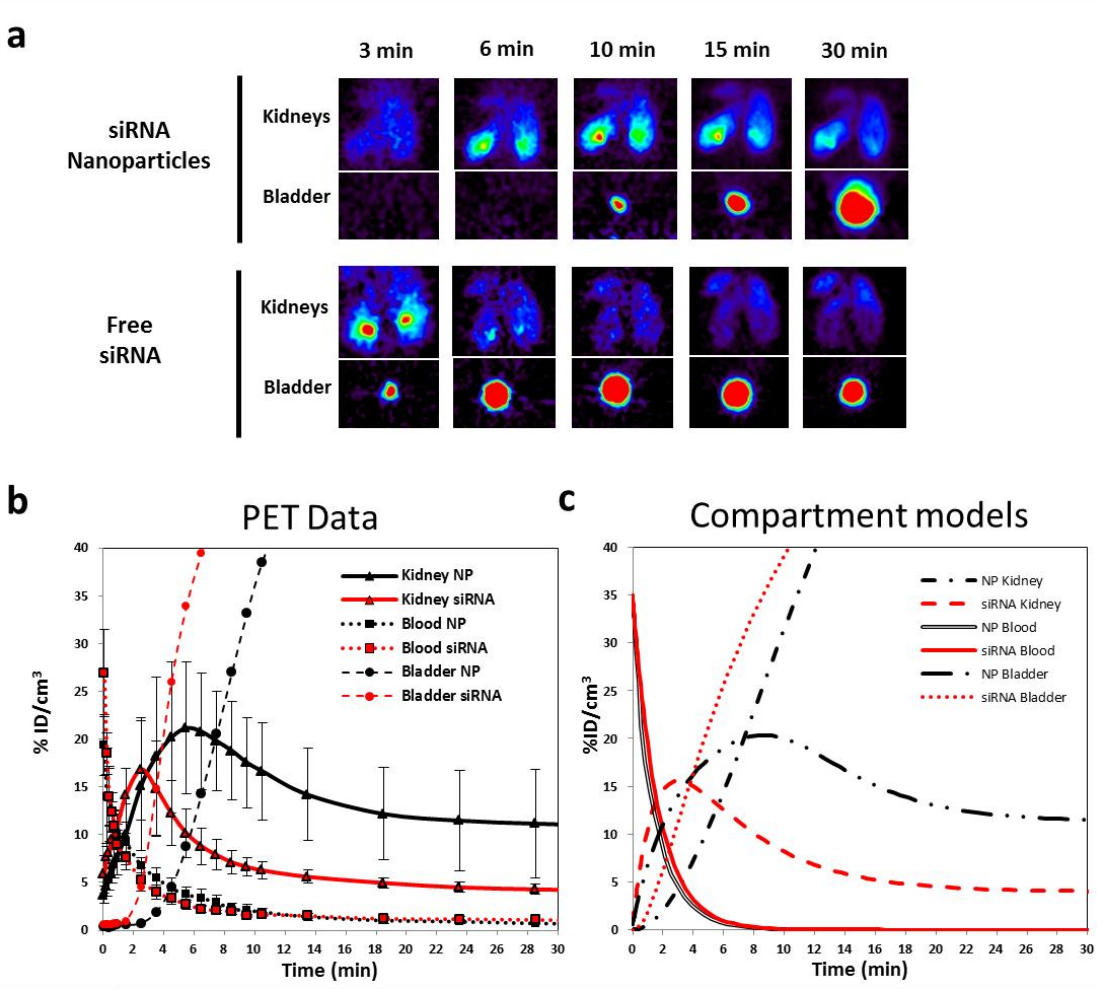

Figure 7.3: Real-time PET imaging and compartment model of GBM induced disassembly of siRNA nanoparticles. (a) Images of PET signal from kidneys and bladder of mice receiving free and nanoparticle formulated ^{64}Cu-DOTA labeled siRNA (Data adapted from ref. 10). (b) Quantification of kidney, blood, and bladder ^{64}Cu-DOTA labeled siRNA intensities from PET studies (Error bars = standard deviation, free siRNA n=4, siRNA nanoparticles (NPs), n=5). (c) Computed results from compartment model of PET data for free siRNA (red) and siRNA nanoparticles (black).

Following administration of free Cy3-labled siRNA, fluorescence signal was observed to accumulate in renal tubules. The fluorescence signal in tubules increased until 10 minutes and then plateaued (Fig. 7.4a). No evidence for glomerular localization of Cy3-siRNA was observed in these animals at any time point. These observations are consistent with previous observations of free siRNA uptake by proximal tubule cells (24).

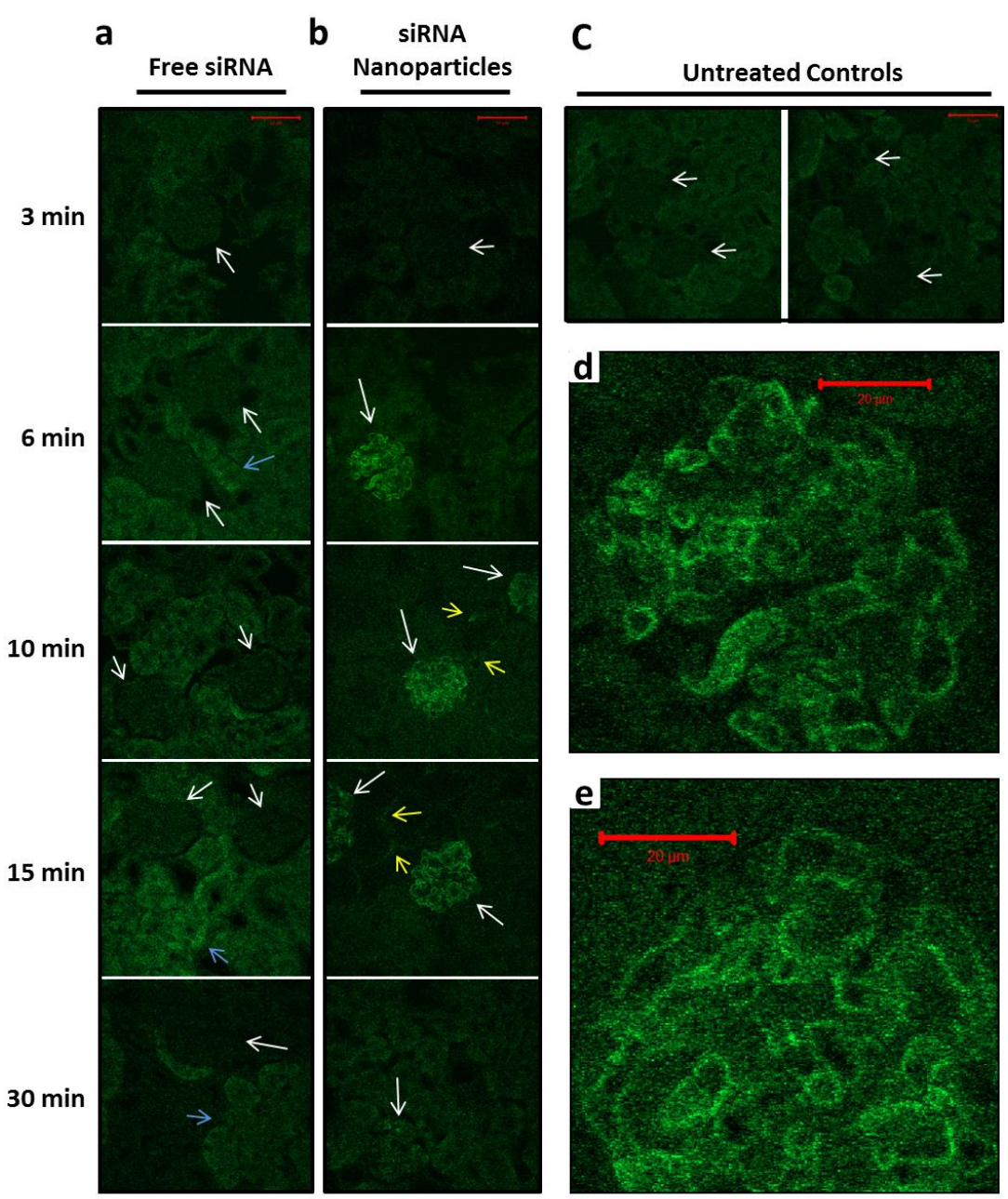

Figure 7.4: siRNA nanoparticles, but not free siRNA, transiently accumulate in glomeruli following i.v. administration. Time course of confocal microcopy images of kidneys extracted from mice receiving: (a) free Cy3-labeled siRNA, (b) Cy3-labled siRNA nanoparticles or (c) no treatment. Higher magnification images of glomeruli from 6 min (d) and 10 min (e) time points. White arrows indicate glomeruli positions, blue arrows indicate areas of tubular Cy3-signal accumulation, yellow arrows indicate cy3-fluorescence in peri-tubule vasculature lining.

In striking comparison, strong Cy3 fluorescence signal localized to glomeruli was observed following administration of siRNA nanoparticles (Fig. 4b). This glomeruluar

siRNA signal was observed first at 6 minutes post injection of the nanoparticles in ca. 75% of glomeruli inspected. Close inspection of the glomeruli (Fig. 7.4d,e) revealed Cy3 fluorescence localized to circular patterns that coincide with the lining the glomerular capillary walls (determined by position of red blood cells in the bright field image). These data demonstrate that the siRNA nanoparticles, but not free siRNA, accumulate in the glomerular capillary walls (the site of the GBM).

The glomerular siRNA nanoparticle Cy3 fluorescence intensity reached a maximum at 10 minutes followed by attenuation at 15 minutes and 30 minutes. Observable glomeruli with fluorescent signal also decreased markedly at 15 minutes and were rarely detected at 30 minutes. These data indicate that siRNA nanoparticles only transiently accumulated within the glomerular capillary walls and ultimately exit the glomerulus. Visual examination of urine following nanoparticle administration revealed the highest Cy3 intensity at and after 10 minutes post injection (Supplementary Fig. S2a), consistent with the assertion that siRNA accumulated in the glomerulus rapidly ends up in the urine, although Cy3 intensity in urine is similar following free siRNA administration (Supplementary Fig. S2b). Additionally, Cy3 was not readily cleaved from the siRNA molecule after 30 minutes in plasma (Supplementary Fig. S2d), indicating that any observed Cy3 fluorescence signals represents distribution of siRNA and not free Cy3.

Less Cy3 fluorescence was detected in tubules following siRNA nanoparticles administration than what was observed following free siRNA administration. These data suggest that the concentration of siRNA within the tubule lumen during clearance of the siRNA nanoparticles was consistently less than the concentration of siRNA when free

siRNA was administered, despite the fact that the both entities are clear from circulation at the same rate. These results support the notion that the renal filtration barrier is impeding the delivery of siRNA into the tubule system, preventing the higher concentrations required to drive higher levels of proximal tubule cell uptake.

7.3.5 Nanoparticles deposit and disassemble at the kidney GBM.

The confocal microscopy data demonstrated that the siRNA nanoparticles were accumulating in the lining of the glomerular vasculature. We employed TEM to confirm that the siRNA signal in these locations resulted from siRNA in nanoparticle form accumulating specifically at the GBM (Fig. 7.5). We examined kidney tissue from mice 10 minutes after receiving free siRNA or siRNA nanoparticles because at this time point we observed maximal glomerular siRNA signals in both PET and confocal microscopy studies. We used uranyl acetate to detect the presence of nucleic acid nanoparticles in tissue sections because it preferentially binds to nucleic acids including the siRNA within the nanoparticles (4, 20).

TEM analysis of kidney tissue following administration of free siRNA revealed typical appearing glomeruli. No darkly staining, globular structures indicative of nanoparticle morphology were observed within or near the GBM or any other structures in the kidney (Fig. 7.5a).

TEM analysis of kidney tissue following administration of siRNA nanoparticles revealed abundant, darkly staining, globular objects lining and within all visible GBMs, with sizes and shapes consistent with those of siRNA nanoparticles (Figs. 5b-d). Most objects were localized to the lamina rara interna with some of the smaller objects localized to the limina rara externa, both are locations of anionic sites within the

GBM(25). Additionally, some objects were observed within the glomerular endothelial fenestrations. No objects of this morphology were observed in the urinary space. The localization of the siRNA nanoparticles observed here matches the high intensity siRNA fluorescent signals along the glomerular capillary walls (site of the GBM) seen in the confocal microscopy studies. These data demonstrate that intact nanoparticles in circulation transit through the glomerular endothelial fenestrations and deposit within the GBM. Moreover, the absence of nanoparticles in the urinary space suggests that intact siRNA nanoparticles cannot cross the podocyte filtration slits of the renal filtration barrier.

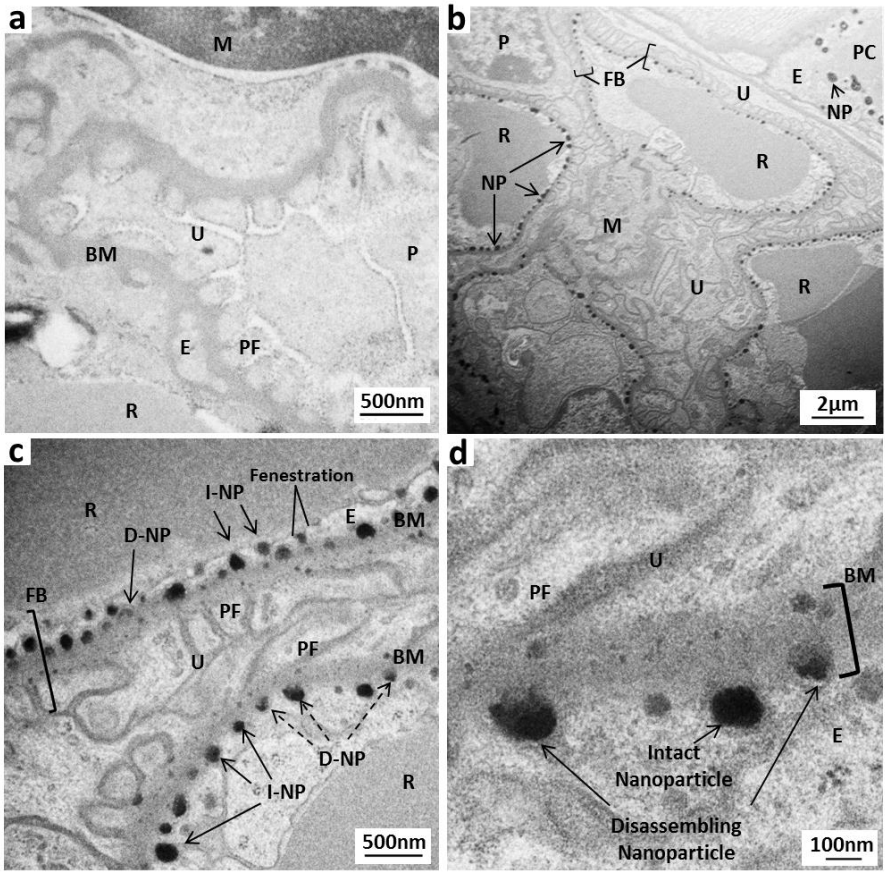

Figure 7.5: Nanoparticles accumulate and disassemble at the kidney glomerular basement membrane. (a) Image of GBM from an animal receiving only free siRNA. (b) Low magnification EM image of glomerular capillaries from a mouse 10 minutes after i.v. administration of siRNA

nanoparticles. (e,d) Higher magnification images of the GBM regions of these glomerular capillaries. BM=Basement membrane, E=Endothelial cell, FB=Filtration barrier, M=Mesangium, (I/D)-NP = (Intact/disassembling) nanoparticle, P=podoyctes, PC=peritubule capillary, PF=podocyte foot process, R=Erythrocyte, U=Urinary space.

Close inspection of these objects within the GBM revealed a subset of nanoparticle sized objects with irregular borders and heterogeneous staining intensity (Fig. 7.5c,d). The objects appeared to have lost their regularity and staining intensity in regions more closely associated with the GBM, implying the loss of some of their nucleic acid content compared to the uniform staining of intact siRNA nanoparticles. These data suggest that, upon GBM association, siRNA can be dissociated from the nanoparticle, i.e. nanoparticle disassembly was occurring at the GBM. Because there is no evidence for intact nanoparticles in the urinary space, these also data support our hypothesis that the transient nature of the GBM accumulation of siRNA nanoparticles observed in the confocal microscopy study stems from their disassembly at the GBM.

Some larger, darkly staining objects were also found within the endothelial cells lining the peri-tubule capillaries following siRNA nanoparticle treatment (Supplementary Figs. S3a, b), consistent in morphology with unpackaging nanoparticles within endosomes (20). These data are consistent with the results from our confocal microscopy study, where we observed some non-glomerular renal vessels with appreciable fluorescence signal in their walls in tissue from mice receiving siRNA nanoparticle treatment. Renal peri-tubule endothelial cell uptake of pegylated gold nanoparticles has been previously observed (14) and may be a generalized phenomenon for nanoparticle systems.

7.3.6 Compartment modeling of kidney transit revealed how siRNA nanoparticle accumulation and disassembly at the GBM could yield the kinetics observed in the PET experiments.

Because non-invasive, real-time monitoring of siRNA nanoparticle behavior at the microscopic level was not possible, we developed a mathematical compartment model of kidney transit to correlate our microscopic observations with the bulk kidney signal from the dynamic PET experiments (Figure 7.3c, Supplementary text).

Kinetic parameters for a model describing the transit of free siRNA through the kidney were derived from anatomic properties of the kidney, and by fitting the PET data for free siRNA ("free siRNA model"). Based on our imaging data, two additional expressions were incorporated into the free siRNA model to create the "siRNA nanoparticle model": (1) an expression to model the binding and disassembly of the nanoparticles within the GBM, and (2) an expression for peri-tubule endothelial cell uptake. All parameter values were fixed to those derived in the free siRNA model, except those pertaining to the two nanoparticle specific expressions (e.g., binding constant of nanoparticle on the GBM and rate of disassembly of nanoparticle) that were determined by fitting the PET data for siRNA nanoparticles. Assimilation of these two expressions into the nanoparticle model allowed us to model the key differences in the PET pharmacokinetics data between free siRNA and siRNA nanoparticles as they pass through the kidney – the delayed bladder accumulation, delayed peak kidney accumulation, and persistent kidney signal for the siRNA nanoparticle experiments.

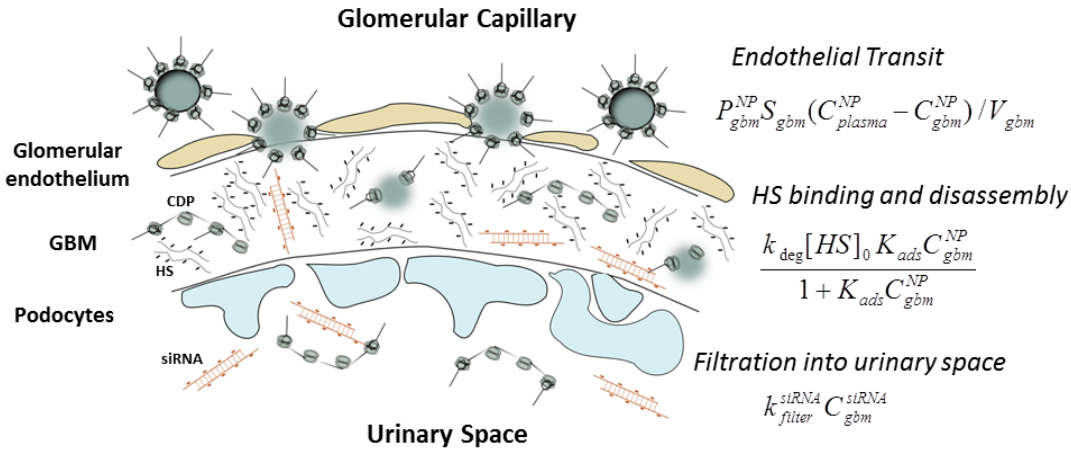

Figure 7.6: Schematic of siRNA nanoparticle deposition and disassembly in the GBM with key modeling expressions highlighted. Nanoparticles cross through fenestrations in the glomerular endothelial cell lining and enter the GBM. Within the GBM, the nanoparticles are disassembled by the abundant heparan sulfate molecules. Once disassembled, the nanoparticle components can cross the remainder of the GBM and the podocyte filtration slits and enter the urinary space.

Kinetic parametric sensitivity analyses of both models confirmed that both GBM and endothelial cell expressions of the nanoparticle model are required to reproduce the observed kidney dynamics of siRNA nanoparticles in the PET data. No arbitrary choice of parameters in the free siRNA model could delay the peak kidney accumulation to fit the nanoparticle PET data, except through the addition of the expression for GBM binding and disassembly in the nanoparticle model. Therefore, mathematical compartment modeling demonstrate that the glomerular accumulation and disassembly of the siRNA nanoparticles revealed by imaging data (confocal and TEM) could be responsible for the dynamics observed in our PET experiments. Additionally, this analysis suggests that siRNA dissociated from nanoparticles in circulation could not recapitulate the dynamics observed in the kidney.

7.4 Discussion:

Here, we have elucidated a new mechanism of nanoparticle disassembly *in vivo* (Fig. 7.6). We have demonstrated siRNA/CDP nanoparticles remain assembled and that their individual components can even self-assemble in circulation. Moreover, using microscopy, we have conclusively demonstrated that siRNA/CDP nanoparticles transiently accumulate in and can be disassembled by the GBM. Finally, using compartment modeling, we illustrated how our microscopic observation of GBM accumulation and disassembly could feasibly result in the bulk dynamics observed by PET, whereas disassembly in circulation could not.

To date, the rapid clearance of siRNA-cationic polymer nanoparticles has been ascribed to instability in circulation and reticuloendothelial system uptake (5-7, 9, 10) . Extracellular matrix mediated disruption of cationic nucleic acid polyplexes within liver sinusoids has also been reported (26). While, our findings do not exclude these alternate explanations for other nanoparticle delivery systems, they reveal another clearance mechanism applicable to a general class of nanoparticles with the following characteristics: (1) ca. 100 nm or smaller in hydrodynamic radius, (2) positive in zeta potential and, (3) held together primarily by electrostatic interaction.

Since the siRNA nanoparticles presented here not only remain assembled in plasma, but their individual components self-assemble *in vivo*, it is unlikely that the components of the nanoparticle prefer to exist freely in circulation. These data also suggest that even if the nanoparticles were disassembled at other locations in the body, the individual components would reassemble in circulation. Thus, only nanoparticle disassembly at that GBM would allow transit of the nanoparticle components into the

urine. In fact, the siRNA nanoparticle components are found to be mostly assembled in urine after excretion (Supplementary Fig. S2c) suggesting that particles re-form in the urine after GBM disassembly and filtration.

Therefore, GBM mediated nanoparticle disassembly is responsible for the rapid clearance of the siRNA/CDP nanoparticles. This phenomenon is likely generalizable to most cationic polymer based nucleic acid delivery systems, or any other delivery vehicles that self-assemble due to electrostatic interactions. For example, 93 nm DNA/PEI polyplexes have been observed to filter through the GBM following direct injection into the renal artery (27) and both Cationic polymers alone (28) as well as positively charged ferritin nanoparticles (29) have been shown to bind to the GBM after i.v. injection.

Avoiding GBM disassembly will be a key design criterion for future nucleic acid delivery vehicles as well as other nanoparticle systems assembled via electrostatic interactions. Future nanoparticle therapeutic development could be facilitated via heparan sulfate stability studies during design. Furthermore, creation of particles with negative zeta potentials may allow avoidance of the GBM due to charge repulsion. Our study of 20-170 nm negatively charged PEGylated gold particles did not reveal any particle deposition in the GBM for nanoparticles of any size (14). Finally, this mechanism of clearance could be utilized to tune the pharmacokinetics of nanoparticles based on their stability to heparan sulfate disassembly, thereby providing a convenient mechanism for more rapid clearance, when desirable, for particles larger than 10 nm such as imaging agents.

7.5 Materials and Methods

siRNA nanoparticle formulation: siRNA nanoparticles were formed by using cyclodextrin-containing polycations (CDP) and AD-PEG as described in ref. 27 (pre-complexation). Nanoparticles were formed in 5 % glucose in deionized water (D5W) at a charge ratio of 3 +/- and a siRNA concentration of 2 mg/ml unless otherwise indicated. Some experiments presented here (NTA, TEM, PET, stability assays) were performed with particles formulated with less than 1mol percent AD-PEG modified with a terminal transferrin targeting ligand. No discernible differences in size, charge, pharmacokinetics, and behavior at the kidney have been observed between particles formulated with or without AD-PEG-Tf(10, 30). 21 base pair unmodified and Cy3 labeled siRNA was purchased from Qiagen.

Nanoparticle tracking analysis (NTA): NTA measurements were performed with a NanoSight NS500 (NanoSight), equipped with a 405-nm laser. All measurements were performed at room temperature. The software used for capturing and analyzing the data was NTA 2.0. For measurements the samples were measured for 30 s with manual shutter and gain adjustments. Three measurements of the same sample, advancing the sample 20-50ul between measurements, were collected. The error bars displayed on the NTA graphs were the standard deviation of the three measurements.

Nanoparticle stability assays: Formulated siRNA nanoparticles were incubated with the indicated amount of mouse plasma (collected from Balb/c mice) and/or heparan sulfate isolated from bovine kidney (Sigma) for 15 minutes at 37°C. 1µg of each sample was

loaded into each well of a 1% agarose gel and voltage was applied for 20-30 minutes. Visualization was achieved via ethidium bromide staining (Sigma).

Animal Studies: All animals were treated according to the NIH Guidelines for Animal Care and Use as approved by the Caltech Institutional Animal Care and Use Committee. 6 to 9-week old, female Balb/c mice (Jackson Laboratory) received i.v. doses of 10 mg/kg siRNA nanoparticles in D5W. Mice were euthanized by CO_2 overdose for organ collection at indicated time points. All organs were fixed in 4 % paraformaldehyde (PFA) in PBS for 3 days. For confocal imaging, nanoparticle formulations contain 80% Cy3-siGL3.

***In vivo* siRNA/CDP assembly/disassembly assays:** *Experiment 1:* Free siRNA was injected at 10 mg/kg dose via tail vein. *Experiment 2:* siRNA nanoparticles were injected at 10mg/kg via tail vein. *Experiment 3:* Free siRNA was injected at 10 mg/kg, 1 minute later CDP/AD-PEG components were injected at a 3 +/- charge ratio of the injected siRNA. *Experiment 4:* CDP/AD-PEG was injected at nanoparticle equivalent concentration. *Experiment 5:* siRNA nanoparticles were injected at 2.5 mg/kg, 1 minute later 10mg/kg plasmid DNA was injected. Blood collection for all 3 experiments was performed via saphenous vein bleed 3 minutes after the first injection and collected using Microvette CB 300 Capillary Blood Collection Tube with EDTA (Sarstedt). Samples were centrifuged for 15 minutes at 1,300xg and the plasma supernatant loaded onto a 1% agarose gel for analysis. All samples were processed within a 1 hour of collection.

Cryo-electron microscopy*:* Samples were vitrified using an automated climate-controlled plunge-freezer (Vitrobot, FEI). Briefly, glow discharged Quantifoil holey carbon grids (SPI Supplies) were loaded into the chamber of the Vitrobot and 5ul of

samples were applied. Grids were blotted for 1s and drained for 1s before being plunged into the center of a Vitrobot cup filled with liquid ethane, they were then quickly transferred into the outer ring of the cup containing liquid nitrogen. The grids were stored under liquid nitrogen for later analysis. Samples were visualized in Techni T12 Cryo-electron microscope (FEI) equipped with a cryo-specimen holder. Acceleration voltage was set at 120kV.

Transmission electron microcopy: Tissue blocks (~1 mm^3) were fixed in 2.5 % glutaraldehyde (in 0.1 M sodium cacodylate, pH = 7.4) for 2 h, stained by 1 % OsO_4 at 4 °C for 2 h, and 0.9 % OsO_4 and 0.3 % $K_4Fe(CN)_6$ at 4 °C for 2 h. Gradual dehydration with ethanol and propylene oxide enabled tissue embedding in Epon 812 resins (Electron Microscopy Sciences). 80 nm thick sections were deposited on carbon and formvar-coated, 200-mesh, nickel grids (EMS) and stained with 3 % uranyl acetate and Reynolds lead citrate for visualization under a 300 kV TF30UT transmission electron microscope (FEI).

Confocal microscopy: Formalin-fixed organs were dehydrated and embedded in molten paraffin to generate sections of 4-μm in thickness. Sections were deparrafinized with xylene, rehydrated, and mounted with ProLong Gold antifade reagent (Invitrogen) for viewing under a Zeiss LSM 510 inverted confocal scanning microscope (with a Plan Neofluar ×40/0.75 objective). The excitation wavelengths of Cy3-siRNAs was 543 nm (HeNe laser) and the corresponding emission filter was 560-610 nm. The measured resolution at which images were acquired is 512×512 pixels, and the image bit-depth is 8-bit. 10 sections from each organ were inspected. Typically, 5 glomeruli from each tissue

section were inspected. The Zeiss LSM Image Browser Software allows the extraction of images.

Micro-PET/CT Imaging: Micro-PET imaging was performed as described previously(10). Briefly, a micro-PET FOCUS 220 PET scanner and a MicroCAT II CT scanner (Siemens) were used for data acquisition. Mice were anesthetized by using 1.5–2% isoflurane. siRNA labeled with ^{64}Cu (100–300 μCi) (1 Ci =37 GBq) was injected via tail vein and a dynamic PET scan was acquired for 1 h. Total siRNA dose was 2.5mg/kg. The image resolution was 1.7 mm. A 7 minute micro-CT scan was then performed. AMIDE software(31) was used to examine the ^{64}Cu signal intensity. Ellipsoid regions of interest were placed to over organs of interest. To ensure accurate anatomical positioning, regions of interest were placed on fused micro-PET/CT images generated by the AMIDE software. Values were normalized to an elliptic cylinder region of interest drawn over the entire mouse.

Compartment modeling: Model variables and parameters are defined in the supplemental text. The system of first-order ODEs was solved by using MATLAB (Mathworks).

7.6 Acknowledgments:

We would like to thank Paul Webster (House Ear Institute,) for providing equipment for TEM sample preparation and Carol M. Garland (Caltech) and Dr. Alasdair McDowall (Caltech) for help obtaining electron microscopy images. This work benefited from the use of the Caltech Materials Science TEM facility which is partially supported by the MRSEC Program of the National Science Foundation under award number DMR-0520565. We thank Derek W. Bartlett and Isabel J. Hildebrandt for performing the PET

experiments. We thank Devin Wiley for reading the manuscript and discussion. This work was supported by National Cancer Institute Grant CA119347 and Sanofi-Aventis. Jonathan E. Zuckerman is also supported by the Caltech-UCLA Joint Center for Translational Medicine.

7.7 References:

1. Castanotto D & Rossi JJ (2009) The promises and pitfalls of RNA-interference-based therapeutics. *Nature* 457(7228):426-433.

2. de Fougerolles A, Vornlocher HP, Maraganore J, & Lieberman J (2007) Interfering with disease: a progress report on siRNA-based therapeutics. *Nature reviews. Drug discovery* 6(6):443-453.

3. Davis ME, Chen ZG, & Shin DM (2008) Nanoparticle therapeutics: an emerging treatment modality for cancer. *Nature reviews. Drug discovery* 7(9):771-782.

4. Davis ME, *et al.* (2010) Evidence of RNAi in humans from systemically administered siRNA via targeted nanoparticles. *Nature* 464(7291):1067-1070.

5. de Wolf HK, *et al.* (2007) Effect of cationic carriers on the pharmacokinetics and tumor localization of nucleic acids after intravenous administration. *International journal of pharmaceutics* 331(2):167-175.

6. Malek A, *et al.* (2009) In vivo pharmacokinetics, tissue distribution and underlying mechanisms of various PEI(-PEG)/siRNA complexes. *Toxicology and applied pharmacology* 236(1):97-108.

7. Merkel OM, *et al.* (2009) Stability of siRNA polyplexes from poly(ethylenimine) and poly(ethylenimine)-g-poly(ethylene glycol) under in vivo conditions: effects on pharmacokinetics and biodistribution measured by Fluorescence Fluctuation Spectroscopy and Single Photon Emission Computed Tomography (SPECT) imaging. *Journal of controlled release : official journal of the Controlled Release Society* 138(2):148-159.

8. Merkel OM, *et al.* (2010) Triazine dendrimers as nonviral vectors for in vitro and in vivo RNAi: the effects of peripheral groups and core structure on biological activity. *Molecular pharmaceutics* 7(4):969-983.

9. Gao S, *et al.* (2009) The effect of chemical modification and nanoparticle formulation on stability and biodistribution of siRNA in mice. *Molecular therapy : the journal of the American Society of Gene Therapy* 17(7):1225-1233.

10. Bartlett DW, Su H, Hildebrandt IJ, Weber WA, & Davis ME (2007) Impact of tumor-specific targeting on the biodistribution and efficacy of siRNA nanoparticles measured by multimodality in vivo imaging. *Proceedings of the National Academy of Sciences of the United States of America* 104(39):15549-15554.

11. Heidel JD, *et al.* (2007) Administration in non-human primates of escalating intravenous doses of targeted nanoparticles containing ribonucleotide reductase subunit M2 siRNA. *Proceedings of the National Academy of Sciences of the United States of America* 104(14):5715-5721.

12. Ribas A, L. Kalinoski, J. D. Heidel, J. Peterkin, D. B. Seligson, J. E. Zuckerman, C. Choi, Y. Yen, M. E. Davis and A. W. Tolcher (2010) Systemic delivery of siRNA via targeted nanoparticles in patients with cancer: Results from a first-in-class phase I clinical trial. *Journal of Clinical Oncology* 28(15s):abstr 3022.

13. Choi HS, *et al.* (2007) Renal clearance of quantum dots. *Nature biotechnology* 25(10):1165-1170.

14. Choi CH, Zuckerman JE, Webster P, & Davis ME (2011) Targeting kidney mesangium by nanoparticles of defined size. *Proceedings of the National Academy of Sciences of the United States of America* 108(16):6656-6661.

15. Kanwar YS, and Farquhar, M.G. (1979) Presence of heparan sulfate in the glomerular basement membrane. *Proc. Natl. Acad. Sci. USA.* 76(3):1303-1307.

16. Ogawa S (1999) High-resolution ultrastructural comparison of renal glomerular and tubular basement membranes. *Am. J. Nephrol.* 19:686-693.

17. Lahdenkari A-T (2004) Podocytes are firmly attached to glomerular basement membrane in kidneys with heavy proteinuria. *J. Am. Soc. Nephrol.* 15:2611-2618.

18. Bartlett DW & Davis ME (2007) Effect of siRNA nuclease stability on the in vitro and in vivo kinetics of siRNA-mediated gene silencing. *Biotechnology and bioengineering* 97(4):909-921.

19. Oney S, *et al.* (2009) Development of universal antidotes to control aptamer activity. *Nature medicine* 15(10):1224-1228.

20. Mishra S, Heidel JD, Webster P, & Davis ME (2006) Imidazole groups on a linear, cyclodextrin-containing polycation produce enhanced gene delivery via multiple processes. *Journal of controlled release : official journal of the Controlled Release Society* 116(2):179-191.

21. Comper WD, Lee AS, Tay M, & Adal Y (1993) Anionic charge concentration of rat kidney glomeruli and glomerular basement membrane. *The Biochemical journal* 289 (Pt 3):647-652.

22. Westberg NG & Michael AF (1970) Human glomerular basement membrane. Preparation and composition. *Biochemistry* 9(19):3837-3846.

23. Takemoto M, *et al.* (2002) A new method for large scale isolation of kidney glomeruli from mice. *The American journal of pathology* 161(3):799-805.

24. Molitoris BA, *et al.* (2009) siRNA targeted to p53 attenuates ischemic and cisplatin-induced acute kidney injury. *Journal of the American Society of Nephrology : JASN* 20(8):1754-1764.

25. Kanwar YS & Farquhar MG (1979) Anionic sites in the glomerular basement membrane. In vivo and in vitro localization to the laminae rarae by cationic probes. *The Journal of Cell Biology* 81(1):137-153.

26. Burke RS & Pun SH (2008) Extracellular barriers to in Vivo PEI and PEGylated PEI polyplex-mediated gene delivery to the liver. *Bioconjugate chemistry* 19(3):693-704.

27. Foglieni C, *et al.* (2000) Glomerular filtration is required for transfection of proximal tubular cells in the rat kidney following injection of DNA complexes into the renal artery. *Gene therapy* 7(4):279-285.

28. Andrews PM & Bates SB (1985) Dose-dependent movement of cationic molecules across the glomerular wall. *The Anatomical record* 212(3):223-231.

29. Bennett KM, *et al.* (2008) MRI of the basement membrane using charged nanoparticles as contrast agents. *Magnetic resonance in medicine : official journal of the Society of Magnetic Resonance in Medicine / Society of Magnetic Resonance in Medicine* 60(3):564-574.

30. Bartlett DW & Davis ME (2007) Physicochemical and biological characterization of targeted, nucleic acid-containing nanoparticles. *Bioconjugate chemistry* 18(2):456-468.

31. Loening AM & Gambhir SS (2003) AMIDE: a free software tool for multimodality medical image analysis. *Molecular imaging* 2(3):131-137.

7.8 Supplementary Information for Chapter 7

Supplemental Figure S1: Plasmid DNA will dissociate siRNA from nanoparticles. siRNA nanoparticles were formulated and then increasing concentrations of ~6kb plasmid DNA were added. Samples were immediately loaded onto the gel.

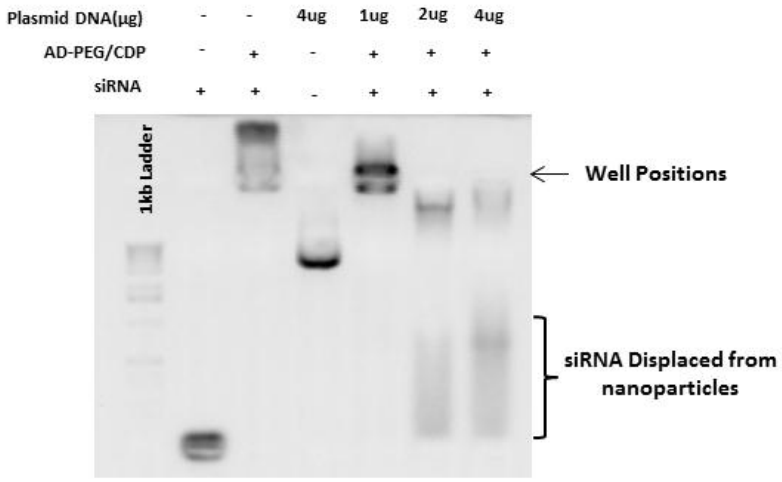

Supplemental Figure S2: Characterization of siRNA nanoparticle components excreted into urine. a,b) Images of urine samples taken at multiple time points after injections of either free Cy3-labled siRNA or Cy3-labled siRNA nanoparticles. Urine was collected from urinary meatus when released at time of euthanasia. c) Gel mobility shift assay on urine samples from mice receiving either free siRNA or siRNA nanoparticles. Most of the siRNA remaining exists in complex with CDP in the urine. d) Cy3 label is not cleaved off siRNA after 30 minute incubation with 95% plasma at 37°C. No staining agent used in this gel, signal results from Cy3 fluorescence.

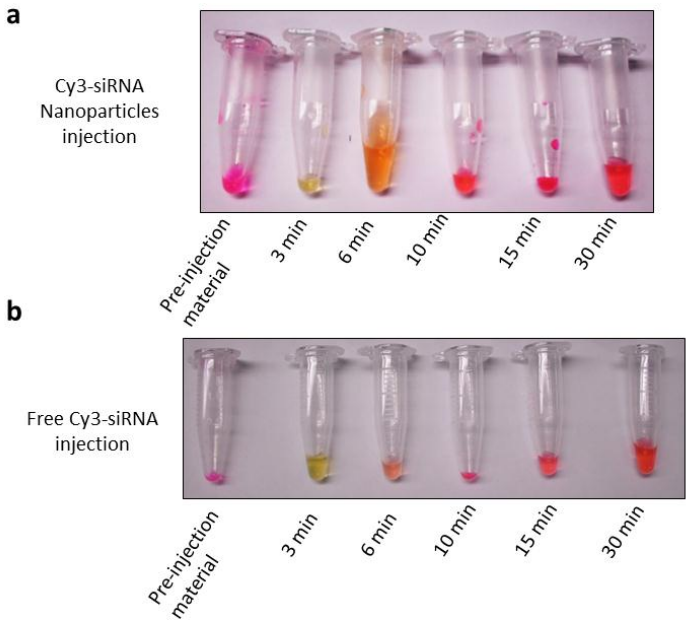

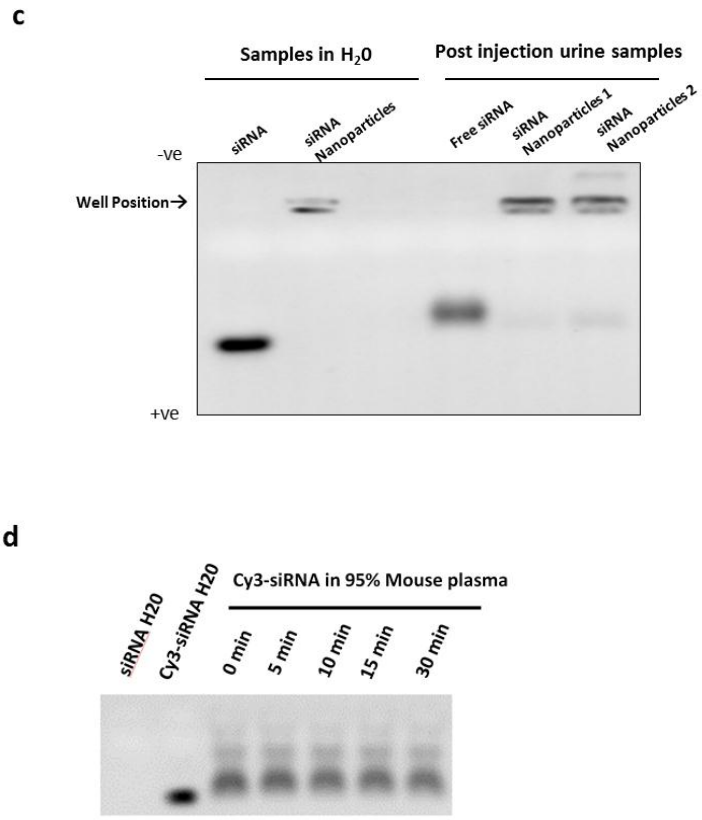

Supplemental Figure S3: (a,b) siRNA nanoparticles are also identified within endothelial cells lining the peritubule capillaries10 min after administration of siRNA nanoparticles but not (c) free siRNA. E=Endothelial cell, NP=nanoparticle, P=podoyctes, PC=peritubule capillary, R=Erythrocyte, T=Tubule. Image sizing was performed with ImageJ software.

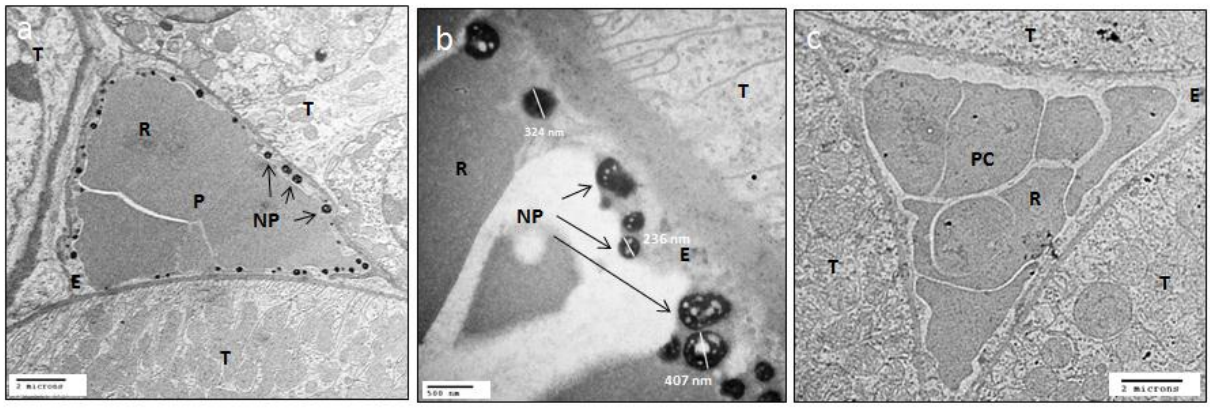

Supplemental Text

Compartment model of kidney transit of free siRNA and siRNA nanoparticles

Because non-invasive, real-time monitoring of siRNA nanoparticle behavior at the microscopic level was not possible, we developed a compartment model of kidney transit to better understand the relationships between our microscopic observations and the bulk kidney signal obtained from the PET study. Specifically, compartment modeling of the kidney was used to demonstrate how GBM accumulation and disassembly of siRNA nanoparticles could result in the dynamics observed in our PET study. The goal of the model was to reproduce three key characteristics of the PET data:

1. Delayed and augmented peak kidney accumulation for siRNA nanoparticles versus siRNA alone
2. Delayed bladder accumulation for the siRNA nanoparticles versus siRNA alone
3. Increased total kidney retention of the siRNA nanoparticles versus siRNA alone

Two models were developed, a free siRNA model and a siRNA nanoparticle model. The free siRNA model replicates the behavior of free siRNA in the kidney. Key reaction parameters that describe the rates and processes of free siRNA filtration used in the free siRNA model were determined by inserting anatomical constraints as well as fitting the free siRNA model predictions to the free siRNA PET data.

The siRNA nanoparticle model reproduces the behavior of siRNA nanoparticles in the kidney. Two additional expressions were included to the siRNA nanoparticle model: (1) deposition and complete disassembly of siRNA nanoparticles to free siRNAs at the GBM, and (2) uptake of siRNA nanoparticles by peri-tubular capillary endothelial cells. Reaction parameters specific to both expressions were fit to the PET data from the siRNA nanoparticles, by holding constant all reaction parameters previously deduced from the free siRNA model (see table below).

Part I: Estimation of anatomical parameters

Total renal corpuscle volume (V_{rc}): Mice have ~10,000 renal corpuscles per kidney (1). We assumed that each renal corpuscle is a sphere of radius 40 μm (2).

$$V_{rc} = (4/3)\,\pi\,(40\ \mu m)^3 \times (2\times10^4 \text{ corpuscles}) = 0.005\ cm^3$$

Total GBM surface area (S_{gbm}) and GBM volume (V_{gbm}): The surface area of GBM in a healthy mouse is ~2.84×10^4 μm^2 per renal corpuscle, or equivalently, 5.7 cm^2 (S_{gbm}) per mouse (3). We assume a GBM thickness of 300nm (5).

$$V_{gbm} = 5.7\ cm^2 \times 3\times10^{-5} cm = 1.7\times10^{-4} cm^3.$$

Total kidney interstitial volume (V_{int}). The cortex, medulla, and pelvis account for 70%, 27%, and 3% of the total kidney volume (4). Here, we combined volume contribution from the pelvis and medulla. The interstitial fraction in the cortex and medulla amounts to 7% and up to 20%, respectively (5).V_{int} amounts to ~10% of the total kidney volume.

Total renal tubules volume (V_{rt}): All remaining parts of the kidney other than renal corpuscles and interstitial space belong to renal tubules throughout the cortex and medulla.

$$V_{rt} = V_{kidney} - V_{rc} - V_{int} = 0.22 \text{ cm}^3$$

Part II: Free siRNA model

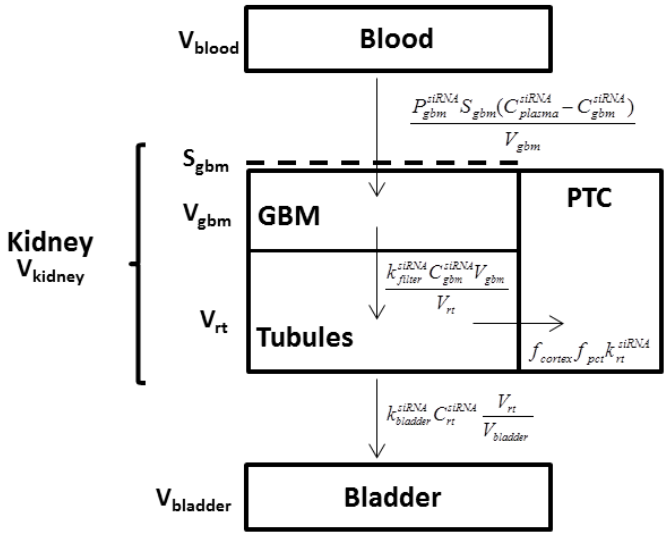

Diagram of the compartmental model for free siRNAs in the kidney. GBM = glomerular basement membrane, PTC = proximal tubule cells, dotted line: fenestrated walls of glomerular capillaries.

Blood concentration of siRNA: In order to limit the number of parameters in the model, we chose to represent the level of siRNA in blood by a simple exponential decay function.

$$C_{plasma}^{siRNA} \approx C_{plasma}^{NP} = A\exp(-\alpha t), \text{ where A = 35\% ID/cm}^3 \text{ and } \alpha = 0.6 \text{ min}^{-1}.$$

Values for A and α were derived by curve fitting the PET data for free siRNA.

Renal filtration of free siRNA: Upon their entry into the glomerular capillary tuft, free siRNAs (MW: c.a. 13 kDa; size: 3.2 nm) pass through the fenestrated endothelium and permeate into the renal filtration barrier (with an apparent permeability P_{gbm}). Once within the filtration barrier, free siRNAs enter the urinary space within the renal tubules at a rate k_{filter}.

$$\frac{dC_{gbm}^{siRNA}}{dt} = \frac{P_{gbm}^{siRNA} S_{gbm} (C_{plasma}^{siRNA} - C_{gbm}^{siRNA})}{V_{gbm}} - k_{filter}^{siRNA} C_{gbm}^{siRNA}$$

In the urinary space, free siRNAs can experience uptake by proximal convoluted tubules (PCTs) (6). This model includes an additional rate constant k_{rt} that depicts the reabsorption of free siRNAs into PCTs. It assumes no reabsorption in other renal tubule components but PCTs. f_{cortex} (= 0.7) and f_{pct} (= 0.64) denote the volume fraction of the cortex in the bulk kidney and the fraction of PCTs in the cortex, respectively (5).

$$\frac{dC_{rt}^{siRNA}}{dt} = \frac{k_{filter}^{siRNA} C_{gbm}^{siRNA} V_{gbm}}{V_{rt}} + f_{cortex} f_{pct} k_{rt}^{siRNA} - k_{bladder}^{siRNA} C_{rt}^{siRNA}$$

Ultimately, unabsorbed siRNAs depart from the kidney and enter the bladder at a rate $k_{bladder}$.

$$\frac{dC_{bladder}^{siRNA}}{dt} = k_{bladder}^{siRNA} C_{rt}^{siRNA} \frac{V_{rt}}{V_{bladder}}$$

For initial conditions, $C_{gbm}^{siRNA} = C_{rt}^{siRNA} = C_{bladder}^{siRNA} = 0$ at t = 0. Curve fitting of the bulk kidney concentration of free siRNAs allows for the determination of the values of P_{gbm}^{siRNA}, k_{filter}^{siRNA}, and $k_{bladder}^{siRNA}$.

$$C_{kidney}^{siRNA} = \frac{V_{glom}(1 - HCRT) C_{plasma}^{siRNA} + V_{gbm} C_{gbm}^{siRNA} + V_{rt} C_{rt}^{siRNA}}{V_{kidney}}$$

Part III: siRNA Nanoparticle model

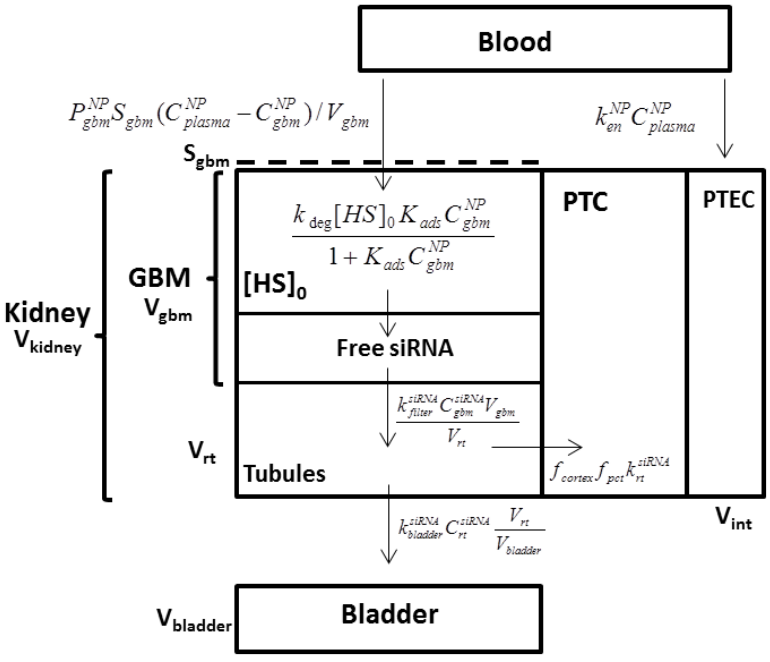

Diagram of the compartmental model for siRNA nanoparticles in the kidney. GBM = glomerular basement membrane, PTC = proximal tubule cells, PTEC = peri-tubule endothelial cells, dotted line: fenestrated walls of glomerular capillaries.

Blood concentration of siRNA nanoparticle: same as free siRNA model

Peri-tubule endothelial cell uptake: Our imaging studies revealed that some siRNA nanoparticles are internalized by peri-tubule endothelial cells within the kidney. This region of nanoparticle accumulation is likely responsible for the majority of the persistent PET signal observed in the kidney at 30 minutes. Because these endothelial cells reside within the interstitial space of the kidney, we used V_{int} to represent the volume of this compartment and deduce the value of k_{en}^{NP}.

$$\frac{dC_{en}^{NP}}{dt} = k_{en}^{NP} C_{plasma}^{NP} \frac{V_{blood}(1-HCRT)}{V_{\text{int}}}$$

Renal filtration of siRNA nanoparticles: Our imaging studies revealed that siRNA nanoparticles accumulated and are disassembled in the GBM. We model the GBM as a collection of binding sites of heparan sulfate ($[HS]_0$). Each nanoparticle can bind to a site with an equilibrium binding constant K_{ads}^{NP}. Upon binding and formation of an intermediate complex NP-HS, the degradation of the nanoparticle will occur. Compared to binding, degradation is the rate-limiting step (with rate k_{deg}^{NP}).

$$NP + HS \xleftarrow{K_{ads}^{NP}} NP \bullet HS \xrightarrow{k_{\text{deg}}^{NP}} siRNA + HS$$

The rate expression describing these processes is as follows:

$$r = \frac{k_{\text{deg}}^{NP}[HS]_0 K_{ads}^{NP} C_{gbm}^{NP}}{1 + K_{ads}^{NP} C_{gbm}^{NP}}$$

The pores of the glomerular endothelium are ~100 nm in diameter. We believe that the net movement of siRNA across this membrane is the same for both free siRNA and siRNA in nanoparticles. Because both formulations of siRNA (free or nanoparticle associated) have similar blood clearance rates, the net rate for siRNA crossing the glomerulular endothelium for both these formulations are necessarily similar. This assertion is further supported by the observations that both siRNA formulations deposit similarly in all other sites in the body besides the kidney.

Physically, the idea of similar rate of endothelial crossing for both siRNA formulations is reasonable. While free siRNA experiences less hydrodynamic drag than nanoparticles when crossing the glomerular endothelium, they face electrostatic repulsion by the GBM, whereas the positively charged siRNA nanoparticles do not. Additionally, each nanoparticle has been estimate to contain ~2000 siRNA molecules. Therefore, even if the permeability of the glomeruluar endothelium for an intact nanoparticle is less than that of free siRNA, the net rate of siRNA crossing this barrier in nanoparticle form could be equivalent. Therefore, we set P_{gbm} of the nanoparticle to be the same as the P_{gbm} determined in curve fitting of the preliminary model for free siRNA.

The governing equations of siRNA nanoparticle accumulation and disassembly in the GBM are:

Nanoparticle accumulation and disassembly:

$$\frac{dC_{gbm}^{NP}}{dt} = \frac{P_{gbm}^{NP} S_{gbm} (C_{plasma}^{NP} - C_{gbm}^{NP})}{V_{gbm}} - \frac{k_{\deg}^{NP} [HS]_0 K_{ads}^{NP} C_{gbm}^{NP}}{1 + K_{ads}^{NP} C_{gbm}^{NP}}$$

Released free siRNA in GBM:

$$\frac{dC_{gbm}^{siRNA}}{dt} = \frac{k_{\deg}^{NP} [HS]_0 K_{ads}^{NP} C_{gbm}^{NP}}{1 + K_{ads}^{NP} C_{gbm}^{NP}} - k_{filter}^{siRNA} C_{gbm}^{siRNA}$$

Total GBM heparan sulfate concentration ($[HS]_0$): Based on the PET experiment, each mouse (20 g) receives infusion of siRNA (in free or nanoparticle form) at an amount of 2.5 mg/kg. This means each whole dose (100% ID) contains 50 μg of siRNA. This translates to ~9×10^{16} anionic charges/ID.

> (50 μg-siRNA/kidneys) × (mol-siRNA/14000 g-siRNA) × (42 mol-saccharide /mol-siRNA) × (1 mol-anionic charge/mol-saccharide) × (6.02×10^{23} anionic charge/mol-charge) = 9×10^{16} anionic charge/ID.

With known amounts of GBM in renal corpuscles and content of heparan sulfate in each corpuscle, we can estimate $[HS]_0$ in equivalent terms of the percent injected dose (%ID) (7, 8).

> (188 μg-GBM/corpuscle) × (13.3 μg-HS/mg-GBM) × (mol-HS/75000 g-HS) × (220 mol-saccharide /mol-HS) × (2 mol-anionic charge/mol-saccharide) × (6.02×10^{23} anionic charge/mol-charge) × (corpuscle/(4π (40 μm)^3/3)) × (100% ID/9×10^{16} anionic charge) = **4×10^6 %ID/cm^3**.

This represents an extremely high and localized concentration of negative charge within the GBM.

The model assumes full degradation of nanoparticles such that the only component filtered out of the glomerular basement membrane to the urinary space is free siRNA. We therefore employ the same equations for PCT uptake and delivery to bladder as in the free siRNA model.

For initial conditions, $C_{en}^{NP} = C_{gbm}^{NP} = C_{gbm}^{siRNA} = C_{rt}^{siRNA} = 0$ at t = 0. Curve fitting of the bulk kidney concentration allows for the determination of the values of K_{ads},and k_{deg}, .

$$C_{kidney}^{Total} = C_{kidney}^{NP} + C_{kidney}^{siRNA} = \frac{V_{\text{int}} C_{en}^{NP} + V_{glom}(1 - HCRT) C_{glom}^{NP} + V_{gbm}(C_{gbm}^{siRNA} + C_{gbm}^{NP}) + V_{rt} C_{rt}^{siRNA}}{V_{kidney}}$$

List of parameters

The governing differential equations (with their initial conditions) were solved with MATLAB using ODE15s with the appropriate initial conditions.

Table I: Anatomical parameters

Name	Description (units)	Determination Method	Value
V_{kidney}	Total kidney volume (cm^3)	Direct measurement	0.25
V_{rc}	Total renal corpuscles volume (cm^3)	Estimated from (1, 2)	5×10^{-3}
V_{gbm}	Total kidney GBM volume (cm^3)	Estimated from S_{gbm}	1.7×10^{-4}
S_{gbm}	Total kidney GBM surface area (cm^2)	Estimated from (3)	5.7
V_{int}	Total kidney interstitial volume (cm^3)	Estimated from (4, 5)	0.025
V_{rt}	Total renal tubules volume (cm^3)	Estimated from V_{kidney}	0.22
f_{cortex}	Volume fraction of cortex	Estimated from (5)	0.7
f_{pct}	Volume fraction of proximal convoluted tubules	Estimated from (5)	0.64
$[HS]_0$	Total heparan sulfate concentration (% ID/cm^3)	Estimated from (7, 8)	4×10^{6}
V_{blood}	Total blood volume (cm^3)	Estimated from (9)	1.5
HCRT	Hematocrit	Estimated from (9)	33%
$V_{bladder}$	Total bladder volume (cm^3)	Estimated from (10)	0.15

Table II: Reaction parameters

Name	Description (units)	Source of data for fitting	Value
A	Plasma concentration (% ID/cm^3)	Blood clearance	35
α	Rate of elimination (min^{-1})	Blood clearance	0.6
P_{gbm}	GBM apparent permeability (cm min^{-1})	Kidney - free siRNA	10000
k_{filter}	Rate of filtration into renal tubules/pelvis (min^{-1})	Kidney - free siRNA	600
$k_{bladder}$	Rate of filtration into bladder (min^{-1})	Kidney - free siRNA	0.2
k_{rt}	Rate of renal tubule reabsorption (% ID cm^{-3} min^{-1})	Kidney - free siRNA	2
K_{ads}	Equilibrium binding constant to GBM (% ID cm^{-3})$^{-1}$	Kidney - nanoparticle	10
k_{deg}	Rate of nanoparticle degradation (min^{-1})	Kidney - nanoparticle	1×10^{-3}
k_{en}	Rate of peri-tubule endothelial uptake (min^{-1})	Kidney - nanoparticle	1.3

References:

1. Takemoto M, et al. A new method for large scale isolation of kidney glomeruli from mice. *Am. J. Pathol.*, **161** (3), 799-805 (2002).
2. Yabuki A, Tanaka S, Matsumoto M and Suzuki S. Morphometric study of gender differences with regard to age-related changes in the C57BL/6 mouse kidney. *Exp. Anim.* **55** (4), 399-404 (2006).
3. Guo M, et al. A stereological study of the renal glomerular vasculature in the db/db mouse model of diabetic nephropathy. *J. Anat.*, **207** (6), 813-821 (2005).
4. Pazvant G, et al. The volume fraction method for the evaluation of the kidney: A stereological study. *Ankara Univ. Vet. Fak. Derg.* **56**, 233-239 (2009).
5. Ross MH and Pawlina W. Histology: A Text and Atlas Edn. 5. (Lippincott Williams & Wilkins 2006).

6. Molitoris BA, et al. siRNA targeted to p53 attenuates ischemic and cisplatin-induced acute kidney injury. *J. Am. Soc. Nephrol.*, **20**, 1754-1764 (2009).
7. Comper WD, Lee AS, Tay M and Adal Y. Anionic charge concentration of rat kidney glomeruli and glomerular basement membrane. *Biochem. J.* **289** (3), 647-652 (1993).
8. Westberg NG and Michael AF. Human glomerular basement membrane. Preparation and composition. *Biochem.*, **9**, 3837-3846 (1970).
9. Riches AC, Sharp JG, Thomas DB and Smith SV. Blood volume determination in the mouse. *J. Physiol.* **228**, 279-284 (1973).
10. Birder LA et al. Altered urinary bladder function in mice lacking the vanilloid receptor TRPV1. *Nat. Neuroscience* **5**, 856-860 (2002).

Chapter 8: Targeted-nanoparticle delivery of siRNA to the kidney glomerulus

8.1 Abstract

The kidney is the site of many acute and chronic conditions that could benefit from the development of kidney targeted therapeutics. Despite this fact, kidney disease remains a relatively overlooked indication for targeted nanoparticle-based therapeutic development. Here, we demonstrate that the kidney is an extremely accessible organ for targeting using nanoparticle-based therapeutics. First, using a well characterized model system of PEGylated gold nanoparticles, we demonstrate the general pattern of nanoparticle kidney distribution in mice following systemic administration using microscopy methods. We show that nanoparticle deposition is restricted to the glomerulus and peri-tubule interstitia. We then show how this model nanoparticle system predicts the major distribution of cationic polymer-based siRNA nanoparticles in the kidney and how the positive surface change and decomposability of the siRNA nanoparticles effect their kidney distribution. We also highlight how the addition of mannose and transferrin targeting ligands can alter the intra-renal distribution of the siRNA nanoparticles to target specific cells within the kidney. Finally, we demonstrate that the siRNA nanoparticles can facilitate delivery of siRNA to the glomerulus and knockdown the expression of glomerular EGFP in transgenic mice.

8.2 Introduction

Nanoparticles have been investigated extensively as therapeutics for tumors and the liver because of their intrinsic proclivity to deposit in these tissues[1,2]. The kidney is another site of nanoparticle accumulation[3]; however, it has been relatively overlooked as

a target for nanoparticle therapeutics. Nanoparticle therapeutics have high therapeutic indexes compared to traditional small molecule drugs, owing to their biodistributions, and enable administration of highly specific therapeutic modalities such as small interference RNA (siRNA)[1].

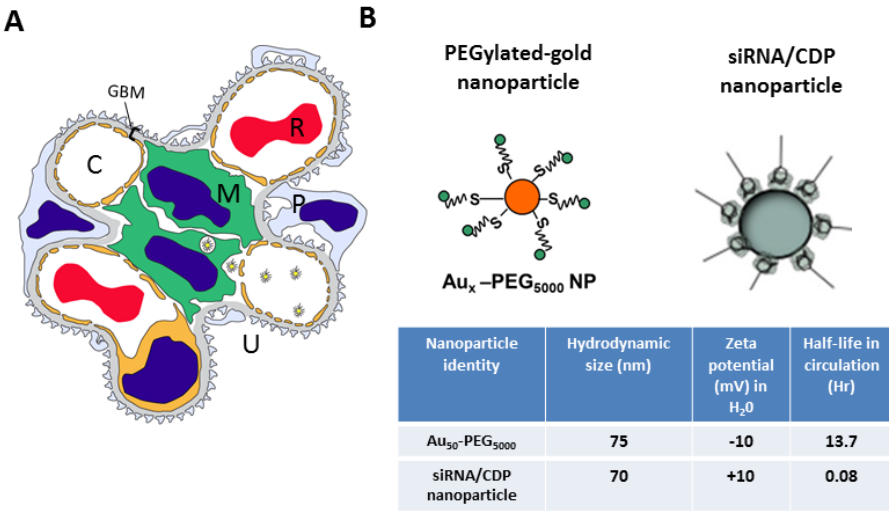

Nanoparticle identity	Hydrodynamic size (nm)	Zeta potential (mV) in H_2O	Half-life in circulation (Hr)
Au_{50}-PEG_{5000}	75	-10	13.7
siRNA/CDP nanoparticle	70	+10	0.08

Figure 8.10: Schematic of kidney glomerulus and nanoparticles used in study. (A) Schematic of glomerular cross section demonstrating nanoparticle deposition into mesangial cells. C=capillary lumen, GBM=glomerular basement membrane, M=mesangium, P=podocyte, U=urinary space. (B) Schematic and physical properties of PEGylated gold nanoparticles and siRNA/CDP nanoparticles.

The glomerulus is a primary site of renal diseases (e.g., IgA nephropathy) and a common secondary site in many systemic disorders (e.g., diabetic nephropathy) that could benefit from kidney specific therapeutics. Mesangial cells are a particularly suitable target for nanoparticles because the glomerular endothelium is fenestrated and there is no basement membrane between the endothelial cells and the mesangium (Fig. 8.1A).

siRNA can be used to inhibit proteins considered to ‘undruggable” by traditional means in a highly specific manner[4]. siRNA requires carriers to facilitate their transport through circulation and uptake at desired sites of actions[5]. We have developed a polymer-

based targeted-nanoparticle formulation of siRNA (Fig. 8.1B) that was shown to accumulate in human tumors and deliver functional siRNA from a systemic, intravenous (i.v.) infusion [6]. This first-in-human study demonstrated the clinical potential for cationic polymer-based siRNA delivery systems.

Here, using a well characterized model system of PEGylated gold nanoparticles we demonstrated that nanoparticles have a characteristic distribution pattern in the kidney following systemic administration. We then show how siRNA nanoparticles of like size follow a similar distribution pattern in the kidney and highlight how differences in the siRNA nanoparticle (positive surface charge and decomposability) alter their distribution. We also investigate how the targeting ligands transferrin and mannose can dramatically alter the intra-renal distribution of the siRNA nanoparticles. Finally, we demonstrate that the siRNA nanoparticle can deliver functional siRNA to the glomerulus and inhibit gene expression.

8.3 Results

8.3.1 Transferrin-targeted PEGylated gold nanoparticles accumulate in glomeruli and peri-tubule interstitia of the kidney following system administration.

Biodistribution studies of nanoparticles composed of micelles or polyplexes can be confounded by their degradation or disassembly *in vivo*. Therefore, we first explored nanoparticle delivery to the kidney using a model system of non-decomposing transferrin-targeted PEGylated gold nanoparticles that mimic the size of the siRNA nanoparticle delivery system (Fig. 8.1B). We employed a silver enhancement technique[3] to visualize the gold nanoparticles in tissue sections via light microscopy and utilized transmission electron microscopy (TEM) to confirm subcellular localization (Fig. 8.2).

Gold nanoparticles with both high (~ 200) and low (~ 2) transferrin contents were found to accumulate within glomeruli in a similar pattern 8 hours after intravenous administration. TEM analysis revealed that within the glomerulus, nanoparticles deposited solely within mesangial cells and matrix. 100% of glomeruli examined were found to contain nanoparticles. We also observed gold nanoparticles in the peri-tubule interstitia throughout the kidney. Transferrin density on the surface of the nanoparticles did not alter the pattern of distribution of the sgold nanoparticles in the kidney, suggesting that nanoparticle uptake by mouse mesangial or peri-tubule interstitial cells was not dependent on the presence of transferrin.

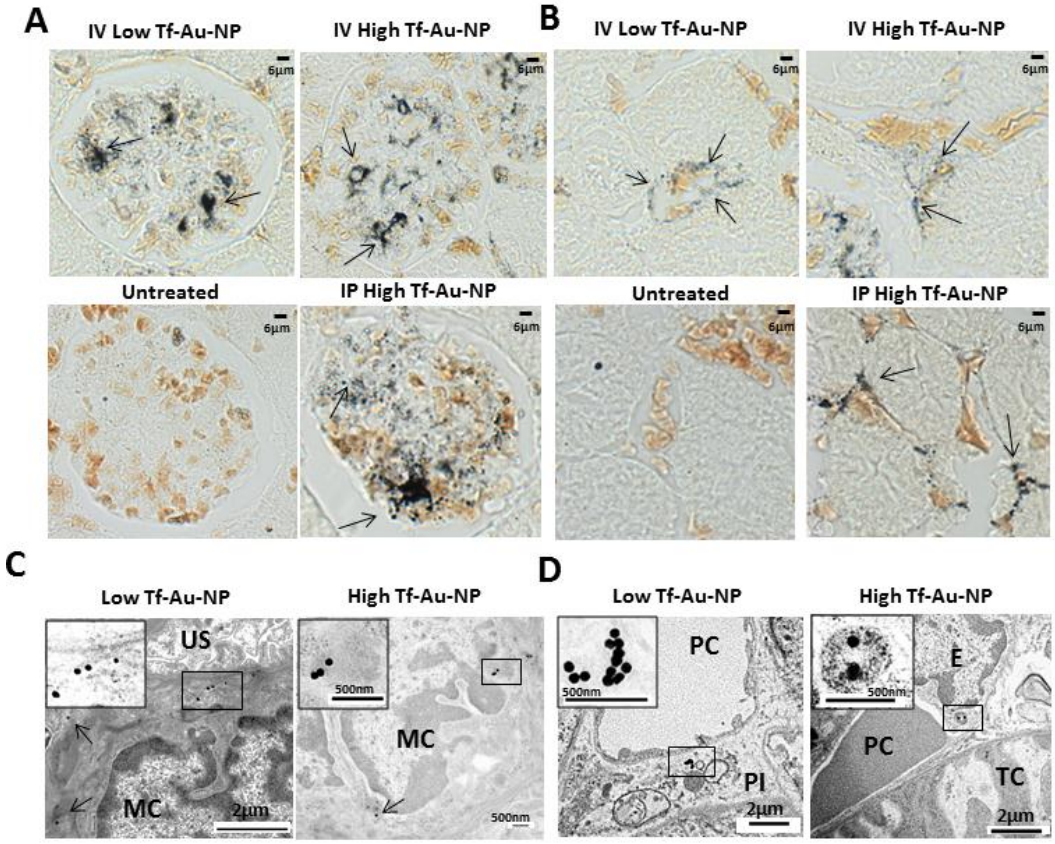

Figure 8.2: Transferrin (Tf) targeted PEGylated gold nanoparticles deposit in the glomerulus following intravenous or intraperitoneal administration. Light micrographs (A) glomeruli and (B) peri-tubule capillaries in kidneys from mice receiving the indicated treatments via intravenous (IV) or intraperitoneal (IP) routes. Low and high indicate ca. 2 and 200 Tf respectively on the PEGylated gold nanoparticles (Au-NPs) surface. Au-NPs appeared as black

speckles on sections following sliver enhancement and red blood cells appear ruddy brown (no counter-stain is used). Scale bar=20 μm. Electron micrographs of (C) mesangial cells and (D) peri-tubule interstitial from kidneys from treated mice. Boxes are magnified view of the boxed gold particles in the micrographs. Scale bars= 200 nm. MC= mesangial cell, US= urinary space, PC=peritubule capillary lumen, PI=peritubule interstitial, TC=tubule cell.

Shimizu et al. have demonstrated that 10-20 nm siRNA micelles can deposit within the glomerulus following intraperitoneal administration [7]. We hypothesized that this phenomenon could be extended to larger size nanoparticles. To test this hypothesis we examined gold nanoparticle distribution in the kidney following an intraperitoneal injection and observed a similar distribution pattern for the gold nanoparticle as observed following intravenous

administration.

8.3.2 siRNA nanoparticle deposition in the kidney is similar to gold nanoparticles but can be influenced by using the targeting ligands mannose or transferrin.

We next examined the kidney biodistribution of intravenously administered siRNA nanoparticles containing fluorescently labeled nucleic acid and polymer components. We also explored how the kidney distribution of the nanoparticles was effected by including different targeting ligands in the siRNA nanoparticle formulation – mannose or transferrin that can facilitate nanoparticle internalization by engaging the mannose receptor (MR) or the transferrin receptor (TfR), respectively. The MR is known to have a restriction expression pattern to mesangial cells within the kidney [8,9], whereas the TfR is a more general receptor expressed by many cell types although not highly in the glomerulus[10]. Confocal microscopy was employed to study the biodistribution of these nanoparticle formulations within the kidney at 10 and 120 minutes post injection.

8.3.3 siRNA nanoparticles, but not free siRNA accumulate in the glomerulus and peri-tubule interstitia.

We examined the distribution of Cy3-labeled siRNA in kidneys from mice receiving intravenous doses of Cy3-siRNA alone or formulated in nanoparticles (Fig. 8.3). We observed fluorescence signal of free Cy3-siRNA localized to proximal tubule cells at 10 minutes post dose, but fluorescence was nearly indistinguishable from background at 120 minutes. In comparison, we detected strong Cy3 fluorescence within all glomeruli at 10 minutes following doses of Cy3-siRNA nanoparticles. The glomerular Cy3 fluorescence signal was localized to the glomerular capillary walls and the mesangium.

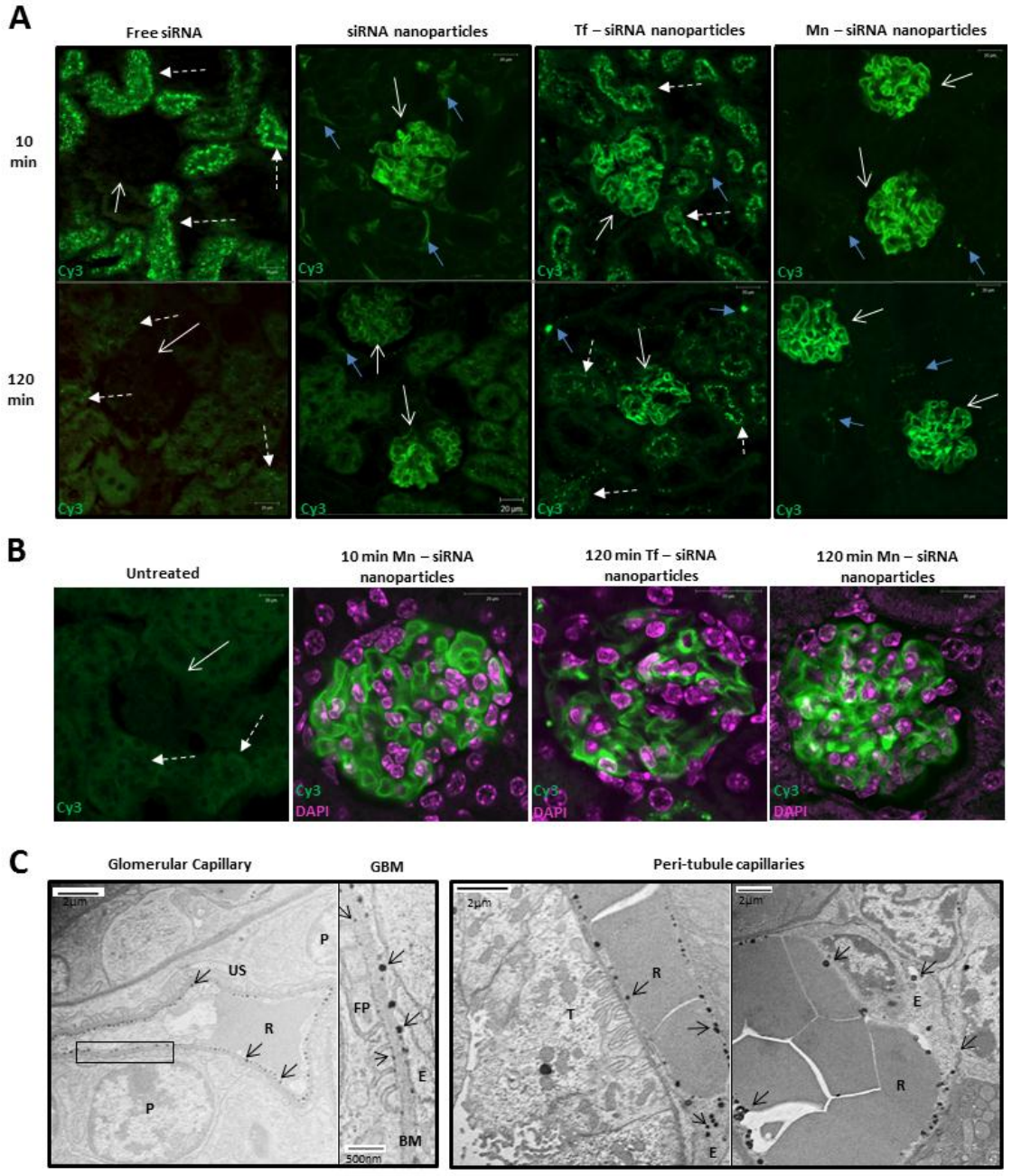

Figure 8.3: siRNA nanoparticles accumulate in mouse glomeruli following i.v. administration (A) Laser scanning confocal microcopy of kidney sections from mice receiving free siRNA or siRNA nanoparticles formulations with Cy3-labeled nucleic acid. (B) Magnified images of glomeruli at 10 min and 120 min from mice receiving either mannose (Mn) or transferrin (Tf)-siRNA nanoparticles. Glomeruli at 10 min appeared similar among all conditions and Tf and non-targeted siRNA nanoparticles appear similar at 2 hours. Detector gain for all images was adjusted for maximal dynamic range or until diffuse green background auto-fluorescence in proximal tubules was apparent (untreated). Images with more visible background are lower in overall fluorescence intensity. White arrows indicate glomeruli, dotted white arrows indicates proximal tubules, blue arrows indicate peri-tubule capillaries, scale bars=20µm. (C) Electron micrographs of kidneys from mice that received doses of untargeted nanoparticles.

Although greatly attenuated, glomerular Cy3 fluorescence was still detected in all glomeruli at 120 min post dose. Whereas at 10 minutes post dose the Cy3 glomerular signal is most intense within the glomerular capillary walls, the Cy3 glomerular signal at 120 minutes is most intense in mesangial regions. Some Cy3 signal was still observed in the glomerular capillary walls.

In a similar fashion to the gold nanoparticles, siRNA nanoparticles were found to deposit within the peri-tubule interstitial of the kidney. The siRNA nanoparticles were found along the walls of the peri-tubule capillaries at 10 minutes and were observed as more punctate structures at 120 minutes.

8.3.4 Transferrin and mannose targeting ligands alter intra-renal distribution of the siRNA nanoparticles.

Transferrin targeting ligand resulted in increased Cy3 fluorescence along the luminal side of the proximal tubule surface at 10 min. At 120 min, this proximal tubule Cy3 signal was observed in deeper locations within the proximal tubule cells. Additionally, Cy3 fluorescence in the proximal tubule cells at 120 min following transferrin-targeted siRNA nanoparticle treatment was much greater than following siRNA administration alone.

Mannose targeting ligand resulted in two changes to siRNA nanoparticle distribution. First, the Cy3 glomerular intensity remained much stronger at the 120 min time point compared to the other nanoparticles formulations. Second, mannose targeting resulted in a more punctate distribution of the siRNA nanoparticles within the peri-tubule interstitia at 10 min and stronger fluorescence at these locations at 120 min compared to the other siRNA nanoparticle formulations.

8.3.5 TEM analyses demonstrate siRNA nanoparticle localization to the GBM and peri-tubule interstitial.

We more closely examined the kidney deposition of the non-targeted siRNA nanoparticles via TEM 10 min after dosing (Fig. 8.3C). We used uranyl acetate staining to detect the presence of nucleic acid nanoparticles in tissue sections because it preferentially binds to nucleic acids including the siRNA within the nanoparticles[11].

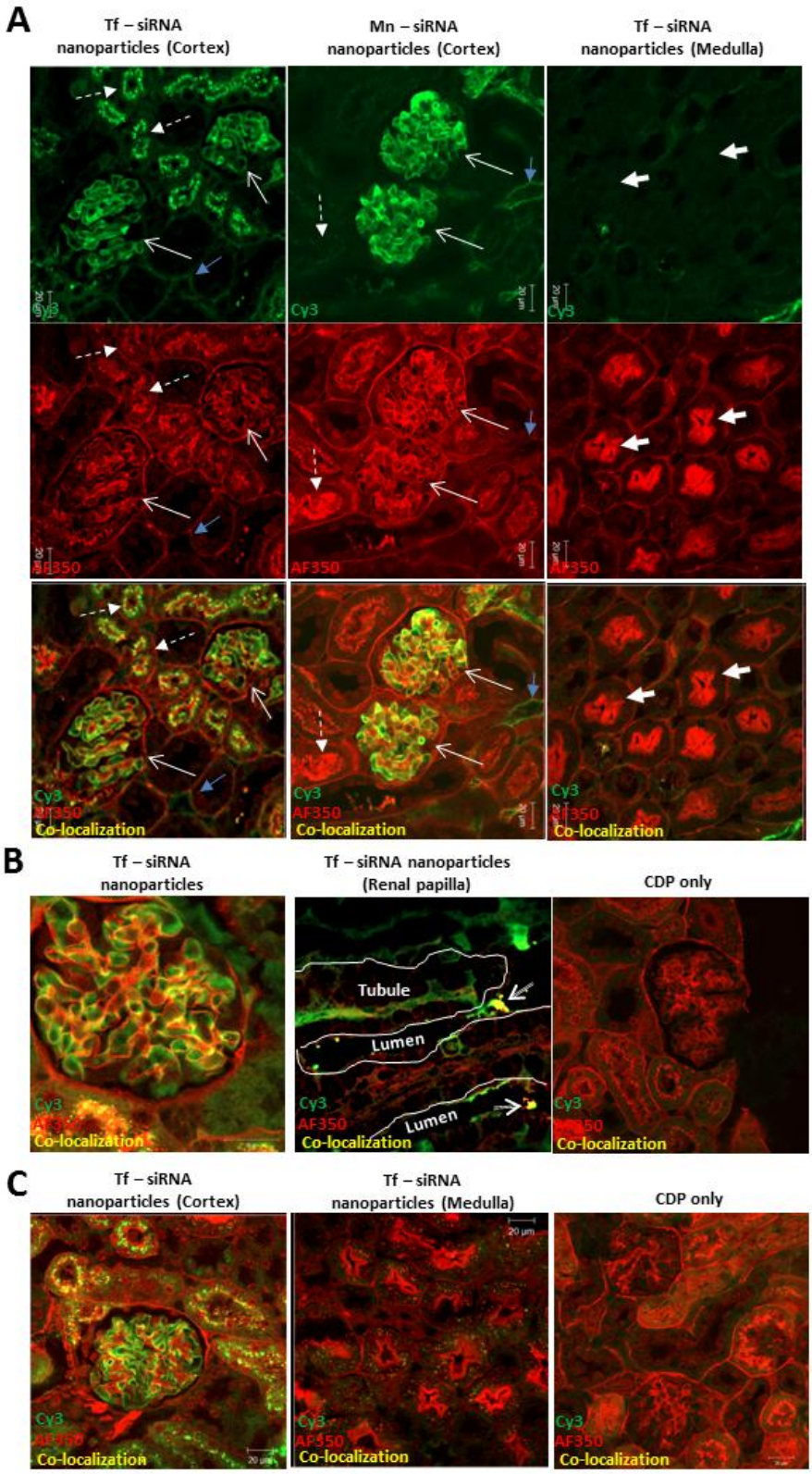

Figure 8.4: Intra-renal distribution of the polymer (CDP) component of the siRNA nanoparticles. (A) Laser scanning confocal microcopy of kidney sections from mice receiving

siRNA nanoparticle formulations with Cy3-labeled nucleic acid and AlexaFluor350 (AF350) labeled CDP at 10 min. White arrows indicate glomeruli, dotted white arrows indicates proximal tubules, blue arrows indicate peri-tubule capillaries, white arrow heads indicate collecting tubules. Green=Cy3-labled nucleic acid, Red= AF350-CDP, yellow=co-localization of Cy3 and AF350 signals. (B) *left* – Images of a glomerulus and *middle* – tip of a renal papilla at 10 min from a kidney of a dual labeled Tf-siRNA nanoparticle treated mouse. Double line arrows = co-localization of Cy3 and AF350 signals in the collecting tubule lumen indicating re-assembly of the nanoparticle components as they are filtered through the kidney. *Right*: image of the kidney cortex from a mouse receiving only AF350-CDP. (C) Images of kidney regions at 120 min from mice receiving the indicated treatment. Images are also reproduced in green and magenta in Supp. Fig. S1.

Within the glomerulus abundant siRNA nanoparticles were observed within the glomerular basement membrane. Many of the smaller siRNA nanoparticles deposited within the lamina rara externa in direct contact with podoctye foot processes. We also observed nanoparticles internalized by endothelial cells lining the peri-tubule capillaries.

8.3.6 The cationic-polymer components (CDP) of the siRNA nanoparticles strongly interacte with different regions of the kidney.

The distribution of the CDP components of the nanoparticles was also examined (Fig. 8.4). Strong AF350-CDP fluorescence that co-localized with the Cy3-siRNA signal was observed in all glomeruli from all siRNA nanoparticle formulations at 10 min. Co-localization of Cy3 and AF350 fluorescence was also observed on the luminal surface of proximal tubules in kidneys from mice that received transferrin targeting nanoparticles. Co-localization between the two nanoparticle components was also observed in these regions at 120 min.

Some CDP was not found to co-localize with the siRNA components of the nanoparticle. AF350-CDP fluorescence was more extensive than Cy3 fluorescence within the mesangial areas of the glomerulus. Also, AF350-CDP signal alone was observed to line the luminal surface of proximal tubules and collecting ducts in kidneys from mice receiving non-targeted and mannose targeted nanoparticles. Examination of kidneys

from mice receiving only the AF350-CDP nanoparticle component revealed similar fluorescence localization; although the free CDP demonstrated a preference for mesanagial deposition compared to CDP administered as nanoparticles which had similar preference for glomerular capillary walls and mesangium.

The pattern of distribution of CDP was persistent at 120 min. These siRNA nanoparticles have been demonstrated to result in elevated BUN and creatinin levels at high doses (27 mg/kg) in monkeys[12] (lower doses 3 and 9 mg/kg did not results in these elevations). The data presented here suggest that the strong interaction between the CDP and kidney components may mediate this toxicity.

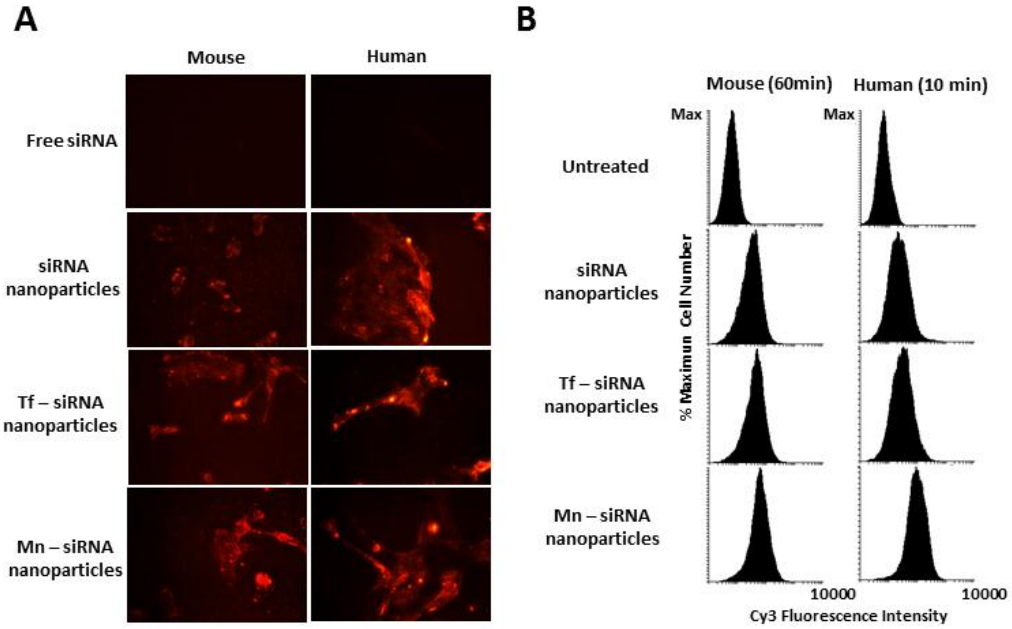

Figure 8.5: siRNA nanoparticles are internalized by mouse and human mesangial cells *in vitro*. (A) Fluorescence microscopy images of mesangial cells following 5 minute incubation with indicated treatment condition. (B) Flow cytometery analysis of mesangial cells following incubation with different Cy3-labeled siRNA nanoparticle formulations. For all expeirments a detergent wash was performed to remove non-internalized nanoparticles/siRNA from the surface of the cells prior to analysis.

8.3.7 Mouse and human mesangial cells internalized siRNA nanoparticles *in vitro*.

To demonstrate the feasibility that human mesangial cells will also internalize siRNA nanoparticles we compared the uptake of siRNA nanoparticles by human and mouse mesangial cells *in vitro*. Mesangial cells from both species internalized the siRNA nanoparticles; even in the absence of a targeting ligand. We observed internalization after only 5 minutes of exposure to the siRNA nanoparticles (Fig. 8.5A). The human mesnagial cells internalized a larger amount of nanoparticles in 10 minutes than their murine counterparts in 1 hour (Fig. 8.5B). Inclusion of transferrin and mannose targeting lingands in the formulation of the siRNA nanoparticles increased their internalization by mouse mesangial cells, but only mannose enhanced uptake by human mesangial cells.

8.3.8 Nanoparticle formulation is required for long term delivery of siRNA to the glomerulus.

We examined for the presence of siRNA in isolated glomeruli from mice 1 or 3 days after they received doses of free siRNA or siRNA nanoparticle formulations (Fig. 8.6A). Real-time PCR was employed to detect the presence of a specific siRNA sequence (siTrace). Although the PCR assay was designed specifically for the siTrace sequence some non-specific background signal was observed in the negative control siCON nanoparticle group.

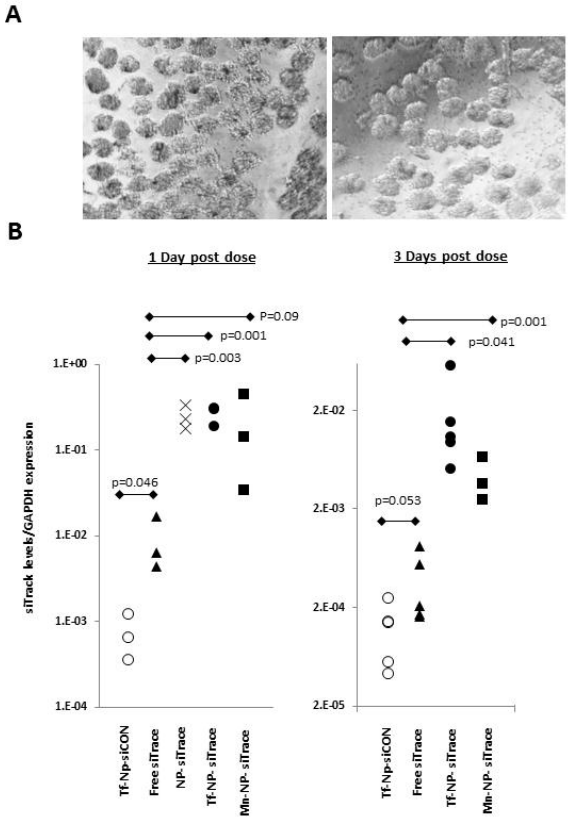

Figure 8.6. Detection of siRNA in isolated glomeruli from mice. (A) Light micrographs of two preparations of isolated glomeruli from mouse kidneys. (B) Real-time PCR based detection of siTrace. siCON= Transferrin-targeted nanoparticles with siCON, Tf-NP siTrace = transferrin-targeted nanoparticles with siTrace, Mn-NP siTrace = mannose-targeted nanoparticles with siTrace. 3 mice (1 day) or 5 mice (3 days) per group, p values are from one tailed t-tests.

At 1 day post dosing we detected siTrace at significant levels above background in glomeruli from all treatment groups. Levels of siTrace in glomeruli from siRNA nanoparticle treatment groups were found to be at least an order of magnitude higher than the free siRNA group. A similar amount of siTrace was detected among glomeruli from all the siRNA nanoparticle treated groups. At 3 days post dosing we detected siTrace at significant levels above background in glomeruli only from animals receiving siRNA in nanoparticle formulation. We observed some increase in average siTrace level over background in the glomeruli from mice receiving free siTrace; however, this level did not reach statistical significance. The transferrin-targeted nanoparticles appeared to deliver

more siTrace to the glomerulus than the mannose-targeted nanoparticles; however, the difference between the two groups did not reach statistical significance.

8.3.9 siRNA nanoparticles silence gene expression in the glomerulus.

We next examined the ability of transferrin and mannose targeted nanoparticle to silence EGFP expression in the glomeruli of transgenic mice. We used fluorescence microcopy to examine EGFP fluorescence in kidney sections from each mouse (Fig. 8.7). Kidneys from mice receiving the control siRNA nanoparticles were found to have strong expression of EGFP throughout their kidneys. Glomerular expression was found to be higher than tubules and podocyte expression appeared higher than mesangial areas. Transferrin and mannose targeted siEGFP nanoparticles were found to reduce glomerular EGFP expression. EGFP knockdown was most noticeable within the mesangial regions of the glomerulus. A significant decrease of high EGFP glomeruli of ~ 2 fold was observed in both Tf- and Mn-nanoparticles. A significant increase in the number of low EGFP glomeruli of ~ 6 fold was observed in the Tf-nanoparticle treated animals, whereas only a 3 fold non-significant increase was noted in the Mn-nanoparticle treatment group. However, a significant increase in the number of intermediate EGFP glomeruli was noted only in the Mn-nanoparticle group.

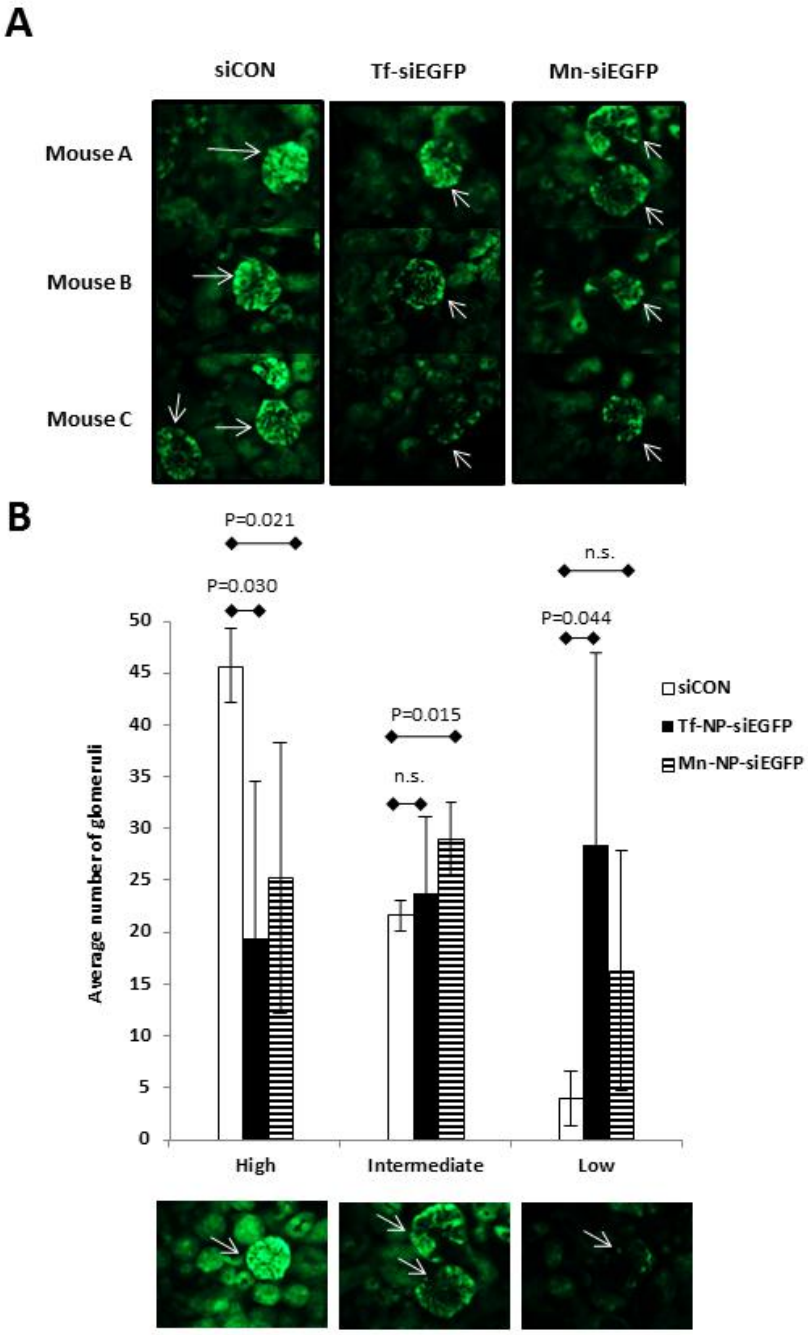

Figure 8.7: EGFP knockdown following administration of siRNA nanoparticles targeting EGFP in EGFP expressing transgenic mice. Mice received control nanoparticles (Tf-nanoparticles siCON), transferrin-targeted nanoparticles with siEGFP (Tf-nanoparticles siEGFP), and mannose-targeted nanoparticles with siEGFP (Mn-nanoparticles siEGFP). Mice received two doses of 10 mg/kg siRNA on day 1 and day3 and kidneys harvested on day 5. (A) Fluorescence micrographs of median intensity glomeruli from each mouse in the experiment. Each column is one treatment condition. White arrows point to position of glomeruli (B) Results of blinded scoring analysis of glomerular EGFP fluorescence intensities. 70-72 glomeruli were imaged from each mouse and scored as high, intermediate, or low EGFP fluorescence (representative examples of each scoring category are pictured). All imaging and scoring were performed in a blinded

fashion. Average number of glomeruli for each scoring bin are shown. Error bars are standard deviation. P values are results of one-tailed t-test.

8.4 Discussion

Here, we have illustrated the feasibility of nanoparticle mediated delivery of therapeutic entities to the kidney glomerulus. We have previously observed kidney accumulation of non-targeted PEGyated gold nanoparticles between 20 and 150nm in size[3]. 75 nm was found to be the optimal size for passive targeting of the kidney due to the competing effects of increased cellular uptake of nanoparticles with increasing size and the ~100nm fenestration size cut off of the glomerular endothelium. Now, we have extended the results of these studies by demonstrating that intraperitoneal administration is also an effective means of nanoparticle delivery to the glomerulus and that glomerular deposition occurred within 8 hours of administration. Furthermore, we demonstrated that the presence of transferrin did not provide for additional uptake by mesangial cells *in vivo* compared to untargeted nanopartilces[3].

We confirmed the generalizability of our findings with the gold nanoparticle model system by demonstrating that similarly sized siRNA nanoparticles deposited in kidney in a nearly identical pattern to the gold nanoparticle system – glomerulus and peri-tubule interstitia. However, there were some differences between the two systems.

First, in addition to mesangial deposition, the siRNA nanoparticles were found to deposit within the GBM. Unlike gold nanoparticles that have a negative surface charge and are likely repelled by the negatively charged GBM, the siRNA nanoparticles have positive surface potentials that allows them to bind there. This localization allowed the siRNA nanoparticles (but not the gold nanoparticles) to contact podocyte foot processes and potentially enable uptake there. Second, tubule uptake was observed for the

transferrin targeted siRNA nanoparticles, but not for the transferrin targeted gold nanoparticle system.

Transferrin targeting resulted in a substantial increase in proximal tubule uptake of siRNA nanoparticles. This phenomenon was not observed with the Tf-gold nanoparticles. Because they are >10nm and are non-decomposable, the gold nanoparticles cannot cross the renal filtration barrier. We have previously demonstrated the siRNA nanoparticles are disassembled by the GBM thereby allowing both siRNA and polymer to be filtered into the urinary space individually[13]. Once in the urinary space the can re-assemble with the CDP in the tubule lumen (Fig. 4B). The re-assembled transferrin targeted siRNA nanoparticles could then engage receptors on the luminal surface of the proximal tubules, enabling their uptake. The receptors responsible for uptake are likely either the transferrin receptor[10] or cubilin, another receptor that has been demonstrated to be responsible for transferrin reabsorption in the proximal tubule [14,15]. Glomerular filtration of the nanoparticle components is required for this type of delivery and a similar phenomenon had been demonstrated for PEI-DNA nanoparticle delivery to proximal tubules[16].

Free siRNA taken up by proximal tubule cells was rapidly degraded, likely because it could not readily escape from the endosome. Transferrin targeted siRNA nanoparticles taken up by the proximal tubule cells were not as rapidly degraded, suggesting that this could be a superior method of delivery to proximal tubules than administration of free siRNA[17]. The siRNA nanoparticles have also been engineered to facilitate endosomal escape[11], whereas the mechanism of endosomal escape for free siRNA is unclear, despite evidence for free siRNA induced silencing of genes in

proximal tubule cells[17]. Additionally, the transferrin receptor has been demonstrated to be up-regulated within the mesangium of patients with IgA nephropathy[18–20] and transferrin targeted particles may also be useful for this indication.

The mannose receptor has been demonstrated to have a restricted expression to the mesangium and interstitial macrophages in the kidney[8,9]. Mannose targeting resulted in an increased residency time for siRNA nanoparticles within the glomerulus. However, these effects may only have been transient as the total amount of siRNA detected in isolated glomeruli by PCR 1 day following intravenous administration was not different among different nanoparticle formulations. Similarly, mannose targeting did not result in any additional benefit in the EGFP knockdown experiment. We speculate that the doses of siRNA nanoparticles used in this study may be saturating and limit the ability of mesangial cells to internalize additional surface bound nanoparticles.

At 3 days post dose a higher amount of siRNA was detected in glomerular isolates from Tf-targeted nanoparticles, it is possible that trace amounts of proximal tubule cell contaminantes may have biased these measurements because only Tf-targeted nanoparticles were demonstrate to accumulate to a high amount in this potential contaminant fraction of tissue.

Mannose receptor 2 has been demonstrated to be upregulated in mouse model of chronic kidney injury induced renal fibrosis and to play a protective role[21]. Mannose targeting could potentially be used to target nanoparticles to sites of kidney fibrosis.

Shimizu et al. have demonstrated that non-targeted 10nm siRNA/cationic polymer micelles can reach the glomerulus following intraperitoneal administration[7]. Administration of these nano-carriers to lpr mice resulted in the decrease of MAPK1

expression and reduced sclerosis within the nephritic glomeruli of these mice. Our data are consistent with this report and further demonstrate the generalizability of this type of approach to other types and sizes of delivery systems and administration methods.

Several other strategies of siRNA delivery to the kidney have been reported. Hauser et al. have demonstrated that a monovalent Ig-protamine conjugate could successfully delivery siRNA to normal murine podocytes *in vivo*[22]. Yuan et al. have also shown that subcutaneous administration of cholesterol conjugated PS modified siRNAs targeting 12/15-lipoxegenase reduced kidney damage in diabetic mice[23]. Other reported examples of siRNA delivery to the glomerulus and kidney in general have employed less clinically applicable direct renal artery injections[24].

We focused our study on healthy kidneys for two reasons. First, we wanted to establish a baseline comparison for future studies in diseased kidneys. Second, we wanted to demonstrate that nanoparticle designed to protect the kidney from effects of systemic diseases could reach healthy regions of the kidney. Reports examining nanoparticle delivery to diseased kidney[25–30] have suggested that nanoparticles have a higher propensity for deposition in the diseased kidney, likely due to increased vascular permeability during states of renal inflammation.

End stage renal failure and chronic kidney disease imposes a large disease burden around the world. Nanoparticle-based therapy has the potential for improving outcome for these patients. The use of siRNA nanoparticles also could facilitate inhibition of well known mediators of renal damage that are difficult to inhibit via traditional small molecule inhibitors. siRNA knockdown may also be a promising strategy to aid in the

understanding of the pathogenesis of renal disease by knockdown of specific in defined locations throughout the kidney.

8.5 Materials and Methods

siRNA nanoparticle formulation: siRNA nanoparticles were formed by using cyclodextrin-containing polycations (CDP) and AD-PEG as previously described (pre-complexation)[31]. Nanoparticles were formed in 5 % glucose in deionized water (D5W) at a charge ratio of 3 +/- and a siRNA concentration of 2 mg/ml unless otherwise indicated. 21 base pair unmodified and Cy3 labeled oligos were purchased from Qiagen. siRNA targeting EGFP is from Novina *et al*. (2002)[32]. siRNA nanoparticle formulated with 80 mole % Cy3-siGL3 and AF350-CDP were similar in size and stability to their non-labeled counterparts (Supp. Fig. S2).

Synthesis and characterization of transferrin and mannose-targeted PEGylated gold nanoparticles: was performed as described previously[33].

Cell culture: SV40-MES (mouse mesangial) cells were obtained from ATCC. Human mesangial cells were obtained from ScienCell. For nanoparticle uptake experiments, cells seeded in 6 well plates were washed with PBS and nanoparticles suspended in 2mL of opti-MEM (Invitrogen) were applied. At the indicated time points the nanoparticle solution was removed and the cells washed with cell scrub buffer (Gene Therapy Systems) to remove surface associated nanoparticles or nucleic acids prior to analysis.

Synthesis of Alexa-Fluor 350 Labeled CDP: CDP (30mg) and Alexa Fluor® 350 succinimidyl ester (5mg, Invitrogen) were transferred to a flask wrapped in aluminum foil and dried under vacuum for 2 hours. 0.5ml of anhydrous dimethyl sulfoxide and

N,N-diisopropylethylamine (0.7ul) were subsequently added under argon. The reaction was allowed to proceed in the dark under argon with constant stirring overnight. The reaction mixture was dialyzed against water three times via a 3kDa membrane centrifuge filter device (Amicon). The retentate was then filtered through a 0.2um filter (Palls) and lyophilized to yield a yellow colored product.

Animal Studies: All animals were treated according to the NIH Guidelines for Animal Care and Use as approved by the Caltech Institutional Animal Care and Use Committee. 6 to 9-week old, female Balb/c mice and C57BL/6-Tg(CAG-EGFP)1Osb/J (Stock #: 003291) mice were obtained from the Jackson Laboratory. Mice were euthanized by CO_2 overdose for organ collection at indicated time points. All organs were fixed in 4 % (w/v) paraformaldehyde (PFA) in PBS overnight. For confocal imaging, nanoparticle formulations contain 80 mole % Cy3-siGL3 and AF350-CDP. Formalin-fixed organs were dehydrated and embedded in molten paraffin to generate sections of 4-μm in thickness.

Histology with silver enhancement: Deparrifinized sections were rehydrated with a reducing ethanol gradient and rinsed with deionized water extensively, dried, and stained for gold nanoparticles using the Silver Enhancement Kit for Light and Electron Microscopy (Ted Pella) for 20 min at RT. After rinsing with running tap water for 2 min, sections were mounted with Permount for viewing under an Olympus X50 fluorescent microscope (with a 40x/1.3 oil objective).

Transmission electron microcopy: Tissue blocks (~1 mm^3) were fixed in 2.5 % glutaraldehyde (in 0.1 M sodium cacodylate, pH = 7.4) for 2 h, stained by 1 % OsO_4 at 4 °C for 2 h, and 0.9 % OsO_4 and 0.3 % $K_4Fe(CN)_6$ at 4 °C for 2 h. Gradual dehydration

with ethanol and propylene oxide enabled tissue embedding in Epon 812 resins (Electron Microscopy Sciences). 80 nm thick sections were deposited on carbon and formvar-coated, 200-mesh, nickel grids (EMS) and stained with 3 % uranyl acetate and Reynolds lead citrate for visualization under a 300 kV TF30UT transmission electron microscope (FEI).

Fluorescent Microscopy: Sections were deparrafinized with xylene, rehydrated, and mounted with ProLong Gold antifade reagent (Invitrogen) for viewing. *Confocal microscopy*: Images were obtained on a Zeiss LSM 510 inverted confocal scanning microscope (with a Zeiss PlanApochormat×63/1.4 oil objective). The excitation wavelengths of Alexa Fluor 350-CDPs and Cy3-siRNAs are 705 nm (two-photon laser) and 543 nm (HeNe laser), respectively. Their corresponding emission filters are 390-465 nm and 565-615 nm, respectively. The measured resolution at which images were acquired is 512×512 pixels, and the image bit-depth is 8-bit. The Zeiss LSM Image Browser Software allows the extraction of images. *Epi-fluorescent microscopy*: Images were obtained on an Olympus IX50 fluorescent microscope (with an Olympus Planfluor 40x/1.3 oil objective). The measured resolution at which images were acquired is 512×512 pixels, and the image bit-depth is 8-bit.

Magnetic bead based Glomerular isolation: Glomeruli were isolated using the method developed by Takemoto et al.[33]. Mice were euthanized prior to magnetic bead perfusion.

RNA isolation: Total RNA was isolated from cells using the miRNeasy kit (Qiagen) following manufacturer's instructions and quantified using a Nanodrop 2000 spectrophotometer (Thermo).

Real time reverse transcriptase PCR: Custom Taqman miRNA qPCR assays (Applied Biosystems) for siTrack were used for quantification of siRNA from total RNA. Real-time PCR analysis was performed using a MyiQ Single Color Real Time PCR Detection System (Bio-Rad).

8.6 Acknowledgments:

We would like to thank Carol M. Garland (Caltech) for help obtaining electron microscopy images. This work benefited from the use of the Caltech Materials Science TEM facility which is partially supported by the MRSEC Program of the National Science Foundation under award number DMR-0520565. This work was supported by National Cancer Institute Grant CA119347 and Sanofi-Aventis. Jonathan E. Zuckerman is also supported by the Caltech-UCLA Joint Center for Translational Medicine.

8.7 Citations:

1. Davis, M.E., Chen, Z.G. & Shin, D.M. Nanoparticle therapeutics: an emerging treatment modality for cancer. Nature Reviews. Drug Discovery 7, 771-82 (2008).

2. Popielarski, S.R., Hu-Lieskovan, S., French, S.W., Triche, T.J. & Davis, M.E. A nanoparticle-based model delivery system to guide the rational design of gene delivery to the liver. 2. In vitro and in vivo uptake results. Bioconjugate Chemistry 16, 1071-80 (2005).

3. Choi, C.H.J., Zuckerman, J.E., Webster, P. & Davis, M.E. Targeting kidney mesangium by nanoparticles of defined size. Proceedings of the National Academy of Sciences of the United States of America 108, 6656-61 (2011).

4. Castanotto, D. & Rossi, J.J. The promises and pitfalls of RNA-interference-based therapeutics. Nature 457, 426-33 (2009).

5. Rettig, G.R. & Behlke, M. a Progress Toward In Vivo Use of siRNAs-II. Molecular Therapy : the journal of the American Society of Gene Therapy 1-30 (2011).

6. Davis, M.E. et al. Evidence of RNAi in humans from systemically administered siRNA via targeted nanoparticles. Nature 464, 1067-70 (2010).

7. Shimizu, H. et al. siRNA-based therapy ameliorates glomerulonephritis. Journal of the American Society of Nephrology : JASN 21, 622-33 (2010).

8. Linehan, S. a, Martínez-Pomares, L., Stahl, P.D. & Gordon, S. Mannose receptor and its putative ligands in normal murine lymphoid and nonlymphoid organs: In situ expression of mannose receptor by selected macrophages, endothelial cells, perivascular microglia, and mesangial cells, but not dendritic cells. The Journal of Experimental Medicine 189, 1961-72 (1999).

9. Zhang, X.S., Brondyk, W., Lydon, J.T., Thurberg, B.L. & Piepenhagen, P. a Biotherapeutic target or sink: analysis of the macrophage mannose receptor tissue distribution in murine models of lysosomal storage diseases. Journal of Inherited Metabolic Disease 34, 795-809 (2011).

10. Zhang, D., Meyron-Holtz, E. & Rouault, T. a Renal iron metabolism: transferrin iron delivery and the role of iron regulatory proteins. Journal of the American Society of Nephrology : JASN 18, 401-6 (2007).

11. Mishra, S., Heidel, J.D., Webster, P. & Davis, M.E. Imidazole groups on a linear, cyclodextrin-containing polycation produce enhanced gene delivery via multiple processes. Journal of Controlled Release 116, 179-91 (2006).

12. Heidel, J.D. et al. Administration in non-human primates of escalating intravenous doses of targeted nanoparticles containing ribonucleotide reductase subunit M2 siRNA. Proceedings of the National Academy of Sciences of the United States of America 104, 5715-21 (2007).

13. Zuckerman, J.E., Choi, C.H.J., Han, H. & Davis, M.E. Polycation-siRNA nanoparticles can disassemble at the kidney glomerular basement membrane. Proceedings of the National Academy of Sciences of the United States of America 2012, (2012).

14. Kozyraki, R. et al. Megalin-dependent cubilin-mediated endocytosis is a major pathway for the apical uptake of transferrin in polarized epithelia. Proceedings of the National Academy of Sciences of the United States of America 98, 12491-6 (2001).

15. Amsellem, S. et al. Cubilin is essential for albumin reabsorption in the renal proximal tubule. Journal of the American Society of Nephrology : JASN 21, 1859-67 (2010).

16. Foglieni, C. et al. Glomerular filtration is required for transfection of proximal tubular cells in the rat kidney following injection of DNA complexes into the renal artery. Gene Therapy 7, 279-85 (2000).

17. Molitoris, B. a et al. siRNA targeted to p53 attenuates ischemic and cisplatin-induced acute kidney injury. Journal of the American Society of Nephrology : JASN 20, 1754-64 (2009).

18. Haddad, E. Enhanced Expression of the CD71 Mesangial IgA1 Receptor in Berger Disease and Henoch-Schonlein Nephritis: Association between CD71 Expression and IgA Deposits. Journal of the American Society of Nephrology 14, 327-337 (2003).

19. Moura, I.C. et al. Identification of the transferrin receptor as a novel immunoglobulin (Ig)A1 receptor and its enhanced expression on mesangial cells in IgA nephropathy. The Journal of Experimental Medicine 194, 417-25 (2001).

20. Berthelot, L. et al. Transglutaminase is essential for IgA nephropathy development acting through IgA receptors. The Journal of Experimental Medicine (2012).

21. López-Guisa, J.M. et al. Mannose Receptor 2 Attenuates Renal Fibrosis. Journal of the American Society of Nephrology : JASN 1-16 (2011).

22. Hauser, P.V. et al. Novel siRNA delivery system to target podocytes in vivo. PloS one 5, e9463 (2010).

23. Yuan, H. et al. Effects of cholesterol-tagged small interfering RNAs targeting 12/15-lipoxygenase on parameters of diabetic nephropathy in a mouse model of type 1 diabetes. American Journal of Physiology. 295, F605-17 (2008).

24. Stokman, G., Qin, Y., Rácz, Z., Hamar, P. & Price, L.S. Application of siRNA in targeting protein expression in kidney disease. Advanced Drug Delivery Reviews 62, 1378-89 (2010).

25. Suana, A.J. et al. Single Application of Low-Dose Mycophenolate Mofetil-OX7-Immunoliposomes Ameliorates Experimental Mesangial Proliferative Glomerulonephritis. Pharmacology 337, 411-422 (2011).

26. Liao, J. et al. Effect of steroid-liposome on immunohistopathology of IgA nephropathy in ddY mice. Nephron 89, 194-200 (2001).

27. Ito, K. et al. Liposome-mediated transfer of nitric oxide synthase gene improves renal function in ureteral obstruction in rats. Kidney International 66, 1365-75 (2004).

28. Tuffin, G., Waelti, E., Huwyler, J., Hammer, C. & Marti, H.-P. Immunoliposome targeting to mesangial cells: a promising strategy for specific drug delivery to the kidney. Journal of the American Society of Nephrology : JASN 16, 3295-305 (2005).

29. Scindia, Y., Deshmukh, U., Thimmalapura, P.-R. & Bagavant, H. Anti-alpha8 integrin immunoliposomes in glomeruli of lupus-susceptible mice: a novel system for delivery of therapeutic agents to the renal glomerulus in systemic lupus erythematosus. Arthritis and Rheumatism 58, 3884-91 (2008).

30. Asgeirsdóttir, S. a et al. Inhibition of proinflammatory genes in anti-GBM glomerulonephritis by targeted dexamethasone-loaded AbEsel liposomes. American journal of physiology. 294, F554-61 (2008).

31. Bartlett, D.W. & Davis, M.E. Physicochemical and biological characterization of targeted, nucleic acid-containing nanoparticles. Bioconjugate Chemistry 18, 456-68 (2007).

32. Novina, C.D. et al. siRNA-directed inhibition of HIV-1 infection. Nature Medicine 8, 681-6 (2002).

33. Choi, C.H.J., Alabi, C. a, Webster, P. & Davis, M.E. Mechanism of active targeting in solid tumors with transferrin-containing gold nanoparticles. Proceedings of the National Academy of Sciences of the United States of America 107, 1235-40 (2010).

8.8 Supplementary Information for Chapter 8

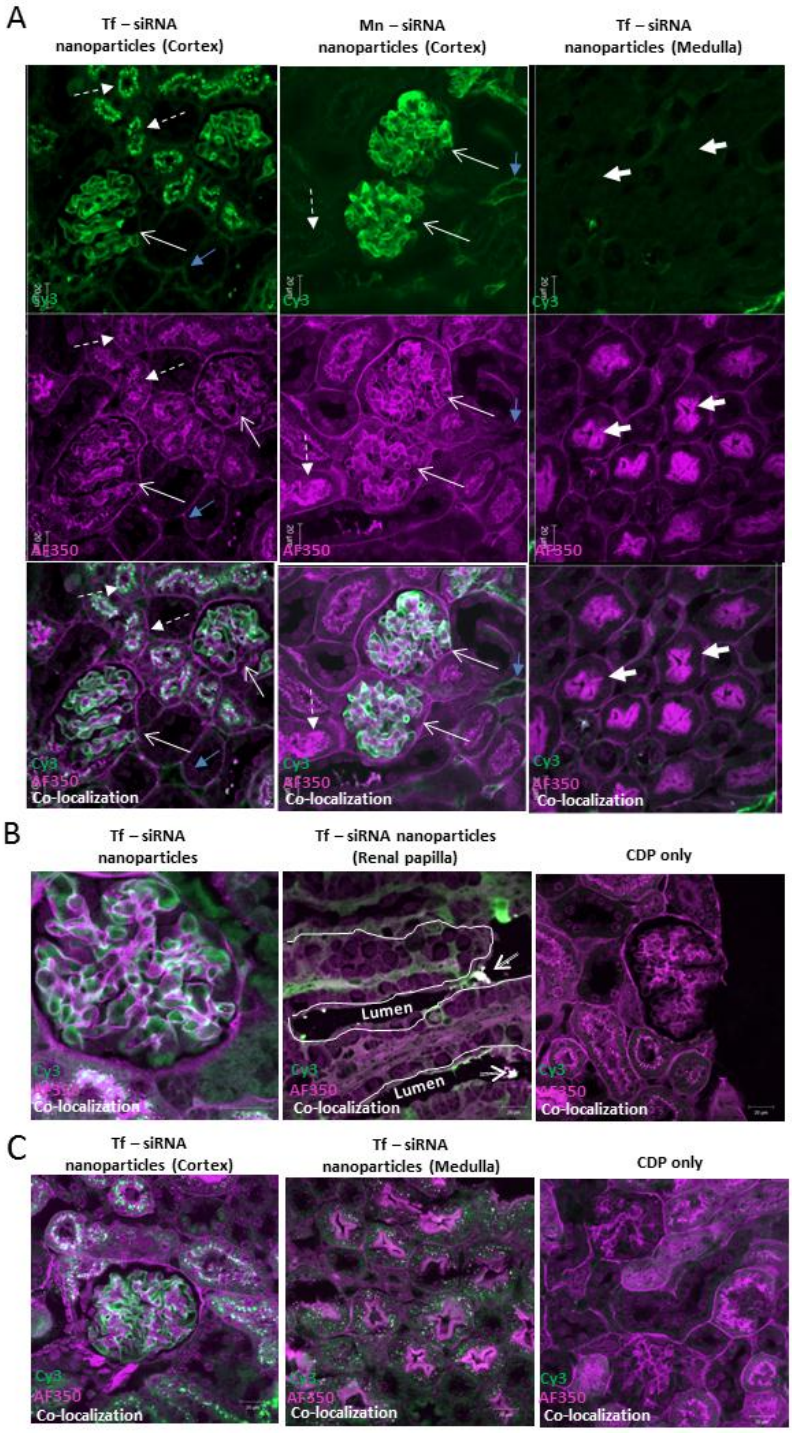

Supplemental Figure S1: Intra-renal distribution of the polymer (CDP) component of the siRNA nanoparticles in green and magenta pseudocolor. (A) Laser scanning confocal microcopy of kidney sections from mice receiving siRNA nanoparticle formulations with Cy3-labeled nucleic acid and AlexaFluor350 (AF350) labeled CDP at 10 min. White arrows indicate glomeruli, dotted white arrows indicates proximal tubules, blue arrows

indicate peri-tubule capillaries, white arrow heads indicate collecting tubules. Green=Cy3-labled nucleic acid, Red= AF350-CDP, yellow=co-localization of Cy3 and AF350 signals. (B) *left* – Images of a glomerulus and *middle* – tip of a renal papilla at 10 min from a kidney of a dual labeled Tf-siRNA nanoparticle treated mouse. Circles indicate co-localization of Cy3 and AF350 signals in the collecting tubule lumen indicating re-assembly of the nanoparticle components as they are filtered through the kidney. *Right*: image of the kidney cortex from a mouse receiving only AF350-CDP. (C) Images of kidney regions at 120 min from mice receiving the indicated treatment.

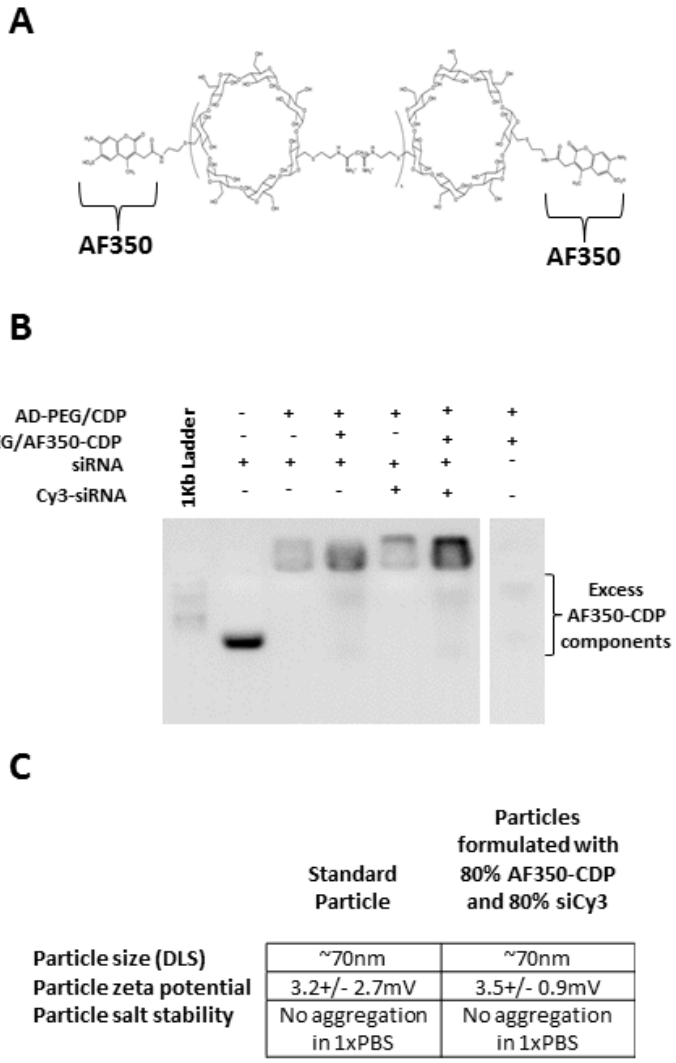

C

	Standard Particle	Particles formulated with 80% AF350-CDP and 80% siCy3
Particle size (DLS)	~70nm	~70nm
Particle zeta potential	3.2+/- 2.7mV	3.5+/- 0.9mV
Particle salt stability	No aggregation in 1xPBS	No aggregation in 1xPBS

Supplemental Figure S2: Characterization of dual-labeled fluorescent siRNA nanoparticles. (A) AlexaFluor 350 (AF350) is conjugated to the terminal ends of the CDP in place of imidazole. (B) The presence of 80% Cy3-siRNA and/or 80% AF350-CDP did not affect siRNA encapsulation. (C) Particles formulated with an 80% fluorescently labeled fraction of CDP and siRNA are similar in size, zeta potential, and stability to the standard particle

formulation. To measure salt stability, particle size was tracked by DLS for 5min, then PBS was added to make 1xPBS solution, the sample was then immediately put back into the DLS machine and tracked for a further 10min.

Chapter 9: Evaluating the potential of using exosomal and plasma microRNAs as markers of drug activity: B-Raf(V600E) inhibition in melanoma as a model system.

9.1 Abstract:

MicroRNAs have emerged as promising biomarkers for cancer owing to their stability in bio-specimens (tissue and blood) and their relative ease of detection. Here, we evaluated the hypothesis that exosomal microRNAs secreted from melanoma cells can be used as marker of drug activity. We first characterized the total RNA content of cell line derived melanoma exosomes by deep sequencing to understand the relationship between intracellular and exosomal RNA. We found that relative abundances of mRNAs and mature microRNAs were correlated between cells and exosomes. Additionally, we found that exosomes were enriched for tRNA, intronic and intergenic sequences of RNA. Using microarray profiling and real-time PCR, we examined the kinetics of intracellular microRNA expression changes following treatment with the B-Raf inhibitor PLX4720. We observed treatment specific microRNA expression alterations that reached maximum magnitudes at 24 hours post treatment. We also examined the microRNA expression profile of two melanoma cell lines with acquired resistance to B-Raf inhibitor therapy and found that different mechanisms of drug resistance were associated with different alterations to the microRNA transcriptome. We demonstrated that PXL4720 treatment resulted in detectable changes to microRNA levels in melanoma cell line derived exosomes. We performed label-free quantitative mass-spectrometery proteomic analysis of exosomes from PLX4720 treated cells. We observed clear changes to protein levels in exosomes related to PLX4720 treated, such as up-regulation of several receptor tyrosine kinases. Finally, we examined the microRNA expression profile in plasma from seven

melanoma patients before and after initiation of B-Raf inhibitor therapy and compared these expression patterns to 5 healthy patient plasma samples. We observed changes in circulating levels of several microRNAs we speculate could have been related to treatment response.

9.2 Introduction:

Incorporation of non-invasively measured markers of drug action and disease response into clinical trial design could aide in the evaluation of therapeutic compounds. For development of targeted therapeutics in particular, trials designed solely to assess maximal tolerable dose (MTD) and treatment efficiency based on Response Evaluation Criteria In Solid Tumors (RECIST) are less applicable than for cytotoxic chemotherapies[1]. In clinical trials evaluating targeted therapeutics other functional determinants of the biologic activity and clinical responses are also necessary for establishing their mechanism in patients. As we learned from the clinical trial whose results we presented in Chapter 2 of this thesis, getting biopsy samples to achieve mechanistic proof of function is challenging. Establishment of non-invasive blood-based analyses that can provide evidence about a targeted therapy's mechanism of action in patients is highly desirable.

MicroRNA (miRNA) are ~22 nucleotide long, endogenous non-coding RNAs that regulate gene expression post-transcriptionally. miRNAs have emerged as an extremely promising new class of biomarkers. Besides their unusually high stability in formalin fixed tissue, miRNAs have been demonstrated to be remarkably stable in human blood[2].

Some circulating miRNAs are believed to be packaged into small membrane bound vesicles known as exosomes (c.a. 10-100nm in diameter) shed from tumors into

circulation [3]. This packaging is thought to protect the RNA from degradation in the extra-cellular environment. Several types of cancer are associated with increases in circulating exosome populations including melanoma, lung, and ovarian cancers[4–6]. In ovarian cancer the increases in circulating exosomes have been demonstrated to be proportional to increasing disease stage[4]. Exosomes can be isolated from patient blood based on their physical characteristics (size, density) and protein markers. Therefore, analysis of this population of vesicles isolated out of blood, if selected via tumor markers, may provide specific information about the tumor itself.

The miRNA profile of tumor derived exosomes has been reported to be representative of the intracellular miRNA profile from the cells they are derived from[7]. However, several reports have demonstrated that there may be preferential enrichment or depletion of certain miRNAs from exosomes[8]. Advanced stage melanoma patients have an increased level of exosomes in their circulation[5] and significant effort has been made to understand the miRNA expression alterations associated with progressive disease, mutational status, and survival[9,10]. Surprisingly, to date, no miRNA profiling has been performed on extracellular RNA derived from melanoma patients or cell lines. A single study has examined miRNA profile from circulating blood cells; however, analysis of miRNA from this population of erythrocytes and white blood cells may not be as informative as analysis of circulating miRNA derived from tumor tissue directly[11]. Additionally, a single study has investigated plasma levels of miR-221 in melanoma patients[12].

We believe that cell-free circulating miRNA encapsulated in tumor derived exosomes could serve as useful, time-dependent biomarkers for melanoma diagnosis and

monitoring of disease progression. Here, we tested the hypothesis that intracellular changes to the microRNA transcriptome induced by drug treatment can be measured in tumor derived exosomes. To test this hypothesis we employed a clinically relevant model system, pharmacologic inhibition of B-RafV600E in melanoma. Vemurafenib is an inhibitor of the mutant B-Raf kinase (V600E). It was discovered using a crystallography-guided, scaffold-based drug design approach[13]. This approach allowed for an inhibitor that preferentially bound to the mutant form of the B-Raf kinase (affinity of 31nM versus 100nM for the wild type) [13]. Only cells harboring B-Raf(V600E) are sensitive to vemurafenib treatment[16,17] Early clinical trials demonstrated a remarkable 80% response rate and since then it has been demonstrated to prolong patient survival and gained FDA approval[14]; however, acquired drug resistance emerges frequently[15]. Paradoxically, vemurafenib treatment results in stimulation of the MAPK pathway in some BRAF wild type cells[18]. Therefore, we hypothesized that inhibition of B-Raf with an analogue of vemurafenib, PLX4720, would result in treatment specific changes to the microRNA transcriptome that will be measureable in exosomes secreted from PLX4720 treated melanoma cell lines and tumors. Additionally, we hypothesized that we could detect treatment related changes in circulating microRNA from the plasma of melanoma patients receiving B-Raf inhibitors.

9.3 Results:

9.3.1 Isolation and characterization exosomes secreted from human melanoma cell lines.

We first developed a protocol for isolation of exosomes from melanoma cell culture media utilizing a differential centrifugation protocol based on previous work[19].

Successful isolation of exosomes was confirmed by electron microscopy (cup shaped morphology) and western blotting (CD63 enrichment in exosomes) (Fig. 9.1). RNA was then isolated from cells and their corresponding exosomes. RNA from exosomes was found to be enriched for low molecular weight RNA species (Fig. 9.1B). Overall, the total amount of RNA in exosomes is several orders of magnitude less than the total amount of RNA found in cells. Melanoma exosomes were also found to contain N-Ras protein and the transferrin receptor (Fig. 9.1C).

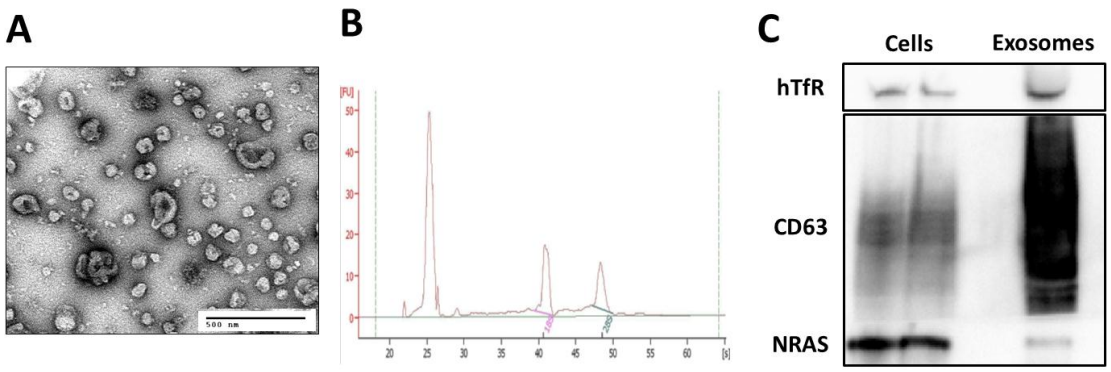

Figure 9.11: Isolation and characterization of exosomes secreted from M202 melanoma cells. (A) TEM analysis of purified exosomes. (B) Bioanalyzer trace of exosomal RNA, peak at 25 seconds is low molecular weight RNA fraction. (C) Western blot analysis of exosomal marker CD63 in cells and exosomes.

9.3.2 Characterization of mRNA and microRNA profiles of exosomes secreted by melanoma cell lines.

We quantitatively examined the levels of mRNA and microRNA in two human melanoma cell lines and their secreted exosomes. RNA-seq analysis revealed global differences in the type of RNA present intracellularly and within exosomes (Fig. 9.2A). We observed depletion in exonic and enrichment in intronic mRNA sequences within exosomes. Additionally, we observed enrichment in intergenic sequences within exosomes. The relative abundances of mRNA were found to be correlated between cells

and exosomes in both cell lines (Fig.9.2B). 711 mRNA transcripts were found to be differentially enriched between cells and exosomes.

A

	Cell Line	Exon%	Intron%	Intergenic%
Intracellular	M202	26	39	35
	M249	38	24	38
Exosomes	M202	6	46	48
	M249	3	46	51

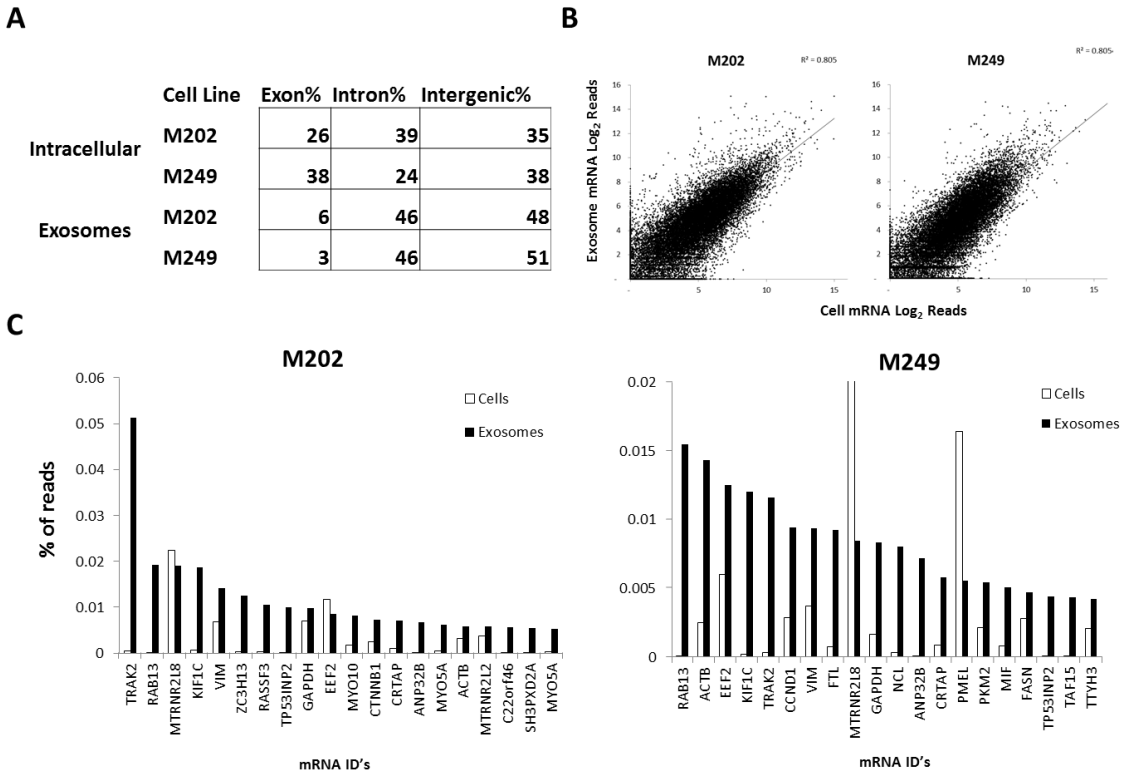

Figure 9.12: RNA-seq analysis of M202 and M249 human melanoma cell lines and their secreted exosomes. (A) Global composition of cellular and exosomal RNA. (B) Scatter plot of Log_2 sequence reads of mRNA transcripts from cells and exosomes. (C) Top twenty most abundant mRNA transcripts in exosomes from both cell lines.

The 464 exosomally enriched transcripts were found to be related to ribonucleoprotein complexes, translation initiation, microtubules, and chromosome assembly. The 247 exosomally depleted transcripts were related to the mitochondrion, protein transport, and ribosomal proteins. The most abundant exosomal transcripts were found to be highly enriched compared to intracellular transcripts (Fig. 9.2C). Several of the highest abundance exosomal transcripts were found to be common between the two cell lines including TRAK2, RAB13, KIF1C, VIM, and EEF2.

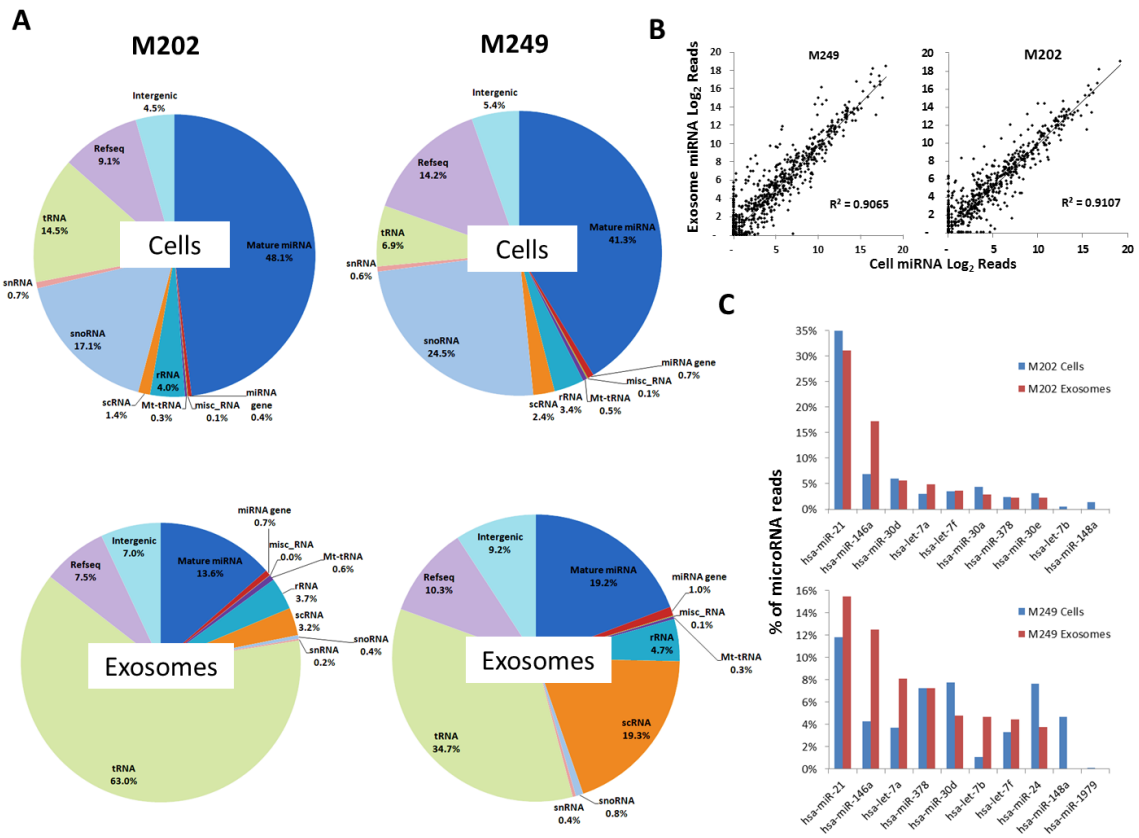

Figure 9.3: smRNA-seq analysis of M202 and M249 human melanoma cell lines and their secreted exosomes. (A) Global composition of cellular and exosomal small RNA. (B) Scatter plot of Log_2 sequence reads of mature microRNAs from cells and exosomes. (C) Histogram of the top 10 most abundant microRNAs in exosomes and their corresponding intracellular levels.

We next characterized the low molecular weight RNA species within the cells and exosomes (Fig. 9.3). Intracellularly, microRNAs made up the majority of small RNA species. In exosomes, tRNA was found to be the dominant small RNA specie while mature microRNA composed only 13-19% of the total small RNA population. The M249 cell line was also found have an enriched population of scRNA. Only trace amounts of immature microRNAs were detected.

Globally, the abundances of microRNA species in cells and exosomes were found to be correlated in both cell lines (Fig. 9.3B). We observed that 2 microRNAs dominated the expression pattern of cells and exosomes of both cell lines– miR-21 and miR -146a.

MiR-30d and let-7a were also found in high abundance in both cell lines. We observed differential enrichment of 53 and 74 microRNAs into exosomes of M202 and M249 cell lines respectively; 43 of which were common between the two cell lines.

9.3.3 Kinetics of miRNA expression changes following B-Raf(V600E) inhibition by PLX4720 treatment.

We examined the microRNA transcriptome of three B-Raf(V600E) positive human melanoma cell lines by microarray analysis at multiple time points after treatment with 1μM PLX4720 (Fig. 9.4). All three cell lines, M249, M229, and HT-144 have PLX4720 EC50s below 1μM. At 6 hours post treatment we observed 28 differentially expressed microRNAs between PLX4720 and DMSO control treated samples. microRNAs were considered differentially expressed if they were found to be significantly up or down regulated at least 1.5 fold in 2 of the 3 cell lines tested. Most PXL4720 induced microRNA changes were increases in expression between 1.5 and 3 fold. Only two microRNAs, miR-29b* and miR-222* were found to respond to PLX4720 treatment (~2 fold decrease) in all three cell lines.

At 24 hours post treatment we observed 58 differentially expressed microRNAs in the PLX4720 treated cells. The magnitude of the expression changes were also increased, although no changes greater than 8.33 fold were observed in any cell line. 15 microRNAs were found to respond to PLX4720 treatment in all three cell lines (14 up regulated, 1 down regulated). miR-3663-3p was up regulated among all three cell lines the most (5.6 fold average) and mR-92a was down regulated the most (0.6 fold average). Several up regulated microRNAs at 6 hours were found to be further up regulated at 24 hours.

At 72 hours the number of differentially expressed microRNAs had decreased to 29. 4 microRNAs were found to be differentially expressed in all PLX4720 treated cells at this time point, miR-211, miR-92a, miR-1972, and miR-338-3p. miR-211 was the only microRNA elevated >2 fold in all cell lines.

To validate the microarray results, we examined the expression of 7 microRNAs via real-time PCR at 48 hours post PXL4720 treatment (Fig. 9.4B). The PCR data matched closely the data obtained from the 72 hours microarray study.

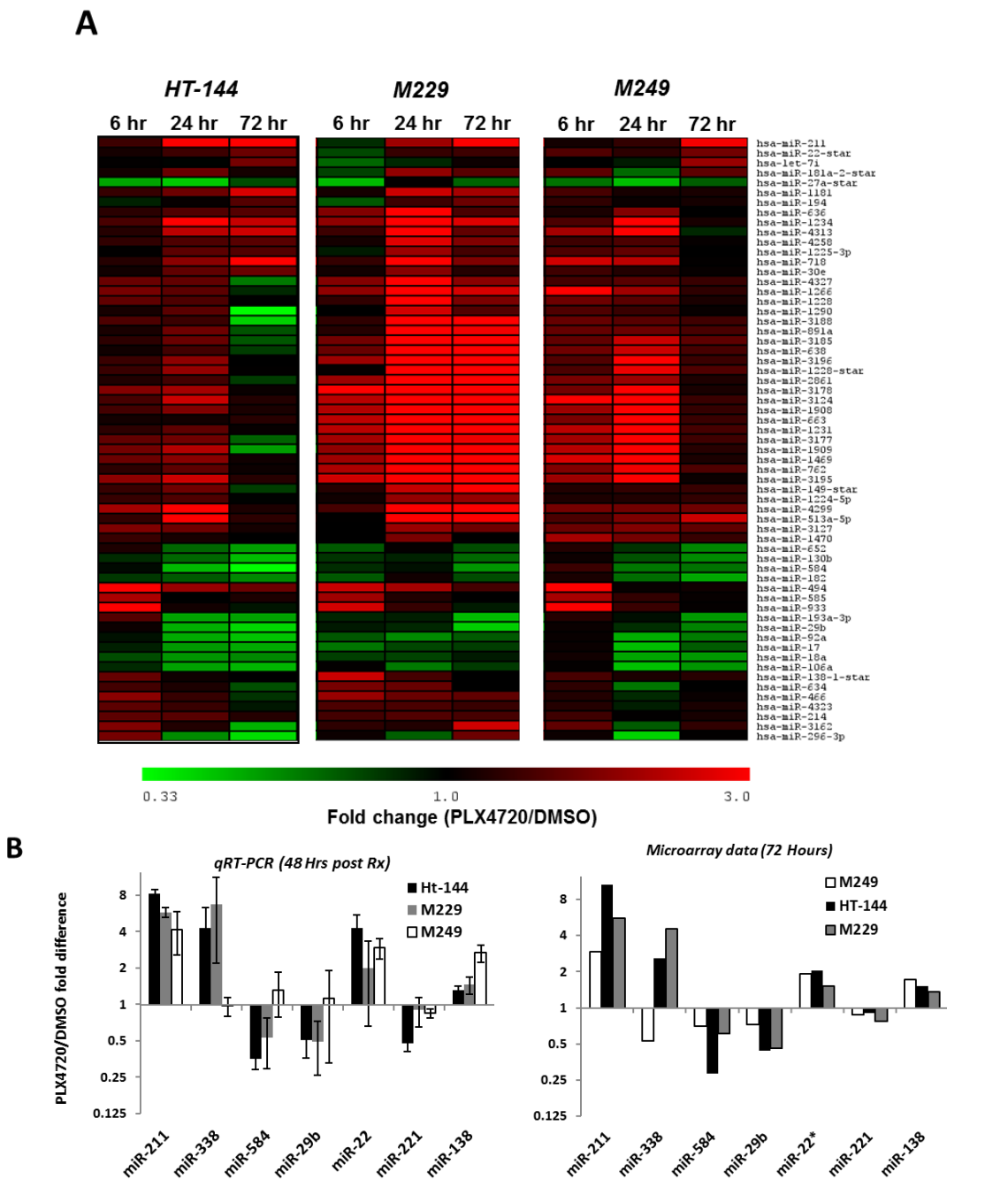

Figure 9.4: Kinetics of miRNA expression changes following B-Raf(V600E) inhibition by PLX4720 treatment. (A) Heat map of differentially expressed microRNA in three cell lines over time. (B) Real-time PCR validation of microarray results.

9.3.4 microRNA expression changes following PLX4720 treatment are specific to treatment response.

We examined the expression of several PXL4720 responsive microRNAs following PLX4720 treatment in two human melanoma cells lines lacking a B-Raf(V600E) mutation (M202, M207) and two cell lines with acquired resistance to Vemurafenib (the clinical version of PLX472) (Fig. 9.5). We did not observe alterations to the expression of treatment responsive microRNA in these cell lines. These data suggested that the microRNA expression changes following PLX4720 resulted from response to BRAF inhibition rather than non-specific effects of the compound itself. Additionally, full microRNA transcriptome analysis of two Vemurafenib resistant cell lines, M229 R5 and M249 R4, following 6 hours of PLX4720 treatment resulted in no significant changes to the expression of any microRNA.

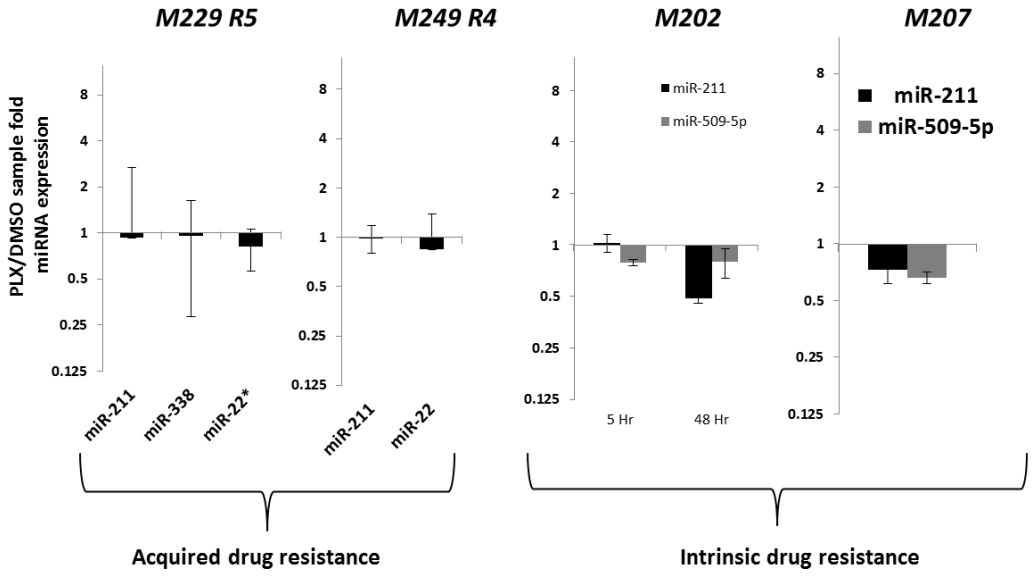

Figure 9.5: PLX4720 did not induce changes in microRNA expression in treatment resistant cell lines. Real-time PCR expression analysis of microRNA expression.

9.3.5 microRNA expression changes following PX4720 are dose dependent.

We examined the dose dependence of PXL4720 induced microRNA expression changes in HT-144 cells. We observed a correlation between PLX4720 concentration and magnitude of the change in microRNA expression.

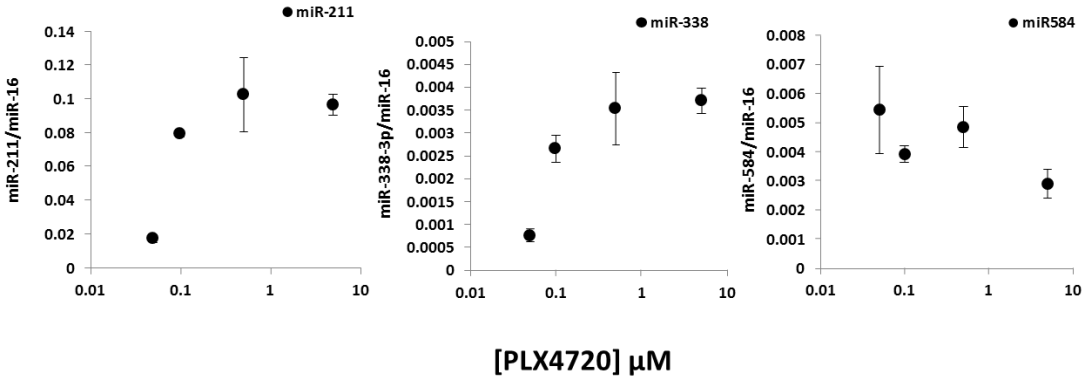

Figure 9.6: Dose dependence of PX4720 microRNA expression changes. Real-time PCR analysis of microRNA expression in HT-144 cells that were treated with the indicated amount of PX4720 for 48 hours. Expression data are normalized to miR-16.

9.3.6 Correlation of PLX4720 induced microRNA changes and cellular responses to PLX4720 treatment.

We next examined the relationship between cellular response to PXL4720 treatment and kinetics of PLX4720 induced microRNA expression changes (Fig. 9.7). MAPK pathway output was rapidly suppressed following B-Raf inhibition (Fig. 9.7A). However, cell cycle arrest did not initiate until 12 hours after treatment and was not complete until 24 hours (Fig. 9.7B). Apoptosis occurred after prolonged B-Raf inhibition (48 hours) (Fig. 9.7C).

The majority of PLX4720 induced microRNA changes were observed at 24 hours after PLX4720 treatment. These changes were temporally correlated with complete induction of cell cycle arrest. The PLX4720 induced microRNA changes detected at 6

hours post dosing preceded cell cycle arrest by several hours and may likely have been more directly due to drop in MAPK pathway output.

The microRNA changes observed in the microRNA study at 72 hours were found to be temporally correlated with apoptosis initiation. We examined miR-211, miR-584, and miR-338-3p expression at multiple time points after PLX4720 treatment (Fig. 9.7D). We found that PLX4720 induced changes in their expressions reached their highest magnitude by 48 hours post treatment, which correlated with significant apoptosis induction. These data suggest that these microRNAs are expressed in the remaining live cells in the culture dish. Therefore, these microRNAs may be both indicators of drug activity and emerging resistance.

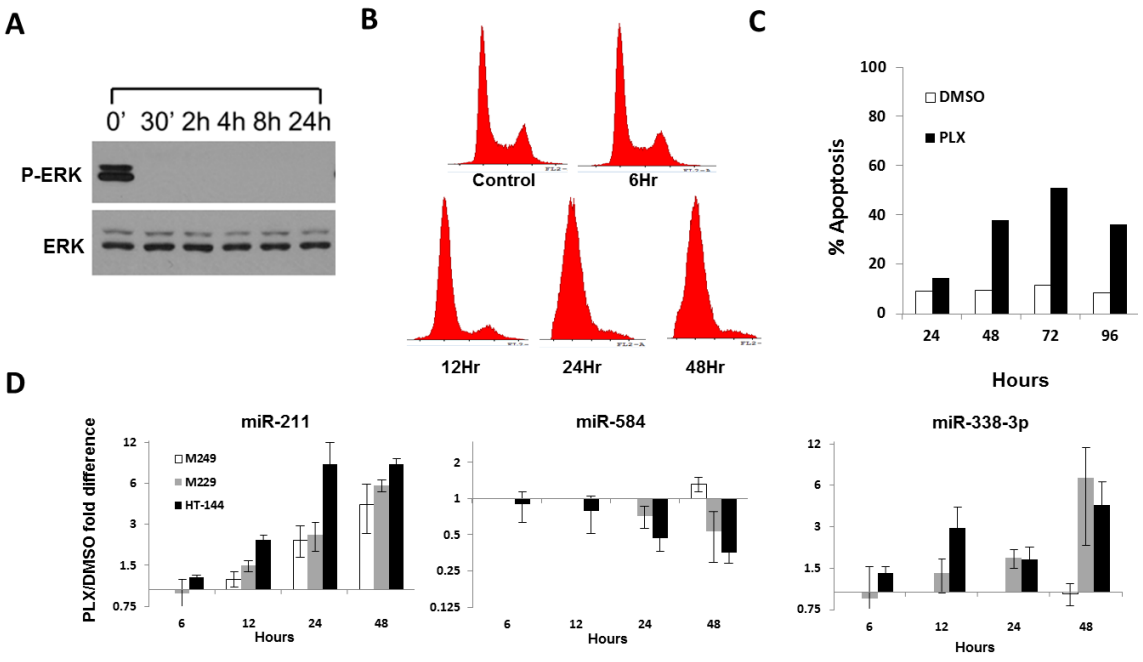

Figure 9.7: Late PLX4720 response microRNAs were temporally correlated with cell cycle arrest and apoptosis rather than MAPK pathway inhibition. (A) Western blot analysis of phosphorylated ERK1/2 levels following B-Raf inhibition with vemurafenib (data reproduced from[17]). Flow cytomerty based (B) cell cycle analysis and (C) Annexin V apoptosis analysis of M229 cells at multiple time points after PLX4720 addition. (D) Real-time PCR analysis of 3

PXL4720 responsive microRNA in M249, HT-144, and M249 melanoma cell lines at several time points after PLX4720 treatment.

9.3.7 BRAF inhibitor resistance is associated with changes in microRNA expression.

We hypothesized that acquired resistance to BRAF inhibitor therapy would result in an altered microRNA expression pattern in those cells. To test this hypothesis, we examined the microRNA expression profile via microRNA analysis on two melanoma cell lines with acquired resistance to Vemurafenib (M229 R5 and M249 R4) in the presence and absence of PX4720. We observed many significant microRNA expression changes in both cell lines compared to their sensitive parent cell lines (Table 9.1).

There were considerably more microRNA expression changes in the M229 R5 cell line than the M249 R4 cell line. The expressions of 93 microRNAs were found to be significantly changed by at least 2 fold (including 15 with >10 fold changes) in M229 R4 cells compared to M229 cells. miR-146a, a microRNA found in high abundance in all the melanoma cell lines profiled, was found to be completely silenced in the M229 R4 cells (>1000 fold decrease in expression). The PLX4720 inducible microRNAs miR-211, miR-338-3p, and miR-204 were all observed to be down regulated in M229 R4 cells. The PLX4720 repressed miR-584 was found to be down regulated in M229 R4. PCR was used to confirm the expression differences in these microRNAs of interest (Fig. 9.8B).

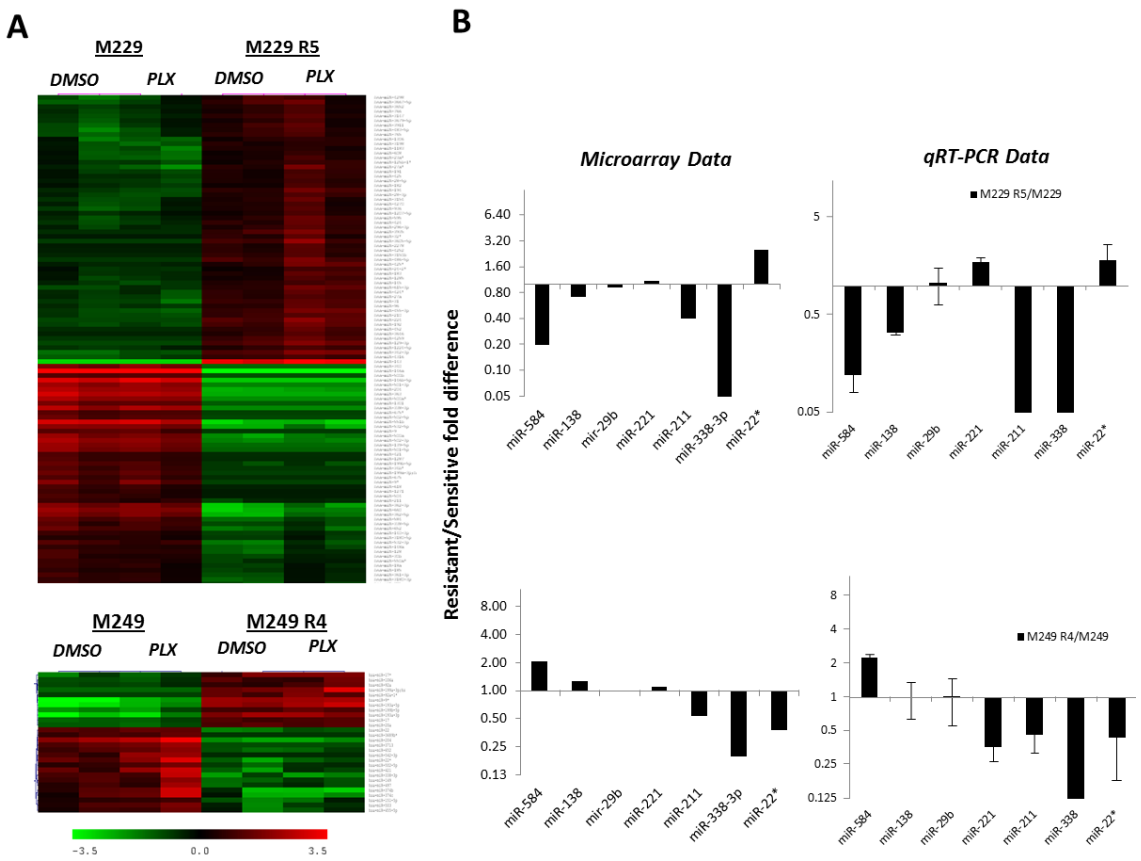

Figure 9.8: microRNA profiling of melanoma cell lines with acquired resistance to B-Raf inhibitor therapy. (A) Heat map of significantly differentially expressed microRNA (Median FDR<0.1%, 2 fold cut off). Cells were grown in 1uM PLX4720 or DMSO control for 6 Hr. (B) Real-time PCR validation of microarray expression data.

M249 R5 cells were observed to have 20 microRNAs differentially expressed at least 2 fold from M249 cells. All microRNAs were within an order of magnitude of expression between the two cell lines.

The mechanisms of Vemurafenib resistance of these two cell lines are known[20]. M229 R4 was found to have up regulated expression and activity or platelet derived growth factor beta (PDGFRβ) that circumvents B-Raf signaling. M249 R5 was found to have acquired an activating N-Ras mutation directly upstream of B-Raf. The microRNAs found to be differentially expressed between M229 R5 and M229 cells likely represent

direct targets of PDGFRβ. microRNAs found to be differentially expressed in M249 R5 versus M249 are likely direct targets of MAPK signaling in melanoma.

9.3.8 PLX4720 treatment induced changes in microRNA levels in exosomes.

We hypothesized that the observed intracellular microRNA expression changes in response to PXL4720 treatment would be recapitulated in the exosomes secreted from these cell lines. To test this hypothesis we examined the microRNA profile of exosomes from melanoma cell lines treated with PLX4720.

We observed significant microRNA level changes after PLX4720 treatment in exosomes secreted from each cell line examined (Fig. 9.9). Between 12 (M249) and 36 (HT-144) micoRNAs were found to be differentially secreted in exosomes from PLX4720 and vehicle treated cells. PLX4720 did not induce any changes in microRNA levels in exosomes from a PLX4720 resistant cell line (M202).

M229 R5

Down-Regulated		Up-Regulated	
microRNA	Fold Change	microRNA	Fold Change
miR-146a	-1179.41	miR-143	79.27
miR-146b-5p	-55.90	miR-342-3p	6.61
miR-551b	-44.94	miR-224	5.23
miR-363	-30.71	miR-129-3p	5.14
miR-204	-22.98	miR-455-3p	4.96
miR-338-3p	-18.31	miR-192	4.47
miR-660	-16.47	miR-3605-5p	4.32
miR-500a-star	-15.83	miR-31	4.14
miR-532-5p	-15.32	miR-27a-star	4.10
miR-501-3p	-14.58	miR-210	3.91
miR-502-3p	-14.03		
miR-362-3p	-13.07		
miR-362-5p	-12.26		
miR-500a	-11.90		
miR-139-5p	-9.72		
miR-340	-9.11		
miR-501-5p	-8.33		
miR-1301	-6.27		
miR-652	-5.14		
miR-9-star	-5.12		
miR-584	-4.98		
miR-500b	-4.95		
miR-502-5p	-4.62		
miR-532-3p	-4.33		
miR-199a/b	-4.21		
miR-9	-4.08		
miR-199b-5p	-3.95		

M249 R4

Down-Regulated		Up-Regulated	
microRNA	Fold Change	microRNA2	Fold Change
miR-204	-6.35	miR-9-star	7.97
miR-374b	-4.15	miR-193a-5p	7.03
miR-22-star	-3.85	miR-193a-3p	6.32
miR-338-3p	-3.61	miR-199a/b	3.89
miR-421	-3.35	miR-199b-5p	2.99
miR-3713	-2.85	miR-17-star	2.93
miR-22	-2.85	miR-20a	2.54
miR-652	-2.73	miR-17	2.48
miR-149	-2.53	miR-106a	2.25
miR-151-5p	-2.05	miR-92a	2.05

Table 9.1: Highly differentially expressed microRNA in Vemurafenib resistant cell lines. Fold change = ratio of expression level in resistant cell line compared to its drug sensitive parental cell line. Only microRNAs with at least a 4 fold change in expression in the M229 R5 cell line were listed. All significantly differentially expressed microRNAs in M249 R5 were listed.

However, there were no significant microRNA level changes common in exosomes among all 3 cell lines. 3 microRNAs were found to be significantly elevated in 2 of the 3 cell lines, miR-211, miR-338-3p, and miR-204. miR-211 and miR-204 were also found to be elevated though not to the level of statistical significance in exosomes from the third cell line, whereas miR-338-3p was only elevated in M229 and HT-144 exosomes. miR-22* was also found to be induced by PLX4720 treatment in M249 and HT-144 exosomes via PCR (Fig. 9.9B).

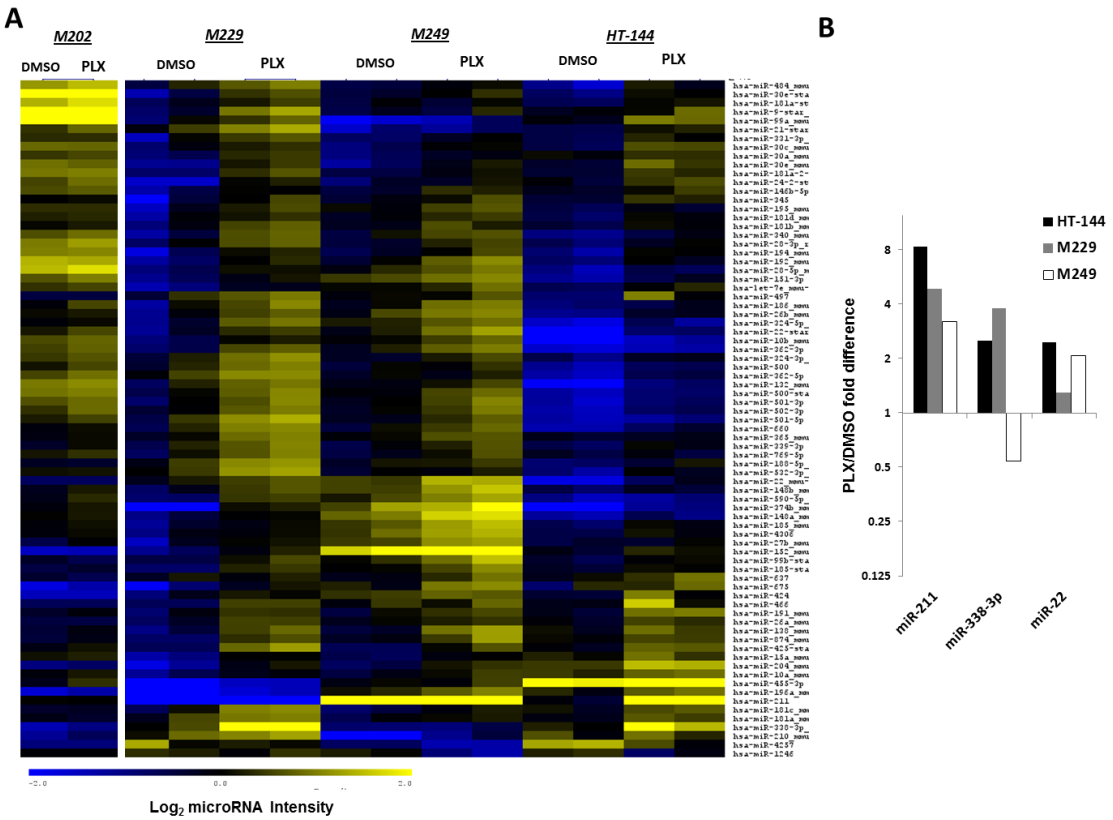

Figure 9.9: (A) Heat map of significantly differentially expressed microRNA in exosomes from the indicated melanoma cell line (Median FDR<0.1%, 1.5 fold cut off). M229, HT-144, and M249 are sensitive to B-Raf inhibition, M202 is resistant. (B) Real-time PCR validation of microRNA levels in exosomes from the indicated cell lines following PLX4720 treatment or vehicle control.

9.3.9 Quantitative proteomic analysis of melanoma exosomes following PLX4720 treatment.

We also hypothesized that PLX4720 treatment would result in detectable changes to the exosomal proteome. To test this hypothesis we employed label-free quantitative mass-spectrometry analyses to examine the M249 exosomal proteome in the presence or absence of PLX4720. We observed clear changes to the exosomal proteome in the presence of PLX4720 (Table 9.2). 84 proteins were found to be uniquely present in exosomes secreted from PLX4720 treated cell lines. 52 proteins identified in exosomes

from vehicle treated cells were not detected in exosomes from the PLX4720 treated cells. Of particular note, was the presence of VEGFRs and PDGFRs only in exosomes from PLX4720 treated samples. Up regulation of these receptor

Uniquely identified in Exosomes following PLX4720 treatment	Enriched in Exosomes following PLX4720 treatment		Depleted from Exosomes following PLX4720 treatment		Not identified in Exosomes following PLX4720 treatment
Gene Symbol	Gene Symbol	PXL4720/DMSO Fold Change	Gene Symbol	PXL4720/DMSO Fold Change	Gene Symbol
H14	RS8	7.13	FN1	0.25	IL1AP
H12	H32	7.06	TSP2	0.18	UBL3
H13	H33	6.99	EDIL3	0.32	TSN9
RPL14	HIST1H3A	6.92	AAAT	0.36	GOG7B
RL10	H31T	6.92	CEACAM1	0.44	CH10
XRCC6	H4	6.69	DNJA1	0.45	IST1
HP1BP3	H3C	6.55	ADA10	0.43	VP37B
BAF	H2A2B	6.39	PLS1	0.48	AT1B1
TYRP1	H2A1H	6.36	RAP2B	0.59	ITIH5
GNB2L1	H2A1C	6.33	RAB7A	0.59	ANXA1
DHX9	H2AX	6.33	IGSF8	0.49	RGAP1
H2AY	H2A1B	6.30	AT1B3	0.60	M4K4
MPRI	H2A1D	6.30	UBA52/RPS27A/UBB/UBC	0.60	CALU
RL15	H2A2A	6.30	AT12A	0.54	DSG2
SYVC	H2A2C	6.30	ITA7	0.56	ANO6
PSD13	H2A1A	6.30	GRP78	0.65	PXDN
VGFR1	H2A1J	6.30	AT1A4	0.57	TENA
GSK3B	H2A3	6.30	AT1A3	0.60	UE2NL
VGFR2	H2A1	6.27	AT1A1	0.60	IF5A1
SRS11	H2AJ	6.23	ATP4A	0.63	VPS4A
PGFRA	H2AZ	6.23	RP1BL	0.63	K1C10
EPRS	H2B3B	6.20	UBA52/RPS27A/UBB/UBC	0.62	RAB23
VGFR3	H2AV	6.17	UBA52/RPS27A/UBB/UBC	0.62	NRP2
PGFRB	H2B1D	6.14	COPT1	0.45	PKHB2
RS3A	H2B2F	6.14	AT1A2	0.61	SCRIB
L1CAM	H2B1O	6.14	RAP1B	0.66	NEDD4L
K6PF	H2B2E	6.14	ICAM1	0.64	SPTAN1
RS27	H2B1H	6.11	ARF1	0.67	EPHA5
RS27L	H2B1J	6.11	FPRP	0.61	TSN14
HNRNPC	H2B1A	6.11	AT2B1	0.69	YES
SRSF3	H2B1K	6.08	SNP23	0.68	SERPINC1
RL10A	H2BFS	6.08	RADI	0.70	TS101
MK03	H2B1L	6.05	SCRB1	0.67	SRC
DDX17	H2B1M	6.05	PDC6I	0.63	PRPS3
COPB	H2B1C	6.05	EZRI	0.71	PZP
KIF5A	H2B1N	6.05	EPHA4	0.60	ACSL3
PLEC	H2B1B	6.05	CSPG4	0.67	SC6A8
PSDE	RL18	5.34	HSP7C	0.68	FARP2
RS24	MVP	4.20	HSP72	0.70	LASP1
RL5	XRCC5	4.03	CD59	0.71	DYN2
RL8	RL7	3.10			K1C15
RS14	CLH1	3.02			UBE2N
PRS10	CLH2	2.83			MOT7
NLK	RL29	2.61			SNTB1
FLT3	RL30	2.57			TBCA
SCAM2	MYH10	2.40			GDF15
NPC2	CAV1	2.35			E41L2
RS23	DYHC1	2.30			PSB9
LMNA	PSMD1	2.24			DLRB1
SYDC	TCPA	2.15			YKT6
DYNC1I2	CLCA	2.12			PSA6
DDX3X	TCPG	2.06			EPHA3
CTL2	AGRIN	2.06			
SMD3	SND1	1.97			
GNA13	SIAS	1.97			
RL32	TCPD	1.91			
RS3	ARP2	1.91			
SSBP	MYH11	1.91			
RL17	RPSA	1.87			

RS16	PLS3	1.85
2ABA	MYPR	1.82
HNRPU	RAN	1.81
YPEL4	TCPQ	1.77
COPG	MYH9	1.76
MAP4	PUR9	1.75
DPYL2	GNS	1.69
CATL2	MYO5A	1.68
EM55	FASN	1.67
RL28	TCPE	1.63
KIF5C	MFGM	1.63
PTGR1	IGSF3	1.59
ACON	UBA1	1.56
S10A6	HSPB1	1.54
FBRL	TBB4Q	1.53
FSCN1	WDR1	1.51
TIF1B	SERA	1.51
TPM4	TBB8	1.48
TPM2	SAHH	1.48
RAB6B	TBB4B	1.41
MYO5B	TBA1B	1.39
LIPB1	TBA1A	1.38
COMT	TBA4A	1.37
RL13		
PABP4		

Table 9.2: Label-free quantitative proteomic analysis of M249 exosomes 72 hours following PLX4720 treatment.

tyrosine kinases has been demonstrated to result from the release of feedback inhibition following treatment with MAPK targeted therapeutics. Increased levels of these proteins in exosomes could be useful for validating target inhibition. The level of Histones in exosomes from PLX4720 treated cells is greatly elevated, suggestive that apoptosis was occurring. These data suggest that exosomal proteins could be used to detect cellular response to B-Raf inhibition.

9.3.10 *In vivo* PLX4720 treatment induced miR-211 up-regulation in HT-144 tumors, but down regulation in circulating exosomes.

We hypothesized that microRNA changes in tumors and exosomes observed *in vitro* could be recapitulated in the *in vivo* setting. To test this hypothesis we treated HT-144 tumor bearing mice with 3 daily doses of 20mg/kg PLX4720 or vehicle control (DMSO) via intraperitoneal administration. 72 hours after initiating treatment the mice were euthanized and blood and tumors were collected.

Total RNA from the tumors were collected and probed for miR-211 levels. We observed a 2 fold significant increase in miR-211 expression in tumors from PLX4720 treated mice compared to vehicle control. These data confirm that microRNA can indicate drug activity *in vivo*.

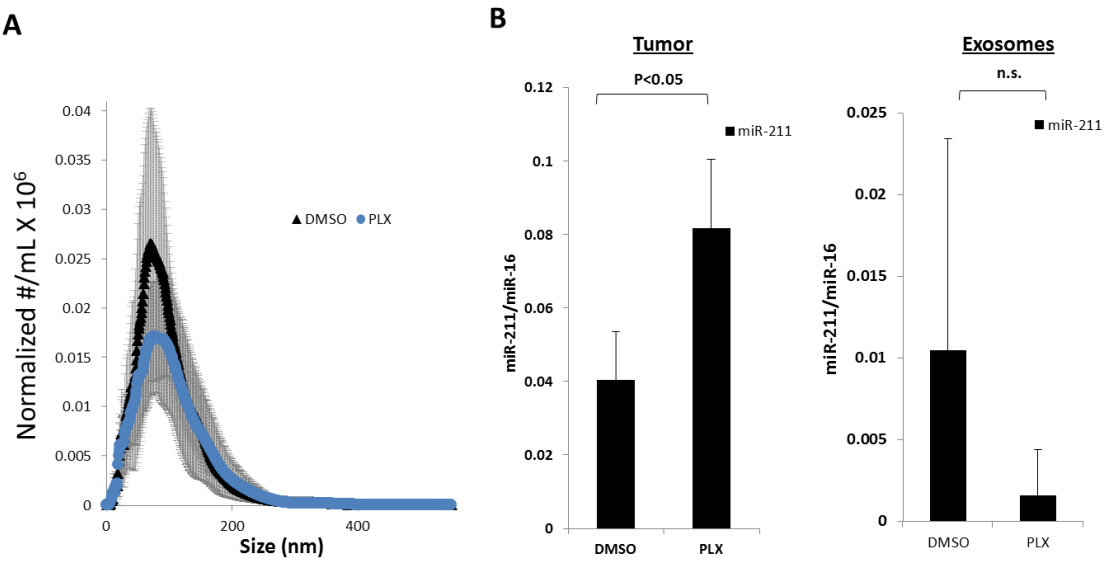

Figure 9.10: Characterization of serum exosomes from HT-144 tumor bearing mice treated with PXL4720. (A) Nanoparticle tracking analysis of exosomes in serum. (B) PCR quantification of miR-211 levels in tumors and serum exosomes. Error bars=S.D., n=5. P-values are from two tailed t-test.

We isolated exosomes from the serum of all mice used in this study via exoquick precipitation. Exosomes from all animals were characterized via nanosight analysis. Exosomes were found to have an average size of ~80nm in both treatment groups. A ~2 fold decrease in the total number of exosomes was observed in the serum of the PLX4720 treated mice; however, this was not statistically significant.

We then isolated RNA from the exosomes and quantified the amount of miR-211 levels from each sample. Surprisingly, we observed a ~80% drop in miR-211 levels in the serum exosomes from PLX4720 treated mice compared to controls. These data were

consistent with the finding of reduced exosome number, but inconsistent with our *in vitro* results of miR-211 induction following PLX4720 treatment.

9.3.11 MicroRNA profiling of plasma from PRE and POST treatment samples from melanoma patients enrolled in BRAF inhibitor clinical trials.

We examined the plasma microRNA profile of 7 melanoma patients and 5 healthy controls via microarray analysis. Paired PRE and POST treatment samples were available for 6 of the melanoma patients. Patients were on therapy with Vemurafenib or GSK2118436 B-Raf inhibitors and remained on therapy continuously in the interim between PRE and POST samples. All patients were responding to drug at the time of the post treatment sample collection. Total plasma RNA was extracted from all plasma samples and subjected to microarray analysis.

Melanoma patient plasma was clearly distinct from the healthy controls (Fig. 9.11A). 188 microRNAs were found have altered expression in the plasma of melanoma patients. Most of these were increases in microRNA levels with only 2 microRNAs, miR-720 and miR-4290 decreased in melanoma patient plasma. Many microRNAs were found to be present at levels greater than tenfold compared to the healthy control plasma (Fig. 9.11B). Several of the most enriched microRNAs in melanoma patient plasma were known oncomirs including miR-20a, miR-19b, and miR-17[21].

We next compared the PRE and POST treatment melanoma plasma pairs (Fig. 9.12). On average, there were no differences between the PRE and POST treatment patient samples. On a patient by patient basis there was some evidence for treatment related microRNA level changes. We observed large changes in plasma microRNA levels following treatment initiation in 4 out of the 6 patients examined (Fig. 9.12). We

observed almost no changes in plasma microRNA levels in patients MR and DJ. In the 4 patients with large changes in microRNA expression levels there was some potential correlation between microRNA level changes among the patients.

A

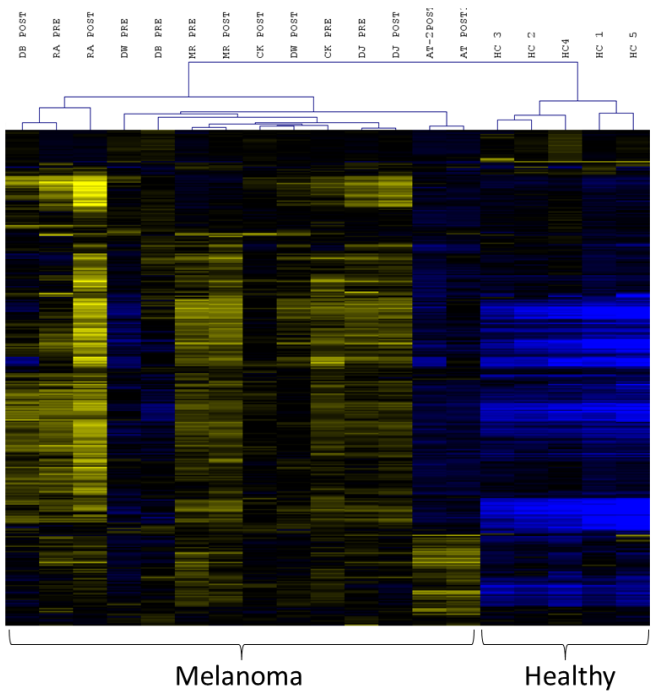

B

	PRE v CON Fold change	POST v CON Fold change	P value	FDR
hsa-miR-223	104.63	73.36	<0.00001	<0.00001
hsa-miR-106a	93.75	94.39	<0.00001	<0.00001
hsa-miR-19b	84.90	72.69	<0.00001	<0.00001
hsa-miR-20a	73.82	83.62	<0.00001	<0.00001
hsa-miR-17	72.69	71.50	<0.00001	<0.00001
hsa-miR-93	66.74	69.48	<0.00001	<0.00001
hsa-miR-130a	65.84	63.72	<0.00001	<0.00001
hsa-miR-199a	56.17	52.75	<0.00001	<0.00001
hsa-miR-15b	54.81	55.44	<0.00001	<0.00001
hsa-miR-185	51.01	47.56	<0.00001	<0.00001

Figure 9.11: MicroRNA profiling of plasma from melanoma patients in B-Raf inhibitor trials and healthy controls. (A) Heat map of all significantly differentially expressed microRNAs between melanoma patients and healthy controls. (B) Table of top 10 most highly increased microRNA in melanoma patient samples compared to health control. Fold change is ratio of average microRNA intensity for the indicated groups. PRE= before starting treatment, POST=after treatment, CON=healthy control.

12 microRNAs were found to be 6-25 fold higher in patients RA and DW whose post treatment plasma samples were collected within one month of treatment initiation (Table 9.3). Many of these same microRNAs were found to be decreased >4 fold in patients CK and DB whose post treatment plasma samples were collected several months after treatment initiation. The data point to these microRNAs as possible indicators of early drug activity and either longer term drug response or emerging resistance. We

observed several of these microRNAs to be responsive to B-Raf inhibition *in vitro* including miR-30e, let-7i, mir-320, and miR-584.

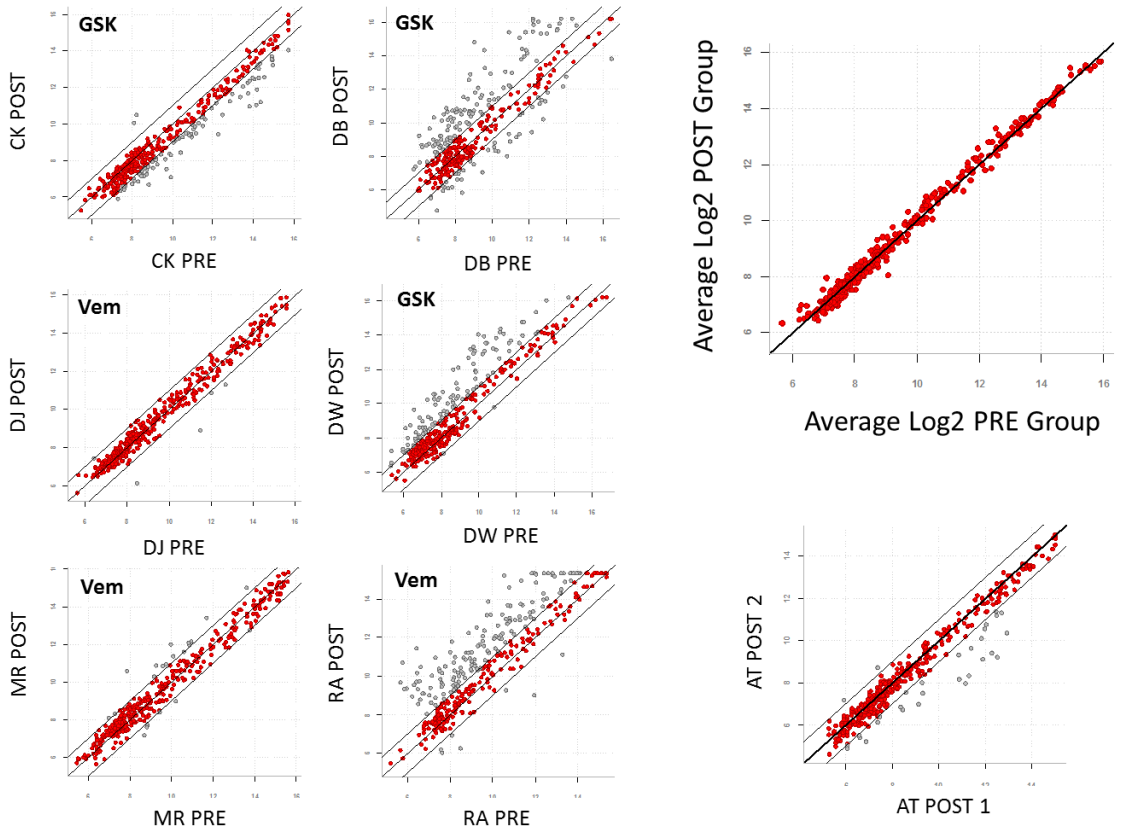

Figure 9.12: Patient by patient comparison of PRE and POST treatment plasma microRNA profiles. Scatter plots of Log_2 microRNA spot intensities from microarray data comparing PRE and POST drug treatment plasma samples. Grey coloring of spots indicates >2 fold change in level of microRNA in POST sample. Vem=Vemurafenib, GSK= GSK2118436 B-Raf inhibitors.

A unique set of microRNAs were found to be elevated in the post dose sample from patient DB. Several of these microRNAs were demonstrated to have highly altered expression in the vemurafenib resistant cell lines including mir-146a, miR-584, and miR-199a. Of note, no changes in miR-211 or miR-338-3p levels were observed in these experiments.

In parallel to the microarray experiment we also performed a more limited study of three microRNAs, miR-211, miR-338-3p, and miR-204, in patient plasma collected

from a larger panel of patients (Fig. 9.13). Plasma RNA was isolated from an additional 13 melanoma patients as well as additional post treatment samples from the 7 melanoma patients described above. Many patients had several post dosing samples including samples where these patients' cancers began progressing on treatment.

Plasma levels of miR-211, miR-338-3p, and miR-204, on average, were found to be elevated in the plasma taken from patients when their disease was progressing on treatment (Fig. 9.13). On average, miR-211 and miR-338-3p were also found to be highly elevated in melanoma patient plasma compared to healthy control plasma. For all these analyses the variability was very high and no data reached statistical significance.

	~5-6 Months after treatment initiation		~1 Month after treatment initiation			
Patient Initials	CK	DB	DJ	MR	RA	DW
DRUG	**GSK2118436**	**GSK2118436**	**Vemerafenib**	**Vemerafenib**	**Vemerafenib**	**GSK2118436**
miRNA	**Fold change POST/PRE**					
hsa-let-7i	0.20	0.48	1.07	0.96	10.31	12.27
hsa-miR-30e	0.25	0.34	0.87	1.45	25.59	10.22
hsa-miR-26b	0.14	0.18	0.70	1.61	17.12	7.82
hsa-let-7f	0.11	0.14	1.16	0.94	14.20	5.30
hsa-let-7d	0.14	0.23	0.86	1.38	12.08	9.25
hsa-let-7g	0.12	0.22	0.69	1.62	11.41	9.24
hsa-miR-19a	0.23	0.17	1.01	0.89	10.26	9.87
hsa-miR-144	0.14	0.17	0.56	2.01	30.96	3.44
hsa-miR-195	0.31	0.28	1.15	0.72	10.79	6.18
hsa-miR-301a	0.22	0.47	0.55	1.90	33.04	3.38
hsa-miR-101	0.60	0.21	0.76	0.77	11.17	3.72
hsa-miR-107	0.30	0.64	0.66	1.31	4.33	12.78
hsa-miR-625	0.34	0.93	1.45	0.59	13.01	8.62
hsa-miR-130a	0.37	0.48	1.36	0.71	6.59	16.92
hsa-miR-103	0.35	0.96	0.70	1.01	5.32	12.31
hsa-miR-182	0.47	0.42	0.71	1.28	16.31	2.46
hsa-miR-1	0.49	0.44	1.07	2.05	14.55	1.31
hsa-miR-16-2*	0.38	0.36	0.78	1.00	13.10	2.23
hsa-miR-410	0.52	0.47	1.96	1.08	12.64	2.59
hsa-miR-183	0.68	0.34	0.93	1.67	10.53	1.81
hsa-miR-487b	0.41	0.96	1.54	1.92	10.36	2.30
hsa-miR-146b-5p	0.39	13.82	1.27	1.18	2.96	1.65
hsa-miR-151-5p	0.51	12.37	1.16	0.85	2.39	1.92
hsa-miR-584	0.52	17.21	1.21	0.79	2.24	1.95
hsa-miR-425*	0.61	11.08	1.15	1.15	1.94	1.97
hsa-miR-199a-5p	0.81	27.46	1.28	0.74	1.80	1.72
hsa-miR-151-3p	0.79	54.38	1.72	0.96	1.12	0.68
hsa-miR-191	0.64	23.06	0.72	1.00	1.02	0.83
hsa-miR-146a	0.75	15.88	1.34	1.11	0.99	1.25
hsa-miR-320b	0.67	11.38	0.95	0.81	0.99	1.18
hsa-miR-320a	0.71	14.66	0.82	0.95	0.99	1.31
hsa-miR-320c	0.74	12.25	0.89	0.94	0.99	0.93
hsa-miR-320d	0.90	11.92	0.82	0.68	0.99	1.03
hsa-miR-320e	0.66	12.16	0.83	0.82	0.97	0.81
hsa-miR-324-5p	0.61	10.50	0.85	0.83	0.81	0.90

Table 9.3: Potential treatment related plasma microRNA level changes in patient plasma. All microRNAs with fold changes greater than 4 between PRE and POST samples in at least one patient are listed. Green=decreased after treatment, Orange=increased after treatment.

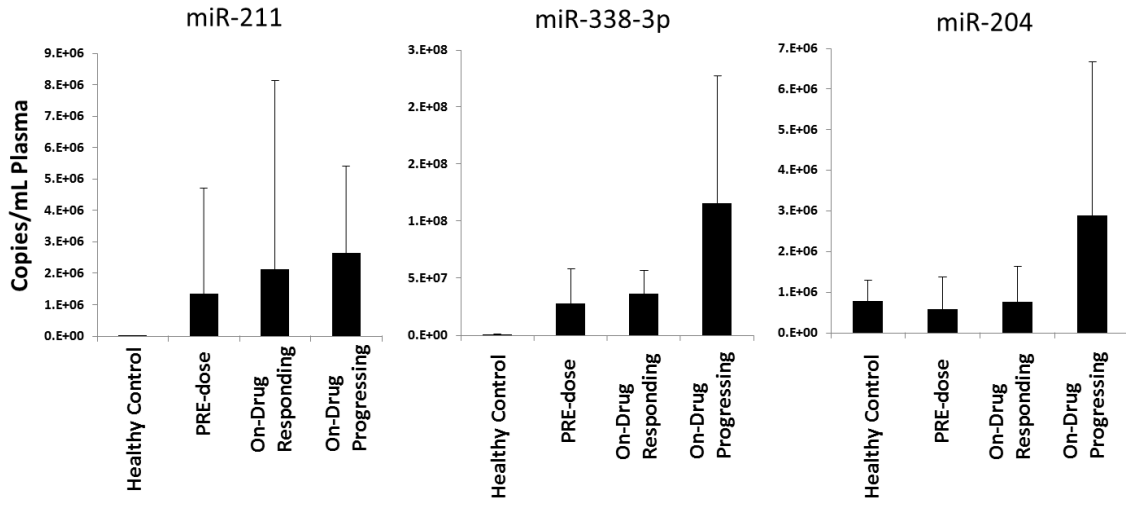

Figure 9.113: Plasma levels of miR-211, miR-338-3p, and miR-204 in melanoma patients and healthy controls. Real-time PCR analysis of plasma levels of the indicated microRNA. Healthy controls n=5; PRE-dose n=13 for miR-211, n=11 for miR-338-3p and mir-204, On-Drug responding n=30 for miR-211, n=14 for miR-338-3p and miR-204; On-Drug progressing n=10 for miR-211, n=8 for miR-338-3p and miR-204. Error bars are SD.

9.4 Discussion

Here, we have evaluated the potential of using the cellular material secreted in exosomes as markers of drug response and resistance.

The global RNA content of exosomes was found to be unique from the intracellular RNA profile. For long RNAs, exosomes were enriched for introns and inter-genic sequences. These data suggest that exosomes may be elimination pathways for these cellular materials. The relative abundances of mRNA gene transcripts were correlated between cells and their secreted exosomes. With small RNAs, exosomes were found to be enriched for tRNA and in M249 exosomes small cytosolic RNAs (scRNA). In a similar fashion to the mRNA transcripts, the relative abundances of mature microRNAs were found to be correlated between cells and their secreted exosomes.

Treatment of sensitive cell lines with the B-Raf inhibitor PLX4720 resulted in specific alterations to their microRNA transcriptomes over time. Several miRNAs have been associated with the MAPK pathway. The expression of miR-7, -221, and -222 can be regulated by the MAPK/ERK pathway[22, 23]. Also, the ERK inhibitor U0126 resulted in expression alterations to miR-17, -20, -92a, and let-7a in HeLa cell[24]. We also observed modulation of these microRNAs in our study as well as some additional microRNAs including miR-211, miR-338-3p, and miR-3663. miR-211 has been demonstrated to function as a tumor suppressor microRNA[25] and miR-338-3p has been demonstrated to be up regulated in N-Ras/B-Raf wild type melanoma tumors compared B-Raf/N-Ras melanomas[9]. The data suggest that these microRNAs may be important for the pathogenesis of B-Raf mutant melanoma.

We also identified microRNAs differential expressed in Vemurafenib resistant cell lines. The M229 R4 cell line, with up regulated PDGRβ signaling, showed more extensive perturbations to its microRNA transcriptome than the M249 R4 cell line that possessed an activating N-Ras mutation. These data suggest that different resistance mechanisms may be detected by analyzing microRNA profiles if these changes are recapitulated in exosomes. Additionally, these data point to many microRNAs that may be regulated by PDGRβ pathway and N-Ras mutations.

We were able to detect changes in the microRNA profile of exosomes secreted from PLX4720 treated cell lines. These data suggest that exosomal microRNA can be used to monitor drug activity. However, no distinctive treatment responsive microRNA profile emerged. Each cell line had distinct microRNA changes in their exosomes. Only miR-211 was found to be up regulated in exosomes following PLX4720 treatment in all

cell lines. Also, the magnitude of the microRNA expression changes in exosomes was rarely above 2 fold following PLX4720. We speculate that a much larger magnitude shift in microRNA levels would be required for successful implementation of exosomal microRNA markers for use in clinical samples.

In vivo we found that miR-211 expression was induced within PLX4720 treated tumors. However, the miR-211 level in circulating exosomes was decreased. However, the variability in these measurements was extremely higher, further suggesting that larger magnitude microRNA changes in response to treatment than those observed in our study would be required for a robust clinical assay.

There were many limitations to the microRNA profiling of the patient plasma samples including small sample size, multiple drugs, and inconsistent sampling times. Despite these limitations, several microRNAs of interest did emerge from this study. However, validation on a much larger and more standardized set of patients samples would be required to determine if these microRNAs can be used as marker so drug response and resistance.

From these studies we came to several conclusions about the use of extracellular microRNAs and exosomes as marker of drug activity. (1) We found that both mRNA and microRNA expression profiles are correlated between cells and their secreted exosomes. Therefore tumor derived exosomes in patient circulation may provide accurate information about the RNA transcriptome of a patient's tumors. (2) We found that microRNA expression alterations in response to B-Raf inhibitor therapy were transient (peaking at 24 hours). These data suggest that circulating microRNAs should be assessed between 24-48 hours after treatment initiation. (3) We found that drug resistance was

associated with many high magnitude (>10 fold) microRNA expression changes. We believe that monitoring circulating levels of these microRNAs may be useful for detecting and characterizing emerging drug resistance in patients. (4) We demonstrated that exosomal microRNA levels could be affected by PLX4720 treatment. These data demonstrate, in principle, that exosomal microRNA could be used to monitor drug activity. However, there was considerable variability in which microRNA levels were affected among the cell lines tested and the changes in these levels were low magnitude. Therefore, their utility for detecting drug activity in patients is still unclear. (5) We demonstrated that exosomal protein levels could be affected by PLX4720 treatment. These data demonstrated that protein markers of apoptosis (increased amounts of histones) and drug activity (detection of RTKs) could be monitored in exosomes. Because up-regulation of receptor tyrosine kinases (RTKs) (e.g., PDGFRβ) due to loss of feedback inhibition following drugging of an oncogenic kinase is emerging as a general phenomenon for these therapeutic agents, we believe that monitoring of these RTKs in tumor derived exosomes in patient circulation may provide confirmation of drug action. (6) Our *in vitro* and *in vivo* studies of miR-211 levels in exosomes secreted from HT-144 cells were inconsistent (up regulated *in vitro* and down regulated *in vivo*). We did observe up regulation of miR-211 within the tumor itself *in vivo*. Therefore, we hypothesized that the presence of non-tumor exosomes in the serum we collected confounded our results. We did observe some down regulation of miR-211 in drug insensitive cell lines (M202 and M207) and it is possible that non-tumor cell exosomal secretion of the murine miR-211 homologue from normal organs decreased in response to therapy and overwhelmed

the tumor signal. These data suggest that tumor exosomes should be isolated specifically for analyses from patient blood.

9.5 Materials and Methods:

Cell lines and culture

Melanoma cell lines M202, M229, and M249 cell lines were established from patient's biopsies under UCLA IRB approval #02-08-067 and have been previously characterized[17]. The HT-144, cell line was obtained from American Type Culture Collection (ATCC, Rockville, MD). All cell lines were cultured in complete serum media containing RPMI 160 with L-glutamine (Mediatech Inc., Manassas, VA) with 10% (all percentages represent v/v) fetal bovine serum (FBS, Omega Scientific, Tarzana, CA), 1% penicillin, streptomycin, and amphotericin (Omega Scientific) at 37°C with 5% CO_2 in filter-top flasks.

Exosome isolation

Cells were grown in media depleted of bovine exosomes (ultracentrifugation for 16hr at 100,00xg) for 72 hours. Media was clarified via centrifugation at 300xg for 5 minutes, the supernatant was centrifuged at 2000xg for 20 minutes to remove cell debris, and subsequently at 10,000xg to remove large vesicles. Exosomes were pelleted via ultracentrifugation at 100,000xg for 90 minutes, washed with 50mL of PBS, and re-pelleted. The final exosome pellet was suspended in PBS. Exosome yield was quantified using a BCA Assay (Thermo).

Electron Microscopy

Exosome samples were fixed in 2% paraformaldehyde. Farmvir carbon coated grids were floated on 5µl of fixed exosomes for 5 minutes, washed for 30 seconds in water, and stained with 3% uranyl acetate for 30 seconds. Grids were dried and visualization under a 120 kV BioTwin CM120 TEM (Philips).

Western Blot analysis

Total cell or exosome protein was extracted using RIPA Buffer (Thermo Fisher Scientific Inc., Waltham, MA). Lysates were diluted to equivalent protein concentration in beta-mercaptoethanol-containing Laimmli sample buffer (Thermo-Fisher) and incubated at 95^{o}C for 5 minutes. Antibodies: mouse polyclonal anti-NRAS antibody, mouse-polyclonal anti-hTFR, horseradish peroxidase-conjugated donkey anti-mouse immunoglobulin G (Santa Cruz Biotechnology, Santa Cruz, CA). Mouse anti-CD63 antibody (BD biosciences). Development was done using SuperSignal West Dura Extended Duration Substrate (Thermo-Fisher). Blot images were captured using a Molecular Imager VersaDoc 3000 system (Bio-Rad, Hercules, CA).

RNA isolation

Total RNA, including the low molecular weight RNA fraction, was isolated from cells using the miRVana isolation kit (Ambion) or TRIzol (Invitrogen) following manufacturer's instructions. Total RNA from exosomes was extracted using TRIzol-LS (Invitrogen) following manufacturer's instructions. RNA from cells was quantified using a Nanodrop 2000 spectrophotometer (Thermo) and RNA form exosomes or cell culture supernatant, was quantified via RiboGreen Assay (Invitrogen).

Microarray analysis and statistics

Fluorescent labeling and microarray hybridization were carried out by Ocean Ridge Biosciences (Jupiter, FL). Low molecular weight (LMW) RNA was purified from each cell sample by ultrafiltration. A set of 11 synthetic microRNAs are added at 1/100,000 dilution to each LMW purified cellular or total exosomal RNA sample. RNA samples are labeled with Alexafluor- 647 fluorophore using Invitrogen's Rapid Labeling kit. Labeled miRNA were hybridized to ORB's version 6.0 multispecies microarray, which provides full coverage of mirBASE version 15. After hybridization, the miRNA arrays were scanned using a GenePix 4000A array scanner (Axon Instruments, Union City, CA). Raw data intensities were Log_2 transformed. Spots with intensities < 2 standard deviations above the negative control spots were removed from further analysis. Data were quantile normalized (Matlab) and triplicate spots were averaged. Data analysis and clustering was performed using MeV 4.4. Differentially expressed miRNA among the 4 cellular and exosome miRNA data sets were determined using a one way ANOVA analysis. Differentially expressed miRNA between cellular and exosome samples or DMSO and PLX4720 treated samples were identified using significance analysis of microarrays (SAM) with the R package 'samr' on median centered normalized data divided into two groups for 2 class paired t-test analysis. Unsupervised hierarchical clustering analysis on the basis of Pearson correlation and complete/average linkage clustering was performed on significant miRNA from each analysis.

Real time reverse transcriptase PCR of miRNA

Taqman miRNA qPCR assays (Applied Biosystems) were used for quantification of miRNA from total RNA from cells, exosomes, or cell culture supernatant and carried out according to manufacturer's instructions. 5-10ng of total RNA was added to each reverse

transcription reactions and PCR reactions were performed in at least duplicate. Real-time PCR analysis was performed using a MyiQ Single Color Real Time PCR Detection System (Bio-Rad).

9.6 Acknowledgments.

This work was supported by the UCLA-Caltech Joint Center for Translational Medicine and the National Cancer Institute gran CA119347. We thank John Rossi, and Daniela Castanotto of City of Hope for facilitating the deep sequencing studies and Antoni Ribas and Charles Ng at the UCLA Jonsson Comprehensive Cancer Center for obtaining the patient plasma samples.

9.7 References:

1. Yap, T. a, Sandhu, S.K., Workman, P. & de Bono, J.S. Envisioning the future of early anticancer drug development. Nature Reviews Cancer 10, 514-523 (2010).

2. Mitchell, P.S. et al. Circulating microRNAs as stable blood-based markers for cancer detection. Proceedings of the National Academy of Sciences of the United States of America 105, 10513-8 (2008).

3. Sokolova, V. et al. Characterisation of exosomes derived from human cells by nanoparticle tracking analysis and scanning electron microscopy. Colloids and Surfaces. B, Biointerfaces 13-17 (2011).

4. Taylor, D.D. & Gercel-Taylor, C. MicroRNA signatures of tumor-derived exosomes as diagnostic biomarkers of ovarian cancer. Gynecologic Oncology 110, 13-21 (2008).

5. Logozzi, M. et al. High levels of exosomes expressing CD63 and caveolin-1 in plasma of melanoma patients. PloS one 4, e5219 (2009).

6. Rabinowits, G., Gerçel-Taylor, C., Day, J.M., Taylor, D.D. & Kloecker, G.H. Exosomal microRNA: a diagnostic marker for lung cancer. Clinical Lung Cancer 10, 42-6 (2009).

7. Skog, J. et al. Glioblastoma microvesicles transport RNA and proteins that promote tumour growth and provide diagnostic biomarkers. Nature Cell Biology 10, 1470-6 (2008).

8. Wang, K., Zhang, S., Weber, J., Baxter, D. & Galas, D.J. Export of microRNAs and microRNA-protective protein by mammalian cells. Nucleic Acids Research 1-12 (2010).

9. Caramuta, S. et al. MicroRNA expression profiles associated with mutational status and survival in malignant melanoma. The Journal of Investigative Dermatology 130, 2062-70 (2010).

10. Mueller, D.W., Rehli, M. & Bosserhoff, A.K. miRNA expression profiling in melanocytes and melanoma cell lines reveals miRNAs associated with formation and progression of malignant melanoma. The Journal of Investigative Dermatology 129, 1740-51 (2009).

11. Leidinger, P. et al. High-throughput miRNA profiling of human melanoma blood samples. BMC Cancer 10, 262 (2010).

12. Kanemaru, H. et al. The circulating microRNA-221 level in patients with malignant melanoma as a new tumor marker. Journal of Dermatological Science (2011).

13. Bollag, G. et al. Clinical efficacy of a RAF inhibitor needs broad target blockade in BRAF-mutant melanoma. Nature 1-5 (2010).

14. Chapman, P.B. et al. Improved survival with vemurafenib in melanoma with BRAF V600E mutation. The New England Journal of Medicine 364, 2507-16 (2011).

15. Grippo, J.F., D, P., Nolop, K. & Chapman, P.B. The New England Journal of Medicine. 809-819 (2010).

16. Joseph, E.W. et al. The RAF inhibitor PLX4032 inhibits ERK signaling and tumor cell proliferation in a V600E BRAF-selective manner. Proceedings of the National Academy of Sciences of the United States of America 107, 14903-8 (2010).

17. Søndergaard, J.N. et al. Differential sensitivity of melanoma cell lines with BRAFV600E mutation to the specific Raf inhibitor PLX4032. Journal of Translational Medicine 8, 39 (2010).

18. Poulikakos, P.I., Zhang, C., Bollag, G., Shokat, K.M. & Rosen, N. RAF inhibitors transactivate RAF dimers and ERK signalling in cells with wild-type BRAF. Nature 464, 427-30 (2010).

19. Théry, C., Amigorena, S., Raposo, G. & Clayton, A. Isolation and characterization of exosomes from cell culture supernatants and biological fluids. Current protocols in cell biology / editorial board, Juan S. Bonifacino ... [et al.] Chapter 3, Unit 3.22 (2006).

20. Nazarian, R. et al. Melanomas acquire resistance to B-RAF(V600E) inhibition by RTK or N-RAS upregulation. Nature 1-7 (2010).

21. Garzon, R., Marcucci, G. & Croce, C.M. Targeting microRNAs in cancer: rationale, strategies and challenges. Nature Reviews Drug Discovery 9, 775-789 (2010).

22. Dai, R. et al. miR-221/222 suppression protects against endoplasmic reticulum stress-induced apoptosis via p27(Kip1)- and MEK/ERK-mediated cell cycle regulation. Biological Chemistry 391, 791-801 (2010).

23. Chou, Y.-T. et al. EGFR Promotes Lung Tumorigenesis by Activating miR-7 through a Ras/ERK/Myc Pathway That Targets the Ets2 Transcriptional Repressor ERF. Cancer Research 70, 8822-8831 (2010).

24. Paroo, Z., Ye, X., Chen, S. & Liu, Q. Phosphorylation of the human microRNA-generating complex mediates MAPK/Erk signaling. Cell 139, 112-22 (2009).

25. Levy, C. et al. Intronic miR-211 Assumes the Tumor Suppressive Function of Its Host Gene in Melanoma. Molecular Cell 1-9 (2010).

Chapter 10: Future directions:

10.1 Improving circulation time is the key challenge for improving the efficacy of the siRNA/CDP nanoparticle system.

In Chapter 8 of this thesis we elucidated the mechanism of rapid clearance of the siRNA/CDP nanoparticle system, disassembly at kidney glomerular basement membrane. Development of nanoparticles that can avoid this mechanism of clearance is necessary to improve their pharmacokinetic profile and thereby their efficacy.

We believe there at least two promising design solutions to this problem. First, we hypothesize that siRNA nanoparticles with slightly negative zeta potentials will avoid this clearance mechanism. In Chapter 6 and 8 we demonstrated that PEGylated gold nanoparticles of similar size to the siRNA nanoparticles deposit within the mesangium, but not the glomerular basement membrane. The key difference between these two nanoparticle systems is their surface changes, positive for the siRNA nanoparticles and negative for the PEGylated gold nanoparticles. A siRNA nanoparticle with a negative surface potential will be repelled by the GBM, thereby preventing its disassembly and elongating its circulation time.

Second, we hypothesize that siRNA nanoparticles assembled via non-electrostatic interactions will not be susceptible to this mechanism of clearance. Disassembly of the siRNA nanoparticles at the GBM resulted from competition between the GBM negatively charged proteoglycans and negatively charged siRNA for binding to the positive CDP. If the nanoparticles were not assembled via electrostatic interactions this type of competition would not occur. We hypothesize that self-assembling polymer based siRNA nanoparticles can be created that do not use electrostatic interactions for assembly. We

propose the development of polymer delivery vehicles that are assembled via RNA base pairing between sense and anti-sense strands of siRNA that are each covalently linked to PEGylated polymer backbones. Creation of DNA nanoparticles through this type of interaction has been reported[1] and we see no barrier to extending this methodology to siRNA.

10.2 Clinical potential for Herceptin targeted siRNA nanoparticles.

In Chapter 4 of this thesis we demonstrated that Herceptin targeted siRNA nanoparticles achieved more potent therapeutic effects than Herceptin alone in a breast cancer mouse xenograft model. We also demonstrated that siRNA induced Her2 knockdown could be an effective therapeutic option for Herceptin resistant Her2 (+) cancers. Future work with this system should be focused on evaluating a panel of Herceptin resistant cell lines with variable resistance mechanisms to learn which patients may benefit most from this treatment strategy. Additionally, subtypes of other cancers, most notably gastric cancers[2], have amplified Her2 expression. The Herceptin targeted siRNA nanoparticle system could also be evaluated for use in these cancer subtypes.

10.3 siRNA nanoparticles have promise for kidney disease.

In Chapters 8 of this thesis we demonstrated the ability of nanoparticles to reach the kidney and delivery siRNA payloads. There are many forms of acute and chronic kidney disease that could benefit from highly specific, kidney targeted therapeutics. Several proteins including, PDGFRβ and TGFRβ, that have been implicated in renal fibrosis in response to both acute and chronic renal injury[3]. These proteins are difficult to drug specifically via traditional small drugs and therefore are promising targets from siRNA based therapeutics. PDGFRβ has an expression pattern the kidney in heath and disease

that matches the deposition pattern of siRNA/CDP nanoparticle delivery system. We believe PDGFRβ is a promising therapeutic target for our delivery system for a multitude of kidney diseases.

10.4 Using microRNA as markers of drug activity in the clinic.

In Chapter 9 of this thesis we evaluated the use of microRNAs as markers of B-Raf inhibitor activity *in vitro, in vivo,* and in patients. Although we demonstrated that extra-cellular microRNAs in exosomes could be used as markers of drug activity, the microRNA changes associated with treatment appeared to be relatively cell line specific. In patients we observed a limited number of microRNAs that we speculate are related to drug treatment; however, they were not recapitulated in the pre-clinical models. Additionally, the magnitudes of the microRNA expression changes observed *in vitro* were low and may be difficult to detect in highly variable patient samples.

We believe future studies on exosomes from patient or animal serum would benefit from selective isolation of tumor derived exosomes. Our *in vitro* and *in vivo* studies of miR-211 levels in exosomes secreted from HT-144 cells were inconsistent (up regulated *in vitro* and down regulated *in vivo*). We did observe up regulation of miR-211 within the tumor itself *in vivo*. Therefore, we hypothesized that the presence of non-tumor exosomes in the serum we collected confounded our results. We did observe some down regulation of miR-211 in drug insensitive cell lines (M202 and M207) and it is possible that non-tumor cell exosomal secretion of the murine miR-211 homologue from normal organs decreased in response to therapy and overwhelmed the tumor signal. We believe that isolation of only the tumor derived exosomes could overcome these confounding factors. For experiments in animal models, tumor exosomes could be

isolated using antibody pull downs with validated antibodies that can distinguish human from animal exososome surface proteins (e.g., transferrin receptor). Isolation of tumor exosomes from patient samples is more challenging and efforts will have to be undertaken to discover specific markers on tumor exosomes to facilitate their isolation.

Another promising observation from our work on exosomes was the detection of certain receptor tyrosine kinases (e.g., PDGFRβ) in exosomes only after PLX4720 treatment. Because up-regulation of receptor tyrosine kinases (RTKs) due to loss of feedback inhibition following drugging of an oncogenic kinase is emerging as a general phenomenon for these therapeutic agents[4–6], we believe that monitoring of these RTKs in tumor derived exosomes in patient circulation may provide confirmation of drug action. We hypothesize that tumor exosomes isolated from melanoma patients on therapy could be analyzed via phosphor-RTK array following treatment initiation to examine for up-regulation of the activity of RTKs that indicate drug activity.

10.5 References:

1. Kim, J., Im, C.-A., Jung, Y., Qazi, A. & Shin, J.-S. Self-assembled nucleic acid nanoparticles capable of controlled disassembly in response to a single nucleotide mismatch. Biomacromolecules 11, 1705-9 (2010).

2. Fornaro, L. et al. Anti-HER agents in gastric cancer: from bench to bedside. Nature reviews. Gastroenterology & Hepatology 8, 369-83 (2011).

3. Perico, N., Benigni, A. & Remuzzi, G. Present and future drug treatments for chronic kidney diseases: evolving targets in renoprotection. Nature Reviews. Drug Discovery 7, 936-53 (2008).

4. Chandarlapaty, S. et al. AKT Inhibition Relieves Feedback Suppression of Receptor Tyrosine Kinase Expression and Activity. Cancer Cell 19, 58-71 (2011).

5. Pratilas, C. a et al. (V600E)BRAF is associated with disabled feedback inhibition of RAF-MEK signaling and elevated transcriptional output of the pathway. Proceedings of the National Academy of Sciences of the United States of America 106, 4519-24 (2009).

6. Duncan, J.S. et al. Dynamic Reprogramming of the Kinome in Response to Targeted MEK Inhibition in Triple-Negative Breast Cancer. Cell 149, 307-321 (2012).